UNIVERSITY OF CALIFORNIA,
IRVINE

Spectral Methods For Solving the Radiative Transport Equation in Single and Double Spherical Harmonics and Their Application to Optical Imaging

DISSERTATION

submitted in partial satisfaction of the requirements
for the degree of

DOCTOR OF PHILOSOPHY

in Mathematics

by

Sean Thomas Horan

Dissertation Committee:
Professor Vasan Venugopalan, Chair
John Lowengrub, Co-Chair
Professor Hongkai Zhao

2020

DEDICATION

For Samantha and my parents, without whose love and support I would never have accomplished half of this.

TABLE OF CONTENTS

LIST OF FIGURES

LIST OF TABLES

ACKNOWLEDGMENTS

I would like to thank the National Institutes of Health's T32 EB009418, National Institute of Biomedical Imaging and Bioengineering P41EB015890 and the National Science Foundation's IGERT Grant 1144901 for their generous financial support of my work. I would also like to thank the Center for Complex Biological Systems and the Beckman Laser Institute, particularly Dr. Carole Hayakawa for her help in understanding the use of her Virtual Tissue Simulator Command Line Monte Carlo as well as interpreting its data, as well as Karen Martin, and Professors Arthur Lander and Bruce Tromberg. I would particularly like to thank my co-advisors, Professors John Lowengrub and Vasan Venugopalan, for their help and mentorship throughout this time in my life. I would also like to gratefully acknowledge Professor Rolf Saager of Linkoping University for his work in constructing and measuring tissue phantoms, and for his guidance in understanding optical measurement design. Finally, I would like to thank my professors at UMSL, particularly Professors A. Prabhakar Rao, Ravindra Girivaru, Adrian Clingher, Ronald Dotzel and David Covert, whose support and confidence was vital in the early stages of my mathematical education.

VITA

Sean Thomas Horan

EDUCATION

Doctor of Philosophy in Mathematics **2020**
University of California, Irvine *Irvine, CA*

Master of Science in Mathematics **2016**
University of California, Irvine *Irvine, CA*

Bachelor of Science in Mathematics **2013**
University of Missouri, St. Louis *St. Louis, MO*

RESEARCH EXPERIENCE

Graduate Research Assistant **2014–2020**
University of California, Irvine *Irvine, California*

TEACHING EXPERIENCE

Teaching Assistant **2016–2020**
University of California, Irvine *Irvine, CA*

ABSTRACT OF THE DISSERTATION

Spectral Methods For Solving the Radiative Transport Equation in Single and Double Spherical Harmonics and Their Application to Optical Imaging

By

Sean Thomas Horan

Doctor of Philosophy in Mathematics

University of California, Irvine, 2020

Professor Vasan Venugopalan, Chair

Mathematical models of light propagation in turbid media are integral components of many optical imaging modalities. The radiative transport equation is a principal model and is commonly used to describe the behavior of light transport at distances larger than the average scattering length of light in a medium. Current deterministic methods tend to be computationally inexpensive but either do not accurately recreate scattered radiance in layered media. However, these methods are sufficient to obtain functionals of radiance such as fluence and reflectance, or only represent them for certain optical properties and at low ($\leq 0.1/l^*$) spatial frequencies. Stochastic methods are capable of higher degrees of accuracy but are often cumbersome to compute. I present a novel deterministic spectral method for solving the Radiative Transport Equation, based on double spherical harmonic functions, which is capable of accurate reconstructions of scattered radiance and is more robust to changes in spatial frequency. It is provides accurate reconstructions of radiance and various useful functionals thereof at much higher spatial frequencies than current best practices. I demonstrate both theory and MATLab implementation for homogeneous as well as layered media, and present a staged inversion method for the recovery of optical properties from layered media using the method of (single) spherical harmonic expansion upon which my proposed double spherical harmonic approach is based. This inversion technique may be

applied to any solution method for the Radiative Transport Equation.

Chapter 1

Background

1.1 Introduction

A rigorous mathematical model of the propagation and distribution of radiative energy such as light is critical to multiple fields of science and engineering, such as biomedical optics[29, 48], computer graphics[1], reactor physics[11] and atmospheric science[65]. Detailed mathematical models are used in applications such as the recovery of optical properties[29] from biological tissues, which in turn contain useful medical information[31]. While many modalities of optical monitoring, diagnostics, imaging, and therapy exist in the field of biophotonics, they all require mathematical models for the propagation and interaction of light in turbid media, i.e., a medium that can both absorb and scatter light.

Because the use of mathematical models for radiative transport is pervasive both in the design and operation of numerous biophotonics modalities, there is great demand for the development of fast, accurate, and efficient computational approaches[39]. This means that there is pressure for such models to be both fast and accurate, so that they can give reliable results in a useful amount of time. This is particularly important for certain types of optical

imaging[61], which often utilize optimization algorithms classical fitting techniques[29] such as Nelder-Mead[49] or Levenberg-Marquardt[47], both of which require numerous radiative transport calculations to obtain simulation results that best match measured data.

This dissertation will describe the development of a new method of quickly and accurately solving a commonly used model for radiative transport, the Radiative Transport Equation, and its application to the problem of optical property recovery from data obtained using a type of optical imaging known as Spatial Frequency Domain Spectroscopy[13]. In this chapter, I will give background information regarding the current understanding of the behavior of light in a turbid medium and mathematical models thereof. I will then describe the process of optical imaging employed in biophotonics application with a particular focus on spatial frequency domain methods. This will then motivate the specific biomedical, mathematical, and computational needs that must be satisfied by a new RTE solution approach for use in biophotonics applications.

Light is known to act as both an electromagnetic wave and as massless charged particles called photons. Descriptions of light both as particles and waves have found validity and utility. While mathematical models of both conceptions of light exist, I will focus on the particle conception. Many thorough treatments of the wave conception of light are given, focusing around Maxwell's Equations[44]. These give a rigorous and complete description of the behavior of electromagnetic waves, including behavior such as diffraction and interference, but are cumbersome to simulate as length scales increase past the nanometer range. While methods based around Maxwell's Equations are valuable for simulations on that range or when dealing with phenomena such which require a rigorous wave description of radiance[9], other conceptions are much more valuable as length scales increase to the point where scattering and absorption are the dominant behaviors of radiant energy and may be modeled as continuous actions rather than discrete ones.

1.2 The Radiative Transport Equation - Light As Energy

For these length scales, which often correspond to roughly 100μm in biological tissue, due to common length scales defined by scattering in this tissue[31], it is efficient to describe light as the motion of massless, charged particles (photons.) This shift in perspective provides an accurate description of the radiant energy, or radiance, of light, but since light is no longer treated as a wave, things like diffraction and interference patterns are no longer accurately captured. It is natural to to raise concerns over of the loss of these phenomena for this conception of light. However, these phenomena have relatively insignificant effects in biological tissue on length scales much greater than the wavelength of the light in question, and so this conception becomes appropriate when considering media on scales at or above that of individual cells.

These drawbacks are important to mention and to be aware of when designing any sort of optical application, but this conception of light still accurately captures radiant energy, a highly useful measure for applications across many fields. The dominant phenomena affecting radiance in this conception are absorption and scattering, and taking this into account yields the Radiative Transport Equation, or RTE (originally proposed in 1887 by Eugen von Lommel):

$$\nabla \cdot \Omega L\left(\Omega, r, t\right) + \tfrac{1}{c}\tfrac{\partial L}{\partial t}\left(\Omega, r, t\right) = -\mu_t L\left(\Omega, r, t\right) + \int_{4\pi} L\left(\Omega', r, t\right) p\left(\Omega', \Omega\right) d\Omega' + q\left(\Omega, r, t\right) \quad (1.1)$$

Here, L is radiant energy as a function of time (t), space (r) and propagation direction (Ω). It is important to note that this function commonly considers three spatial dimensions and

two angular ones, so that at any point in space and time, radiance becomes a distribution. This is not immediately obvious when attempting to build a mathematical description of radiance from the ground up, but is well illustrated when considering a common laser: at any point along its beam, radiance is high in the propagation direction of the beam but low in all other directions. The other quantities mentioned are the scattering (μ_s) and absorption (μ_a) coefficients, which describe the probability per photon of being scattering or absorbed per millimeter, the total attenuation coefficient ($\mu_t = \mu_a + \mu_s$), the speed of light in a given medium (c), the scattering phase function ($p(\Omega', \Omega)$) which describes the probability density function of radiance scattering from one propagation direction (Ω') to another (Ω) and the gain of radiance from any source (q). All of these quantities are functions of space and, in the case of q, time. It is important to note here that while scattering and absorption are discrete phenomena when referring to an individual photon, they are considered to be continuous processes in mathematical models of the RTE.

The RTE can be understood as stating that the total change in radiance in a given direction at a point in space and time is equal to the loss due to all attenuation, any gain due to scattering from other directions. It provides a complete and accurate description of scattering, absorption and radiation in any multiply scattering medium. Application of RTE solutions exist in fields such as atmospheric science and reactor physics, but the work in this dissertation will be constrained to simulating light propagation in biological media.

When modeling radiative transport with the RTE, it is often helpful to define length scales in terms of the rates of scattering and absorption, rather than absolute units. Since both μ_s and μ_a give an expected number of scattering and absorption events per millimeter, their multiplicative inverses give the expected distances between scattering and absorption events. This perspective is particularly helpful when considering variation in these values with respect to space, since some solution methods may have difficulty accurately reconstructing radiance in media where these values change rapidly compared to their own length scales.

When considering the scattering phase function, several quantities of interest arrive. First, it must be noted that this function must integrate to 1 over its domain, since it is a probability distribution. Second, its anisotropy, denoted g, is the average value of the cosine of the angle between the direction of light pre and post scattering. This is often of value when considering simplifications of the scattering phase function, and gives rise to the notion of a reduced scattering coefficient, μ_s', which is defined as $\mu_s(1-g)$. This value describes the average a length scale over which light can be treated as scattering isotropically, and may therefore be treated similarly to diffusion[68, 12]. This length scale is called the Transport Mean Free Path and commonly denoted l^*. This phenomenon arises from the fact as more scattering events occur, the probability of light being propagated in a given direction approaches a uniform distribution. Another way to phrase this is that information regarding the original propagation direction becomes lost as the number of scattering events increases, at a rate determined by the directionality of scattering.

While g has been used to characterize multiple classes of scattering phase functions, it is impossible to accurately form a basis for all possible, or even all useful functions, from a one dimensional value since any non-negative function defined on [-1,1] which integrates to 1 will serve as a scattering phase function. Other measures have been introduced as well[6], from linear or higher order moments of scattering, to relations between g and such moments. While these approaches and others have shown the utility of more robust classes of scattering phase functions, there is yet to be a universally accepted set of useful parameters. It therefore behooves any model of radiative transport to be as general as possible when considering potential scattering phase functions.

1.3 Approaches to Solving the RTE

1.3.1 Stochastic RTE Solutions

Stochastic, or Monte Carlo methods for solving the radiative transport mirror the quantum behavior of photons. While there are many variations[62, 77, 43, 42], they function on a common theme of scattering (and possibly absorption) happening as random events to photons, or packets of photons, traveling through a medium. The most basic estimators, known as analog, simulate individual photons and calculate the distance between scattering and absorption moments using exponential distributions defined by their attenuation coefficients. Directionality of scattering is likewise defined by random numbers generated according to the scattering phase function.

More complex estimators such as Discrete and Continuous Absorption Weight[27] work by simulating packets of photons rather than individual ones. In these cases, each packet is considered to have a given "weight" of intensity, which drops either continuously as it moves through a medium, or at discrete moments such as when scattering events occur. Packets may be deleted once they drop below a certain weight threshold or through random schemes. These methods have an advantage over analog ones in that each packet of photons can expect to survive much longer and still contribute detailed information of direction and intensity of radiance.

Monte Carlo methods have several distinct advantages relative to deterministic ones[78]. First, they can accurately reconstruct radiance in complex geometries because they build solutions through a series of simple interactions. Second, while the implementations can be quite complex, the behavior of light is often easier to understand through a local conception, which deals with individual photons or packets of photons, than a global conception, which demands a solution to radiant energy at all points and angles in a medium at once. Of course,

such methods have disadvantages as well. One of the most prominent of these is the high degree of computational power that it requires[75]. Since Monte Carlo methods are build around probability distributions and random numbers, they can require up to hundreds of millions of simulation runs to obtain desired levels of confidence in simulation results. This is particularly the case when dealing with complex media geometries[**?**] with features more thin than their own scattering and absorption lengths[72]. These mean that the average photon or packet passing through those regions may not interact, which further raises the number of simulation repetitions required to gain any desired level of confidence in an overall result. Despite this high expense, the potential for accurate simulations in complex media has led to Monte Carlo methods becoming a "gold standard" for judging other solution methods.

However, the computational expense associated with such results can become a limiting step when trying to solve an inverse problem, i.e., when trying to determine optical properties from a set of optical measurements. This is a necessary step in many optical imaging modalities. While some utility has been found through the use of Radon-Nikodym differentiation[26] to examine the effects of small changes in probability measures on precalculated Monte Carlo results, the most common approach to the curve fitting problem is the creation of large lookup tables of regenerated results[77]. These tables have the advantage of the highest possible computational efficiency, but are commonly used with various simplifying assumptions, such as identical scattering properties at all points in a given medium. Furthermore, the dimensionality of such a table increases with medium complexity. A biological tissue composed of an indeterminate number of layers each with different scattering and absorption properties, as well as high degrees of variation in scattering phase function, can make the generation and storage of such a table highly impractical.

1.3.2 Deterministic RTE Solutions

In the field of biomedical optics two main classes of deterministic approaches have been pursued to provide solutions to the RTE.

The first class of approaches is defined by the application of the Finite Element Method to discretize the medium through which radiance is transported, as well as potentially the time of transportation into a mesh. Radiance is then calculated at each point in this mesh via linearization. Finite Element Method approaches such as Gao and Zhao's Multigrid RTE[20] and the NIRFast project[15] have shown consistent, promising results for the simulation of radiance in a complex scattering environment. However, while these methods are not as computationally expensive as current Monte Carlo based solutions, they still tend to be much more expensive than those of the second group of interest. They also rely on linearizations which may not accurately capture angular radiance at a point and may require highly detailed meshes to simulate radiance in more complex media, such as biological tissue composed of multiple thin layers.

This class is of solutions based around the Spectral Method, or projection of the radiance L onto a functional basis. These bases are most commonly the Legendre Polynomials or Laplace's Spherical Harmonic Functions, which are based on the Associated Legendre Polynomials. These methods do not require a mesh based approach or any spatial, angular or temporal discretization, though angular resolution is limited by the order of expansion of the chosen basis. For this reason, many of these methods are often used to reconstruct functionals of radiance, rather than computing radiance directly. One common functional is fluence[10], the integral of radiance over all angles at a given point in spacetime, given here:

$$\mathrm{F(L(z))}=\int_{4\pi} L(z,\Omega)d\Omega \quad (1.2)$$

Another is transmittance, the integral of all radiance exiting a medium opposite an external

source. It is given here with z^* denoting the depth of the opposite end of a medium, $\gamma_F(\Omega)$ denoting Fresnel's law for internal reflectance and $2\pi^-$ denoting the hemisphere of propagation directions leaving that medium:

$$\mathrm{T(L)}=\int_{2\pi^-} L(z^*,\Omega)(1-\gamma_F(\Omega))\,d\Omega \quad (1.3)$$

A final is reflectance[21], the integral of all radiance exiting a medium on the same side of an external source. It is given here with $2\pi^+$ denoting the hemisphere of angles of propagation directions leaving that medium:

$$R(L) = \int_{2\pi^+} L(z^*,\Omega)(1-\gamma_F(\Omega))\,d\Omega \quad (1.3)$$

It should be noted that the $1-\gamma_F(\Omega)$ term in both reflectance and transmittance eliminates the effect of internally reflected at the boundary.

This focus on functionals is not a hard and fast rule, however, as some of these methods have been able to reconstruct radiance with a high degree of accuracy in certain situations[21] when compared to a Monte Carlo gold standard.

Several important methods from this group bear mention. The first is the Standard Diffusion Approximation[68], the computation of which is highly efficient. It treats light as a diffusive process with a diffusion constant of $1/3(l^*)$. The Standard Diffusion Approximation has been been shown to be accurate over length scales larger than l^* when media is highly scattering, which is often the case when considering biological tissue. The second is the $\delta-P_1$ method[10], which has been shown to provide more accurate reconstructions of fluence as a function of depth in a medium than the Standard Diffusion Approximation without increasing computational expense. It accomplishes this via the incorporation of a forward directed Dirac delta function into the expressions for radiance and the scattering phase

function, which captures some amount of higher order behavior in what would normally simply be a low order expansion.

The general P_N method[11] refers to the expansion of L in terms of Legendre Polynomials to order N and has been extensively studied and applied both for specific and general values of N. It is more computationally expensive than simpler methods such as the Standard Diffusion Approximation, but is capable of much higher levels of accuracy. The general P_N and several based upon it have been able to reconstruct radiance in several cases, though even the most accurate of them have achieved limited success. The simplified P_N, or SP_N, method first introduced by Gelbard[22] and more strongly justified by Larsen[36] and Pomraning[53] generalizes the one dimensional case of P_N to a three dimensional space. These, and all methods based purely on Legendre Polynomial expansion, however, have one major drawback: They cannot represent azimuthal asymmetry in radiance at any point[21]. This is because the Legendre Polynomials, when applied to the unit sphere, are all azimuthally symmetric.

This problem was first addressed by Gardner with his SHEF$_N$, or Spherical Harmonic Expansion with Fourier coefficients to order N, method[21]. As its name implies, this approach relies on the projection of L onto the space spanned by Laplace's Spherical Harmonic Functions, which form an orthonormal basis for $L^2(S^2)$. This allows SHEF$_N$ to properly simulate situations where radiance is not azimuthally symmetric at a point, such as those with spatially detailed or oblique sources. However, this method is more expensive than its cousin P_N, particularly at higher values of N. Laplace's Spherical Harmonic Functions, like the Legendre Polynomials on which they are based, have two index values, one for order and one for degree. This causes a quadratic growth in basis size when truncated to a specific N, as opposed to P_N's linear growth.

Due to SHEF$_N$'s expanded basis, it has been able to reconstruct scattered radiance, though even at higher orders of expansion ($N \geq 8$), this has required the use of sequential order smoothing, a technique in which solutions from SHEF$_N$ and SHEF$_{N+1}$ are both calculated

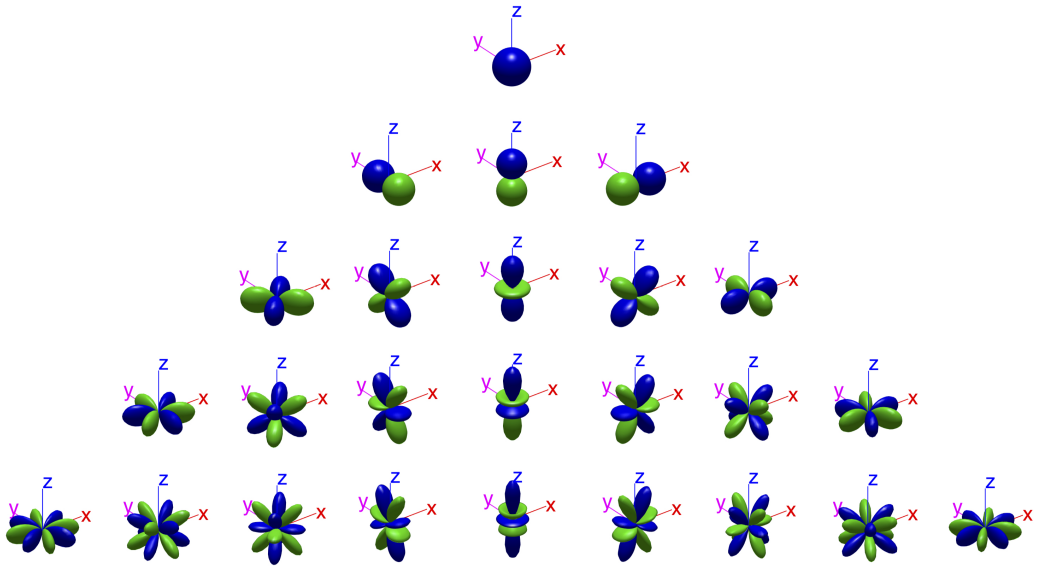

Figure 1.1: Illustration of Spherical Harmonics from order 0 (top row) to order 4 (bottom row), taken from [52]

and averaged together. Furthermore, it will be shown in this dissertation that large errors in angularly resolved radiance can occur in media composed of layers which are more thin than their own mean free path, in media where the rate of absorption approaches that of scattering and when light sources have spatially modulated components. Despite these, it remains a best practice in terms of spectral, deterministic solutions to the Radiative Transport Equation.

A method capable of delivering equal or better accuracy to SHEF$_N$ without post processing techniques such as sequential order smoothing and which is more robust to parameter selection is therefore highly desirable.

1.4 Optical Imaging

While mathematical models of light and other forms of radiant energy have many applications, the focus of this dissertation will be on biophotonics and optical imaging. Many optical

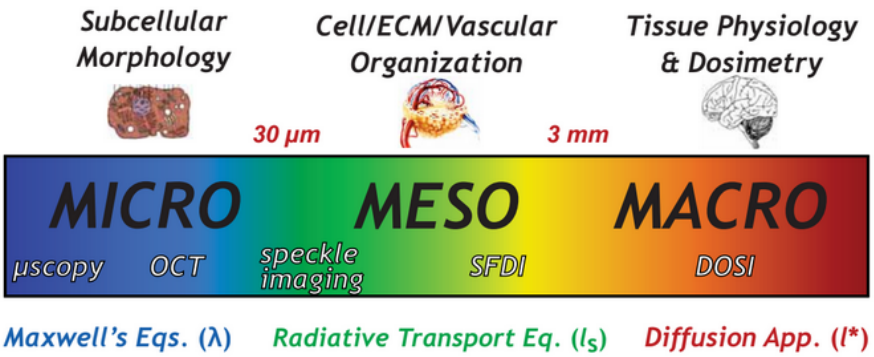

Figure 1.2: Length scales of light with corresponding imaging modalities and physiological phenomena, adapted from [67]

imaging modalities rely on the recovery of various optical properties[58, 71] of a biological medium and the relation of those properties to to biological function[31].

There are multiple imaging modalities with their own strengths and weaknesses and which focus on imaging at different length scales. Imaging at the micron scale begins with the various forms of microscopy available, as well as optical coherence tomography[30] and laser speckle imaging[17]. At this scale, wave models of light are often the most useful, leading to a dependence on Maxwell's equations. As length scales grow past ten times the average distance between scattering events, however, phenomena such as diffraction and interference which are captured by Maxwell's Equations but lost in the RTE have effects that become relatively small. Therefore, modalities operating at these scales which do not utilize these phenomena, such as spatial frequency domain imaging/spectroscopy become more useful, and the utility of models based around the RTE increases[46]. As length scales grow into and past the millimeter range, models based around light as a diffusive process[68], such as the standard diffusion approximation are of greater benefit. It should be noted that this conception is useful at wider length scales because the scattering coefficient of most biological tissue for light in the visible spectrum may be up to several orders of magnitude greater than the absorption coefficient corresponding to the same case.

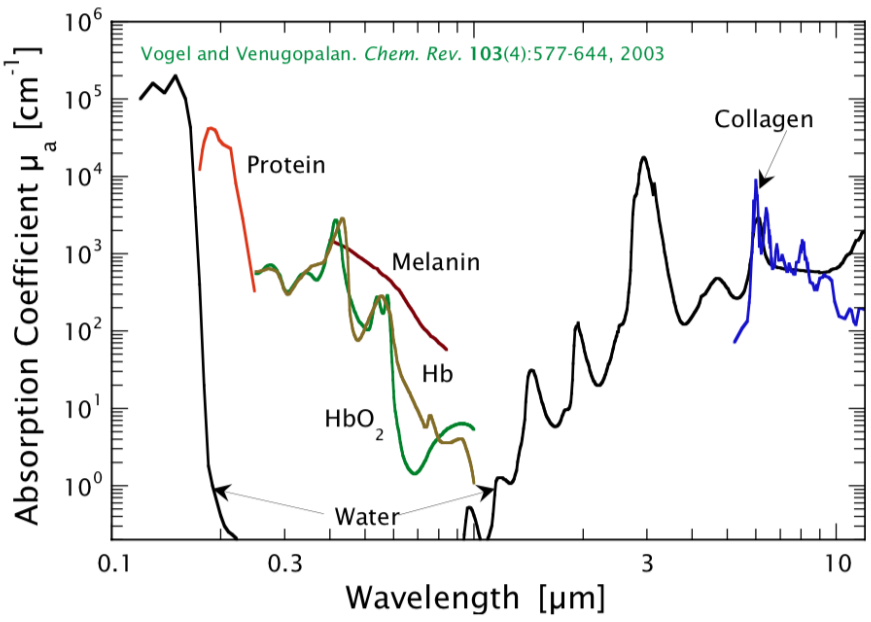

Figure 1.3: Scattering and Absorption Spectra of Common Chromophores in Human Tissue, adapted from [69]

1.4.1 Optical Properties and Physiological Information

The physiological significance of optical properties of tissue is perhaps most evident in the scattering and absorption spectra of that tissue[31]. Both of these values vary with the wavelength of light being considered, which means that μ_s and μ_a are properly thought of as functions of wavelength. They are commonly referred to as the scattering and absorption spectra.

While both scattering and absorption are functions of wavelength, the physics behind each phenomenon is quite different. Scattering is based on the size and shape of scattering particles in a medium. Its spectrum tends to follow either a single exponential decay or a sum of them, and depends on the concentration of scatterers and the distribution of their sizes and the fractal, or Hausdorff, dimensions of each scatterer. Common scatterers in biological media include mitochondria, melanocytes, lysosomes, nuclei and collagen. Some of these are roughly spherical spherical in shape, which simplified scattering phase functions. Since light modeled

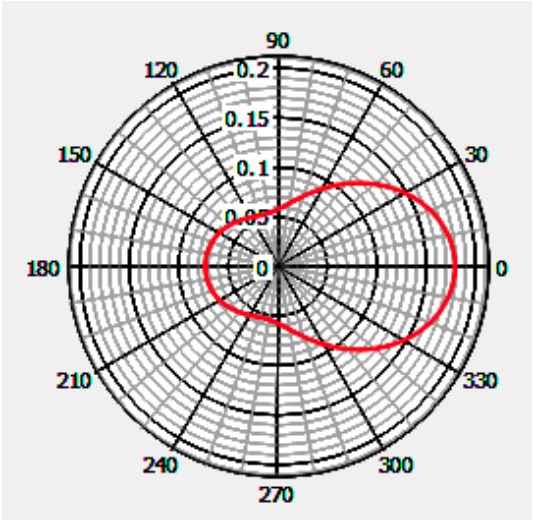

Figure 1.4: Scattering phase function for poly dispersed spherical scatterers with radius given by log normal distribution, mean 0.075μm, standard deviation 0.5μm, refractive index of scatterers = 1.5, medium = 1.3, created using [55]

as a planar wave must impact a sphere's surface at a normal angle, scattering of such a wave has no bias in any azimuthal direction. For those particles which are not spherical, phase functions based on The scattering phase function p of a given medium is also a function of wavelength and is derived from the size, shape and relative concentrations of these scattering particles[16].

A medium's absorption spectrum, on the other hand, is defined by its chemical composition. Chemicals which strongly absorb light at different wavelengths are known as chromophores, and each will have its own absorption spectrum, which may be highly structured[31]. A medium with multiple chromophores will have an overall absorption spectrum given by a linear combination of the spectra of each contained chromophore[70], with moments determined by their concentrations. The chromophores which most define absorption for light in the visible and near infrared spectra (roughly 400–1000nm wavelength) in biological tissue tend to be water, bulk lipids, hemoglobin and deoxyhemoglobin[31]. The functions of these chemicals imply that knowledge of their relative concentrations in tissue encode important physiological information, such as blood flow and oxygen saturation. It is for this reason

that the recovery of the absorption spectrum in particular is an objective of many types of optical imaging[38]. In addition, the highly structured nature of these spectra informs the choices of wavelengths used in various imaging modalities. When attempting to recover relative chromophore concentrations, it is necessary to choose wavelengths such that covariance of impact on absorption between each chromophore is minimized, as well as enough wavelengths to ensure a well defined problem in terms of dimensionality.

Several things are important to note when considering mathematical models of radiative transport in biological media. First, while optical properties of a given media may vary with respect to wavelength, mathematical approaches to radiative transport may be solved either one wavelength at a time, or many wavelengths in parallel. Therefore, RTE solutions generally do not need to explicitly consider wavelength but rather treat each spectrum and the scattering phase function as fixed. Second, while both scattering and absorption spectra encode different biological information, one cannot be considered in the absence of the other since each contributes strongly to the RTE.

1.4.2 Spatial Frequency Domain Imaging

One optical imaging modality in particular is strongly suited to the models which will be discussed in this dissertation: Spatial Frequency Domain Imaging, or SFDI[13]. This modality functions by projecting different wavelengths of light with various spatially modulated patterns onto a tissue and recording reflectance at different points of the tissue's surface as functions of both wavelength and spatial frequency of modulation. This method may be referred to as Spatial Frequency Domain Spectroscopy, or SFDS, when a wide variety of wavelengths are considered.

Biological tissue acts as a low pass filter with respect to spatial frequency[50]. This is due to the phenomenon by which the Standard Diffusion Approximation functions: As light

propagates in turbid media, spatial and angular distributions of radiance become smoother and less featured. Therefore, this reflectance will be more strongly influenced by shallow tissue at higher spatial frequencies, while it will be more strongly influenced by deeper tissue at lower spatial frequencies. Imaging depth varies based upon the type of tissue examined, but may function on length scales up to centimeters. In theory, this allows for depth resolved imaging of optical properties in biological tissue. In practice, however, detailed imaging as a function of depth is difficult to perform. This is partly due to a lack of mathematical models of the RTE which can quickly provide high fidelity results.

It should be noted that while detailed depth resolved imaging using SFDI/S has proven difficult[29], methods which treat biological tissue as having homogeneous optical properties with respect to depth have shown utility in diagnosing various maladies. The detection of pressure ulcers[73] and breast cancer[37], as well as the categorization of burn wounds[54] have all been accomplished through SFDI/S. Depth resolved optical property recovery using SFDI/S would enhance these applications and allow others to be developed.

1.5 Goals

Both deterministic and stochastic solutions to the RTE have been shown to be of utility in various optical imaging modalities. However, no model currently exists which can provide a high degree of accuracy for radiance in layered media on a fast time scale over a wide variety of optical properties and spatial frequencies. Monte Carlo simulations take hours to days, or even longer, to return approximations with high degrees of confidence. This is often mitigated through the use of look up tables[77] by which inversions can be performed, but these tables are limited in terms of dimensionality. While these tables provide the theoretical best performance in terms of computation, a highly complex medium composed of many layers of biological tissue has absorption and scattering spectra, as well as scattering

phase function, to consider for each layer. The expense of creating and storing such a table increase geometrically with the number of layers. In practice, these tables often contain simplifications such as the assumption that all layers of a medium share the same scattering spectrum and phase functions.

Conversely, the faster deterministic methods have been unable to approach the accuracy of Monte Carlo based ones in terms of radiance and have had particular difficulty in layered media with layer thicknesses significantly smaller than l^*. Therefore, a model which can provide accuracy approaching that of Monte Carlo methods at speeds on the order of magnitude of commonly used deterministic ones would be highly valuable. It would enable the use of detailed inversion methods in complex tissues without the need for many of the simplifying assumptions in common use. In particular, it would be a key component for the improvement of depth resolved SFDI/S methods, especially for the eventual development of SFD tomography methods.

The goal of this dissertation is to demonstrate a new deterministic, spectral solution method for the RTE based around a double spherical harmonic basis that fulfills these requirements. A rigorous mathematical justification for this method will be provided, as well as simulation results showing its ability to accurately and efficiently reconstruct radiance as a function of depth and angle in homogeneous and layered medium. Finally, the utility of this model in the recovery of optical properties from layered media using SFDS data will be demonstrated.

Chapter 2

Double SHEF$_N$ In Homogeneous Media

2.1 Introduction

In this chapter, I lay out a new approach to solving the RTE using on a double spherical harmonic functional basis. In recognition of its roots in Gardner's SHEF$_N$ approach mentioned in §1.3.2, which utilizes a single spherical harmonic expansion to approximate the entire angular distribution of the radiance, this method is named the Double Spherical Harmonic Expansion with Fourier coefficients to order N, or DSHEF$_N$. This method expresses radiance using a "compressed" spherical harmonic function basis to decouple the northern and southern hemispheres of functions in its span, representing each as separate linear combinations of these functions. By allowing for the radiance to be discontinuous at the equator, this approach is capable of handling, this method is capable of handling discontinuities in angular radiance at any medium boundary where a refractive index mismatch exists. The decoupled nature of the chosen basis also allows easier computation of boundary conditions

governed by internal reflection. It also allows accurate reconstruction of internal reflection due to the same mismatch, since the effect is limited to a single hemisphere.

The solution detailed in this chapter is the simplest version of DSHEF$_N$, because it assumes a medium with homogeneous optical properties. A version which deals with multiple disparate, homogeneous layers is given in Chapter 4.

2.2 The Radiative Transport Equation

As in the introduction, I restrict consideration to the temporal steady state form of the RTE, given in equation (1.1). This assumption is reasonable for many optical imaging modalities since this state is reached so quickly relative to light source intensity changes and image acquisition time. This version of the RTE is as follows:

$$\nabla \cdot \Omega L\left(\Omega, r, t\right) = -\mu_t L\left(\Omega, r, t\right) + \int_{4\pi} L\left(\Omega', r, t\right) p\left(\Omega' \cdot \Omega\right) d\Omega' + q\left(\Omega, r, t\right) \quad (2.1)$$

Here, r is a spatial vector consisting of x, y and z coordinates, and Ω is an angular vector as described. Therefore, radiant energy will be considered to be a function of five dimensions: three spatial and two angular. Radiance will be considered vary smoothly in both angle and space inside the medium. Scattering will be considered to be a continuous process, rather than happening at discrete intervals. This is different than Monte Carlo based RTE solutions, which consider photons or packets of photons that have discrete energy levels and scatter at discrete locations. Light in the medium considered has two components: L_C, which represents unscattered light from a source, moving in direction Ω_0, and L_S, which represents light that has been scattered at least once:

$$L(r,\Omega) = L_C(r,\Omega) + L_S(r,\Omega) \quad (2.2)$$

For a medium, I will consider a semi-infinte slab in a three dimensional space. This slab extends infinitely in the x and y directions as well as positive z direction only. This creates a boundary at the plane $z = 0$. This medium's optical properties, detailed in chapter 1, are considered to be homogeneous with respect to space. While it may seem an oversimplification to consider a homogeneous medium, there have been meaningful medical diagnostics using such assumptions[14][56].

For simplicity, I consider a planar light source beginning directly inside the medium, traveling in a direction $\Omega_0 = (\theta_0, \mu_0)$. This is a spherical angle consisting of a polar component and an azimuthal one. I do this purely for ease of explanation; an external light source undergoes a loss due to specular reflectance and a change of direction in accordance with Snell's law, both of which are well understood and easily accounted for. Spatial variations in this planar source may be considered in Fourier space. This is not only an easy example to consider, but many imaging applications use plane waves with such spatial variations[29][14] or more complex terms such as Gaussian beams and point sources[21], both of which may be understood in Fourier space.

I consider that the total amount of energy put into the system in the form of collimated light is 1. Conservation of energy states that all energy in L_C is eventually directly absorbed or scattered. Since loss due to absorption and scattering is a continuous process, this gives the following expression for collimated light[21]:

$$L_C(r,\Omega) = \mu_t \exp\left(\frac{-\mu_t z}{\cos(\theta_0)}\right) \delta_{\Omega_0} \quad (2.3)$$

Here, δ is the Dirac Delta Function. The decay comes from a basic differential equation governing constant fractional loss and the constant μ_t comes from normalization along a path integral starting at the origin and moving infinitely far in the Ω_0 direction.

All radiant energy in L_C which is not lost due to absorption will eventually be transferred to L_S. The energy in L_S is either absorbed or escapes the medium. The RTE as stated in (2.1) governs the behavior of L_S and dictates that in any direction, the instantaneous change with respect to space of L_S is given by the loss due to attenuation plus the gain due to L_S being scattered plus any gain due to L_C being scattered, which is commonly represented as $Q(r, \Omega)$. The statement of the RTE in (2.1) bears repetition in light of this physical explanation:

$$\nabla \cdot \Omega L_S(r, \Omega) = -\mu_t L_S(r, \Omega) + \mu_s \int_{4\pi} L_S(r, \Omega')\, p(\Omega' \cdot \Omega) d\Omega' + Q(r, \Omega) \quad (2.4)$$

The following expression for Q is also obtained using the definition of the Dirac Delta and the same integral operator used in (2.4):

$$Q(r, \Omega) = \mu_s p(\Omega \cdot \Omega_0) \exp\left(\frac{-\mu_t z}{\cos(\theta_0)}\right) \quad (2.5)$$

To fully describe radiative transport in the medium described, one must find L_S such that it provides a solution to (2.4), along with an appropriate boundary condition (this is easier said than done!) To understand such a solution, it is useful to choose a functional basis which handles the complexity of (2.4) as easily as possible.

2.3 Double Spherical Harmonic Basis

The SHEFN method developed by Gardner relies on the orthonormality of Laplace's Spherical Harmonic Functions (hereinafter referred to simply as spherical harmonic functions), as well as recurrence relations rising from their structure, to simplify the integral-differential equation of (2.4) into a system of ordinary differential equations. These functions provide a convenient orthonormal basis for the subspace of smooth functions in $L^2(S^2)$. Unfortunately, as with all smooth functional bases, difficulties may arise when attempting to

project any functions with discontinuities or non-differentiable points onto this basis. Further compounding this issue is the fact that both of these must accomodate a refractive index mismatch at the medium boundary, which is commonly encountered in biophotonic imaging applications[31]. To deal with potential discontinuities at the equator of the unit sphere, DSHEF$_N$ follows a similar strategy to that used in SHEF$_N$, but uses a basis composed of two sets of functions, both based on the spherical harmonics. Its functions have different constants to ensure that orthonormality is not lost and use a "compression" of the polar angle. The so called double spherical harmonic functions used are defined as:

$$Y_{l,m}(\Omega) = K_{l,m} P_{l,m} \left[\cos(\theta)\right] \exp(im\phi) \quad (2.6)$$

Here l is the order of the function and m is the degree, which ranges from $-l$ to l. $K_{l,m}$ is a constant to ensure orthonormality and $P_{l,m}$ is the Associated Legendre Polynomial of order m and degree l. When constructing double spherical harmonic functions for use in the northern hemisphere the argument for $P_{l,m}$ becomes $2\cos(\theta) - 1$ and the domain for θ becomes π to $\pi/2$. This coordinate change will not interfere with the orthogonality of the spherical harmonic functions, but does break their normalization. To correct for this, a factor of $\sqrt{2}$ is included. This gives the following functions:

$$\tilde{Y}^{+}_{l,m}(\Omega) = \sqrt{2} K_{l,m} P_{l,m} \left[2\cos(\theta) - 1\right] \exp(im\phi) \quad (2.7)$$

When constructing these functions for use in the southern hemisphere, the same adjustment to the constant term is used but the direction of θ is reversed. $\tilde{\theta} = \pi - \theta$ is used instead, which does introduce a change of coordinates with a determinant of -1 between the two sets of functions. This gives the following:

$$\tilde{Y}^{-}_{l,m}(\Omega) = \sqrt{2} K_{l,m} P_{l,m} \left(2\cos(\tilde{\theta}) - 1\right) \exp(im\phi) \quad (2.8)$$

Taken together, orthonormality is preserved in each hemisphere and coupling between the hemispheres is possible, though the angular coordinate change must be kept in mind. This allows scattered radiance to be described in the following manner:

$$L_S(r,\Omega) = \sum_{l,m}\left[\chi_{\theta\geq 0}\psi^{+}_{l,m}(r)\,\tilde{Y}^{+}_{l,m}(\Omega) + \chi_{\theta<0}\psi^{-}_{l,m}(r)\,\tilde{Y}^{-}_{l,m}(\Omega)\right] \quad (2.9)$$

Here, χ is the characteristic (or indicator) function and $\psi^{\pm}_{l,m}$ are unknown functions of position serving as moments of the double spherical harmonic functions. The solution to the RTE relies upon finding these moments; once they are known, scattered radiance is well described.

2.4 Restating the RTE

The RTE is made up of four components: A differential operator, an integral operator, a decay term and a source gain term. I will project each of these terms onto my proposed orthonormal basis and then combine them. My overall goal is to create elements of, and operators on, a finite dimensional vector space corresponding to the double spherical harmonic functions. These are stated in matrix form and solved as a system of ODEs. I therefore simplify and rephrase each section to focus on a specific double spherical harmonic function, defined on the northern hemisphere. This shows the interconnections between the eventual ODE system produced. The same process follows without loss of generality on the southern hemisphere.

The differential operator is a directional derivative in angular coordinates. It can be represented as sum of partial derivatives in Cartesian space:

$$\nabla\cdot\Omega = \sin(\theta)\cos(\phi)\frac{\partial}{\partial x} + \sin(\theta)\sin(\phi)\frac{\partial}{\partial y} + \cos(\theta)\frac{\partial}{\partial z} \quad (2.10)$$

The operator is then applied to the function for scattered radiance, described in (2.9):

$$\nabla \cdot \Omega L_s(r,\Omega) = \sin(\theta)\cos(\phi)\frac{\partial}{\partial x}L_s(r,\Omega) + \sin(\theta)\sin(\phi)\frac{\partial}{\partial y}L_s(r,\Omega) + \cos(\theta)\frac{\partial}{\partial z}L_s(r,\Omega) \quad (2.11)$$

Each component is then broken down:

$$\begin{aligned}
\sin(\theta)\cos(\phi)\left[\tfrac{\partial}{\partial x}\psi^+_{l,m}(r)\right]\tilde{Y}^{\pm}_{l,m}(\Omega) &= \sqrt{2}K_{l,m}\left[\sin(\theta)P_{l,m}(2\cos(\theta)\mp 1)\right]\left[\cos(\phi)\exp(im\phi)\right] \\
\sin(\theta)\sin(\phi)\left[\tfrac{\partial}{\partial y}\psi^+_{l,m}(r)\right]\tilde{Y}^{\pm}_{l,m}(\Omega) &= \sqrt{2}K_{l,m}\left[\sin(\theta)P_{l,m}(2\cos(\theta)\mp 1)\right]\left[\sin(\phi)\exp(im\phi)\right] \quad (2.12) \\
\cos(\theta)\left[\tfrac{\partial}{\partial z}\psi^+_{l,m}(r)\right]\tilde{Y}^{\pm}_{l,m}(\Omega) &= \sqrt{2}K_{l,m}\left[\sin(\theta)P_{l,m}(2\cos(\theta)\mp 1)\right]\left[\exp(im\phi)\right]
\end{aligned}$$

The bracketed portions of the right half of (2.12) provide recurrence relations which spring from the properties of the Associated Legendre Polynomials and Euler's Identity. These relations have weights given by the L^2 inner product on the hemisphere:

$$\begin{aligned}
A^{\pm}_x(l,m\to l',m') &= \left\langle \tilde{Y}^{\pm}_{l,m}, \sin(\theta)\cos(\phi)\tilde{Y}^{\pm}_{l',m'}\right\rangle \\
A^{\pm}_y(l,m\to l',m') &= \left\langle \tilde{Y}^{\pm}_{l,m}, \sin(\theta)\sin(\phi)\tilde{Y}^{\pm}_{l',m'}\right\rangle \quad (2.13) \\
A^{\pm}_z(l,m\to l',m') &= \left\langle \tilde{Y}^{\pm}_{l,m}, \cos(\theta)\tilde{Y}^{\pm}_{l',m'}\right\rangle
\end{aligned}$$

These inner products are easily calculated by quadrature on the hemisphere in a similar method to Atkinson's Gauss-Legendre quadrature[3]. In practice, these only have non-zero values when $l' = l \pm 1$ and $m' = m \pm 1$. This gives the following:

$$\begin{aligned}
\sin(\theta)\cos(\phi)\tfrac{\partial}{\partial x}\psi^{\pm}_{l,m}(r)\tilde{Y}^{\pm}_{l,m}(\Omega) &= \tfrac{\partial}{\partial x}\psi^+_{l,m}(r)\textstyle\sum A^{\pm}_x(l,m\to l\pm 1,m\pm 1)\tilde{Y}^{\pm}_{l\pm 1,m\pm 1}(\Omega) \\
\sin(\theta)\sin(\phi)\tfrac{\partial}{\partial y}\psi^{\pm}_{l,m}(r)\tilde{Y}^{\pm}_{l,m}(\Omega) &= \tfrac{\partial}{\partial y}\psi^+_{l,m}(r)\textstyle\sum A^{\pm}_y(l,m\to l\pm 1,m\pm 1)\tilde{Y}^{\pm}_{l\pm 1,m\pm 1}(\Omega) \quad (2.14) \\
\cos(\theta)\tfrac{\partial}{\partial z}\psi^{\pm}_{l,m}(r)\tilde{Y}^{\pm}_{l,m}(\Omega) &= \tfrac{\partial}{\partial z}\psi^+_{l,m}(r)\textstyle\sum A^{\pm}_z(l,m\to l\pm 1,m\pm 1)\tilde{Y}^{\pm}_{l\pm 1,m\pm 1}(\Omega)
\end{aligned}$$

The relations defined by the y term of the directional derivative are quite similar, while those of the z term vary only with respect to l, since there is no function of ϕ involved. They still have nonzero values only for $l' = l \pm 1$. This gives a restatement of the directional derivative, when applied to a single moment of scattered radiance, as:

$$\nabla \cdot \Omega \psi^{\pm}_{l,m}(r)\tilde{Y}^{\pm}_{l,m}(\Omega) = \left[\tfrac{\partial}{\partial x}\psi^{\pm}_{l,m}(r)\right]\left[\sum A^{\pm}_{x}(l, m \to l \pm 1, m \pm 1)\tilde{Y}^{\pm}_{l\pm1,m\pm1}(\Omega)\right] +$$
$$\left[\tfrac{\partial}{\partial y}\psi^{\pm}_{l,m}(r)\right]\left[\sum A^{\pm}_{y}(l, m \to l \pm 1, m \pm 1)\tilde{Y}^{\pm}_{l\pm1,m\pm1}(\Omega)\right] +$$
$$\left[\tfrac{\partial}{\partial z}\psi^{\pm}_{l,m}(r)\right]\left[\sum A^{+}_{x}(l, m \to l \pm 1, m)\tilde{Y}^{\pm}_{l\pm1,m}(\Omega)\right] \quad (2.15)$$

A restatement of the right hand side of (2.15), focusing on a specific double spherical harmonic $\tilde{Y}^{\pm}_{l,m}$ gives:

$$\Bigg[\sum A^{\pm}_{x}(l \pm 1, m \pm 1 \to l, m)\tfrac{\partial}{\partial x}\psi^{\pm}_{l\pm1,m\pm1}(r) +$$
$$\sum A^{\pm}_{y}(l \pm 1, m \pm 1 \to l, m)\tfrac{\partial}{\partial y}\psi^{\pm}_{l\pm1,m\pm1}(r)$$
$$\sum A^{\pm}_{z}(l \pm 1, m \to l, m)\tfrac{\partial}{\partial z}\psi^{+}_{l\pm1,m}(r)\Bigg]\tilde{Y}^{\pm}_{l,m}(\Omega) \quad (2.16)$$

One important point to note is that due to the parity of sine and cosine as well as the coordinate change from northern to southern hemispheres, $A^{+}_{x} = A^{-}_{x}$ and $A^{+}_{y} = A^{-}_{y}$ for any choice of l and m, while $A^{+}_{z} = -A^{-}_{z}$. This is because a coordinate change alone would imply multiplication by its previously mentioned determinant of -1, so a further multiplication by an odd function (sine) and reflection of θ over 0 would cancel out this change in sign, while further multiplication by an even function (cosine) with the same reflection preserves it.

Next, I consider the integral operator, which represents the redistribution of scattered radiance. This requires the expansion of the scattering phase function, $p\,(\Omega' \cdot \Omega)$, in a spherical harmonic basis. It is tempting to simply apply the double spherical harmonic basis immediately, but commonly used methods such as delta-Eddington approximation for radiative flux

transfer[32] or the use of parameters relating higher order moments of anisotropy[5][6] rely on the use of single spherical harmonic functions or Associated Legendre Polynomials. To allow for their usage, but maintain the advantages provided by a double spherical harmonic basis, I first expand the scattering phase function in Legendre Polynomials thusly:

$$p\left(\Omega' \cdot \Omega\right) = \sum_l (2l+1) g_l P_l\left(\Omega' \cdot \Omega\right) \quad (2.17)$$

Here, g_l is the inner product of p and P_l, while $(2l+1)$ is a normalizing constant. This allows for operations such as delta-Eddington, but since $\Omega' \cdot \Omega$ is a one dimensional number, it does not allow for conversion to single or double spherical harmonics. This is solved with the Spherical Harmonic Addition Theorem[2], which states that:

$$P_l(\mu) = \sum_{m=-l}^{l} \frac{4\pi}{2l+1} Y^*_{l,m}(\Omega') Y_{l,m}(\Omega) \quad (2.18)$$

Substitution into (2.15) gives:

$$\mathrm{p}(\Omega' \cdot \Omega) = \sum_l (2l+1) g_l \sum_{m=-l}^{l} 4\pi Y^*_{l,m}(\Omega') Y_{l,m}(\Omega) \quad (2.19)$$

The asterisk here denotes complex conjugation. Equation (2.19) gives p in terms of single spherical harmonic functions. Each single spherical harmonic function has an expansion in double spherical harmonics, performed in the same manner as those detailed in (2.13). However, unlike in (2.19), the weights of these conversions are limited in terms of degree but not order, since they come from the definitions of the Associated Legendre Polynomials, as well as a multiple of $\sqrt{2}$, which stems from the compression of the polar angle, as in (2.7). I denote these weights as $c^{\pm}(l, m \to l', m)$ and they are derived using inner products as before:

$$c^{\pm}(l, m \to l', m) = \left\langle Y_{l,m}, \tilde{Y}^{\pm}_{l',m} \right\rangle \quad (2.20)$$

Therefore, it can be said that:

$$Y_{l,m} = \sum_{l'} c^{\pm}(l, m \to l', m)\tilde{Y}^{\pm}_{l',m} \quad (2.21)$$

The same can be said of conjugate spherical harmonic functions. Substituting (2.21) into (2.18) for both regular and conjugate spherical harmonics gives:

$$p\left(\Omega' \cdot \Omega\right) = \sum_l g_l \sum_{m=-l}^{l} 4\pi$$

$$\left[\sum_{l'} c^{\pm}(l, m \to l', m)\tilde{Y}^{\pm,*}_{l',m}(\Omega')\right]\left[\sum_{l'} c^{\pm}(l, m \to l', m)\tilde{Y}^{\pm}_{l',m}(\Omega)\right] \quad (2.22)$$

Putting (2.21) into the integral operator of (2.4) and once again restricting L_S to a single l, m function gives the following:

$$\mu_s \int_{4\pi} p(\Omega' \cdot \Omega) d\Omega' =$$

$$\mu_s \int_{4\pi} \sum_l g_l \sum_{m=-l}^{l} 4\pi \left[\sum_{l'} c^{\pm}(l, m \to l', m)\tilde{Y}^{\pm,*}_{l',m}(\Omega')\right]$$

$$\left[\sum_{l'} c^{\pm}(l, m \to l', m)\tilde{Y}^{\pm}_{l',m}(\Omega)\right] d\Omega' \quad (2.23)$$

Since this integration occurs with respect to Ω' only, the double spherical harmonic functions with Ω' as arguments need stay inside the integral. Therefore, (2.23) may be restated as:

$$\mu_s \int_{4\pi} p(\Omega' \cdot \Omega) d\Omega' =$$

$$\mu_s \sum_l g_l \sum_{m=-l}^{l} 4\pi \left[\sum_{l'} c^{\pm}(l, m \to l', m) \int_{4\pi} \tilde{Y}^{+}_{l,m}(\Omega')\tilde{Y}^{\pm,*}_{l',m}(\Omega') d\Omega'\right]$$

$$\left[\sum_{l'} c^{\pm}(l, m \to l', m)\tilde{Y}^{\pm}_{l',m}(\Omega)\right] \quad (2.24)$$

From here, it is useful to note that the integral term involved is the L^2 inner product on half of the hemisphere. Again, the coordinate change between hemispheres becomes relevant. This

inner product applied to two functions constructed for the same hemispheres is orthonormal, but when the two functions are defined on opposite hemispheres this negative determinant of this change must apply. The inner product then simplifies to $-\delta_{l,l'}\delta_{m,m'}$, taking on a sort of negative orthonormality. Taking this into account and restating (2.24) to focus on a specific double spherical harmonic function as in (2.16) gives:

$$\mu_s \int_{4\pi} p(\Omega' \cdot \Omega) d\Omega' =$$

$$\mu_s \sum_{l'} g_{l'} 4\pi \left[\sum_{l'} c^{\pm}(l', m \rightarrow l, m) \left(\pm\delta_{l,l'}\right)\right]$$

$$\left[\sum_{l'} c^{+}(l', m \rightarrow l, m)\right] \tilde{Y}^{+}_{l,m}(\Omega) \quad (2.25)$$

These statements are becoming more difficult to parse, but they fortunately have a more elegant statement when expressed in matrix formulation. I will show this when reconstructing the overall RTE in §2.5.

Fortunately, the decay term and source vector are much more easily dealt with. The decay term, in particular, when applied to a specific function barely needs mention; it is a simple multiplication by $-\mu_t$. The source gain term behaves in a similar fashion to the integral operator. It is first expanded in single Legendre Polynomials. From here, a delta–Eddington rescaling may be performed[32]. This allows for better reconstruction of collimated radiance and has been shown[21] [10] to have positive effects in the reconstruction of fluence as a function of depth in various RTE solutions. Briefly, this rescaling keeps the same overall anisotropy of the scattering phase function by creating new values for the Legendre Polynomial moments of the scattering phase function. It does so by constructing a new phase function equal to a linear combination of the old one and a Dirac Delta in the direction of the collimated source. The weight of the Delta Distribution, denoted f_δ is equal to the moment that the Legendre Polynomial of order $N+1$ would have in the original expansion, had it been included. This gives the following representation:

$$p_{\delta-Edd}\left(\cos(\theta)\right) = f_\delta \delta_{\cos(\theta),\cos(\theta_0)} + \left(1 - f_\delta\right) p\left(\cos(\theta)\right) \quad (2.26)$$

This new phase function $p_{\delta-Edd}$ is used in lieu of p in calculating Q. Its Legendre Polynomial moments are given by:

$$g_l^\star = \frac{g_l - f_\delta}{1 - f_\delta} \quad (2.27)$$

If, as is the case in the simulations presented in Chapters 3 and 4, the user does not wish to perform this rescaling, then simply changing $f - \delta$ to 0 will eliminate its effect.

The reason behind the decision not to include this approximation in Chapters 3 and 4 bears some mention. As it can be seen in Figs 2.1–2, error for scattered radiance is not always improved by the use of this approximation. These figures show radiance as a function of depth and cosine(θ) as well as relative error thereof for a plane wave source normally incident on a 2 layer medium. Both layers have an l^* of 1. The top layer has a thickness of $0.1l^*$ and a ratio of $\mu_s'/\mu_a = 3$. The bottom layer is semi–infinite with a ratio of $\mu_s'/\mu_a = 100$. DSHEF_5 is shown both with and without this approximation. It is clear from examination that while error decays with respect to depth when not using δ-Eddington, it does when the approximation is adopted. However, all expansion orders of single SHEF_N shown in this dissertation do use δ–Eddington, since it has been well observed[21] that it is beneficial to this method.

Once the source gain term is represented in Legendre Polynomials using these moments, it is converted to single spherical harmonics using the addition theorem, then to double spherical harmonics using conversion weights as in (2.21). Substituting (2.21) and (2.26) together with (2.5), as well as applying the Spherical Harmonic Addition Theorem and then restricting to a specific double spherical harmonic function gives a source gain term of:

$$Q(z) = 4\pi\mu_s C \exp\left(\frac{-\mu_t^* z}{\mu_0}\right)$$

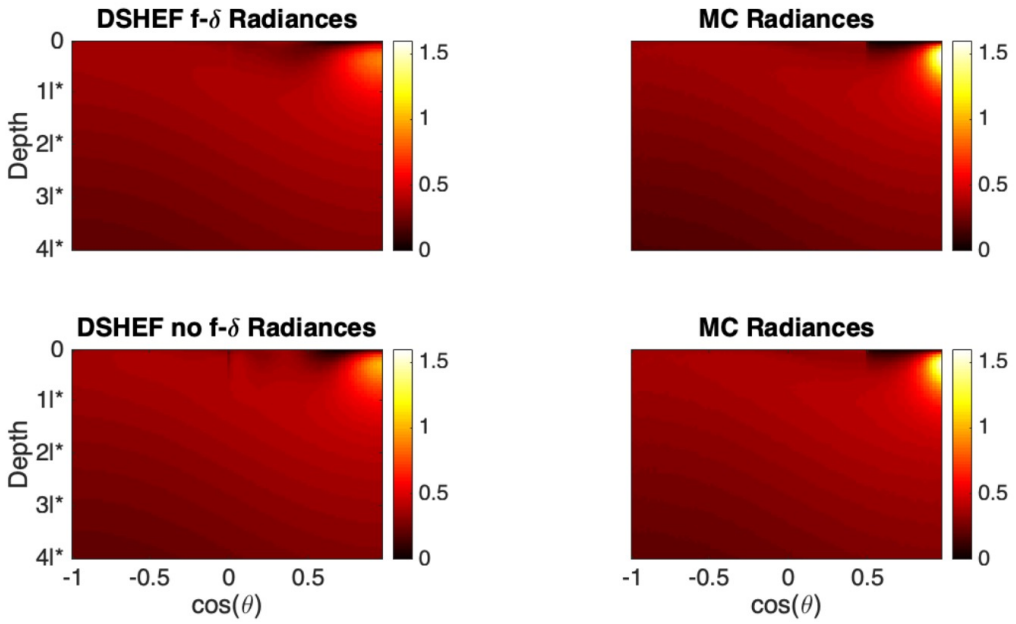

Figure 2.1: Radiance as a function of depth and $\cos(\theta)$ for a two layered medium. Top layer is $0.1l^*$ thick and has $\mu_s'/\mu_a = 3$, bottom layer is semi–infinite and has $\mu_s'/\mu_a = 100$. Top left shows DSHEF_5 with δ–Eddington, bottom left shows DSHEF_5 without, both right hand figures show MC results for gold standard comparison.

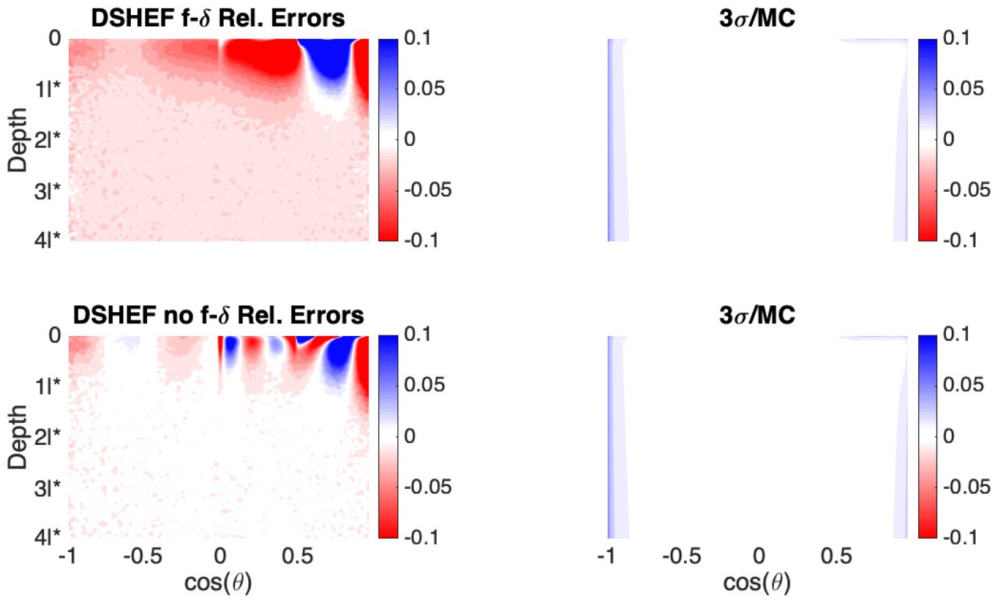

Figure 2.2: Relative error vs MC gold standard comparison for DSHEF_5 in a two layer medium with and without δ–Eddington, as a function of depth and $\cos(\theta)$. Top left shows error for DSHEF_5 with the approximation, bottom left without. Both right heatmaps show 3σ/MC to indicate confidence in MC prediction.

$$\sum_{l'} g^{\star}_{l'} 4\pi \left[\sum_{l'} c^{\pm}(l', m \rightarrow l, m)\left(\pm\delta_{l,l'}\right)\right]\left[\sum_{l'} c^{\pm}(l', m \rightarrow l, m)\right] \tilde{Y}^{\pm}_{l,m}(\Omega) \quad (2.28)$$

Here, $\mu^{*}_{t} = \mu_{a} + \mu_{s}*$ and $\mu^{*}_{s} = (1 - f_{\delta})\mu_{s}$. Considering (2.28) if f_{δ} is set to zero instead gives the following statement for the source:

$$Q(z) = 4\pi\mu_{s} C \exp\left(\frac{\mu_{t}}{\mu_{0}} z\right)$$
$$\sum_{l'} g_{l'} 4\pi \left[\sum_{l'} c^{\pm}(l', m \rightarrow l, m)\left(\pm\delta_{l,l'}\right)\right]\left[\sum_{l'} c^{\pm}(l', m \rightarrow l, m)\right] \tilde{Y}^{\pm}_{l,m}(\Omega) \quad (2.29)$$

I denote the coefficient of $\tilde{Y}^{\pm}_{l,m}(\Omega)$ as $q^{\pm}_{l,m}$ for brevity. From here, it should be noted that I have placed every single term of the RTE as a coefficient of $\tilde{Y}^{\pm}_{l,m}$. Therefore, the actual double spherical harmonic functions may be cancelled out, leaving a system of partial differential equations. The system is more easily stated with the introduction of matrices A_{x}, A_{y} and A_{z} (which were derived from the directional derivative term) to capture the recurrence relations introduced by each partial derivative and S to capture those introduced by the integral operator. I also introduce the vectors Q and Ψ to represent the terms of the source and scattered radiance, respectively. These vectors are given the following form:

$$\Psi(r) = \begin{bmatrix} \psi^{+}_{0,0}(r) \\ \psi^{+}_{1,-1}(r) \\ \psi^{+}_{1,0}(r) \\ \cdots \\ \psi^{+}_{N,N}(r) \\ \psi^{-}_{0,0}(r) \\ \psi^{-}_{1,-1}(r) \\ \psi^{-}_{1,0}(r) \\ \cdots \\ \psi^{-}_{N,N}(r) \end{bmatrix} \quad (2.30)$$

This gives the following system:

$$A_x \frac{\partial}{\partial x}\Psi(r) + A_y \frac{\partial}{\partial y}\Psi(r) + A_z \frac{\partial}{\partial z}\Psi(r) = -\mu_t \Psi(r) + S\Psi(r) + Q(r) \quad (2.31)$$

Here, I recall the assumption of medium homogeneity in the x and y directions. This allows me to perform Fourier Transforms in the those directions without concern for optical properties, which eliminates those partial derivatives and allows (2.31) to be restated as a traditional system of ordinary differential equations:

$$\begin{aligned} A_z \frac{d}{dz}\tilde{\Psi}\left(z, k_x, k_y\right) = -2\pi k_x A_x \tilde{\Psi}\left(z, k_x, k_y\right) - 2\pi k_y A_y \tilde{\Psi}\left(z, k_x, k_y\right) \\ -\mu_t \tilde{\Psi}\left(z, k_x, k_y\right) + S\tilde{\Psi}\left(z, k_x, k_y\right) + \tilde{Q}\left(z, k_x, k_y\right) \quad (2.32) \end{aligned}$$

Here, it should be noted that the both the mathematical construction of S and the fact that radiance is scattered in relative, rather than absolute, frames of reference, give it an interesting structure. Note that the conversion factors used in (2.32) can be used to make the following matrix to convert vectors from single to double spherical harmonic bases:

$$C = \begin{bmatrix} C^+ \\ C^- \end{bmatrix} \quad (2.33)$$

Here C^+ is responsible for contributions to the northern double spherical harmonic function while C^- is responsible for those to the southern. It is interesting to note that the only differences between corresponding entries of C^+ and C^- are sign; the coordinate change from (2.7) to (2.8) along with the fact that $P_{l,m}$ is even or odd exactly when $l - m$ is even or odd is responsible for this.

C allows for the projection of a vector representing single spherical harmonic moments into the space spanned by the double spherical harmonics. As can be inferred from (2.33), the

construction of S is performed by taking a diagonal matrix whose non-zero entries are the single spherical moments of the scattering phase function p, (obtained in (2.30)) hereafter denoted D, then left and right multiplying by C and C^T, respectively. This gives the following:

$$S = CDC^T = \begin{bmatrix} S_1 & S_2 \\ S_2 & S_1 \end{bmatrix} \quad (2.33)$$

When deconstructing this matrix, it should be seen that $S_1 = C^+DC^{+,T} = C^-DC^{-,T}$ and $S_2 = C^+DC^{-,T} = C^-DC^{+,T}$. These equalities are borne out by the similarities between C^+ and C^- mentioned above. This makes sense phenomenologically; it means that radiance scattered within the southern hemisphere is treated exactly as radiance scattered within the northern hemisphere. It also means that radiance being scattered from the northern to the southern hemisphere is treated exactly as radiance scattered from the southern hemisphere to the northern hemisphere.

In any case, further simplification of (2.32) may be performed. A case of particular interest is spatial frequency domain imaging, planar sources with sinusoidal intensity modulations are utilized. Moreover, any source of finite lateral extent can be expressed in terms of a sum of simusoids of harmonic frequencies of x and y. Therefore, it is often prudent to fix k_x and k_y. I will consider only such fixed wave numbers, and remove those numbers from the arguments for $\tilde{\Psi}$ and $\tilde{Q}$ for the sake of brevity. I also introduce another matrix $B = -2\pi k_x A_x - 2\pi k_y A_y - \mu_t I + P$ and rename A_z to simply A. This means that (2.32) is equivalent to:

$$A\tilde{\Psi}'(z) + B\tilde{\Psi}(z) = \tilde{Q}(z) \quad (2.35)$$

It is important to note here that A will necessarily be nonsingular due to its diagonal component, and that B is not necessarily nonsingular, but in practice will commonly be

so, because B is a nondiagonal matrix added to a constant times the identity matrix. This formulation provides an RTE that is more amenable to solution.

2.5 Solving the RTE

Now that (2.4) is restated as (2.35), all that remains is to find a solution and apply an appropriate boundary condition (which is, of course, much easier said than done.) The matrix form of the RTE hints that $\tilde{\Psi}$ has two components: a particular solution and a homogeneous solution. To understand the particular solution, recall from (2.29) that $\tilde{Q}$ decays exponentially in z with a rate of μ_t/μ_0. I therefore use an ansatz featuring that decay. This is done in the same manner in the SHEF$_N$ approach introduced by Gardner[21]. Simple calculus and linear algebra shows that this solution, which I call $\tilde{\Psi}^p$, is the following:

$$\tilde{\Psi}^p(z) = \left(-\tfrac{\mu_t}{\mu_0}A + B\right)^{-1}\tilde{Q}(z) \quad (2.36)$$

The homogeneous solution is slightly more complicated to obtain. Because of the structure of the homogeneous problem $A\tilde{\Psi}'(z) = -B\tilde{\Psi(z)}$, I use an ansatz that is a linear combination of exponential decays with unknown rates. Again, this is done similarly as in the SHEF$_N$ approach[21]. This gives a function of the form $\tilde{\Psi}^h(z) = \sum_i G_i \exp\left(\frac{z}{\lambda_i}\right)$. Here G_i are unknown vectors. Substituting this into the homogeneous problem, restricting to a specific index i and cancelling out the decay on each side gives $AG_i = -\lambda_i BG_i$, a generalized eigenvalue problem. Therefore, (λ_i, G_i) are simply the eigenpairs of this problem. The only thing which remains is to calculate their specific weights, which I denote w_i. This gives the homogeneous solution the following form:

$$\tilde{\Psi}^h = \textstyle\sum_i w_i G_i \exp\left(\frac{z}{\lambda_i}\right) \quad (2.37)$$

Here it must be noted that due to conservation of energy, it is required that as z approaches ∞, radiant energy must approach zero. Therefore, only terms which actually decay, which are those involving negative eigenvectors, will have nonzero weights.

Equation (2.37) may be restated in matrix form, using G as a columnar matrix of eigenvectors G_i, w as a vector and E as a diagonal matrix of the decay terms:

$$\tilde{\Psi}^h = GwE \quad (2.38)$$

Because of the aforementioned nonsingularity of both matrices involved in the generalized eigenvalue problem, the dimension of w will be $2(N+1)^2$. All that remains is now to solve for w, for which I use two boundary conditions. The first is that since radiance is expected to decay to zero as depth approaches infinity, all w_i corresponding to positive λ_i must be zero. The second is known as the Marshak Boundary Condition. It states that at the boundary of a medium featuring a refractive index mismatch, the only scattered radiance directed into the medium is that which was originally directed out of the medium and internally reflected[11]. This provides a coupling between the radiance in the forward and backward hemispheres as follows:

$$\int_{\theta<\frac{\pi}{2}} L_S(z=0,\Omega)\tilde{Y}^{+,*}_{\Lambda,M}(\Omega)d\Omega = \int_{\theta>\frac{\pi}{2}} L_S(z=0,\Omega)\gamma_F(-\cos(\theta))\tilde{Y}^{-,*}_{\Lambda,M}(\Omega)d\Omega \quad (2.39)$$

Here, $\gamma_F(-\cos(\theta))$ is Fresnel's law for internal reflection and the pair (Λ, M) is simply the index of any specific double spherical harmonic, used along with integration to make meaningful connections between components of L_S. Due the the orthonormality of the double spherical harmonics, the left hand side simply reduces to $\tilde{\Psi}(0)$, while the right can be replaced by a matrix R whose entries correspond to the integrals of the right hand side, with the appropriate $\tilde{\psi}_{l,m}(0)$ moments factored out.

The internal reflection is given as follows for $\mu = \cos(\theta)$ and a refractive index n:

$$\gamma_F(\mu) = \frac{\left|n\left(\sqrt{1-n^2(1-\mu^2)}-\mu\right)\right|}{2\left|n\left(\sqrt{1-n^2(1-\mu^2)}+\mu\right)\right|} + \frac{\left|n\mu-\sqrt{1-n^2(1-\mu^2)}\right|}{2\left|n\mu+\sqrt{1-n^2(1-\mu^2)}\right|} \quad (2.40)$$

This gives the following statement of a boundary condition:

$$\begin{bmatrix} I & -R \end{bmatrix} \tilde{\Psi}(0) = 0 \quad (2.41)$$

For the solution I am detailing, this means that $\tilde{\Psi}(0) = \tilde{\Psi}^p(0) + \tilde{\Psi}^h(0)$ resides in the null space of $\begin{bmatrix} I & -R \end{bmatrix}$. This means that after all of the work shown in this chapter, the ultimate solution boils down to an intersection between this null space and the vector space defined by the generalized eigenvalue problem detailed above, when restricted to $z = 0$. This restriction means that decay terms of both the particular and homogeneous components of $\tilde{\Psi}$ become 1, and so they need not be listed. This gives the following:

$$\begin{bmatrix} I & -R \end{bmatrix} Gw = \begin{bmatrix} -I & R \end{bmatrix} \tilde{\Psi}^p(0) \quad (2.42)$$

From here, matrix inversion may be applied to solve for w:

$$w = \left(\begin{bmatrix} I & -R \end{bmatrix} G \right)^{-1} \begin{bmatrix} -I & R \end{bmatrix} \tilde{\Psi}^p(0) \quad (2.43)$$

If necessary, Inverse Fourier Transforms may also be applied to obtain Ψ from $\tilde{\Psi}$. It is worth noting that this is not necessary for applications involving imaging in the Spatial Frequency Domain[29]. Describing scattered radiance or any quantity derived from it becomes a matter of plugging w and z back into $\tilde{\Psi}$.

The overall structure of the solution as a sum of decay terms deserves mention. This means that as depth increases, the contributions of all but the slowest decaying term (or terms, in the case of degenerate eigenvalues or the unlikely one of an eigenvalue equalling μ_t) to radiance, and therefore fluence and any other functionals of radiance, becomes negligible.

This, in turn, means that the vectors corresponding to the slowest rates of decay describe deep field radiance, if this solution is accurate.

Chapter 3

MATLab Implementation of Homogeneous DSHEF$_N$ and Results

3.1 Introduction

In this chapter, I will detail the MATLab implementation of the single layer DSHEF$_N$ method. The main file of implementation is dSHEF_clean.m, shown in appendix A.2.1, as well as associated scripts and functions used in support . I will both describe the workings of the code and provide instructions for its use and modification. While this implementation, includes support for a two layer medium, this chapter will cover only the case of a medium composed of a single, semi–infinite, homogeneous layer. To use the code from A.2.1 to simulate a single layered medium, the simplest approach is to set the same optical properties for each layer. All files mentioned in this chapter are explicitly listed in appendix A.2.

3.2 MATLab Implementation of DSHEF$_N$

3.2.1 Initializing Variables and Matrices

The first step in the MATLab implementation of DSHEF$_N$ is to initialize several variables and matrices. The scattering coefficient, absorption coefficient and refractive index of the medium must be set. Additionally, the anisotropy of the scattering phase function, the spatial frequencies of the source in both the x and the y directions and initial direction (before change due to potential refractive index mismatch) and the decision to use the δ–Eddington approximation for the scattering phase function when applied to the source must be set as well. Finally and perhaps most important, the order of expansion N must be set. Most of these initializations are performed in dSHEF_clean.m, though several are performed by other files called by dSHEFinit.m, which must be executed prior to dSHEF_cleam.m.

In particular, four matrices are created through the use of dSHEF_clean.m. Those matrices representing the recurrence relations given in equation (2.12) as A_x and A_y are created through Gaussian quadrature using MATLab's quadgk function applied to inner products defined in (2.12). These are created in makeDerivMats.m. The matrix representing the internal reflection from Fresnel's Laws used in the Marshak boundary condition, represented as R in equation (2.38) are created using the same quadrature method applied to equation (2.37). This is performed in makeDSHEFbdry.m, and required the definition of the refractive index of the medium, which is defined in dSHEFinit.m. Finally, a matrix for the conversion of a vector of single spherical harmonic moments into a vector of double spherical harmonic moments is created using the same method applied to the inner product detailed in equation (2.19). This is performed in createConvMatHD.m. All of these matrices are created for orders 1 through 13 by a single execution of dSHEFinit.m. While all of the integrals in question could be approximated by Atkinson's Gauss-Legendre quadrature, this method is only exact when approximating polynomial functions of order less than or equal to N. None

of these integrals have finite order expansions, and in fact Fresnel's function for internal reflectance possesses a non-differentiable point at the critical angle.

However, Gauss-Legendre quadrature[3] may be applied to the creation of the A matrix from equation (2.33). That is because every entry in this matrix comes from A_z as described in (2.12). When considering spherical harmonics in terms of $\mu = \cos(\theta)$, the right argument of the inner product defining entries of A_z simplifies to a finite polynomial in μ of order less than or equal to $2N + 1$, which then becomes an ideal target for Gauss-Legendre. This method is performed via matrix multiplication since the weights and angles used in it depend only on the order of expansion.

3.2.2 Scattering Phase Function

One of the features of this implementation of DSHEF$_N$ is the ability to quickly and easily simulate media with different scatting phase functions. While several commonly used phase functions are included in the code, the Henyey-Greenstein[28] function is set as the default. Results will also be shown using this function. Recall that, as detailed in equations (2.21) through (2.24), any scattering phase function used in this method is expanded in a single spherical harmonic basis. The first step is decomposing the function into standard Legendre polynomials. This is again accomplished via Gaussian quadrature and quadgk. Once these moments are obtained, they are used in conjunction with the Spherical Harmonic Addition Theorem[2] to expand the scattering phase function in terms of single spherical harmonics. As in equation (2.24), the expansion of the scattering phase function in terms of single spherical harmonics must be multiplied on the left and the right by matrices converting from single spherical harmonics to double, and from double spherical harmonics to single, respectively. This is accomplished through the use of the conversion matrix created by createConvMatHD.m and the createIPlus.m function, respectively. It should be noted that

the conversion from single to double spherical harmonics is not done through the creation of a separate matrix but rather targeted use of the entries of such a matrix, which are made by calls to createIPlus.m. The resulting matrix is the one described in equation (2.32).

Once the resulting matrix is created and stored in the variable scatterMat, all components of the A and B matrices from equation (2.33) have been created. This is done via simple addition of the components and their coefficients, as in equation (2.30).

The scattering phase function of choice is also represented in terms of double spherical harmonic functions, again using Gaussian quadrature. Two separate vectors are created, one for the representation of this function in the upward facing hemisphere, and one for the downward facing hemisphere. These are not used in the construction of the matrix B, but rather in the construction of the vector Q described in equation (2.27), which represents the contribution of a source to scattered radiance.

3.2.3 Generalized Eigenvalue Problems

Once the A and B matrices are obtained, their eigenspaces are calculated via MATLab's eig function. Note that in dSHEF_clean.m, the arguments for eig are A and $-B$. This is because generalized eigenvalue system resulting from equation (2.33) is of the following form:

$$A\tilde{\Psi}'(z) = -B\tilde{\Psi}(z) \quad (3.1)$$

It should be noted that the call to eig is the single most computationally expensive step of this implementation of DSHEF$_N$, being responsible for over 90 percent of the overall compute time. Once this is completed, the vectors and values describing this space are sorted in terms of eigenvalues from most negative to most positive, and separated to identify vectors corresponding to both positive and negative eigenvalues as well vector components

applying to both upward and downward hemispheres.

3.2.4 Source Vector Construction

The vector representing source contribution, Q, defined in equation (2.27), is constructed at the medium boundary $z = 0$. It may be constructed in one of two ways, defined by the sourceToggle flag, which is set by default to 0. The default method, as described in (2.27), takes the moments of the scattering phase function in a double spherical harmonic basis and multiplying them by the accompanying conjugate double spherical harmonic functions evaluated in the direction of the collimated source, defined earlier. The alternate method, which occurs when the sourceToggle flag is set to 1, has once key difference. In this method, a source contribution vector is calculated for a single spherical harmonic matrix and multiplied by the the conversion matrix convMat.

It should be noted that this implementation of DSHEF$_N$ can be made to function both with and without the δ–Eddington approximation of the scattering phase function when considering the vector representing source contribution. This decision is set by the useFDelta flag, which is set to 0, disabling the approximation, by default. This decision was made due to increases in accuracy seen when opting not to use this approximation. When the flag is set to 0, the coefficient for the approximation, detailed in equation (2.25), is set to 0. In all other cases, it is adjusted from the spherical harmonic moments for the scattering phase function in the method described in equation (2.26). Likewise, the extinction coefficient for the source vector are adjusted by the f_delta variable in the manner shown in equation (2.27). As in the adjustment to the source moments, when this variable is forced to zero, the extinction coefficient is automatically adjusted.

3.2.5 Solution Construction

Recall that the solution obtained by DSHEF$_N$ is composed of a particular and a homogeneous component. In each case, regardless of the value chosen for depth in z, each component is first calculated at the medium boundary $z = 0$ and then adjusted to the specified depth.

First, the particular solution is obtained exactly as in equation (2.34) for $z = 0$. This constriction simply eliminates the decay term of Q described in (2.27).

Second, the Marshak boundary condition is applied to calculate the homogeneous solution. Recall that in equations (2.39) and (2.40), the vector w, which is composed of the weights of eigenvector contributions to the homogeneous solution, is solved through matrix inversion. Once this vector w, which is stored as eigen_moments in dSHEF_clean.m, has been obtained, it is used to construct the total solution. Note that these moments will only be calculated for eigenvectors corresponding to negative eigenvalues, as detailed in section 2.5.

This final calculation is performed by first adjusting the particular solution to the specified depth in z via its native rate of decay. Once this is set, the contribution of each eigenvector is added, adjusted for its own decay in terms of its associated eigenvalue as defined in equation (2.35).

Once the moments of the total solution in a double spherical harmonic basis are calculated, the getCenterSHF.m, doublePGraphGen.m and doublePGraphGenUnified.m are applied to create plots of radiance as a function of μ at the specified depth. These plots will show the average radiance for any value of μ in case there is any azimuthal asymmetry to radiance.

3.3 The Use and Modification of This Implementation

3.3.1 Overview

To execute the DSHEF$_N$ implementation found in dSHEF_clean.m, first ensure that all files are place in MATLab's working directory. Then, set all parameters within dSHEF_clean.m and dSHEFinit.m to your desired values. Once these parameters are set, execute dSHEFinit.m a single time to construct matrices for use in dSHEF_clean.m at various orders. After that, execute dSHEF_clean.m.

3.3.2 Initialization

When using this implementation of DSHEF$_N$, only two files need to be executed. The first is dSHEFinit.m, and the second is dSHEF_clean.m. The actual model is computed by dSHEF_clean.m, but dSHEFinit.m must be run one time before dSHEF_clean. Once the initializer has been executed, the matrices representing the recurrence relations introduced by the x and y portions of the directional derivative operator in the RTE, as well as the matrix representing the internal reflection portion of the Marshak boundary condition and the conversion matrix for single to double spherical harmonics are created and stored in local variables for orders 1 through 13.

To initialize for higher orders, simply add lines to dSHEFinit.m in the same manner as the ones listed. Furthermore, add the appropriate cases to the switch statement in dSHEF_clean.m which selects these matrices based on order.

The only case in which dSHEFinit.m must be executed again is when simulating a medium with a different refractive index. This value is stored as n in dSHEFinit.

3.3.3 Parameters

Other than the refractive index n, all relevant optical properties are set in dSHEF_clean.m. Most are located in the beginning of the file and are marked with comments. When simulating, it is important to recall that the code in dSHEF_clean.m is set for a two layer medium. To simulate a single layer medium, as shown in this chapter, the values for top layer scattering and absorption must be the same as the values for bottom layer scattering and absorption.

The only parameter not immediately defined in the beginning of dSHEF_clean.m is the scattering phase function. Any function may be defined, but it must first be written as an anonymous function in MATLab. Several examples are provided in the code. Once the desired function has been constructed, set the phaseFunc function to be equal to it. The code will then automatically calculate all single and double spherical harmonic moments corresponding to it.

3.3.4 Simulation Output

The output of dSHEF_clean.m comes in three varieties. First, the variable final_depth_moments contains a double spherical harmonic expansion for angularly resolved radiance at the depth specified by the user. Second, the vectors x_out_sym and y_out_sym provide the independent and dependent variables for a graph of radiance as a function of μ, the cosine of the polar angle. As mentioned above, any azimuthal asymmetry in this radiance will not feature, and the values listed will be averages over all azimuthal angles. It should be noted that the value of radiance for $\mu = 0$ is composed of an average of the values given by the upward hemispherical expansion and the downward hemispherical expansion. Finally, x_out_sym_up and y_out_sym_up, as well as their counterparts x_out_sym_down and y_out_sym_down provide independent and dependent variables for similar plots, but split into halves for the upward

and downward facing hemispheres.

3.4 Results and Discussion

To show the results of DSHEF_N in a homogeneous case, I will consider results generated using two different media. These media will have different optical properties but both will have mean free paths normalized to $l^* = 1$. One will be highly scattering, with a ratio of $\mu_s'/\mu_a = 100$. The other will be less scattering, with a ratio of $\mu_s'/\mu_a = 3$. Both will have a refractive index $n = 1.4$, and both will use a Henyey-Greenstein[28] scattering phase function with an anisotropy $g = 0.8$. Normally incident sources will be used, and spatial frequencies $f_x = 0$, $f_x = 0.1/l^*$, $f_x = 0.2/l^*$ and $f_x = 0.3/l^*$ will all be shown. These values were chosen to be relevant to imaging applications in biological tissue [31, 29].

Simulations will be shown for DSHEF_3, DSHEF_5, DSHEF_7 and DSHEF_{13}. A high order single SHEF_N expansion, SHEF_{13}, will also be included as a reference to current best practices. A 10M photon packet DAW Monte Carlo simulation will also be included as a gold standard, using Hayakawa's Virtual Tissue Simulator Command Line Monte Carlo software[24]. The δ–Eddington approximation for the source term will be used for SSHEF_{13}, but not for any expansion order of DSHEF_N.

Results will be shown for radiance as a function of depth and $\cos(\theta)$, radiance as a function of $\cos(\theta)$ near the medium surface, fluence as a function of depth and reflectance as a function of spatial frequency.

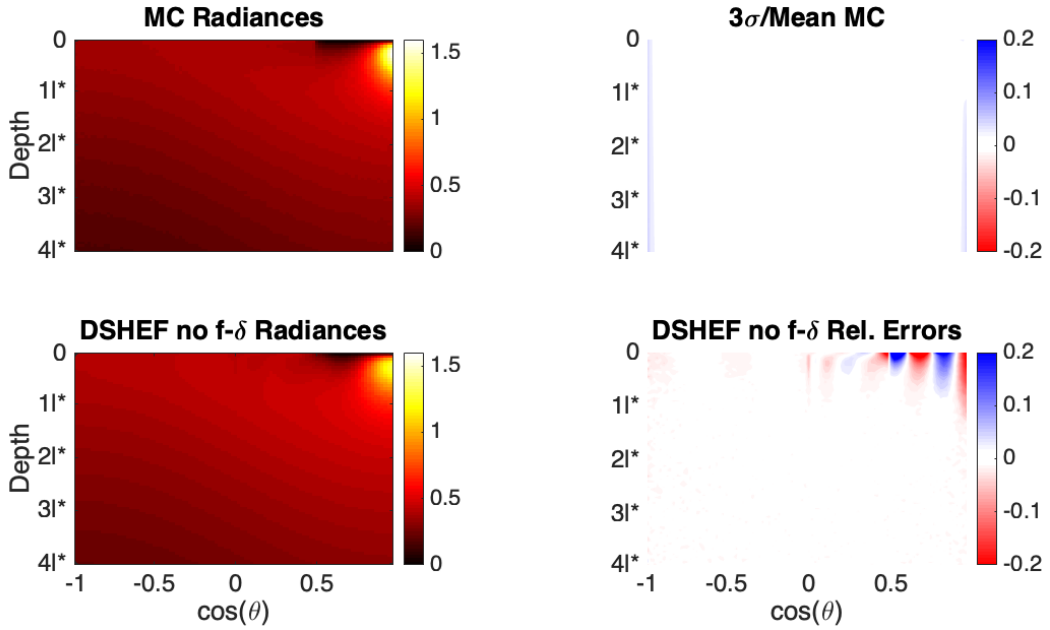

Figure 3.1: Radiance vs depth and $\cos(\theta)$, $l^* = 1$, $\mu_s'/\mu_a = 100$, $f_x = 0$. Top left is Monte Carlo simulation, bottom left is DSHEF_7. Top right is 3σ/mean for Monte Carlo, bottom right is relative error between DSHEF_7 and Monte Carlo.

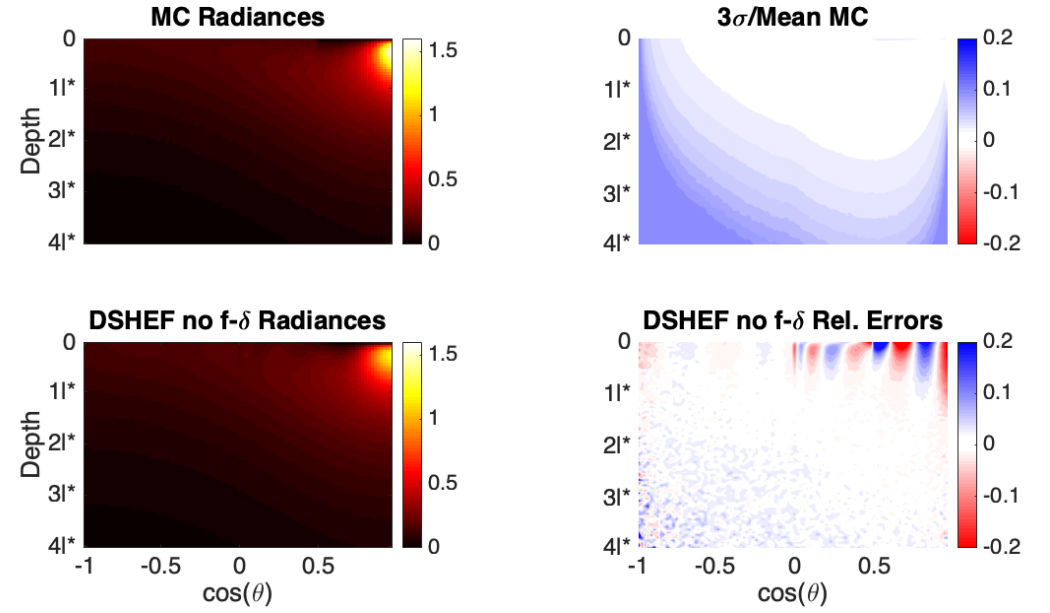

Figure 3.2: Radiance vs depth and $\cos(\theta)$, $l^* = 1$, $\mu_s'/\mu_a = 100$, $f_x = 0.1/l^*$. Top left is Monte Carlo simulation, bottom left is DSHEF_7. Top right is 3σ/mean for Monte Carlo, bottom right is relative error between DSHEF_7 and Monte Carlo.

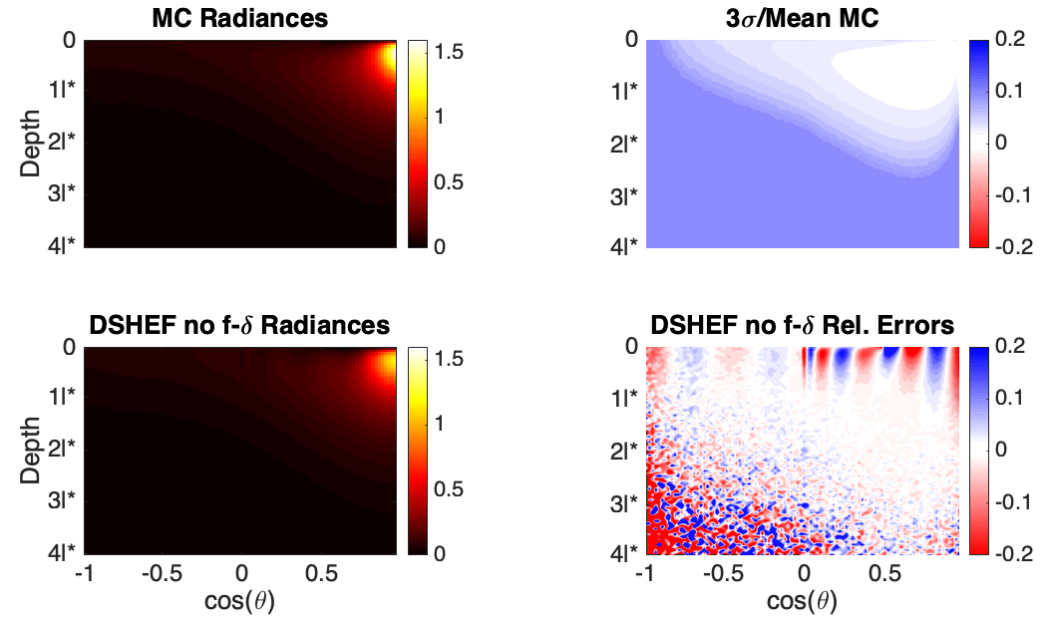

Figure 3.3: Radiance vs depth and $\cos(\theta)$, $l^* = 1$, $\mu_s'/\mu_a = 100$, $f_x = 0.2/l^*$. Top left is Monte Carlo simulation, bottom left is DSHEF_7. Top right is 3σ/mean for Monte Carlo, bottom right is relative error between DSHEF_7 and Monte Carlo.

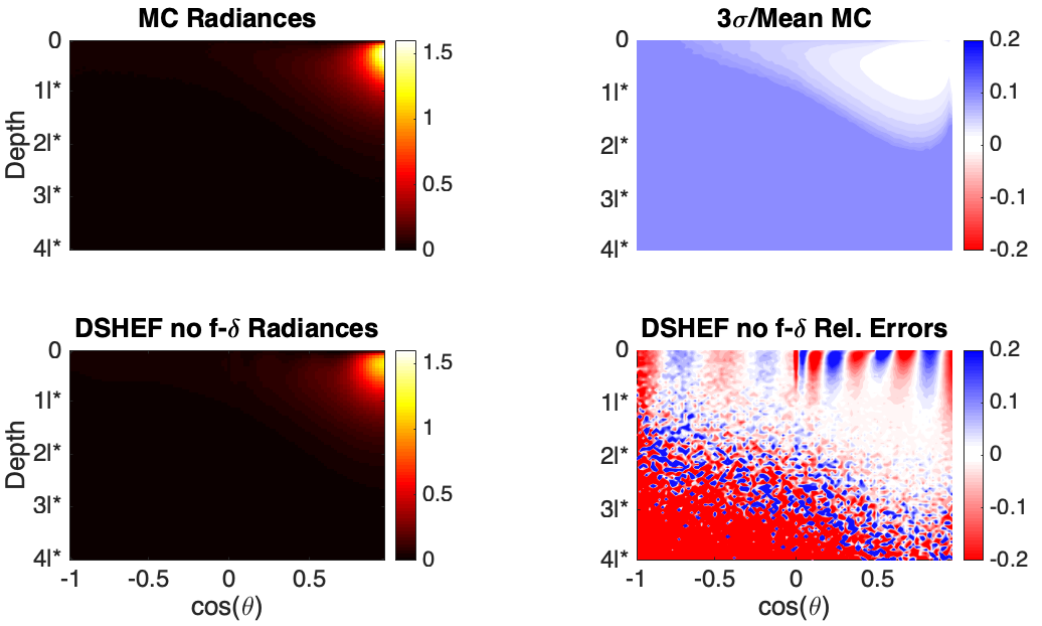

Figure 3.4: Radiance vs depth and $\cos(\theta)$, $l^* = 1$, $\mu_s'/\mu_a = 100$, $f_x = 0.3/l^*$. Top left is Monte Carlo simulation, bottom left is DSHEF_7. Top right is 3σ/mean for Monte Carlo, bottom right is relative error between DSHEF_7 and Monte Carlo.

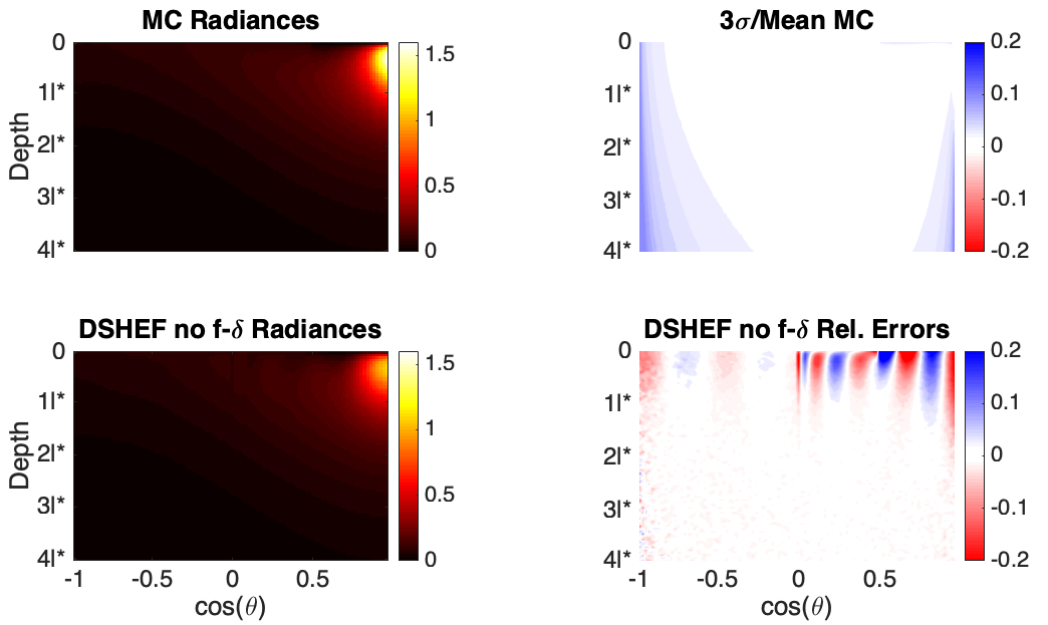

Figure 3.5: Radiance vs depth and $\cos(\theta)$, $l^* = 1$, $\mu_s'/\mu_a = 3$, $f_x = 0$. Top left is Monte Carlo simulation, bottom left is DSHEF_7. Top right is 3σ/mean for Monte Carlo, bottom right is relative error between DSHEF_7 and Monte Carlo.

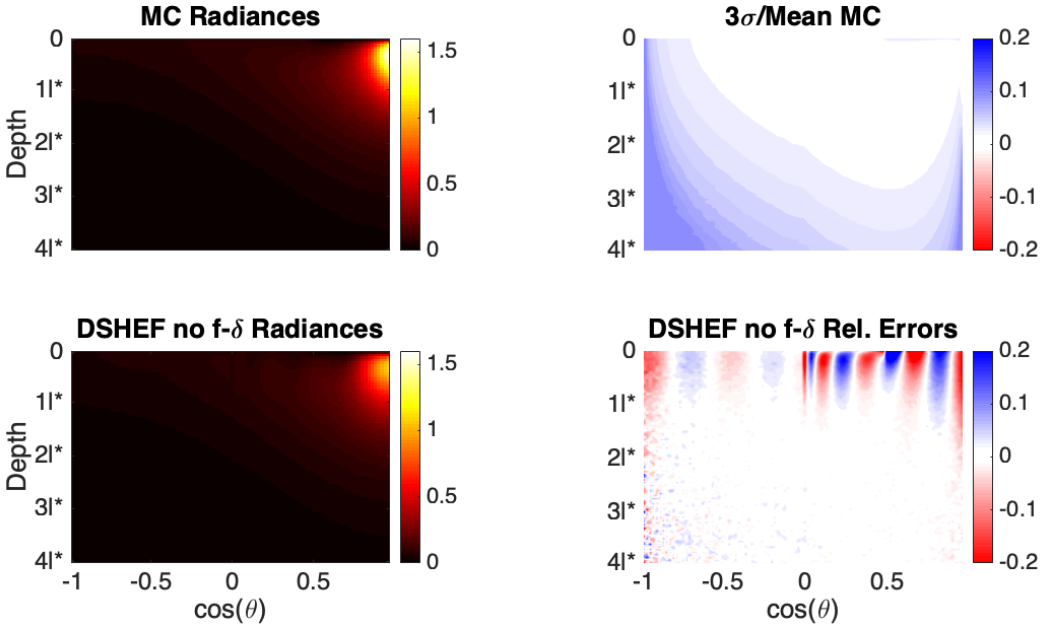

Figure 3.6: Radiance vs depth and $\cos(\theta)$, $l^* = 1$, $\mu_s'/\mu_a = 3$, $f_x = 0.1/l^*$. Top left is Monte Carlo simulation, bottom left is DSHEF_7. Top right is 3σ/mean for Monte Carlo, bottom right is relative error between DSHEF_7 and Monte Carlo.

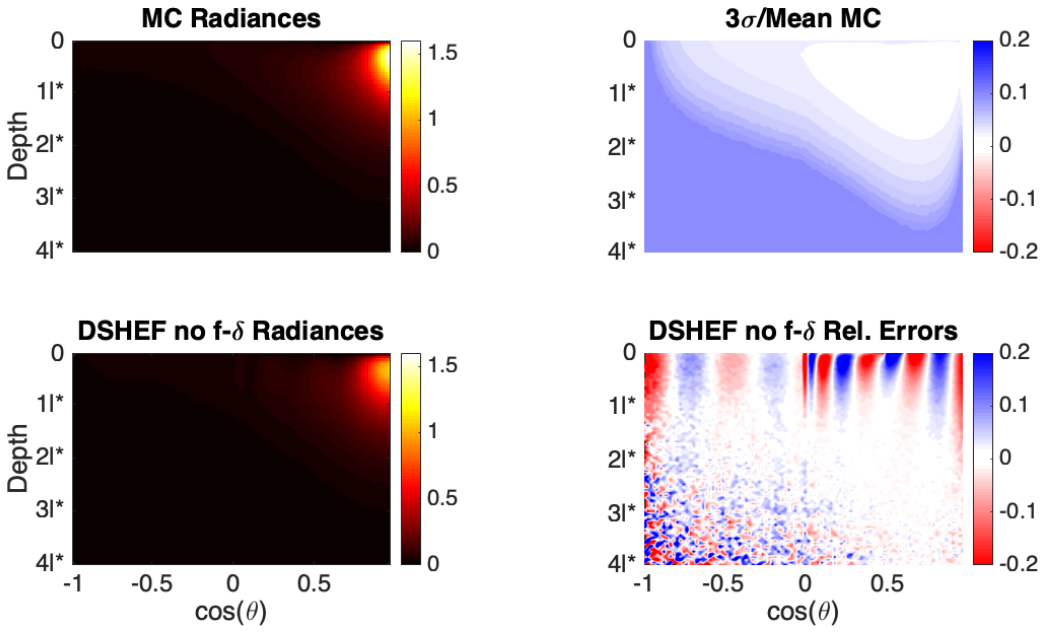

Figure 3.7: Radiance vs depth and $\cos(\theta)$, $l^* = 1$, $\mu_s'/\mu_a = 3$, $f_x = 0.2/l^*$. Top left is Monte Carlo simulation, bottom left is DSHEF_7. Top right is 3σ/mean for Monte Carlo, bottom right is relative error between DSHEF_7 and Monte Carlo.

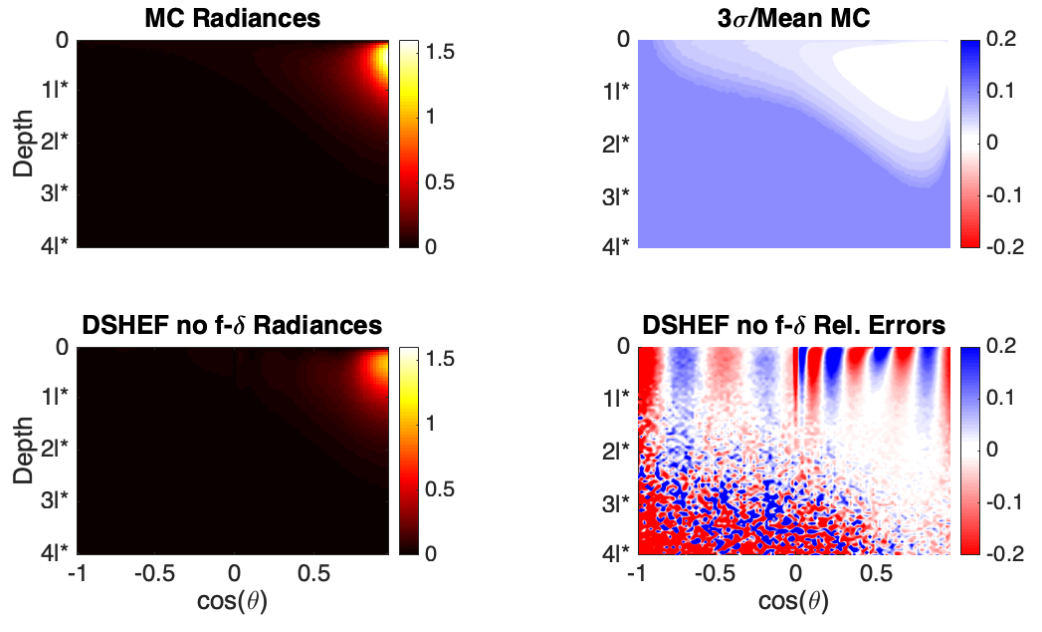

Figure 3.8: Radiance vs depth and $\cos(\theta)$, $l^* = 1$, $\mu_s'/\mu_a = 3$, $f_x = 0.3/l^*$. Top left is Monte Carlo simulation, bottom left is DSHEF_7. Top right is 3σ/mean for Monte Carlo, bottom right is relative error between DSHEF_7 and Monte Carlo.

3.4.1 Radiance vs Depth and Cos(θ)

Figs 3.1–8 show radiance as a function of cosine of polar angle θ and depth z from $z = 0$ to $z = 4l^*$. These depths were chosen because by $z = 4l^*$, only one eigenvector is commonly making a significant contribution to radiance and because as these figures show, error for the Monte Carlo simulation increases in both depth z and spatial frequency f_x.

Only DSHEF_7 is included in this subsection. This order of expansion was chosen as a compromise between quality and computational expense.

In each figure, the top left heat map shows radiance as a function of $\cos(\theta)$ and z as simulated by Monte Carlo. The top right shows three standard deviations of error for this Monte Carlo simulation divided by the simulations mean value, again as functions of $\cos(\theta)$ and z. The bottom left heat map shows the same simulation performed by DSHEF_7 and the bottom right shows relative error between DSHEF_N and Monte Carlo.

Figs 3.1 and 3.5 show the results for highly ($\mu_s'/\mu_a = 100$) and less highly ($\mu_s'/\mu_a = 3$) scattering media, respectively with $f_x = 0$. These figures show the largest area of high confidence in Monte Carlo predictions, as indicated by the small values for $3\sigma/MC$ shown in the top right. Errors for these results are concentrated in angles directed in the positive z direction ($\cos(\theta) > 0$, and are a result of the inability for a smooth, spectral method of finite order to properly reconstruct the non-differentiable point of the internal reflectance function at its critical angle. These errors are more pronounced in the less highly scattering case ($\mu_s'/\mu_a = 3$) depicted in Fig. 3.1, but are largely gone for $z \geq 1l^*$, though in both there is a small (> -0.01) underestimation of the Monte Carlo result by DSHEF_7. Overall, these results are highly consistent with radiance according to Monte Carlo.

Figs 3.2 and 3.6 show the results for highly ($\mu_s'/\mu_a = 100$) and less highly ($\mu_s'/\mu_a = 3$) scattering media, respectively, with $f_x = 0.1/l^*$. Here it should be noted that the region of

depth z and $\cos(\theta)$ over which Monte Carlo error is insignificant is much smaller, extending no deeper than $z = 3l^*$ for any angle. However, in this region, similar error rates, mostly within ± 0.1, are observed and again, DSHEF_7 enjoys a strong similarity to Monte Carlo. It should be again noted that the nature of the error is oscillatory and concentrated in shallow depths (z near 0) and angles directed in the positive z direction. This is beneficial to applications focused on reflectance, and will be further explored in the next section. Once more, errors are smaller in the more highly scattering case shown in Fig. 3.6, which is consistent with results seen from single SHEF_N[21].

Figs 3.3 and 3.7 show the results for highly ($\mu_s'/\mu_a = 100$) and less highly ($\mu_s'/\mu_a = 3$) scattering media, respectively, with $f_x = 0.2/l^*$. Here, the region of high confidence in Monte Carlo simulations has grown smaller still, though within this region the same oscillatory error is seen in both figures. This error is more pronounced, now exceeding ± 0.2 close to the surface ($z = 0$). This is again due to the harmonic nature of the functional basis and will be shown in greater detail in the next section. Once again, error rates for angles directed in the negative z direction ($\cos(\theta) < 0$) have smaller errors than those directed in the positive z direction.

Figs 3.4 and 3.8 show the results for highly ($\mu_s'/\mu_a = 100$) and less highly ($\mu_s'/\mu_a = 3$) scattering media, respectively, with $f_x = 0.3/l^*$. Here, the region of high confidence in Monte Carlo is the smallest still, with most gone for $z > 1.5l^*$. The same pattern of behavior shown in the previous figures is repeated; simulations with more highly scattering media are experience lower error, though both have an oscillatory relative error which decays as z increases.

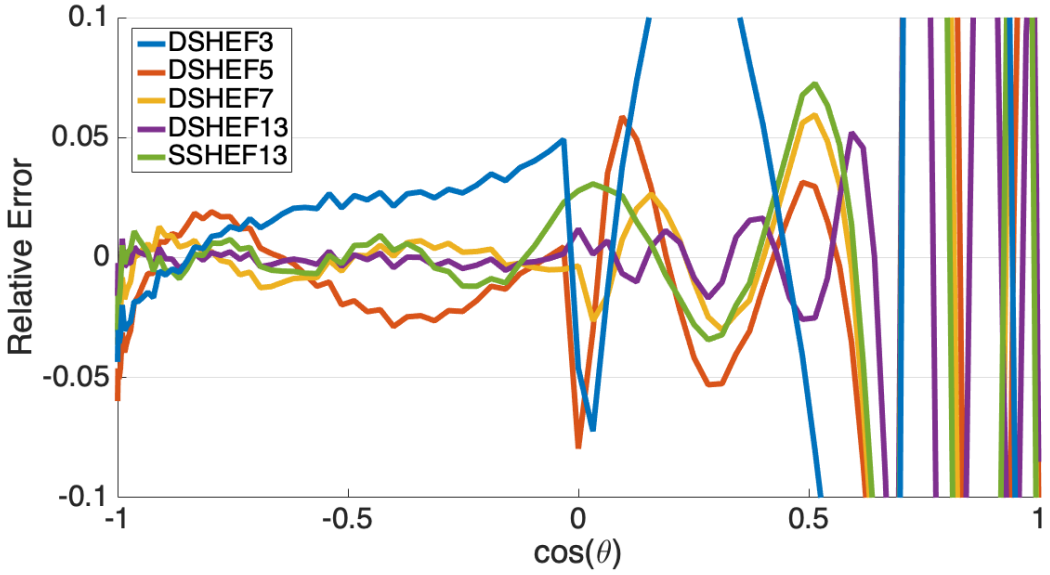

Figure 3.9: Relative error of radiance vs $\cos(\theta)$, $l^* = 1$, $\mu_s'/\mu_a = 100$, $f_x = 0$, $z = 0.025l^*$. DSHEF_3 is given in blue, DSHEF_5 is given in orange, DSHEF_7 is given in gold, DSHEF_{13} is given in purple, single SHEF_{13} is given in green.

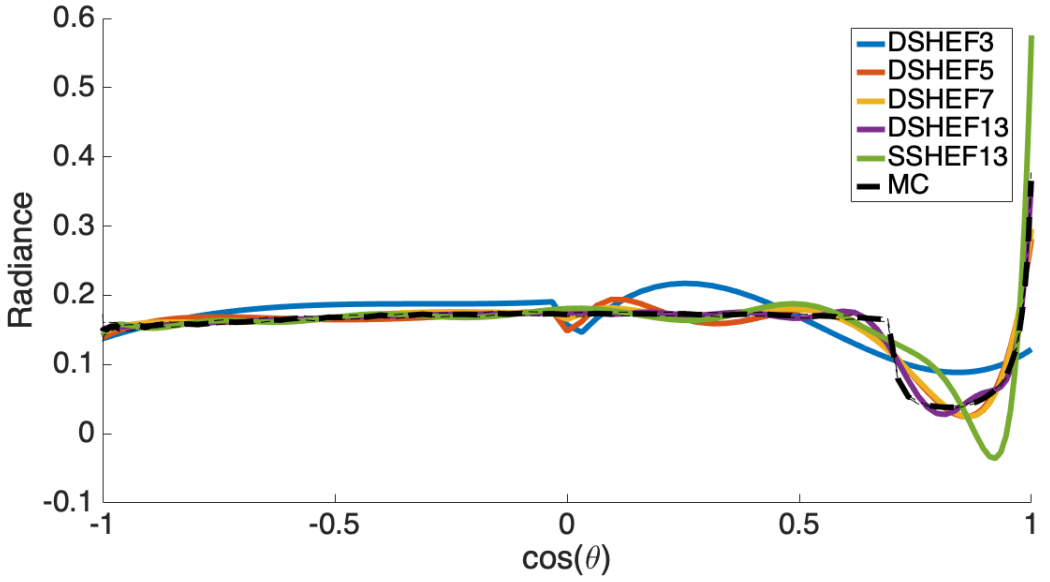

Figure 3.10: Radiance vs $\cos(\theta)$, $l^* = 1$, $\mu_s'/\mu_a = 100$, $f_x = 0.1/l^*$, $z = 0.025l^*$. DSHEF_3 is given in blue, DSHEF_5 is given in orange, DSHEF_7 is given in gold, DSHEF_{13} is given in purple, single SHEF_{13} is given in green and Monte Carlo is given in dashed black. Error bars for the MC results are $\pm 3\sigma$.

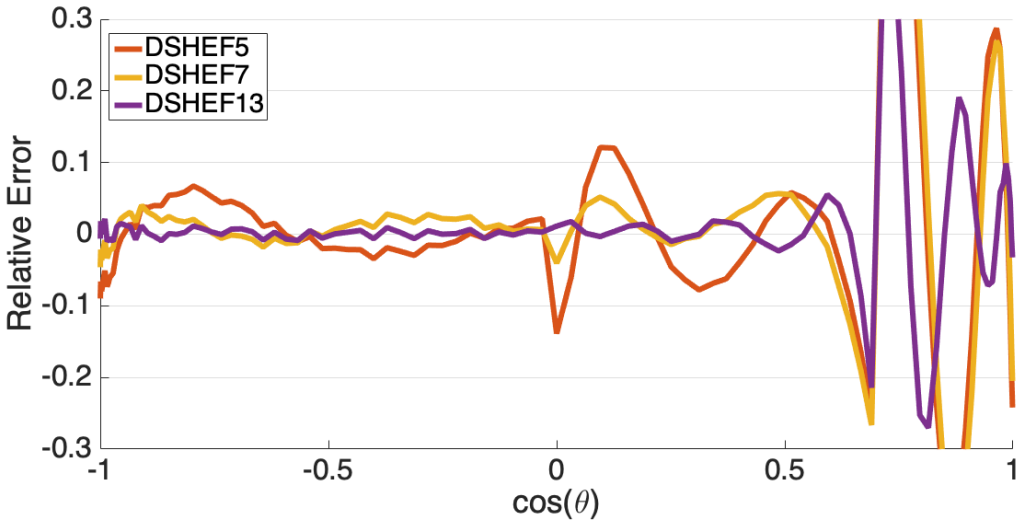

Figure 3.11: Relative error of radiance vs $\cos(\theta)$, $l^* = 1$, $\mu_s'/\mu_a = 100$, $f_x = 0.1/l^*$, $z = 0.025l^*$. DSHEF_3 is given in blue, DSHEF_5 is given in orange, DSHEF_7 is given in gold, DSHEF_{13} is given in purple, single SHEF_{13} is given in green.

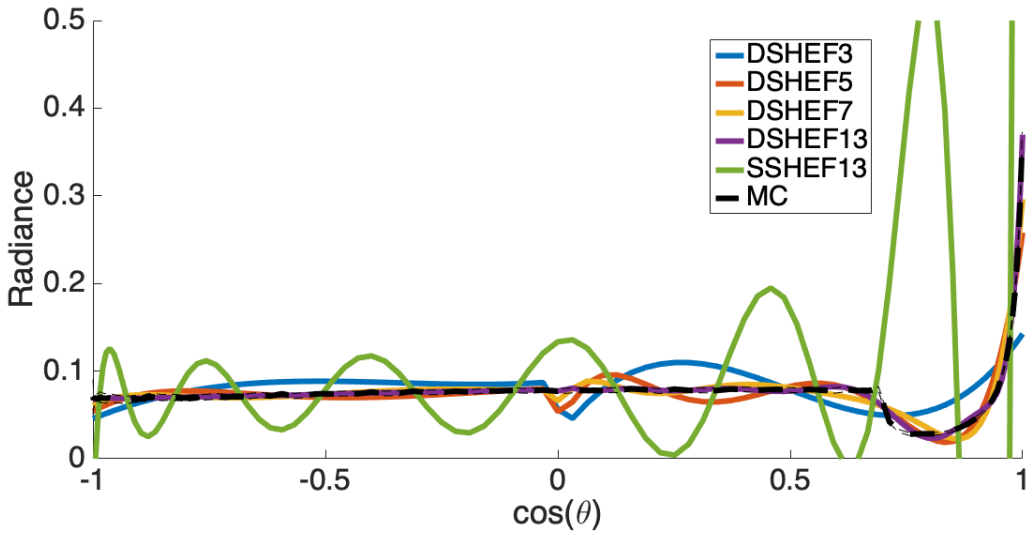

Figure 3.12: Radiance vs $\cos(\theta)$, $l^* = 1$, $\mu_s'/\mu_a = 100$, $f_x = 0.2/l^*$, $z = 0.025l^*$. DSHEF_3 is given in blue, DSHEF_5 is given in orange, DSHEF_7 is given in gold, DSHEF_{13} is given in purple, single SHEF_{13} is given in green and Monte Carlo is given in dashed black. Error bars for the MC results are $\pm 3\sigma$.

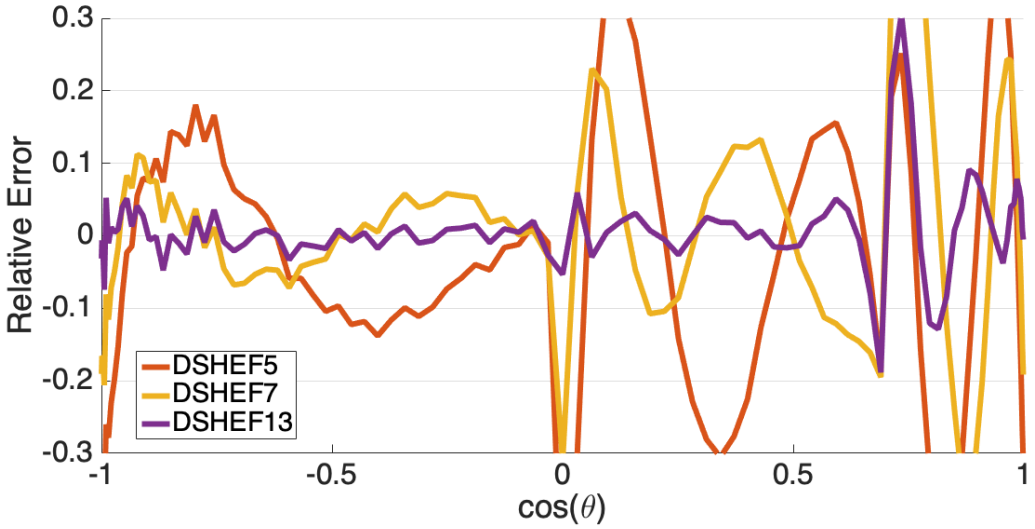

Figure 3.13: Relative error of radiance vs $\cos(\theta)$, $l^* = 1$, $\mu_s'/\mu_a = 100$, $f_x = 0.2/l^*$, $z = 0.025l^*$. DSHEF_3 is given in blue, DSHEF_5 is given in orange, DSHEF_7 is given in gold, DSHEF_{13} is given in purple, single SHEF_{13} is given in green.

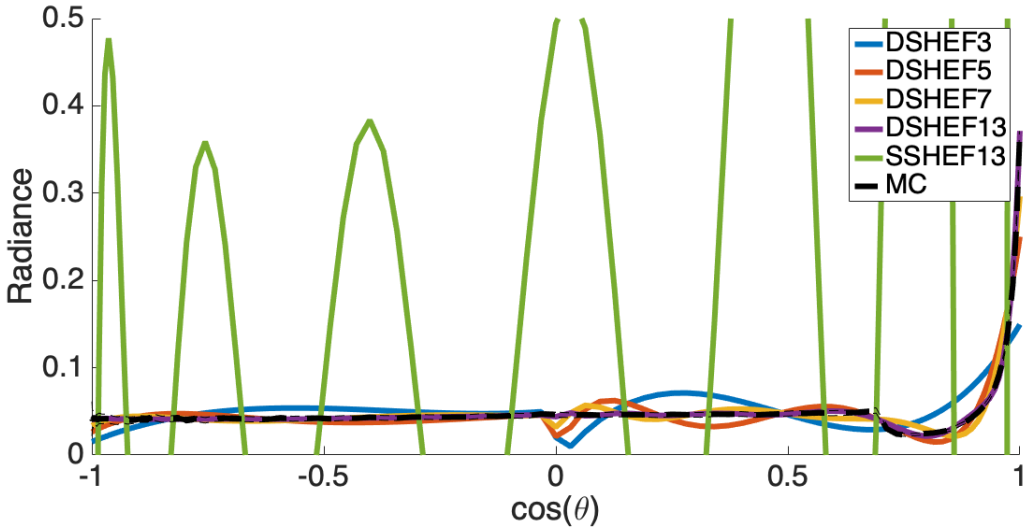

Figure 3.14: Radiance vs $\cos(\theta)$, $l^* = 1$, $\mu_s'/\mu_a = 100$, $f_x = 0.3/l^*$, $z = 0.025l^*$. DSHEF_3 is given in blue, DSHEF_5 is given in orange, DSHEF_7 is given in gold, DSHEF_{13} is given in purple, single SHEF_{13} is given in green and Monte Carlo is given in dashed black. Error bars for the MC results are $\pm 3\sigma$.

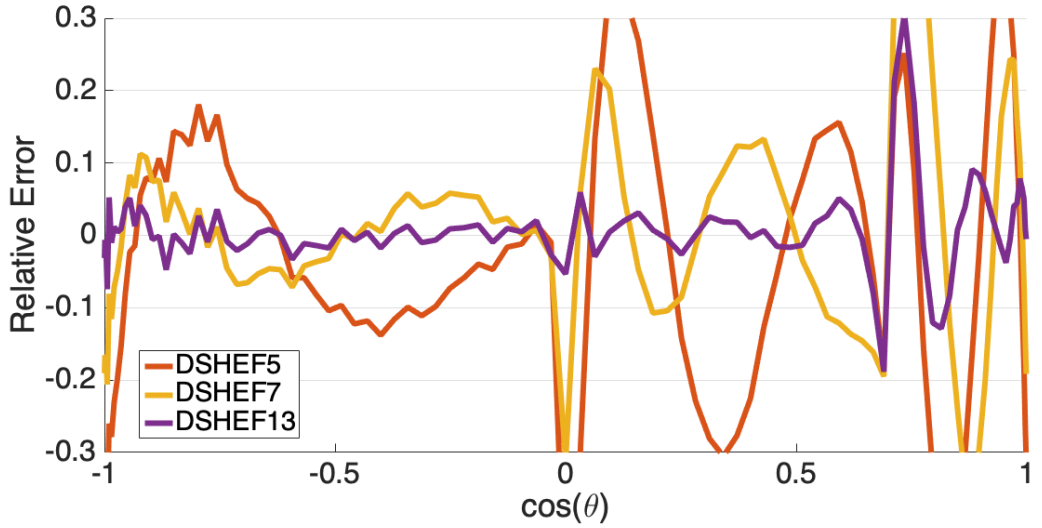

Figure 3.15: Relative error of radiance vs $\cos(\theta)$, $l^* = 1$, $\mu_s'/\mu_a = 100$, $f_x = 0.3/l^*$, $z = 0.025l^*$. DSHEF_3 is given in blue, DSHEF_5 is given in orange, DSHEF_7 is given in gold, DSHEF_{13} is given in purple, single SHEF_{13} is given in green.

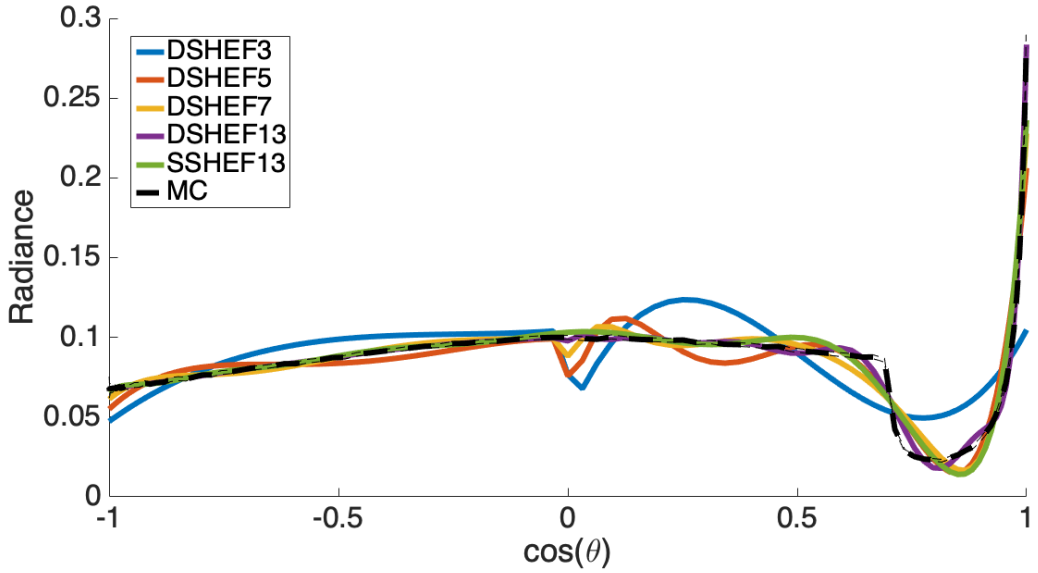

Figure 3.16: Radiance vs $\cos(\theta)$, $l^* = 1$, $\mu_s'/\mu_a = 3$, $f_x = 0$, $z = 0.025l^*$. DSHEF_3 is given in blue, DSHEF_5 is given in orange, DSHEF_7 is given in gold, DSHEF_{13} is given in purple, single SHEF_{13} is given in green and Monte Carlo is given in dashed black. Error bars for the MC results are $\pm 3\sigma$.

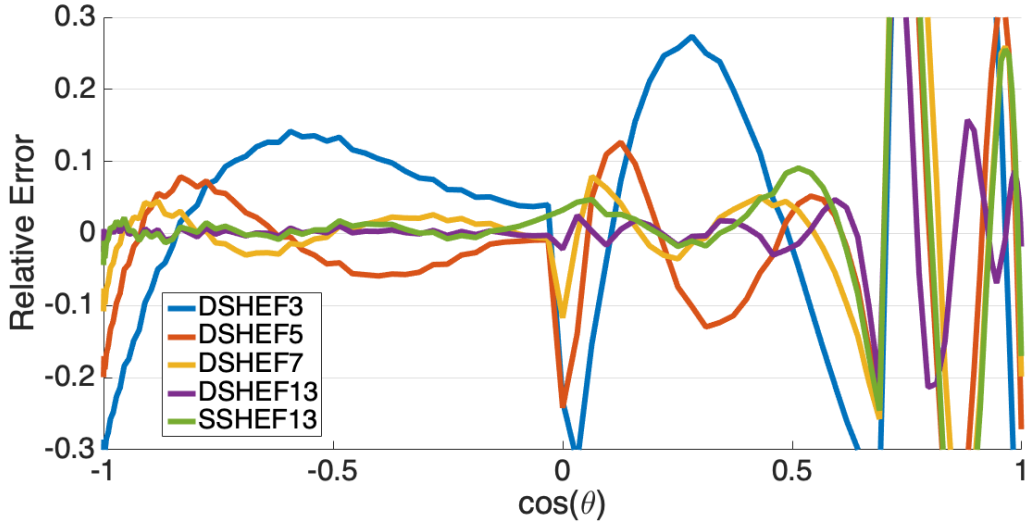

Figure 3.17: Relative error of radiance vs $\cos(\theta)$, $l^* = 1$, $\mu_s'/\mu_a = 3$, $f_x = 0$, $z = 0.025l^*$. DSHEF_3 is given in blue, DSHEF_5 is given in orange, DSHEF_7 is given in gold, DSHEF_{13} is given in purple, single SHEF_{13} is given in green.

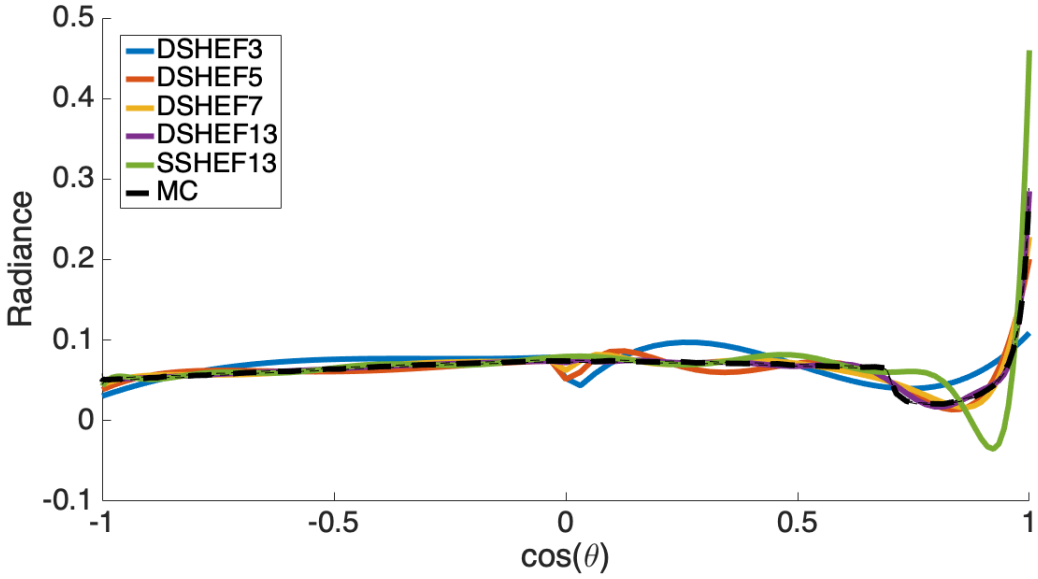

Figure 3.18: Radiance vs $\cos(\theta)$, $l^* = 1$, $\mu_s'/\mu_a = 3$, $f_x = 0.1/l^*$, $z = 0.025l^*$. DSHEF_3 is given in blue, DSHEF_5 is given in orange, DSHEF_7 is given in gold, DSHEF_{13} is given in purple, single SHEF_{13} is given in green and Monte Carlo is given in dashed black. Error bars for the MC results are $\pm 3\sigma$.

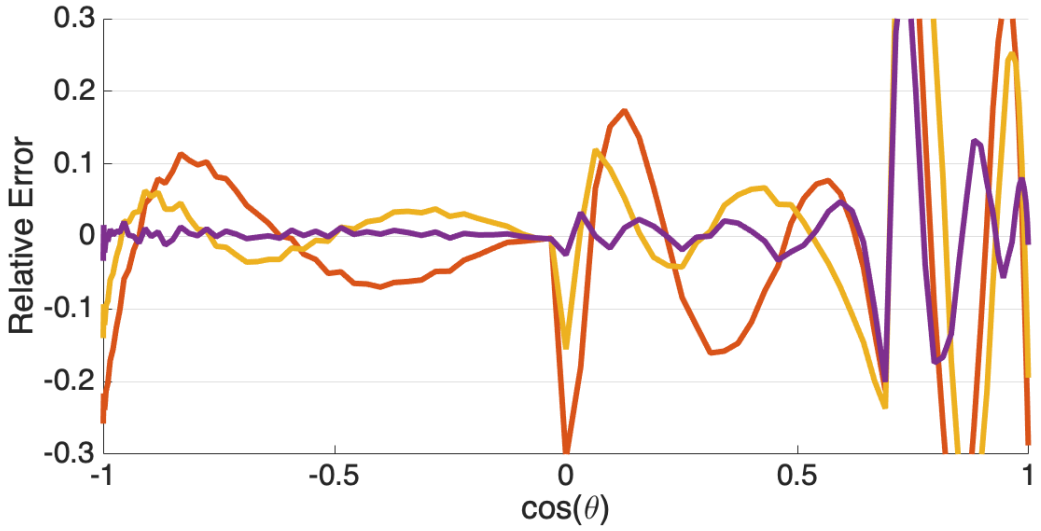

Figure 3.19: Relative error of radiance vs $\cos(\theta)$, $l^* = 1$, $\mu_s'/\mu_a = 3$, $f_x = 0.1/l^*$, $z = 0.025l^*$. DSHEF_3 is given in blue, DSHEF_5 is given in orange, DSHEF_7 is given in gold, DSHEF_{13} is given in purple, single SHEF_{13} is given in green.

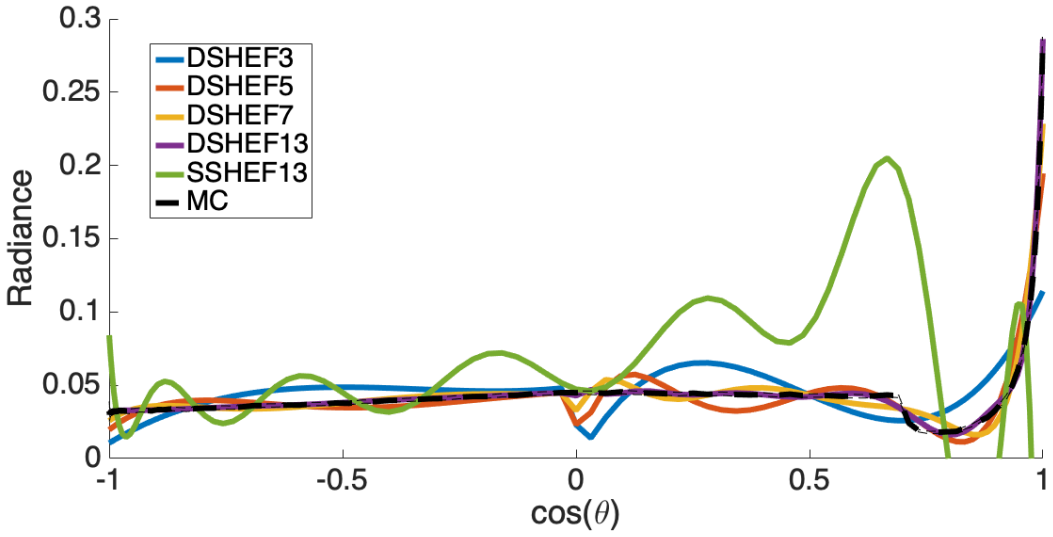

Figure 3.20: Radiance vs $\cos(\theta)$, $l^* = 1$, $\mu_s'/\mu_a = 3$, $f_x = 0.2/l^*$, $z = 0.025l^*$. DSHEF_3 is given in blue, DSHEF_5 is given in orange, DSHEF_7 is given in gold, DSHEF_{13} is given in purple, single SHEF_{13} is given in green and Monte Carlo is given in dashed black. Error bars for the MC results are $\pm 3\sigma$.

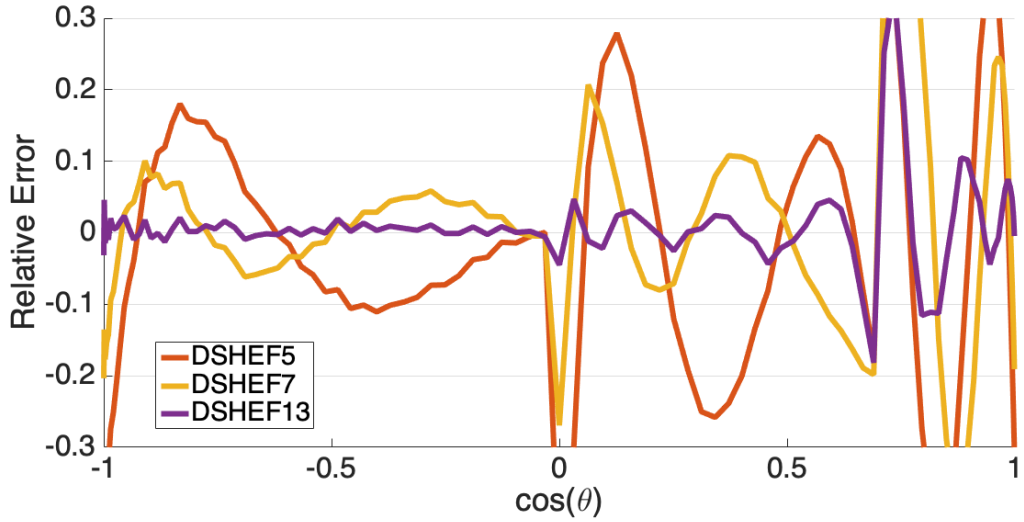

Figure 3.21: Relative error of radiance vs $\cos(\theta)$, $l^* = 1$, $\mu_s'/\mu_a = 3$, $f_x = 0.2/l^*$, $z = 0.025l^*$. DSHEF_3 is given in blue, DSHEF_5 is given in orange, DSHEF_7 is given in gold, DSHEF_{13} is given in purple, single SHEF_{13} is given in green.

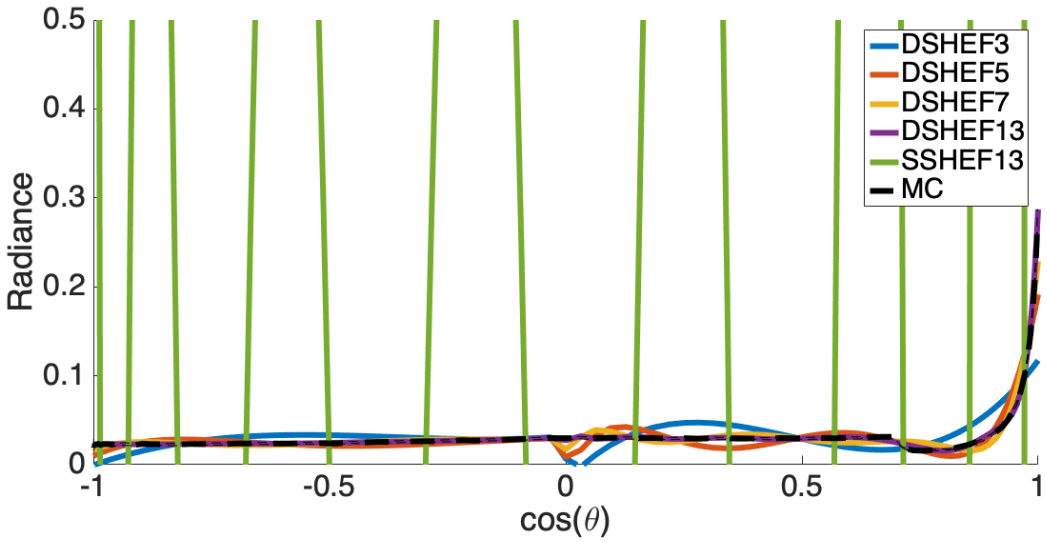

Figure 3.22: Radiance vs $\cos(\theta)$, $l^* = 1$, $\mu_s'/\mu_a = 3$, $f_x = 0.3/l^*$, $z = 0.025l^*$. DSHEF_3 is given in blue, DSHEF_5 is given in orange, DSHEF_7 is given in gold, DSHEF_{13} is given in purple, single SHEF_{13} is given in green and Monte Carlo is given in dashed black. Error bars for the MC results are $\pm 3\sigma$.

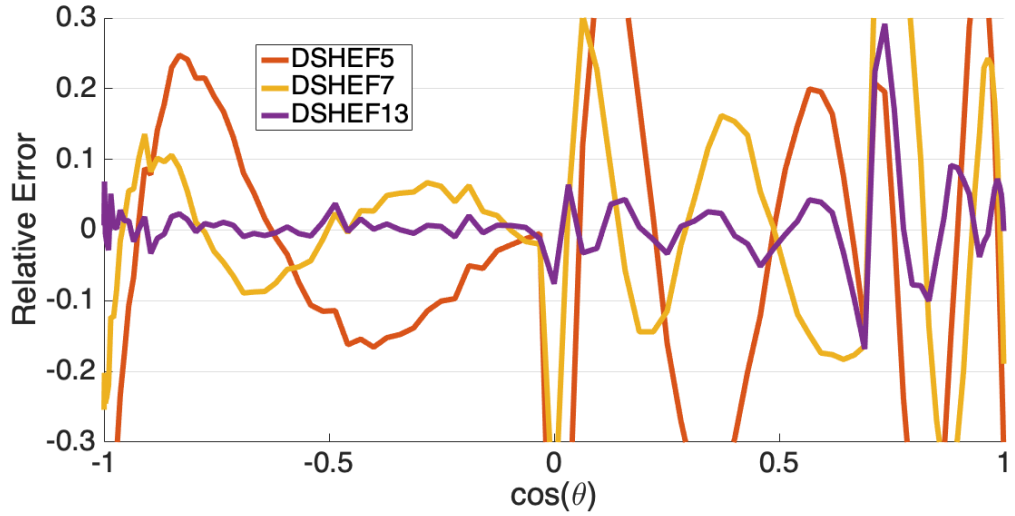

Figure 3.23: Relative error of radiance vs $\cos(\theta)$, $l^* = 1$, $\mu_s'/\mu_a = 3$, $f_x = 0.3/l^*$, $z = 0.025l^*$. DSHEF_3 is given in blue, DSHEF_5 is given in orange, DSHEF_7 is given in gold, DSHEF_{13} is given in purple, single SHEF_{13} is given in green.

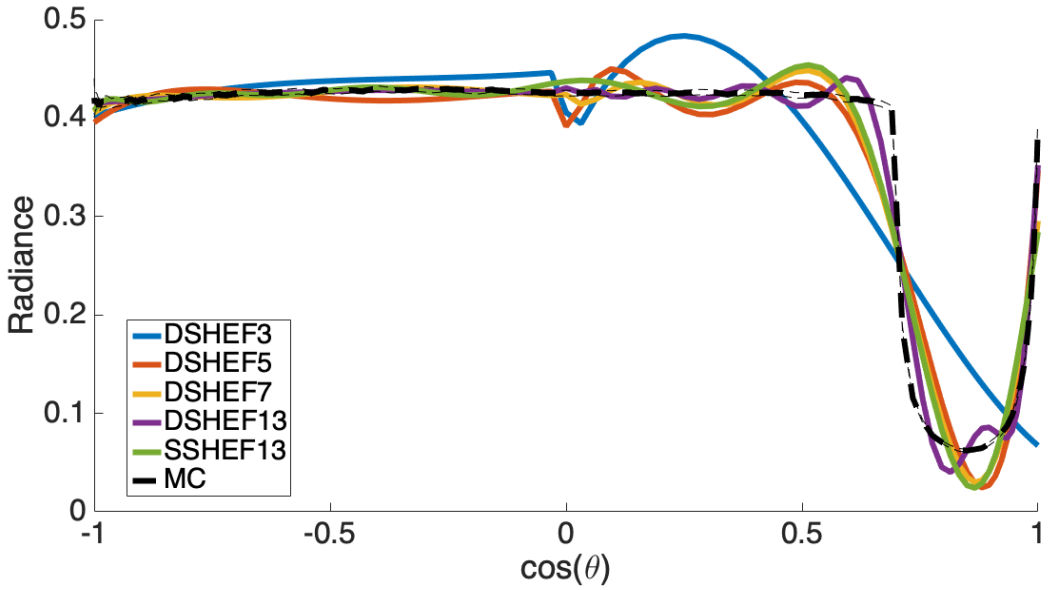

Figure 3.24: Radiance vs $\cos(\theta)$, $l^* = 1$, $\mu_s'/\mu_a = 100$, $f_x = 0$, $z = 0.025l^*$. DSHEF_3 is given in blue, DSHEF_5 is given in orange, DSHEF_7 is given in gold, DSHEF_{13} is given in purple, single SHEF_{13} is given in green and Monte Carlo is given in dashed black. Error bars for the MC results are $\pm 3\sigma$.

3.4.2 Radiance vs Cos(θ) Near Medium Surface

Figs 3.9–24 show radiance as a function of $\cos(\theta)$ at a depth of $z = 0.025l^*$, as well as relative error between deterministic methods and the provided Monte Carlo gold standard. This depth was chosen because of the nature of data collection for this Monte Carlo software; radiance is tallied by arithmetic mean in bins for angle, depth and spatial frequency, and the bins with the lowest depth z begin at $z = 0$, so no bin may be centered around $z = 0$. The Monte Carlo simulations performed used bin widths of $0.05l^*$, and therefore the bins most close to the surface were centered around $z = 0.25l^*$.

In each of these figures, DSHEF_3 is given in blue, DSHEF_5 is given in orange, DSHEF_7 is given in gold, DSHEF_{13} is given in purple, SSHEF_{13} is given in green and Monte Carlo is given in dashed black. Odd numbered figures display radiance as a function of $\cos(\theta)$ while even numbered figures display relative error thereof.

It should first be noted that in each set of figures in this subsection, all methods shown experience difficulty reconstructing radiance directed in the positive z direction, or when $\cos(\theta) > 0$. This is due to the non-differentiable point of the internal reflectance function at its critical angle. Such a point is well known to be impossible to properly create using a linear combination of smooth functions. Furthermore, errors tend to be oscillatory in nature, due to the polynomial component of the basis used.

Figs 3.9–10 and 3.17–18 show radiance and error for highly ($\mu_s'/\mu_a = 100$) and less highly ($\mu_s'/\mu_a = 3$) scattering media, respectively, with spatial frequency $f_x = 0$. In each of these cases, DSHEF_{13} showes the lowest relative error rates. For radiance in the negative z direction, or when $\cos(\theta) > 0$, DSHEF_{13} shows relative errors mostly within ± 0.01. In the less highly scattering case shown in Figs. 3.17–18, the next best performer in this angular range is single SHEF_{13}, which shows error rates within ± 0.015. It is followed by followed by DSHEF_5, with relative error rates within ± 0.06. DSHEF_3, on the other hand, shows relative

error rates in excess of ± 0.1, displaying difficulty in constructing radiance at this depth. In the more highly scattering case shown in Figs 3.9–10, however, all of these error rates are smaller. $DSHEF_7$ stays within ± 0.015, along with single $SHEF_{13}$, while $DSHEF_5$ experiences an underestimation of -0.06 at $\cos(\theta) = -1$, followed by relative error rates within $\pm 0.025 l^*$. In each case, methods experience more strongly oscillating errors when $\cos(\theta) > 0$. These errors increase as $\cos(\theta)$ approaches 1, but are always the smallest for $DSHEF_{13}$. In the more hihghly scattering case, $DSHEF_7$ shows smaller errors than single $SHEF_{13}$, while the opposite is true for the less highly scattering case. Finally, across all angles, $DSHEF_3$ shows smaller error rates in more highly scattering media, staying within ± 0.05 when $-1 \leq \cos(\theta) < 0$.

Figs 3.11–12 and 3.19–20 show radiance and error for highly ($\mu_s'/\mu_a = 100$) and less highly ($\mu_s'/\mu_a = 3$) scattering media, respectively, with spatial frequency $f_x = 0.1/l^*$. As in the previous cases, each method experiences growing oscillations for $\cos(\theta) > 0$, as $\cos(\theta)$ goes to 1. It should also be noted that single $SHEF_{13}$ actually sees a small region of negative radiance, a physical impossibility, around $\cos(\theta) = 0.9$. It also now experiences worse error rates than $DSHEF_7$ when $-1 \leq \cos(\theta) < 0$ in less highly scattering media, in contrast to the opposite when $f_x = 0$. Overall, in this direction, $DSHEF_{13}$ shows error rates within ± 0.015, while $DSHEF_7$, apart from an underestimation by approximately -0.1 at $\cos(\theta) = -1$, has relative error rates between -0.035 and 0.065. $DSHEF_5$ sees the same dampening oscillation in this direction as $\cos(\theta)$ approaches 0, with a maximum overestimation of approximately 0.11 at $\cos(\theta) = -0.8$ and a maximal underestimation of approximately -0.04 at $\cos(\theta) = -0.065$. $DSHEF_3$ sees extreme under and overestimation, as when $f_x = 0$, showing the difficulty this order of expansion has when a medium is less highly scattering.

Figs 3.13–14 and 3.21–22 show radiance and error for highly ($\mu_s'/\mu_a = 100$) and less highly ($\mu_s'/\mu_a = 3$) scattering media, respectively, with spatial frequency $f_x = 0.2/l^*$. Here, single $SHEF_{13}$ shows extreme error in high harmonics in both media examined. This error increases as $\cos(\theta)$ approaches 1, and is in any event unacceptable for any task involving a detailed

description of radiance. In contrast, while each expansion order of DSHEF_N does experience higher relative errors than the previous cases, the absolute errors shown are similar. This leads to larger absolute errors because radiance itself decreases as spatial frequency increases. When considering angles such that $-1 \leq \cos(\theta) < 0$, and less highly scattering media shown in Figs 3.21–22, DSHEF_{13} is once again showing the smallest error rates of any method shown, staying largely within ± 0.02. DSHEF_7 sees a maximal overestimation of approximately 0.1 at $\cos(\theta) = -0.8$ and a maximal underestimation of approximately -0.065 at $\cos(\theta) = -0.065$. DSHEF_5, on the other hand, exceeds overestimations of 0.1 in a neighborhood around $\cos(\theta) = -0.07$ and underestimations of -0.1 in a neighborhood around $\cos(\theta) = -0.4$. DSHEF_3 sees extemes in both over and under estimation. In the more highly scattering case shown in Figs 3.21–22, these error rates and locations are quite similar, except for DSHEF_{13}, which shows more extreme rates. These are as bad as ± 0.05, but stay largely within ± 0.03. In both cases, the same growing oscillations of relative error as $\cos(\theta)$ increases are seen in all orders of expansion of DSHEF_N for $0 < \cos(\theta) \leq 1$, with convergence to smaller error rates as N increases.

Figs 3.15–16 and 3.23–24 show radiance and error for highly ($\mu_s'/\mu_a = 100$) and less highly ($\mu_s'/\mu_a = 3$) scattering media, respectively, with spatial frequency $f_x = 0.3/l^*$. As when $f_x = 0.2/l^*$, single SHEF_{13} exhibits a harmonic error orders of magnitude stronger than the actual Monte Carlo simulation. Meanwhile, when considering the angular range such that $0 < \cos(\theta) \leq 1$, relative error osccilations which grow in $\cos(\theta)$ but dampen in N are shown for all orders of expansion for DSHEF_N. In the angular range such that $-1 \leq \cos(\theta) < 0$, the pattern shown at lower spatial frequencies continues. In the less highly scattering cases shown in Figs 3.23–24, the relative error for DSHEF_{13} stays largely within ± 0.03, while DSHEF_7 sees a maximal overestimation of 0.1 near $\cos(\theta) = -0.75$ and a maximal underestimation of -0.9 near $\cos(\theta) = -0.065$. DSHEF_5 sees the same regions of extreme overestimation (¿0.1) in a neighborhood around $\cos(\theta) = -0.7$ and extreme underestimation (¡-0.1) in a neighborhood around $\cos(\theta) = -0.4$. The fact that the most extreme errors are always

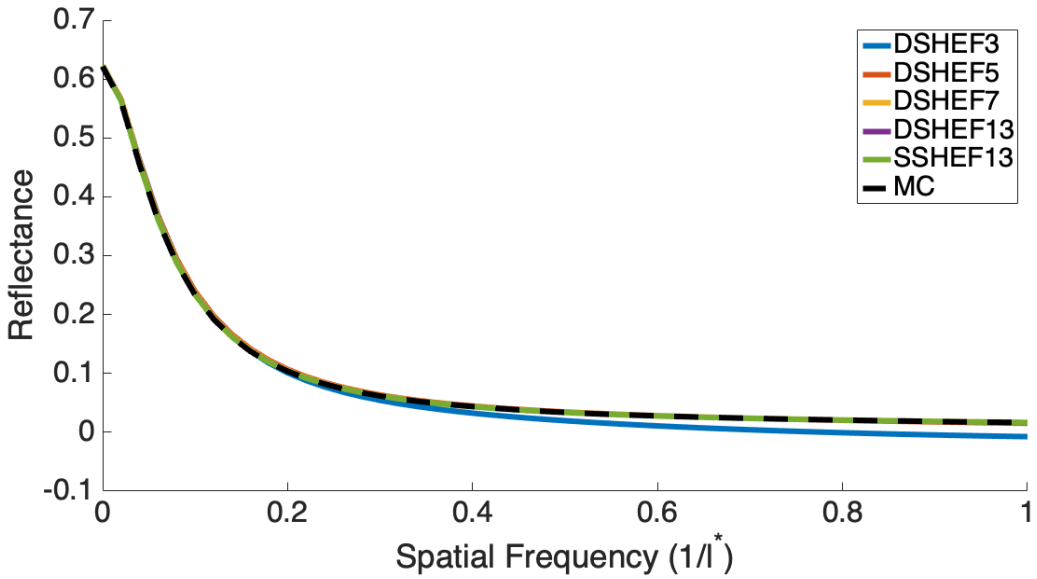

Figure 3.25: Reflectance vs Spatial Frequency, $l^* = 1$, $\mu_s'/\mu_a = 100$. SHEF_3 is given in blue, DSHEF_5 is given in orange, DSHEF_7 is given in gold, DSHEF_{13} is given in purple, single SHEF_{13} is given in green and Monte Carlo is given in dashed black. Error bars for the MC results are $\pm 3\sigma$.

in similar angle ranges is due to the nature of the polynomial component of the spherical harmonics; the extrema in $\cos(\theta)$ will always be located at the same angles for the same functions. In the more highly scattering case shown in Figs 3.15–16, these errors are smaller. DSHEF_{13}'s relative error sees apprxomately the same range, with a few spikes to ± 0.05 but largely within ± 0.03. The error rates and locations of maximal under and over estimation are similar to the less highly scattering case for DSHEF_5 and DSHEF_7.

3.4.3 Reflectance vs Spatial Frequency

Figs 3.25–28 show reflectance as a function of spatial frequency from $f_x = 0$ to $f_x = 1$. As before, odd numbered figures show reflectance, while even numbered figures show the relative error between the deterministic models used and the Monte Carlo gold standard presented.

In each of these figures, DSHEF_3 is given in blue, DSHEF_5 is given in orange, DSHEF_7 is

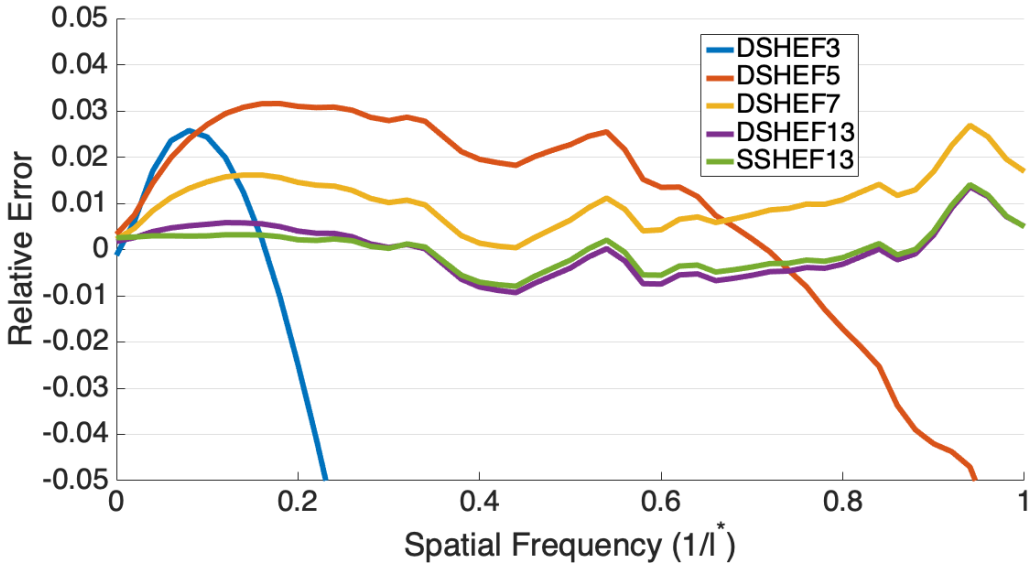

Figure 3.26: Relative error of reflectance vs Spatial Frequency, $l^* = 1$, $\mu_s'/\mu_a = 100$. SHEF_3 is given in blue, DSHEF_5 is given in orange, DSHEF_7 is given in gold, DSHEF_{13} is given in purple and single SHEF_{13} is given in green.

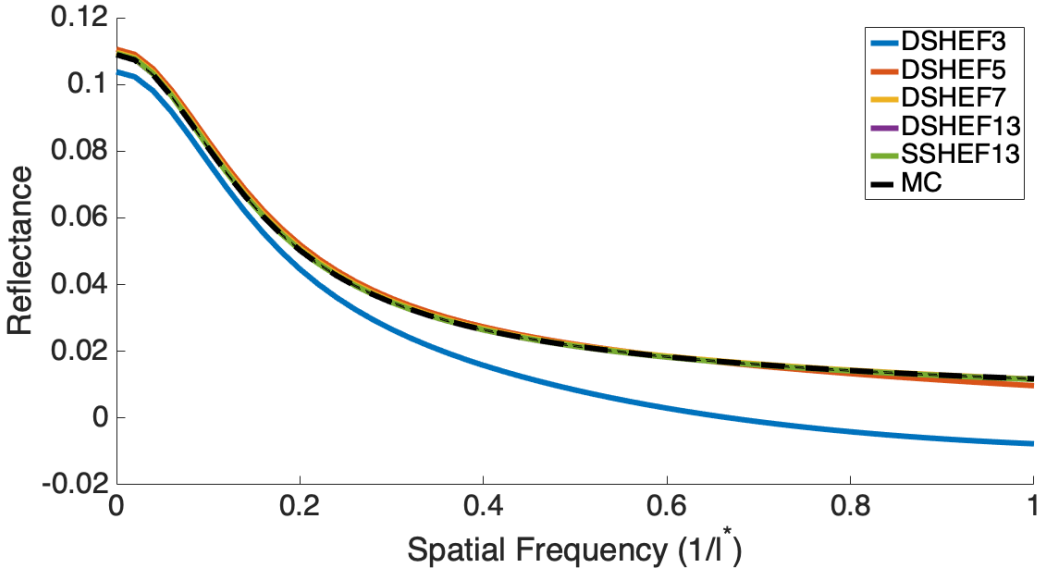

Figure 3.27: Reflectance vs Spatial Frequency, $l^* = 1$, $\mu_s'/\mu_a = 3$. SHEF_3 is given in blue, DSHEF_5 is given in orange, DSHEF_7 is given in gold, DSHEF_{13} is given in purple, single SHEF_{13} is given in green and Monte Carlo is given in dashed black. Error bars for the MC results are $\pm 3\sigma$.

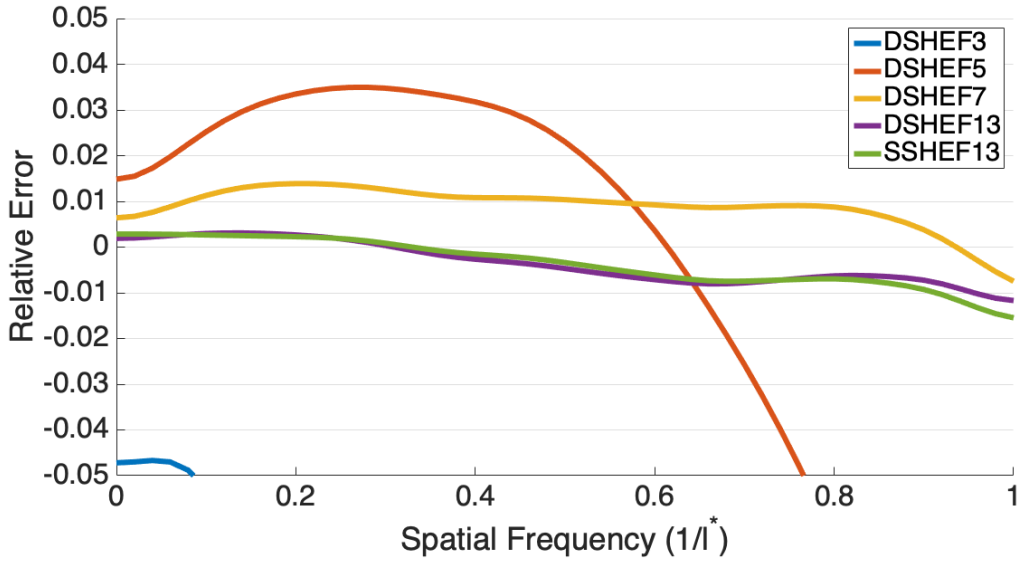

Figure 3.28: Relative error of reflectance vs Spatial Frequency, $l^* = 1$, $\mu_s'/\mu_a = 3$. SHEF_3 is given in blue, DSHEF_5 is given in orange, DSHEF_7 is given in gold, DSHEF_{13} is given in purple and single SHEF_{13} is given in green.

given in gold, DSHEF_{13} is given in purple, SSHEF_{13} is given in green and Monte Carlo is given in dashed black.

It must be noted that the Monte Carlo simulations shown in Figs 3.25–26 were performed using 20M photon packets instead of 10M. This was due to input error, but since the result is increased confidence in the MC results, I decided to leave them in.

Figs 3.25–26 show reflectance and relative error, respectively, for a more highly scattering medium ($\mu_s'/\mu_a = 100$). In these figures, it is clear that DSHEF_3 experiences error rates in excess of the other models shown, though these errors are still less extreme than those seen in the more highly scattering case. When $f_x = 0$, it, along with all other models examined, experiences a relative error within ± 0.002. However, as spatial frequency increase, it sees an initial overestimation, peaking at approximately 0.026 when $f_x = 0.09/l^*$, followed by a slide into extreme underestimation. This underestimation exceeds -0.05 for $f_x \geq 0.23/l^*$, and the separation between DSHEF_3 and Monte Carlo results increases with f_x. DSHEF_5 shows a similar behavior on a much wider scale: It approaches a maximal overestimation of 0.031

near $f_x = 0.2/l^*$, then a slow decay into underestimation. Its relative error becomes negative at approximately $f_x = 0.76/l^*$ and becomes progressively more negative as f_x increases. DSHEF_7, DSHEF_{13} and single SHEF_{13}, however, do not appear to decay in this manner over the spatial frequencies examined. Instead, DSHEF_7 exhibits over estimation between 0 and 0.28, while DHSEF_{13} and single SHEF_{13} both exhibit very similar results, with relative errors largely within ± 0.01, except for a small spike to 0.013 at $f_x = 0.95/l^*$.

Figs 3.27–28 show reflectance and relative error, respectively, for a less highly scattering medium ($\mu_s'/\mu_a = 3$). Here, it is clear that DSHEF_3 experiences extreme underestimations which are exacerbated by increases in f_x. DSHEF_5 experiences a switch from overestimation for $0 \leq f_x \leq 0.62/l^*$ to underestimation for $f_x > 0.62/l^*$. This underestimation increases with f_x without any indication of correction at higher frequencies. DSHEF_7, DSHEF_{13} and single SHEF_{13}, on the other hand, show much smaller changes in error over spatial frequencies examined, as well as smaller overall relative errors. They do go from maximal overestimations 0.014 at $f_x = 0.2/l^*$ for DSHEF_7, 0.0031 at $f_x = 0.14/l^*$ for DSHEF_{13} and 0.0029 at $f_x = 0$ for single SHEF_{13}, to underestimations of -0.0075 for DSHEF_7, -0.012 for DSHEF_{13} and -0.015 for single SHEF_{13}, all at $f_x = 1/l^*$.

3.4.4 Fluence vs Depth

Figs 3.29–36 show fluence and relative error as a function of depth from $z = 0$ to $z = 5l^*$. Both highly scattering ($\mu_s'/\mu_a = 100$) and less highly scattering ($\mu_s'/\mu_a = 3$) media are considered. Results and relative errors are shown for spatial frequencies $f_x = 0$, $f_x = 0.1/l^*$, $f_x = 0.2/l^*$ and $f_x = 0.3/l^*$.

It must be noted that by definition, fluence is the integral of all radiance at a point r with respect to spherical angle Ω. However, both DSHEF_N and single SHEF_N produce solutions for $L_S(r, \Omega)$, scattered radiance. Recall that as noted in Chapter 2, total radiance due to

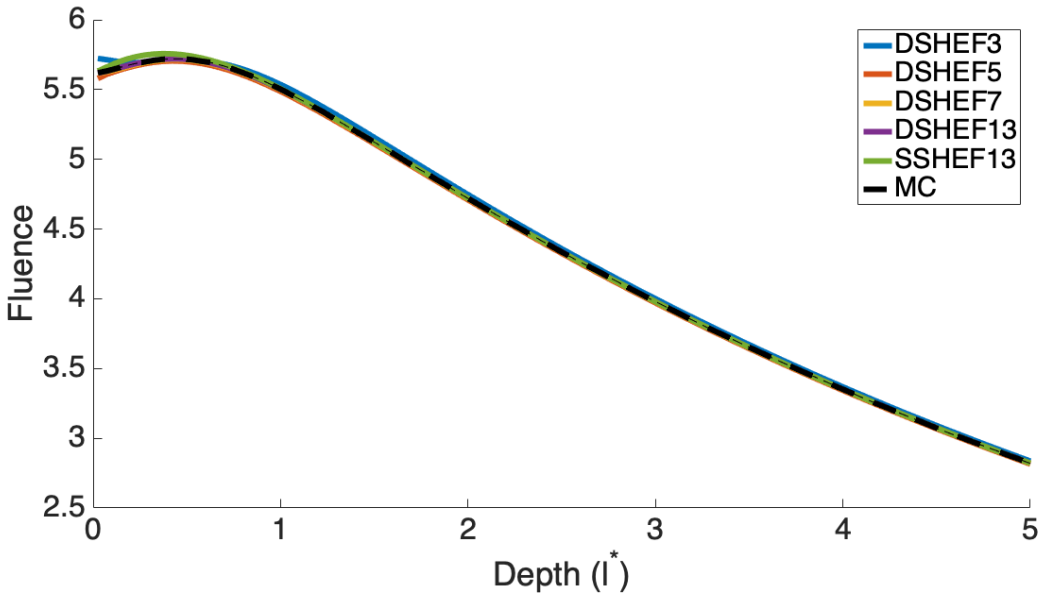

Figure 3.29: Fluence vs. Depth, $l^* = 1$, $\mu_s'/\mu_a = 100$, $f_x = 0$. DSHEF_3 is given in blue, DSHEF_5 is given in orange, DSHEF_7 is given in gold, DSHEF_{13} is given in purple, single SHEF_{13} is given in green and Monte Carlo is given in dashed black. Error bars for the MC results are $\pm 3\sigma$.

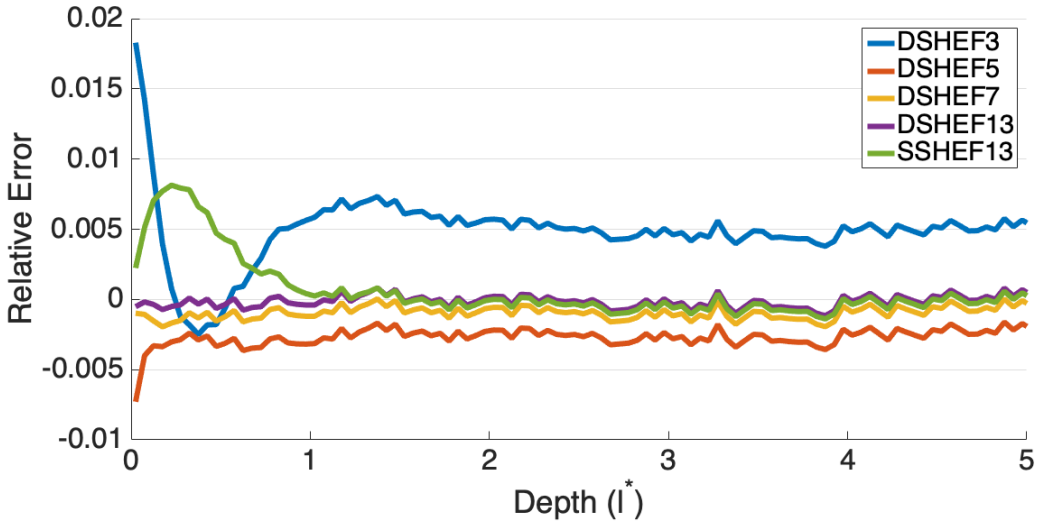

Figure 3.30: Relative Error of Fluence vs. Depth, $l^* = 1$, $\mu_s'/\mu_a = 100$, $f_x = 0$. DSHEF_3 is given in blue, DSHEF_5 is given in orange, DSHEF_7 is given in gold, DSHEF_{13} is given in purple, single SHEF_{13} is given in green.

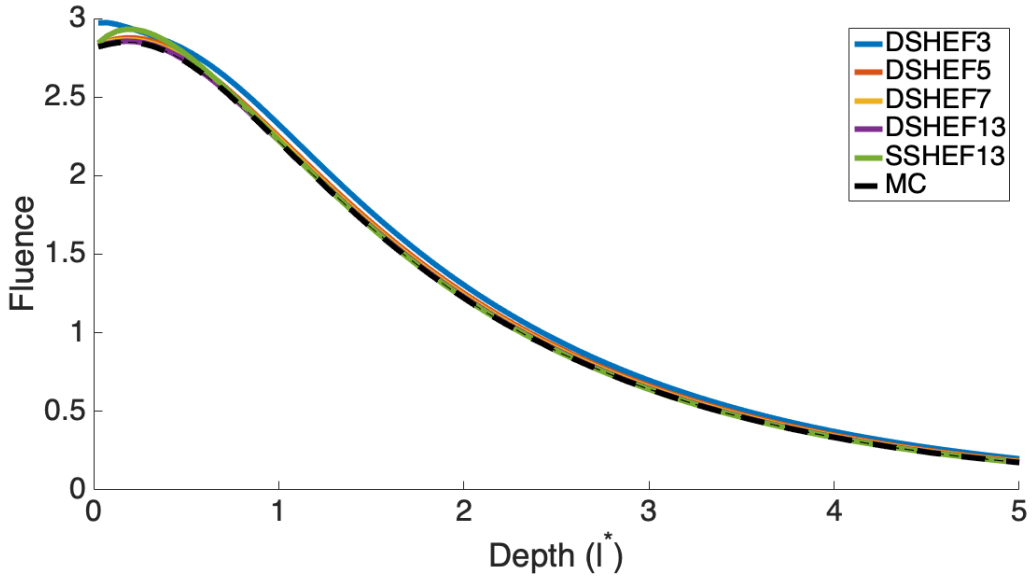

Figure 3.31: Fluence vs. Depth, $l^* = 1$, $\mu_s'/\mu_a = 100$, $f_x = 0.1/l^*$. DSHEF_3 is given in blue, DSHEF_5 is given in orange, DSHEF_7 is given in gold, DSHEF_{13} is given in purple, single SHEF_{13} is given in green and Monte Carlo is given in dashed black. Error bars for the MC results are $\pm 3\sigma$.

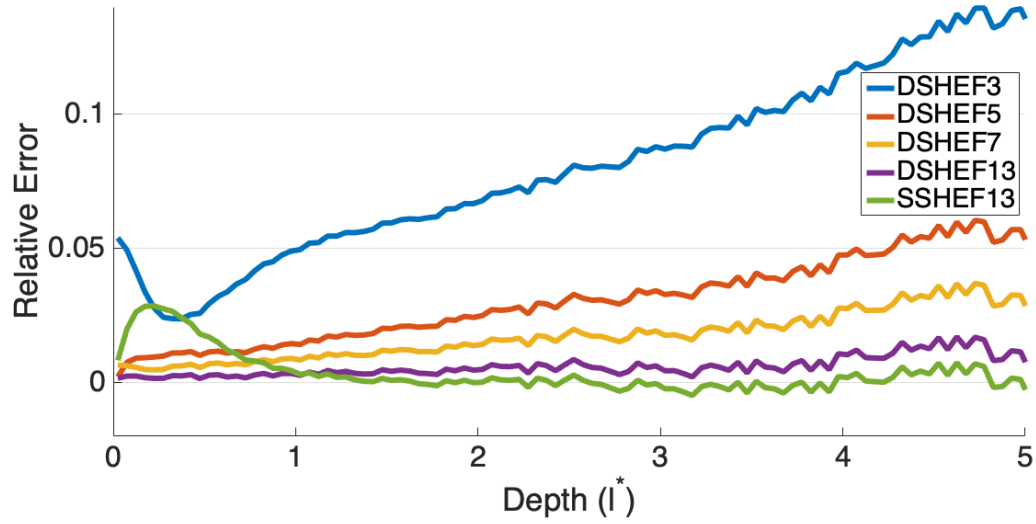

Figure 3.32: Relative Error of Fluence vs. Depth, $l^* = 1$, $\mu_s'/\mu_a = 100$, $f_x = 0.1l^*$. DSHEF_3 is given in blue, DSHEF_5 is given in orange, DSHEF_7 is given in gold, DSHEF_{13} is given in purple, single SHEF_{13} is given in green.

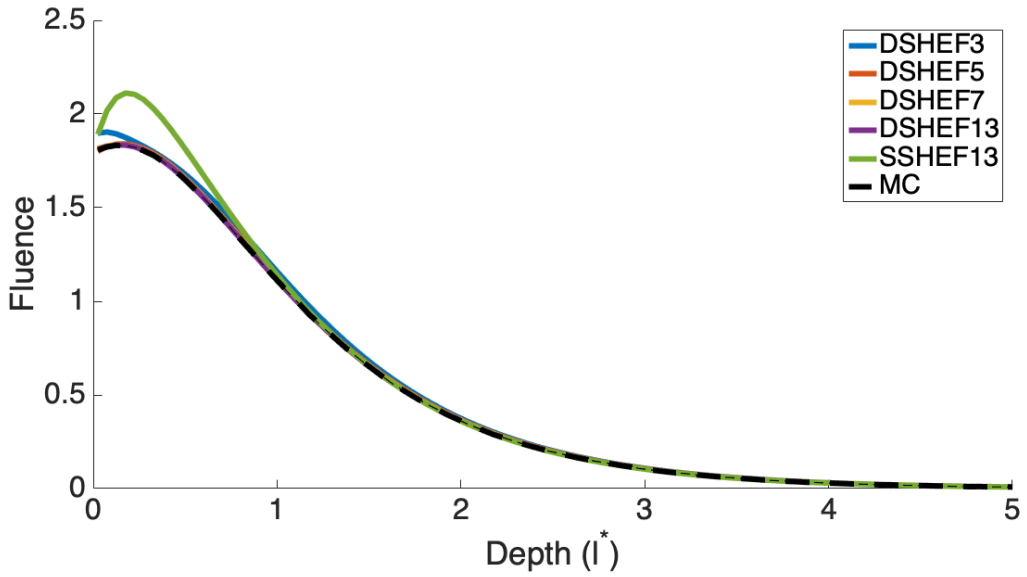

Figure 3.33: Fluence vs. Depth, $l^* = 1$, $\mu_s'/\mu_a = 100$, $f_x = 0.2/l^*$. DSHEF_3 is given in blue, DSHEF_5 is given in orange, DSHEF_7 is given in gold, DSHEF_{13} is given in purple, single SHEF_{13} is given in green and Monte Carlo is given in dashed black. Error bars for the MC results are $\pm 3\sigma$.

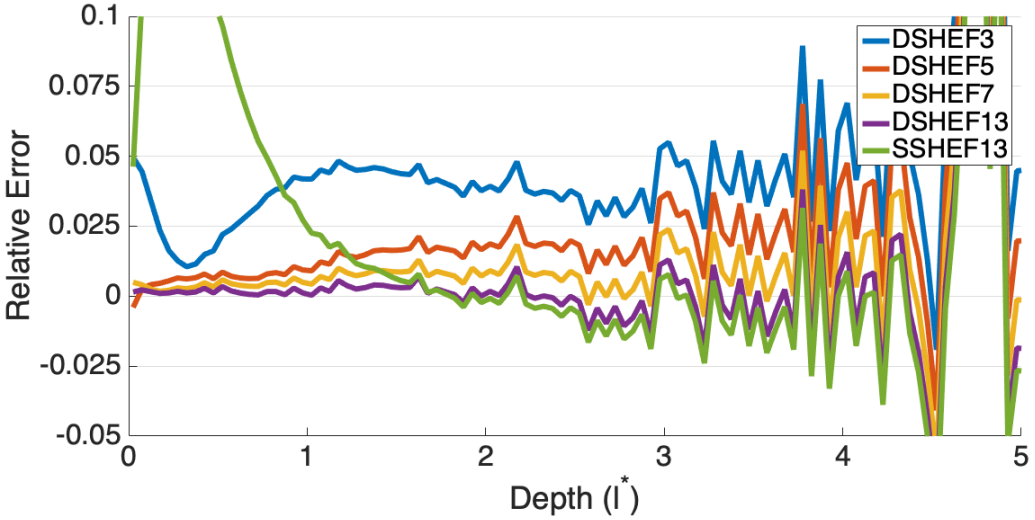

Figure 3.34: Relative Error of Fluence vs. Depth, $l^* = 1$, $\mu_s'/\mu_a = 100$, $f_x = 0.2l^*$. DSHEF_3 is given in blue, DSHEF_5 is given in orange, DSHEF_7 is given in gold, DSHEF_{13} is given in purple, single SHEF_{13} is given in green.

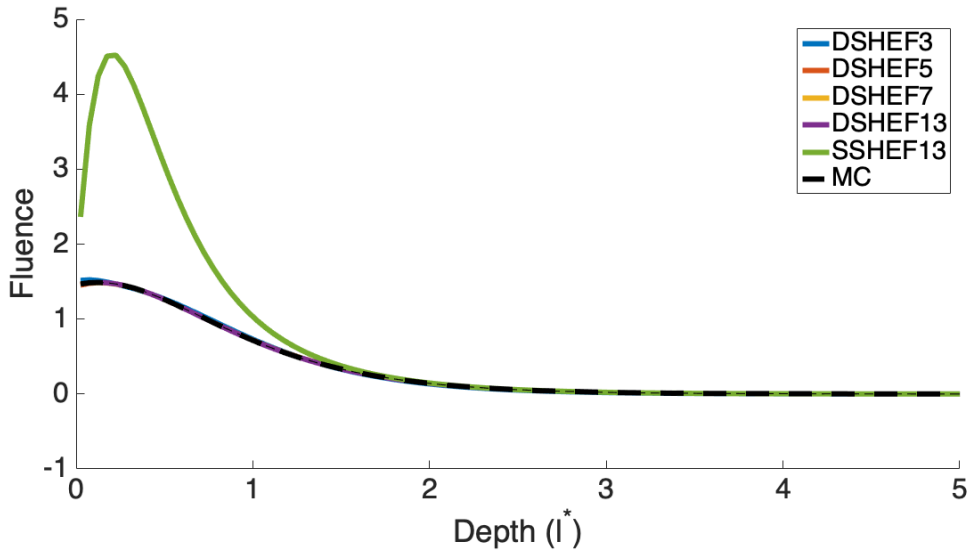

Figure 3.35: Fluence vs. Depth, $l^* = 1$, $\mu_s'/\mu_a = 100$, $f_x = 0.3/l^*$. DSHEF_3 is given in blue, DSHEF_5 is given in orange, DSHEF_7 is given in gold, DSHEF_{13} is given in purple, single SHEF_{13} is given in green and Monte Carlo is given in dashed black. Error bars for the MC results are $\pm 3\sigma$.

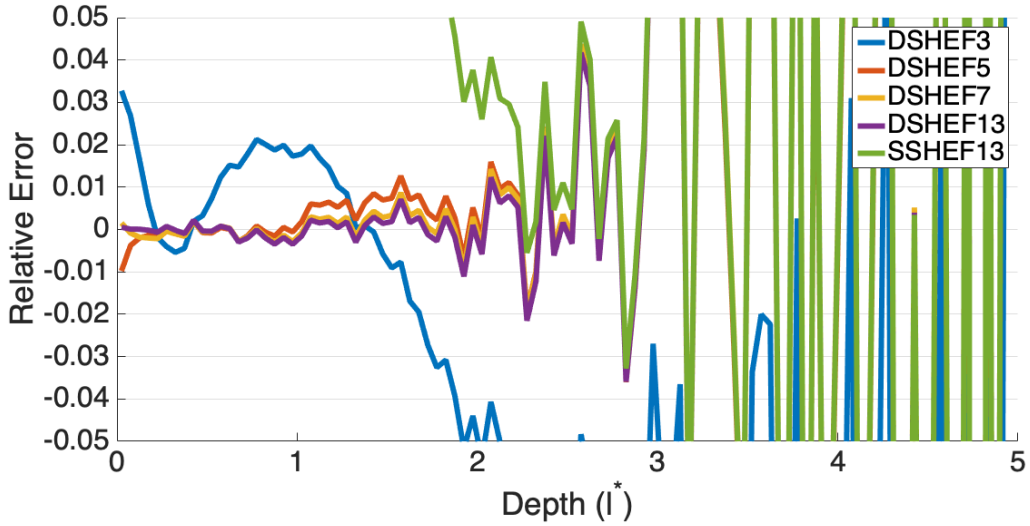

Figure 3.36: Relative Error of Fluence vs. Depth, $l^* = 1$, $\mu_s'/\mu_a = 100$, $f_x = 0.3l^*$. DSHEF_3 is given in blue, DSHEF_5 is given in orange, DSHEF_7 is given in gold, DSHEF_{13} is given in purple, single SHEF_{13} is given in green.

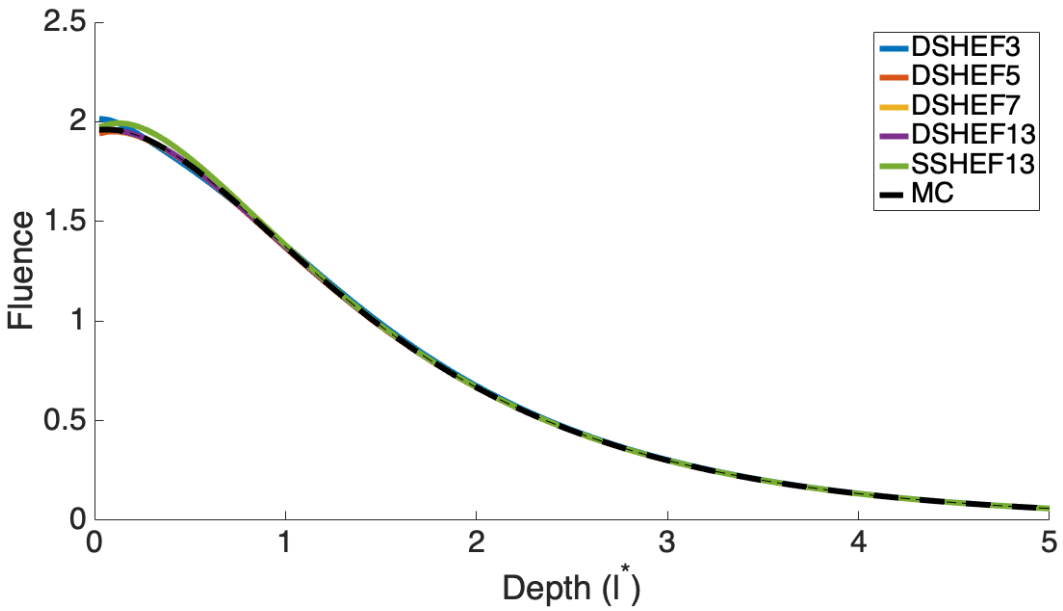

Figure 3.37: Fluence vs. Depth, $l^* = 1$, $\mu_s'/\mu_a = 3$, $f_x = 0$. DSHEF_3 is given in blue, DSHEF_5 is given in orange, DSHEF_7 is given in gold, DSHEF_{13} is given in purple, single SHEF_{13} is given in green and Monte Carlo is given in dashed black. Error bars for the MC results are $\pm 3\sigma$.

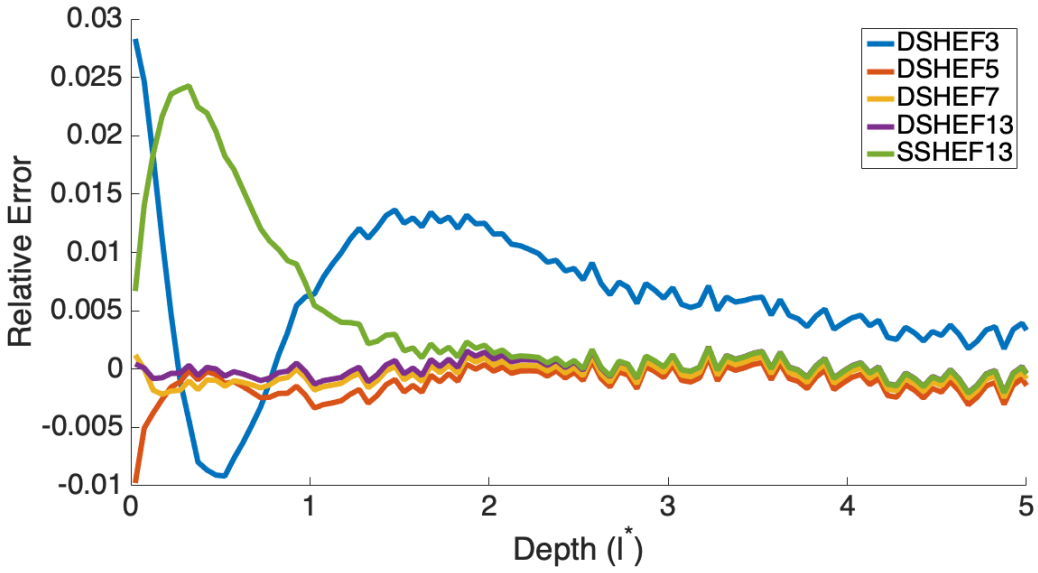

Figure 3.38: Relative Error of Fluence vs. Depth, $l^* = 1$, $\mu_s'/\mu_a = 3$, $f_x = 0$. DSHEF_3 is given in blue, DSHEF_5 is given in orange, DSHEF_7 is given in gold, DSHEF_{13} is given in purple, single SHEF_{13} is given in green.

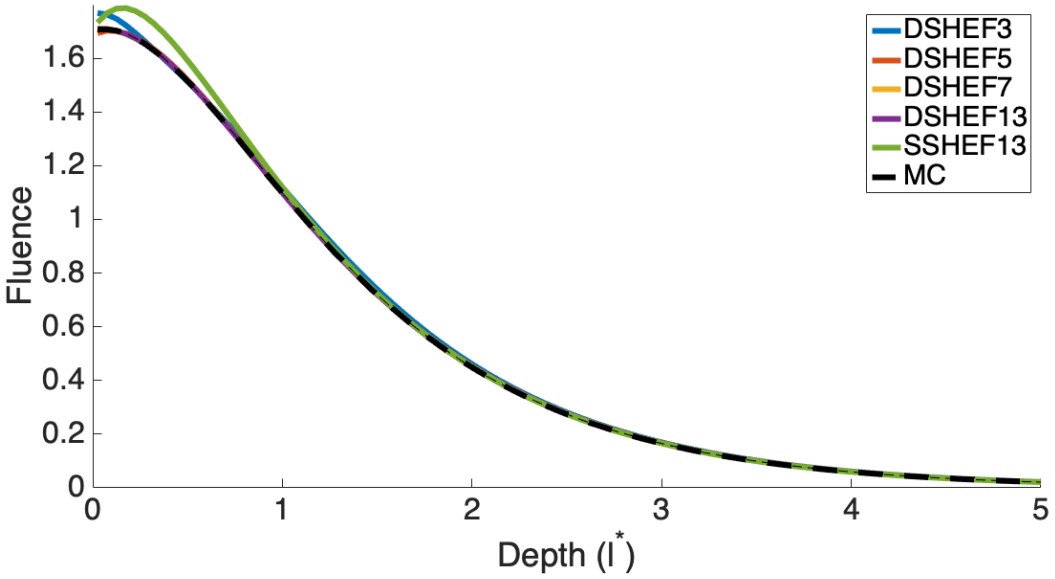

Figure 3.39: Fluence vs. Depth, $l^* = 1$, $\mu_s'/\mu_a = 3$, $f_x = 0.1/l^*$. DSHEF_3 is given in blue, DSHEF_5 is given in orange, DSHEF_7 is given in gold, DSHEF_{13} is given in purple, single SHEF_{13} is given in green and Monte Carlo is given in dashed black. Error bars for the MC results are $\pm 3\sigma$.

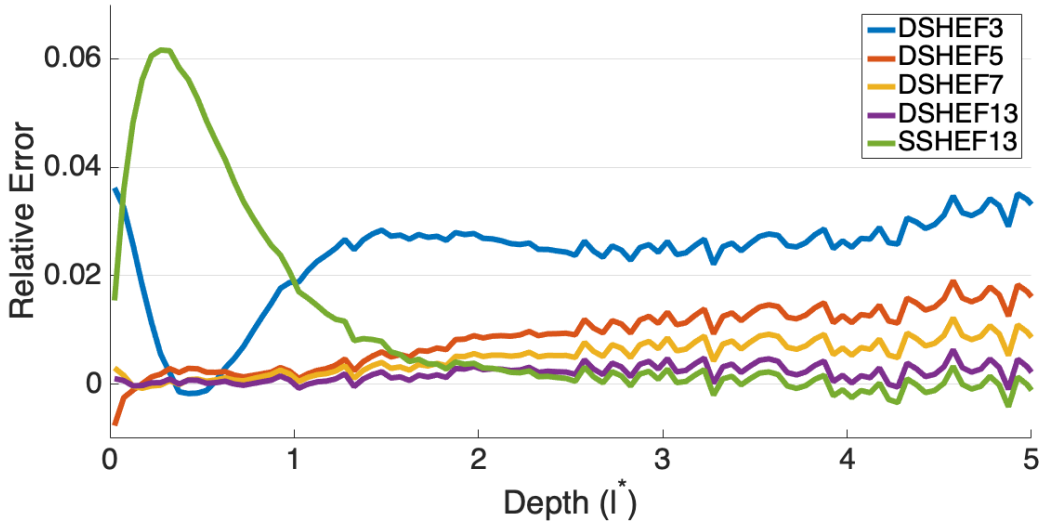

Figure 3.40: Relative Error of Fluence vs. Depth, $l^* = 1$, $\mu_s'/\mu_a = 3$, $f_x = 0.1/l^*$. DSHEF_3 is given in blue, DSHEF_5 is given in orange, DSHEF_7 is given in gold, DSHEF_{13} is given in purple, single SHEF_{13} is given in green.

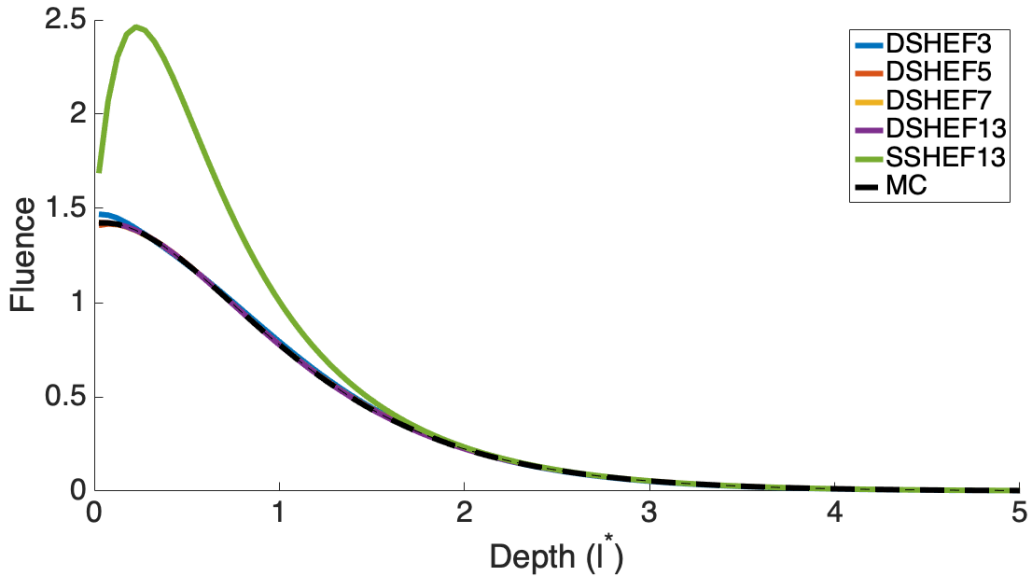

Figure 3.41: Fluence vs. Depth, $l^* = 1$, $\mu_s'/\mu_a = 3$, $f_x = 0.2/l^*$. DSHEF_3 is given in blue, DSHEF_5 is given in orange, DSHEF_7 is given in gold, DSHEF_{13} is given in purple, single SHEF_{13} is given in green and Monte Carlo is given in dashed black. Error bars for the MC results are $\pm 3\sigma$.

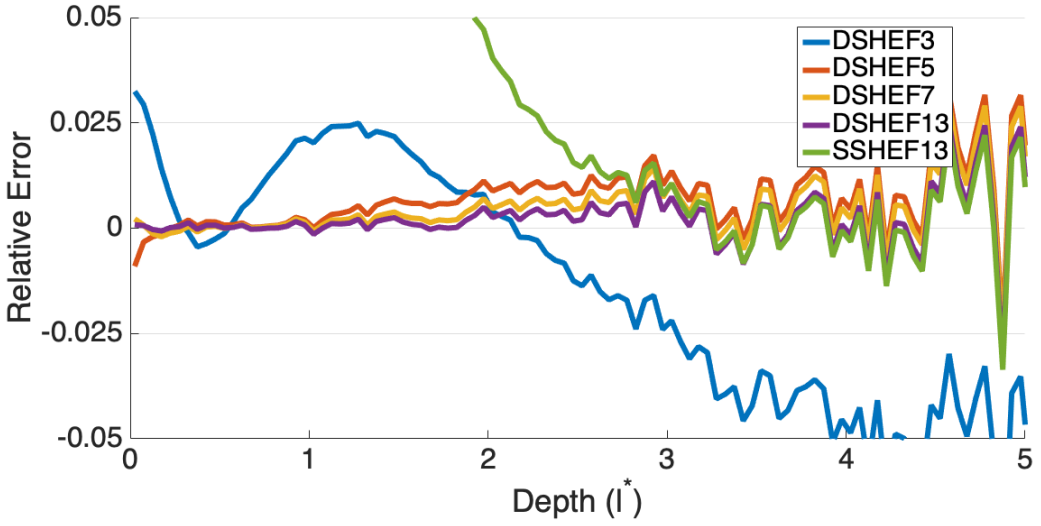

Figure 3.42: Relative Error of Fluence vs. Depth, $l^* = 1$, $\mu_s'/\mu_a = 3$, $f_x = 0.2/l^*$. DSHEF_3 is given in blue, DSHEF_5 is given in orange, DSHEF_7 is given in gold, DSHEF_{13} is given in purple, single SHEF_{13} is given in green.

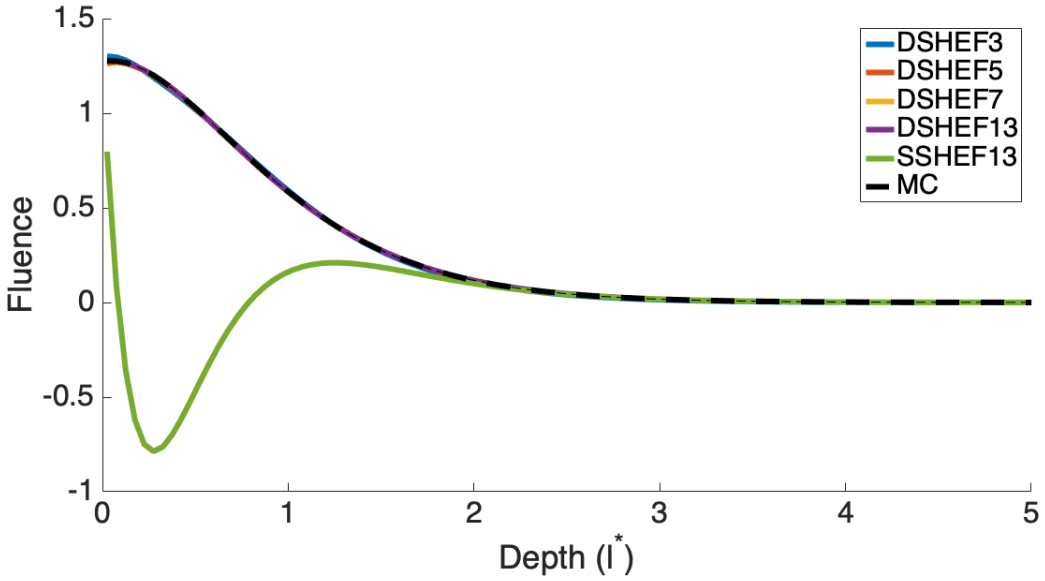

Figure 3.43: Fluence vs. Depth, $l^* = 1$, $\mu_s'/\mu_a = 3$, $f_x = 0.3/l^*$. DSHEF_3 is given in blue, DSHEF_5 is given in orange, DSHEF_7 is given in gold, DSHEF_{13} is given in purple, single SHEF_{13} is given in green and Monte Carlo is given in dashed black. Error bars for the MC results are $\pm 3\sigma$.

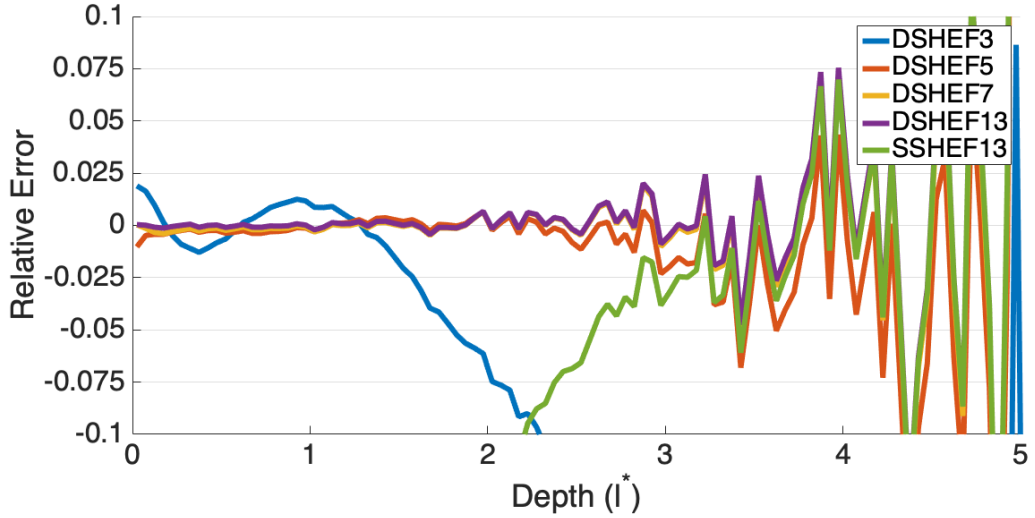

Figure 3.44: Relative Error of Fluence vs. Depth, $l^* = 1$, $\mu_s'/\mu_a = 3$, $f_x = 0.3/l^*$. DSHEF_3 is given in blue, DSHEF_5 is given in orange, DSHEF_7 is given in gold, DSHEF_{13} is given in purple, single SHEF_{13} is given in green.

a collimated source, $L_C(r,\Omega)$, is normalized to 1. Since at any fixed point r, $L_C(r,\Omega)$ is a delta distribution with respect to angle in the direction Ω_0, the fluence due to $L_C(r,\Omega)$ at any point is equal to the value of $L_C(r,\Omega_0)$.

$L_C(r,\Omega)$ decays exponentially with respect to z at a rate of $\mu_a+(1-f_\delta)\mu_s/\mu_0$. The DSHEF$_N$ simulations shown did not utilize the δ–Eddington approximation, so f_δ is considered to be 0 and feature a normally directed source, therefor $\mu_0 = 1$ and rate of decay is equal to μ_t. Since the media consdered here is homogeneous, μ_t is constant.

It can therefore be said that the fluence due to $L_C(r,\Omega)$ can be expressed entirely as a function of z, denoted here as $F_C(z) = k*\exp(-\mu_t(z)*z)$. Here, k is a normalizing constant, the since μ_t is a constant, basic calculus shows that $k = 1/\mu_t$. In all results shown, F_C is included in total fluence.

Figs 3.29–30 and 3.37–38 show fluence and relative error vs depth for highly scattering media ($\mu_s'/\mu_a = 100$) and less highly scattering media ($\mu_s'/\mu_a = 3$), respectively, with spatial frequency $f_x = 0$. As has been the case thus far, agreement between all deterministic methods shown and Monte Carlo is higher in simulations using more highly scattering media, as shown in Figs 3.37–38. However, in both cases, single SHEF$_{13}$ experiences a small spike in error between $z = 0.1l^*$ and $z = 0.3l^*$ before converging to very small error rates, within ± 0.001 just after $z = 1l^*$ in the more highly scattering case. In the less highly scattering case, this peak is at approximately $z = 0.3l^*$, where it reaches an over estimation of 0.024, and convergence to such low errors is not seen until $z \geq 2l^*$. DSHEF$_{13}$ shows error rates within this range for all z in both cases, with DSHEF$_7$ behaving similarly except for an extremely small underestimation. DSHEF$_5$ experiences a slightly more extreme underestimation, but stays within ± 0.002, except for underestimations as low as -0.01 a. In both cases, however, DSHEF$_3$ exhibits an overestimation for high values of z, rather than converging to a low error as in all other examples. Its relative error levels off at roughly 0.005 in both cases. This is coupled with an initial overestimation of 0.28 at $z = 0$, followed by an underestimation of

-0.095 at $z = 0.5l^*$ for the less highly scattering case and an overestimation of 0.018 at $z = 0$ and a small underestimation of -0.002 at $z = 0.35l^*$ in the more highly scattering case.

Figs 3.31–32 and 3.39–40 show fluence and relative error vs depth for highly scattering media ($\mu_s'/\mu_a = 100$) and less highly scattering media ($\mu_s'/\mu_a = 3$), respectively, with spatial frequency $f_x = 0.1/l^*$. Here, single SHEF_{13} begins to experience error for $z \leq 1l^*$ in the more highly scattering case and for $z \leq 2l^*$ in the less highly scattering case. That error is smaller in the more highly scattering case, achieving a maximum overestimation of approximately 0.025 at $z = 0.2l^*$. In the less highly scattering case, this error is more extreme, reaching just over 0.06 at approximately $z = 0.3l^*$. Meanwhile, DSHEF_3 sees overestimation near $z = 0$ for both cases. When the medium is more less scattering, this overestimation is by approximately 0.038. In the more highly scattering medium, this overestimation is by approximately 0.018. In both cases, DSHEF_3 expereinces a small underestimation error near $z = 0.4l^*$, before going back to overestimation. DSHEF_3 converges to relative error rates of roughly 0.005 in the more highly scattering medium, but in the less highly scattering medium, it sees error rates continue to rise as z increases. It has this in common with the higher expansion orders of DSHEF_N shown. These rising errors are due to small, roughly constant offsets which drop away as N increases. Due to the nature of DSHEF_N's solution as a linear combination of decaying terms, this will eventually converge to zero, but will require $N \geq 13$ if relative error within ± 0.005 is desired for high values of z. However, for $0 \leq z \leq 1l^*$, DSHEF_N for $N \geq 5$ shows relative error rates mostly within ± 0.005 in each case.

Figs 3.33–34 and 3.41–42 show fluence and relative error vs depth for highly scattering media ($\mu_s'/\mu_a = 100$) and less highly scattering media ($\mu_s'/\mu_a = 3$), respectively, with spatial frequency $f_x = 0.2/l^*$. Here, single SHEF_N begins to show extreme overestimation for $z/leq1l^*$ in the more highly scattering tissue and for $z \leq 2l^*$ in the less highly scattering tissue. However, in each case, as z increases, single SHEF_N does show convergence to the

Monte Carlo solution. DSHEF_3 displays similar behavior to when $f_x = 0.1/l^*$; in the more highly scattering case, it shows convergence to relative errors of approximately 0.04, while in the less highly scattering case it shows a divergence to more extreme underestimation. DSHEF_N for $N \geq 5$, however, shows small error rates, generally within ± 0.01, in the less highly scattering media. It converges to Monte Carlo as N increase in more highly scattering media, showing approximately constant error rates of 0.015 for DSHEF_5, 0.0075 for DSHEF_7 and staying within ± 0.005 for DSHEF_{13}. The fact that DSHEF_N performs better in less highly scattering media in this case is interesting; these spectral methods for solving the Radiative Transport Equation generally perform better as scattering coefficients increase, since this reduces the length scale over which discrete scattering events may be modeled as a continuous process.

Figs 3.35–36 and 3.43–44 show fluence and relative error vs depth for highly scattering media ($\mu_s'/\mu_a = 100$) and less highly scattering media ($\mu_s'/\mu_a = 100$), respectively, with spatial frequency $f_x = 0$. In these cases, single SHEF_N now shows even more extreme overestimation for $Z \leq 2l^*$. Likewise, DSHEF_3 has error rates which briefly oscillate when $0 \leq z$ $1.5l^*$, then converge to extreme underestimation. Converesely, in both highly and less highly scattering media, DSHEF_5, DSHEF_7 and DSHEF_{13} show relative errors within ± 0.01 for $z \leq 2l^*$. For larger values of z, more Monte Carlo simulations with higher photon packet counts will need to be run; after this point, high variance in the Monte Carlo results make comparisons useless.

3.4.5 Ratio of Fluence in Negative z Direction:Total Fluence

An interesting side note to consider is the ratio of fluence in the negative z direction (that is, the integral at some point r of all radiance directed towards the medium boundary) to total fluence. The Standard Diffusion Approximation[68], which is commonly accepted to

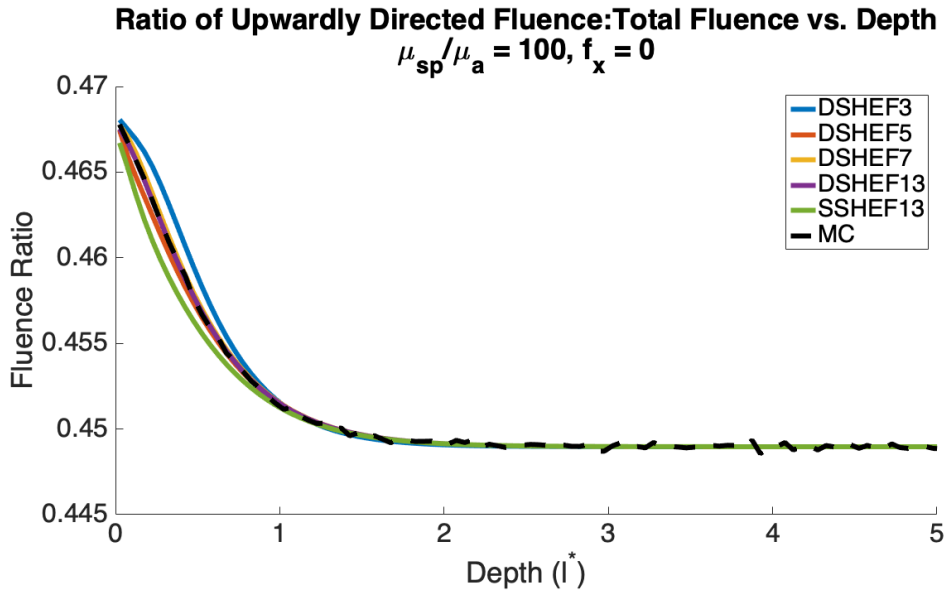

Figure 3.45: Ratio of Fluence directed in negative z direction:Total Fluence vs. Depth, $l^* = 1$, $\mu_s'/\mu_a = 100$, $f_x = 0$. DSHEF_3 is given in blue, DSHEF_5 is given in orange, DSHEF_7 is given in gold, DSHEF_{13} is given in purple, single SHEF_{13} is given in green and Monte Carlo is given in dashed black.

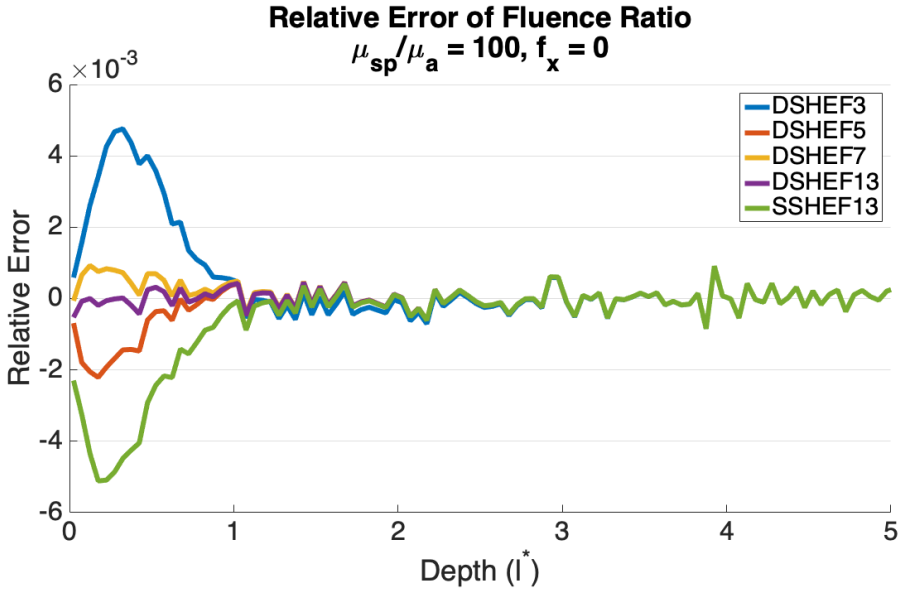

Figure 3.46: Relative Error of Ratio of Fluence directed in negative z direction:Total Fluence vs. Depth, $l^* = 1$, $\mu_s'/\mu_a = 100$, $f_x = 0$. DSHEF_3 is given in blue, DSHEF_5 is given in orange, DSHEF_7 is given in gold, DSHEF_{13} is given in purple, single SHEF_{13} is given in green.

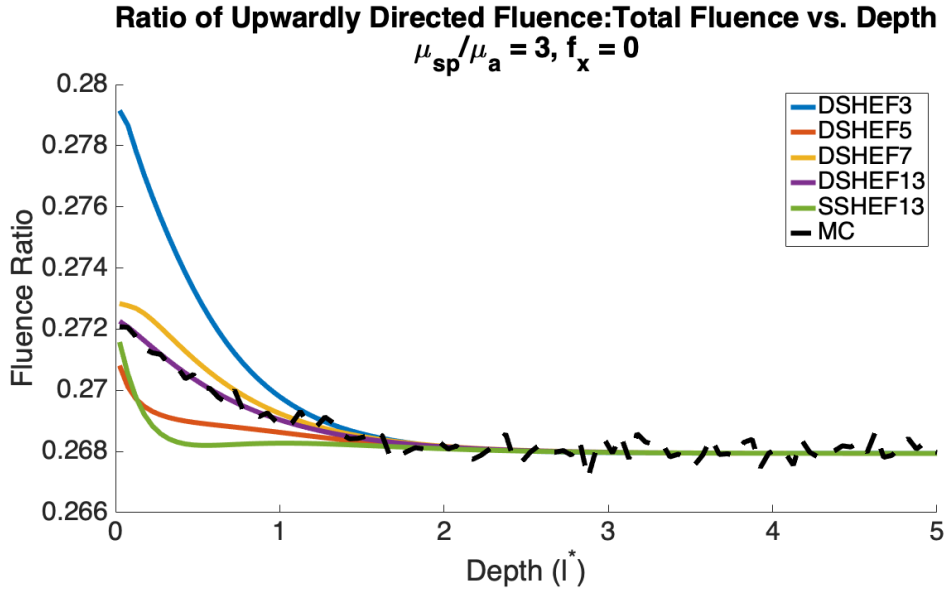

Figure 3.47: Ratio of Fluence directed in negative z direction:Total Fluence vs. Depth, $l^* = 1$, $\mu_s'/\mu_a = 3$, $f_x = 0$. DSHEF_3 is given in blue, DSHEF_5 is given in orange, DSHEF_7 is given in gold, DSHEF_{13} is given in purple, single SHEF_{13} is given in green and Monte Carlo is given in dashed black.

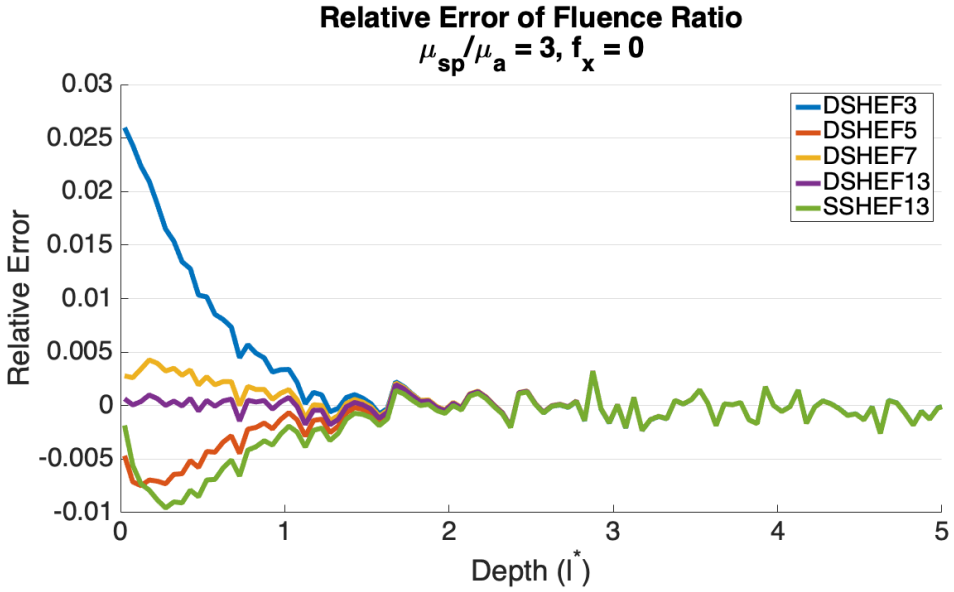

Figure 3.48: Relative Error of Ratio of Fluence directed in negative z direction:Total Fluence vs. Depth, $l^* = 1$, $\mu_s'/\mu_a = 3$, $f_x = 0$. DSHEF_3 is given in blue, DSHEF_5 is given in orange, DSHEF_7 is given in gold, DSHEF_{13} is given in purple, single SHEF_{13} is given in green.

be accurate in highly scattering media over length scales ¿¿ l^*, provides approximations for diffuse fluence and reflectance. Since this method solves for diffuse reflectance, it treats radiance at any point as constant with respect to angle. Therefore, the ratio of fluence in any one direction to total fluence, according to this approximation, would be 1:2. The fact that this is an accepted standard would lead one to determine that radiance should behave in this manner.

However, it is clear from Figs 3.45–46 that this is not the case even in highly scattering (μ_s'/μ_a=100) media. The ratio for this simulation converges to approximately 0.449. This convergence occurs when only one (or in the case of eigenvalue degeneracy, several) eigenvector corresponding to the slowest rate of decay is making a significant contribution to radiance. Even low order approximations of DSHEF$_N$ are able to reconstruct this behavior, which is verified by Monte Carlo simulation.

Figs 3.47–48 displays the same phenomenon for less highly scattering ($\mu_s'/\mu_a = 3$) media. Here the ratio converges to approximately 0.268. This shows a clear link between optical properties and the behavior of radiance deep (several times l^*) within a medium.

Furthermore, it shows that both single SHEF$_N$ and DSHEF$_N$ are capable of predicting radiance distributions deep within tissue simply by examining eigenpairs from the generalized eigenvalue problem stated between Equations (2.36) and (2.37). This is interesting on its own and provides a strong motivation for an investigation into the spectral properties of both the single SHEF$_N$ and DSHEF$_N$ methods to better understand this link and to see what other understandings may be gained about the link between optical properties of a given medium and the behavior of radiance within that medium.

Perhaps most importantly, these results, combined with verification by Monte Carlo, show that the commonly held idea of the Standard Diffusion Approximation's accuracy over large length scales requires further scrutiny.

3.5 Conclusion

In this chapter, I have detailed the creation and use of a MATLab implementation of DSHEF$_N$, as well as provided results to verify both this implementation and the theory behind it. This was done through thorough examination of radiance and commonly used functionals of radiance in homogeneous media with highly scattering ($\mu_s'/\mu_a = 100$) and less highly scattering ($\mu_s'/\mu_a = 3$) media.

I have shown that as order increases, DSHEF$_N$ experiences decreasing relative error rates in both highly scattering and less highly scattering media, even as spatial frequency increases. The current best practice, SHEF$_N$, is highly accurate when $f_x = 0$, but experiences difficulty in reconstructing radiance and fluence as spatial frequency increases. It should be noted that while relative error rates for DSHEF$_N$ increase with f_x, absolute error rates remain much more stable. The increase in relative error is largely due to the fact that radiance, and therefore positive definite functionals based upon it, decrease as f_x increases. DSHEF$_N$ has also shown more robustness in terms of optical properties; when comparing error rates in each simulation shown between highly ($\mu_s'/\mu_a = 100$) and less highly ($\mu_s'/\mu_a = 3$) scattering media, DSHEF$_N$ experienced smaller changes in error than single SHEF$_{13}$, regardless of N.

These results do not mean that SHEF$_N$ should be ignored; the matrices which is uses are of order $(N+1)^2 * (N+1)^2$, whereas those used in DSHEF$_N$ are of order $2(N+1)^2 * 2(N+1)^2$. Therefore, situations in which single SHEF$_N$ is shown to be robust may call for this method. Those situations, and the exact orders of expansion necessary for each method to show given levels of accuracy, are a valuable future direction for this research.

Finally, I have shown a flaw in the Standard Diffusion Approximation that is both exposed and remedied by single SHEF$_N$ and DSHEF$_N$. Even in deep ($z >> l^*$) within highly scattering media, radiance does not equilibrate to a uniform angular distribution at any point. There are strong links between the structure of the generalized eigenvalue problems

presented by both single SHEF_N and DSHEF_N and the behavior of radiance at all depths in a medium. This strongly motivates an investgation into the spectral properties of these problems.

Chapter 4

Double SHEF$_N$ For Layered Media

4.1 Introduction

In this chapter, I lay out the theory and provide example results for the implementation of DSHEF$_N$ in the case of media consisting of multiple homogeneous layers of the same refracive index, all with boundaries parallel to the $z = 0$ plane. This similarity of refractive index is considered both because of biological relevance [31] and to simplify the boundary condition at the layer interface. A similar implementation for layers with mismatched refractive indices would simply require that Fresnel's law be applied as in the boundary condition at the surface stipulated in equation (2.38). This takes the form of a system of coupled equations, one for each layer, with the stipulation that radiance directed in the positive z direction in each layer is equal at all angles. The same condition applied for radiance directed in the negative z direction. These equalities come together in the form of a new boundary condition, to be applied concurrently with the condition at the tissue surface.

4.2 Layered Media

For the solutions detailed in this chapter, I will assume a tissue similar to that which is used in Chapter 2. The medium will be semi-inifinte in the positive z direction, with a boundary at the $z = 0$ plane. The medium will be further broken down into K layers, each with boundaries parallel to the $z = 0$ plane. These layers will be denoted M_1, M_2, ..., M_K. Within each layer, optical properties will be homogeneous, and each will be assumed to have the same refractive index. A collimated source external to the medium will be used, and will decay exponentially through each layer according to the local optical properties. The simulation results presented here will be from the $K = 2$ case, but this method may be implemented using higher integer values of K may be in the same manner.

4.3 Coupled Equations

Within this framework of a layered medium, I will consider a system of Radiative Transport Equations, each with a solution describing scattered radiance in a single layer:

$$\begin{aligned}
\nabla \cdot \Omega L_{S,1}(r,\Omega) &= -\mu_{t,1} L_{S,1}(r,\Omega) + \mu_{s,1} \textstyle\int_{4\pi} L_{S,1}(r,\Omega')\, p(\Omega' \cdot \Omega) d\Omega' + Q_1(r,\Omega) \\
\nabla \cdot \Omega L_{S,2}(r,\Omega) &= -\mu_{t,2} L_{S,2}(r,\Omega) + \mu_{s,2} \textstyle\int_{4\pi} L_{S,2}(r,\Omega')\, p(\Omega' \cdot \Omega) d\Omega' + Q_2(r,\Omega) \\
&\cdots \\
\nabla \cdot \Omega L_{S,K}(r,\Omega) &= -\mu_{t,K} L_{S,K}(r,\Omega) + \mu_{s,K} \textstyle\int_{4\pi} L_{S,K}(r,\Omega')\, p(\Omega' \cdot \Omega) d\Omega' + Q_K(r,\Omega)
\end{aligned} \tag{4.1}$$

The definitions here are as one might expect: $\mu_{t,i}$, $\mu_{s,i}$, Q_i and $L_{S,i}$ are the total attentuaion coefficient, the scattering coefficient, the contribution of the source to scattered radiance, and the total scattered radiance in layer i at any location r. Total radiance at any location r is still the sum of scattered and collimated radiance, denoted in layer i as follows:

$$L_i(r,\Omega) = L_{S,i}(r,\Omega) + L_{C,i}(r,\Omega) \tag{4.2}$$

The actual coupling between the equations of (4.1) is dealt with by making sure that radiance is continuous at layer boundaries. I will denote the depth of the layer between M_i and M_{i+1} as z_i^*. Assuming that the layers have identical refractive indices, the Marshak condition is reduced to:

$$L_i(r,\Omega)_{z=z_i^*} = L_{i+1}(r,\Omega)_{z=z_i^*} \quad (4.3)$$

Here, it must be noted that $L_{C,i}$ decays exponentially at a rate given by the total attenuation coefficient for M_i, or $\mu_{t,i}$. Since it is a collimated term, $L_{C,i}$ is a Dirac delta distribution in angle with respect to the direction of the source, Ω_0, with the following structure:

$$\begin{aligned} L_{C,1}(z,\Omega) &= \exp(-z\mu_{t,1})\delta_{\Omega_0}(\Omega) \\ L_{C,2}(z,\Omega) &= \exp(-z_1^*\mu_{t,1} - (z-z_1^*)\mu_{t,2}))\delta_{\Omega_0}(\Omega) \\ &\ldots \\ L_{C,i}(z,\Omega) &= \exp(-z_1^*\mu_{t,1} - (z_2^*-z_1^*)\mu_{t,2} - \ldots - (z-z_{i-1}^*)\mu_{t,i})\delta_{\Omega_0}(\Omega) \end{aligned} \quad (4.4)$$

It should be noted by (4.4) that at $z = z_i^*$, $L_{C,i-1} = L_{C,i}$. This, combined with the boundary condition expressed in (4.3) that radiance in any fixed direction Ω is continuous over z implies that at the $z = z_i^*$ boundary, the following equality holds:

$$L_{S,i}(r,\Omega)_{z=z_i^*} = L_{S,i+1}(r,\Omega)_{z=z_i^*} \quad (4.5)$$

Now recall that DSHEF_N relies on the decomposition of $L_{S,i}$ into double spherical harmonic functions, detailed in (2.6-7), and that these moments of these functions have a vector representation $\tilde{\Psi}$, detailed in (2.27). In layer i, this will be denoted $\tilde{\Psi}_i$ and further decomposed into homogeneous $\tilde{\Psi}_i^{(h)}$ and particular $\tilde{\Psi}_i^{(p)}$ components, as in Chapter 2. Each can be further split into components facing in the positive z direction, denoted with a $+$ superscript, and components facing the negative z direction, denoted with a $-$ superscript. Bearing this in mind, (4.5) leads to the following:

$$\tilde{\Psi}_i^{\pm}(z = z_i^*) = \tilde{\Psi}_{i+1}^{\pm}(z = z_i^*) \quad (4.6)$$

$$\tilde{\Psi}_i^{(p),\pm}(z = z_i^*) + \tilde{\Psi}_i^{(h),\pm}(z = z_i^*) = \tilde{\Psi}_{i+1}^{(p),\pm}(z = z_i^*) + \tilde{\Psi}_{i+1}^{(h),\pm}(z = z_i^*) \quad (4.7)$$

Any statement of either homogeneous or particular solution without a $+$ or $-$ should be taken to mean the total solution consisting of radiance in both hemispheres.

4.4 A 2 Layered Boundary Condition

To actually solve the system described in (4.1) in parallel, (4.7) must be adapted to a boundary condition to be used at the same time as the Marshak Condition at the medium's surface. I will first demonstrate how this is done in the two layered case and layer demonstrate the extension to the K layered case.

To understand this formulation, it is wise to first recall the final matrix inversion problem performed in the single layer case of DSHEF$_{\mathrm{N}}$, given in (2.39). The vector w in that statment was composed of moments of various eigenvectors (G_i) used in the construction of the homogeneous solution $\tilde{\Psi}^{(h)}$. Only vectors corresponding to positive eigenvalues were used because of the necessity of $\tilde{\Psi}$ to approach 0 as z approaches infinity. However, in this new medium, only the bottom layer, M_2, extends infinitely. Therefore, $\tilde{\Psi}_1^{(h)}$ (and layers 2 through $K-1$ in the K layered case) must consider eigenvectors corresponding to both positive and negative eigenvalues. I will denote the vectors of moments corresponding to positive or negative eigenpairs in M_i as $w_i^{\pm}$. In the two layer case, this means that DSHEF$_N$ must calculate w_1^+, w_1^- and w_2^+. I will also denote the eigenvector column matrix corresponding to M_i as G^i, with submatrices for vectors corresponding to positive and negative eigenvalues as $G^{i,+}$ and $G^{i,-}$, respectively. Finally, the positive and negative eigenvalues for layer i will be denoted as $\lambda^{i,\pm}$. Recall that the homogeneous solution in single layered DSHEF$_N$ is given by:

$$\tilde{\Psi}^{(h)} = Gw \exp(-\tfrac{z}{\lambda^+}) \quad (4.8)$$

For the two layered case, both the expanded eigenspace utilized in the solution as well as the depth of the layer boundary must be considered. I will calculate w_1^+ as before, with weights corresponding to the homogeneous solution at $z = 0$. However, the new vectors to be found, w_1^- and w_2^+, will be considered at $z = z_1^*$. This is done for ease of formulation and calculation; any arbitrary depth between 0 and z_1^* could be used for $w_1^\pm$ and any arbritrary depth greater than z_2^* could be used for w_2^-. Taken together, these create the following definitions of homogeneous solutions in each layer:

$$\tilde{\Psi}_1^{(h)} = G^{1,+} w_1^+ \exp\left(\tfrac{z}{\lambda^+}\right) + G^{1,-} w_1^- \exp\left(\tfrac{(z-z^*)}{\lambda^-}\right) \quad (4.9)$$

$$\tilde{\Psi}_2^{(h)} = G^{2,+} w_2^+ \exp\left(\tfrac{(z-z^*)}{\lambda^+}\right) \quad (4.10)$$

Note that (4.9) applies for $0 \leq z \leq z^*$ and (4.1) applies for $z^* < z \leq \infty$.

The last components to be examined are the particular solutions $\tilde{\Psi}_1^{(p)}$ and $\tilde{\Psi}_2^{(p)}$. This is given very similarly to the particular solution of the single layered case given in (2.34), but must take into account the z location at which each layer begins:

$$\tilde{\Psi}_1^{(p)} = \left(-\tfrac{\mu_{t,1}}{\mu_0} A_1 + B_1\right)^{-1} \tilde{Q}(0) \quad (4.11)$$

$$\tilde{\Psi}_2^{(p)} = \left(-\tfrac{\mu_{t,2}}{\mu_0} A_2 + B_2\right)^{-1} \tilde{Q}(z^*) \quad (4.12)$$

To create a boundary condition for the layer interface, (4.9), (4.10) and (4.11) must be substituted into (4.7), creating the following:

$$\left(-\tfrac{\mu_{t,1}}{\mu_0} A_1 + B_1\right)^{-1} \tilde{Q}(0) + \tilde{\Psi}_1^{(h)} + G^{1,+} w_1^+ \exp\left(\tfrac{z}{\lambda^+}\right) + G^{1,-} w_1^- \exp\left(\tfrac{(z-z^*)}{\lambda^-}\right)$$

$$= \left(-\tfrac{\mu_{t,2}}{\mu_0} A_2 + B_2\right)^{-1} \tilde{Q}(z^*) + G^{2,+} w_2^+ \exp\left(\tfrac{(z-z^*)}{\lambda^+}\right) \quad (4.13)$$

This can be rearranged into the following, with the difference of the particular solutions denoted $\Delta_{1,2} = \tilde{\Psi}_1^{(p)} - \tilde{\Psi}_2^{(p)}$:

$$G^{2,+}w_2^+ - G^{1,+}w_1^+ \exp\left(\tfrac{z^*}{\lambda^+}\right) - G^{1,-}w_1^- \exp = \Delta_{1,2} \quad (4.14)$$

Next, I will restate the Marshak Boundary Condition at $z = 0$ expressed in (2.38) and (2.39) to take w_1^- into account. Recall that this represents scattered radiance at the topmost layer boundary and states that any scattered radiance at this depth ($z = 0$) was originally upwardly directed radiance which was internally reflected downwards due to refractive index mismatch. The amount of radiance internally reflected at a given angle is given by Fresnel's Law. It is represented here using an argument of $\mu = \cos(\theta)$, and it should be noted that this function returns 1 for all $\mu < \mu_c$, the critical angle past which there is total internal reflection:

$$\gamma_F(\mu) = \frac{\left|n\left(\sqrt{1-n^2(1-\mu^2)}-\mu\right)\right|}{2\left|n\left(\sqrt{1-n^2(1-\mu^2)}+\mu\right)\right|} + \frac{\left|n\mu-\sqrt{1-n^2(1-\mu^2)}\right|}{2\left|n\mu+\sqrt{1-n^2(1-\mu^2)}\right|} \quad (4.15)$$

This function is applied to the Marshak boundary condition stated in (2.38), which simplifies the expression of the condition to the following matrix equations:

$$\begin{bmatrix} I & -R \end{bmatrix} \tilde{\Psi}_1^{(h)}(0) = \begin{bmatrix} -I & R \end{bmatrix} \tilde{\Psi}_1^{(p)}(0) \quad (4.16)$$

$$\begin{bmatrix} I & -R \end{bmatrix} \left(G^{1,+}w_1^+ + G^{1,-}w_1^- \exp\left(\tfrac{z^*}{\lambda_1^-}\right)\right) = \begin{bmatrix} -I & R \end{bmatrix} \tilde{\Psi}_1^{(p)}(0) \quad (4.17)$$

Equations (4.14) and (4.17) are then considered to be a system defining the new, total boundary condition for the system and then expressed as a single matrix:

$$\begin{bmatrix} I & -R \end{bmatrix} \left(G^{1,+}w_1^+ + G^{1,-}w_1^- \exp\left(\tfrac{z^*}{\lambda_1^-}\right)\right) = \begin{bmatrix} -I & R \end{bmatrix} \tilde{\Psi}_1^{(p)}(0) \quad (4.18)$$
$$G^{2,+}w_2^+ - G^{1,+}w_1^+ \exp\left(\tfrac{z^*}{\lambda_1^+}\right) - G^{1,-}w_1^- \exp = \Delta_{1,2}$$

$$\begin{bmatrix} \begin{bmatrix} I & -R \end{bmatrix} G^{1,+} & \begin{bmatrix} I & -R \end{bmatrix} G^{1,-} \exp\left(\frac{z^*}{\lambda_1^-}\right) & 0 \\ -G^{1,+} \exp\left(\frac{z^*}{\lambda_1^+}\right) & -G^{1,-} & G^{2,+} \end{bmatrix} \begin{bmatrix} w_1^+ \\ w_1^- \\ w_2^+ \end{bmatrix} = \begin{bmatrix} \begin{bmatrix} -I & R \end{bmatrix} \tilde{\Psi}_1^{(p)}(0) \\ \Delta_{1,2} \end{bmatrix} \tag{4.19}$$

While it may not appear to be at first glance, the matrix on the left hand side of (4.19) is square so long as the matrices A_i and B_i are full rank for each layer. This is always the case for A_i and expected to be the case for B_i, as explained in Chapter 2. The lack of a null space to the associated generalized eigensystems for each layer implies that the column matrix of all eigenvectors, which can be expressed as $\begin{bmatrix} G_i^+ & G_i^- \end{bmatrix}$, is square. This, combined with the fact that $\begin{bmatrix} I & -R \end{bmatrix} G^{1,+}$ and $\begin{bmatrix} I & -R \end{bmatrix} G^{1,-} \exp\left(\frac{z^*}{\lambda^-}\right)$ are also square matrices with sides half those of $\begin{bmatrix} G_i^+ & G_i^- \end{bmatrix}$, creates a square matrix which is nonsingular due to the linear independence of the eigenvectors. Therefore, this system can be solved using simple matrix inversion.

Finally, it is important to note that the while the block matrix on the left side of (4.19) has one row for each layer of the medium, the coupling of the two systems means that neither row alone contains the information necessary to determine either, the weights of the eigenvectors used in the homogeneous solutions for the first and second layers, respectively.

4.5 A K Layered Boundary Condition

I will now generalize the boundary condition stated in (4.19) to consider a system with K layers. As mentioned in (4.1), this will require a coupling of K different DSHEF$_N$ systems. Similar nomenclature will be used in this case: $w_i^{\pm}$ will indicate weight vectors for the homogeneous solutions of each system and $\Delta_{i,i+1}$ will indicate the difference between the

particular solutions of layers i and $i+1$ at the interface z_i^*. As in the two layered case, the weight vectors w_i^- and w_{i+1}^+ will both be defined at $z = z_i^*$ (z_0^* may trivially be considered to be 0 in this case.)

There are three fundamental cases to consider for the equations which will ultimately define the boundary condition. The boundary condition at $z = 0$ outlined in (4.16) requires only minor restatement, replacing z^* with z_1^*:

$$\left[\begin{array}{cc} I & -R \end{array} \right] \left(G^{1,+} w_1^+ + G^{1,-} w_1^- \exp\left(\frac{z_1^*}{\lambda^-}\right)\right) = \left[\begin{array}{cc} -I & R \end{array} \right] \tilde{\Psi}_1^{(p)}(0) \quad (4.20)$$

Likewise, the equation defining radiance at the final layer boundary, z_{K-1}^*, requires only index changes from its statement in (4.16):

$$G^{K,+} w_K^+ - G^{K-1,+} w_{K-1}^+ \exp\left(\frac{\left(z_{K-1}^* - z_{K-2}^*\right)}{\lambda_{K-1}^+}\right) - G^{K-1,-} w_{K-1}^- = \Delta_{K-1,K} \quad (4.21)$$

That leaves only the general case of the equations defining radiance at intermediary boundaries z_1^* through z_{K-2}^*. Unlike in the two layered case, eigenvectors corresponding to both positive and negative eigenvalues for each layer in such a case must be considered for all the intermediate layers. As in (4.21), these layers are specific cases of (4.7), with values filled in for specific layers as in (4.14). The statement will be for the boundary between layers i and $i+1$ with i between 1 and $K-1$.

$$\begin{array}{c} \mathrm{G}^{i+1,+} w_{i+1}^+ + G^{i+1,-} w_{i+1}^- \exp\left(\frac{\left(z_{i+1}^* - z_i^*\right)}{\lambda_i^+}\right) \\ -G^{i,+} w_i^+ \exp\left(\frac{\left(z_i^* - z_{i-1}^*\right)}{\lambda_i^+}\right) - G^{i,-} w_i^- \exp = \Delta_{i,i+1} \end{array} \quad (4.22)$$

Now that the equations for each layer have been stated in (4.20) through (4.22), they can be put into a system of equations, a la (4.18):

$$
\begin{aligned}
\left[\begin{array}{cc} I & -R \end{array}\right]\left(G^{1,+}w_1^+ + G^{1,-}w_1^- \exp\left(\frac{z_1^*}{\lambda_1^-}\right)\right) &= \left[\begin{array}{cc} -I & R \end{array}\right]\tilde{\Psi}_1^{(p)}(0) \\
&\cdots \\
G^{i+1,+}w_{i+1}^+ + G^{i+1,-}w_{i+1}^- \exp\left(\frac{\left(z_{i+1}^* - z_i^*\right)}{\lambda_{i+1}^+}\right) & \\
-G^{i,+}w_i^+ \exp\left(\frac{\left(z_{i-1}^* - z_i^*\right)}{\lambda_i^+}\right) - G^{i,-}w_i^- &= \Delta_{i,i+1} \\
&\cdots \\
G^{K,+}w_K^+ - G^{K-1,+}w_{K-1}^+ \exp\left(\frac{\left(z_{K-1}^* - z_{K-2}^*\right)}{\lambda_{K-1}^+}\right) - G^{K-1,-}w_{K-1}^- &= \Delta_{K-1,K}
\end{aligned}
\tag{4.23}
$$

This system can be expressed as a matrix equation in the same manner as (4.19). However, stating the general matrix is unwieldy on paper. I will therefore present the matrix equation for the case $K = 3$, since it is the smallest such equation which provides an example of each case listed in (4.23). I will use the substitution $J = [I - R]$ for brevity, since the expression is large:

$$
\begin{aligned}
&\left[\begin{array}{ccccc}
JG^{1,+} & JG^{1,-}\exp\left(\frac{z_1^*}{\lambda_1^-}\right) & 0 & 0 & 0 \\
-G^{1,+}\exp\left(\frac{z_1^*}{\lambda_1^+}\right) & -G^{1,-} & G^{2,+} & G^{2,-}\exp\left(\frac{\left(z_2^* - z_3^*\right)}{\lambda_2^+}\right) & 0 \\
0 & 0 & -G^{2,+}\exp\left(\frac{\left(z_3^* - z_2^*\right)}{\lambda_2^+}\right) & -G^{2,-} & G^{3,+}
\end{array}\right] * \\
&\qquad\qquad \left[\begin{array}{c} w_1^+ \\ w_1^- \\ w_2^+ \\ w_2^- \\ w_3^+ \end{array}\right] = \left[\begin{array}{c} J\tilde{\Psi}_1^{(p)}(0) \\ \Delta_{1,2} \\ \Delta_{2,3} \end{array}\right]
\end{aligned}
\tag{4.24}
$$

Equation (4.24) helps illustrate the general structure of the matrix equation corresponding to the K layered case. When considering this system, it is important to recall that each row in the matrix equation corresponds to the behavior of radiance at a specific layer boundary. As in the two layer case, it is easy to think in terms of which row defines which set of eigenvalue

weights, but the nature of the coupling involved necessitates that no one vector $w_i^{\pm}$ will be determined by a single row. Instead, note that the top row is determined by radiance at $z = z_0^* = 0$, the second at $z = z_1^*$ and the third at $z = z_2^*$. Since the structure of row i is determined by the radiance at z_{i-1}^*, which in turn involves only the radiance at in M_{i-1} and M_i, all blocks corresponding to homogeneous solutions for other layers must be zero. This leads to only two populated blocks in the first row, three in the last (owing to the fact that w_K^- is not used) and four in each other row.

While the matrix on the left hand side of (4.23) will be square if B_i is nonsingular for each layer, as in the 2 layered case, the blocks themselves do not follow a square layout. Instead, it will have K rows of $2K - 1$ blocks. This can be shown simply from the number of layers, K, each of which has an upper boundary which in turn forms a row, and the number $w_i^{\pm}$ vectors, $2K - 1$, of which one is lost due to the non-use of w_K^-. When viewing the blocks in this manner, a pseudo-diagonal structure is observed. I call this "pseudo-diagonal" since each new row between the first and the last involves a shift of two blocks for the non-zero terms. Blocks could be chosen which set a structure that has blocks only along the main and first upper block diagonal, but that would involve combining the terms for weights and vectors corresponding to positive and negative eigenvalues, which creates computational complications when applying decay terms to half of the corresponding blocks and does not actually make anything easier.

4.6 Results and Discussion

To showcase the results of the layered implementation of DSHEF$_N$, I will consider four different media, each consisting of two layers. Each layer will have optical properties such that l^* is normalized, but one layer will have a ratio of reduced scattering to absorption of 100 while the other will be 3. The thickness of the top layer will be set to either $0.1l^*$ or $1l^*$,

and each permutation of thick and thin top layer, as well as highly scattering top and highly scattering bottom, will be simulated. The medium will be considered to have a refractive index of 1.4 and the scattering phase function of each layer will be the Henyey-Greenstein function with anisotropy $g = 0.8$. Normally incident planar wave sources will be considered. Four spatial frequencies are examined: 0, $0.1l^*$, $0.2l^*$ and $0.3l^*$. The results of each show the effect of a source's spatially modulated component on the spatially modulated component of the quantity to be examined. That is, each plot will be isolated to one value in the Fourier domain in terms of both source and output. These parameters were chosen to represent a wide variety of media and to showcase the results of DSHEF_N in challenging regimes and because these spatial frequencies represent a range shown to be useful in Spatial Frequency Domain Imaging[29].

Results will be shown for radiance as a function of $\cos(\theta)$ and depth z, as well as for fluence as a function of depth and reflectance as a function of spatial frequency. These functions were chosen to both show DSHEF_N's ability to capture basic radiance as a function of angle and position as well as its capability to capture important functionals which are commonly used in imaging applications.

DSHEF_3, DSHEF_5, DSHEF_7, and DSHEF_{13} will be shown, as well as SHEF_{13}. This last method is included to provide a comparison to a current best practice executed at a high order of expansion. An exception to this list of orders is the presentation of radiance as a function of depth and $\cos(\theta)$, for which only DSHEF_7 will be shown. The δ–Eddington approximation will not be used for any DSHEF_N results. This is because greater accuracy was found without it. All results are compared to a Monte Carlo gold standard obtained using Hayakawa's Virtual Tissue Simulator Command Line Monte Carlo program using ten million photon packets using discrete absorption weight.

In all simulations, the source is considered to be emanating from just inside the medium, so specular reflectance is not considered.

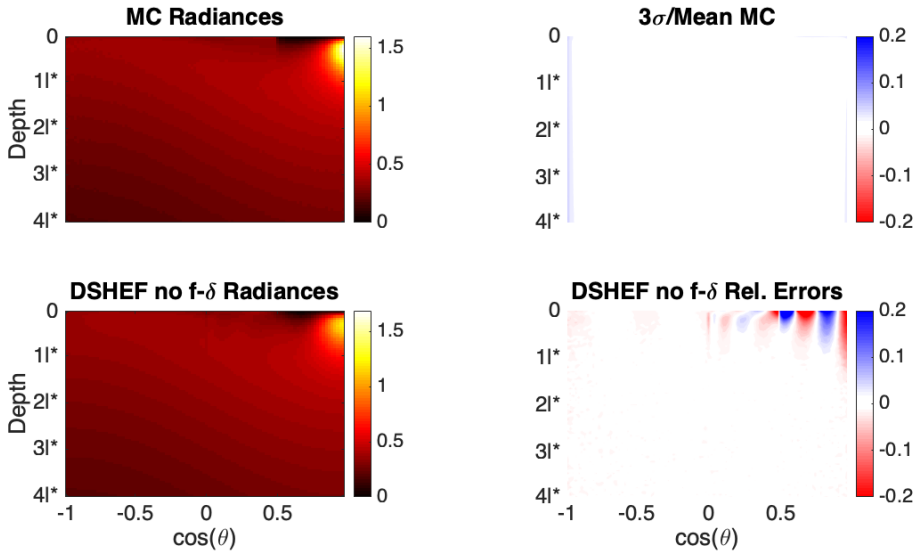

Figure 4.1: Radiance vs depth and cos(θ), thin, highly scattering bottom layer, $f_x = 0$. (Top Left) Radiance as a function of depth and polar angle, obtained by Monte Carlo. (Bottom Left) Radiance as a function of depth and polar angle DSHEF$_7$. (Top Right) 3 standard deviations from MC results divided by MC mean. (Bottom Right) Relative error of DSHEF$_7$.

4.6.1 Radiance vs Depth and Cos(θ)

Figures 4.1–16 show radiance as a function of cosine of polar angle θ for depths from 0 to $4l^*$. These depths were chosen because as the top right section of these figure show, as spatial frequency increases, the region of high certainty (white) becomes more shallow in z. Figures 4.1–8 show results obtained with a thin top layer and figures 4.9–16 show results obtained with a thick top layer. In each of these figures, it is important to keep in mind that cos(θ) = 1 indicates the positive z direction, while cos(θ) = -1 indicates the negative z direction. Figs 4.1–4 and 4.9–12 show results obtained with a highly scattering ($\mu_s'/\mu_a = 100$) top layer and a less scattering ($\mu_s'/\mu_a = 100$) bottom layer while Figs 4.5–8 and 4.13–16 show the opposite. In these, the top layer is less highly scattering ($\mu_s'/\mu_a = 3$) while the bottom layer is more highly scattering ($\mu_s'/\mu_a = 100$).

Results for DSHEF$_7$ were shown in each case to provide a balance between detail and efficiency, and to showcase the limits of the method. Error in each figure is shown to be of an

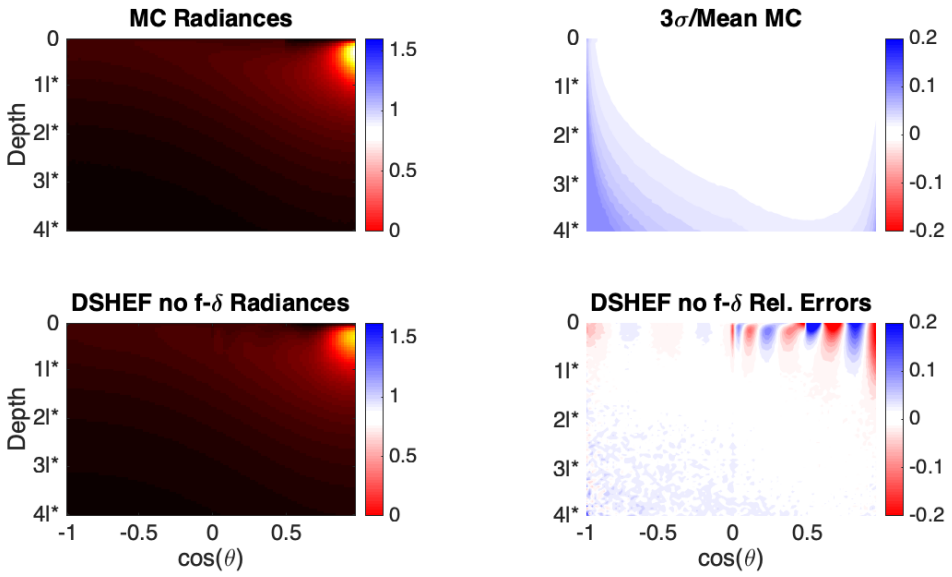

Figure 4.2: Radiance vs depth and $\cos(\theta)$, thin, highly scattering bottom layer, $f_x = 0.1/l^*$. (Top Left) Radiance as a function of depth and polar angle, obtained by Monte Carlo. (Bottom Left) Radiance as a function of depth and polar angle DSHEF_7. (Top Right) 3 standard deviations from MC results divided by MC mean. (Bottom Right) Relative error of DSHEF_7.

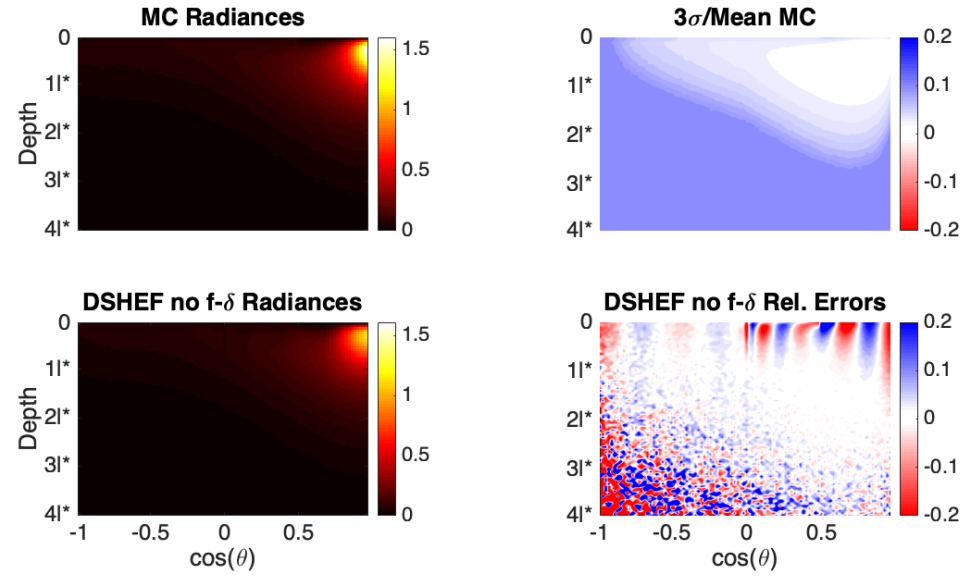

Figure 4.3: Radiance vs depth and $\cos(\theta)$, thin, highly scattering bottom layer, $f_x = 0.2/l^*$. (Top Left) Radiance as a function of depth and polar angle, obtained by Monte Carlo. (Bottom Left) Radiance as a function of depth and polar angle DSHEF_7. (Top Right) 3 standard deviations from MC results divided by MC mean. (Bottom Right) Relative error of DSHEF_7.

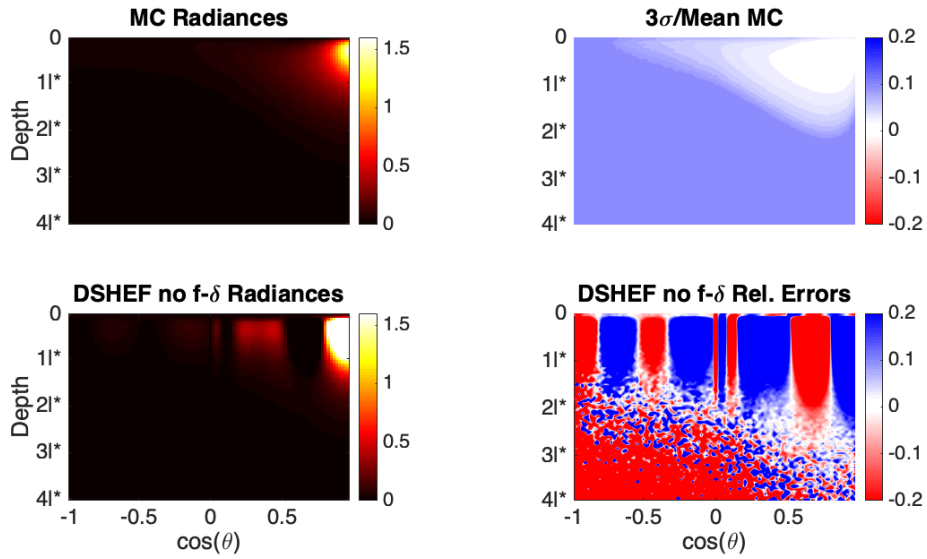

Figure 4.4: Radiance vs depth and $\cos(\theta)$, thin, highly scattering bottom layer, $f_x = 0.3/l^*$. (Top Left) Radiance as a function of depth and polar angle, obtained by Monte Carlo. (Bottom Left) Radiance as a function of depth and polar angle DSHEF_7. (Top Right) 3 standard deviations from MC results divided by MC mean. (Bottom Right) Relative error of DSHEF_7.

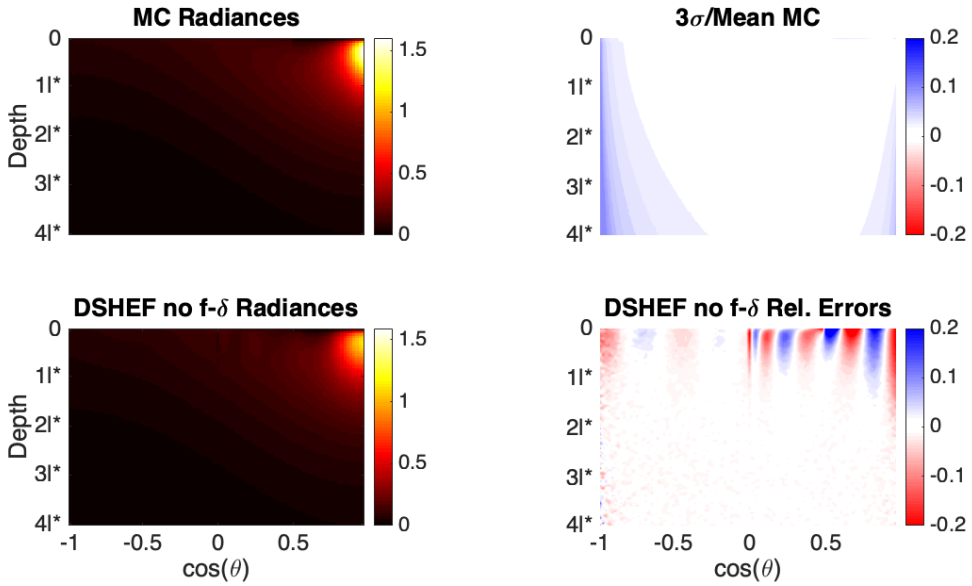

Figure 4.5: Radiance vs depth and $\cos(\theta)$, thin, highly scattering top layer, $f_x = 0$. (Top Left) Radiance as a function of depth and polar angle, obtained by Monte Carlo. (Bottom Left) Radiance as a function of depth and polar angle DSHEF_7. (Top Right) 3 standard deviations from MC results divided by MC mean. (Bottom Right) Relative error of DSHEF_7.

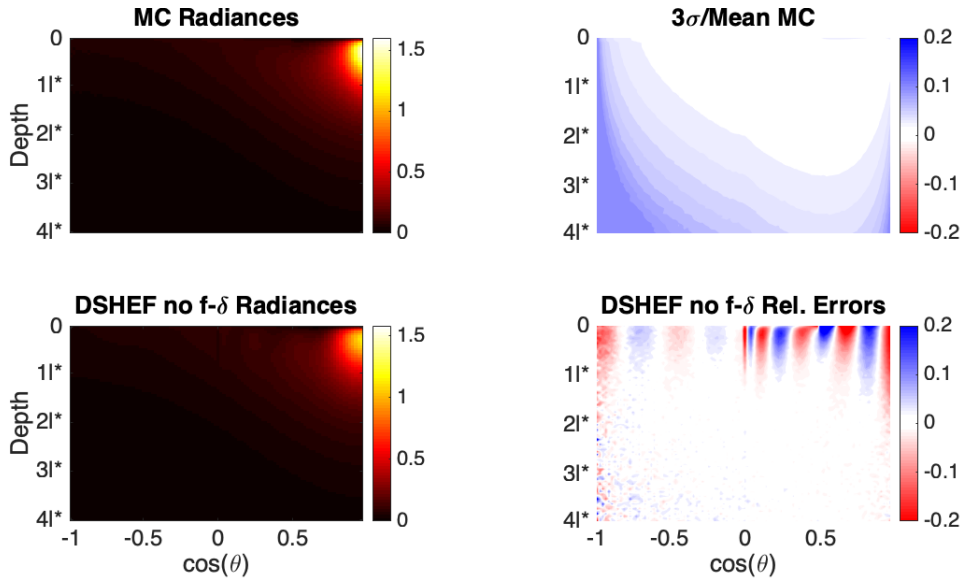

Figure 4.6: Radiance vs depth and $\cos(\theta)$, thin, highly scattering top layer, $f_x = 0.1/l^*$. (Top Left) Radiance as a function of depth and polar angle, obtained by Monte Carlo. (Bottom Left) Radiance as a function of depth and polar angle DSHEF_7. (Top Right) 3 standard deviations from MC results divided by MC mean. (Bottom Right) Relative error of DSHEF_7.

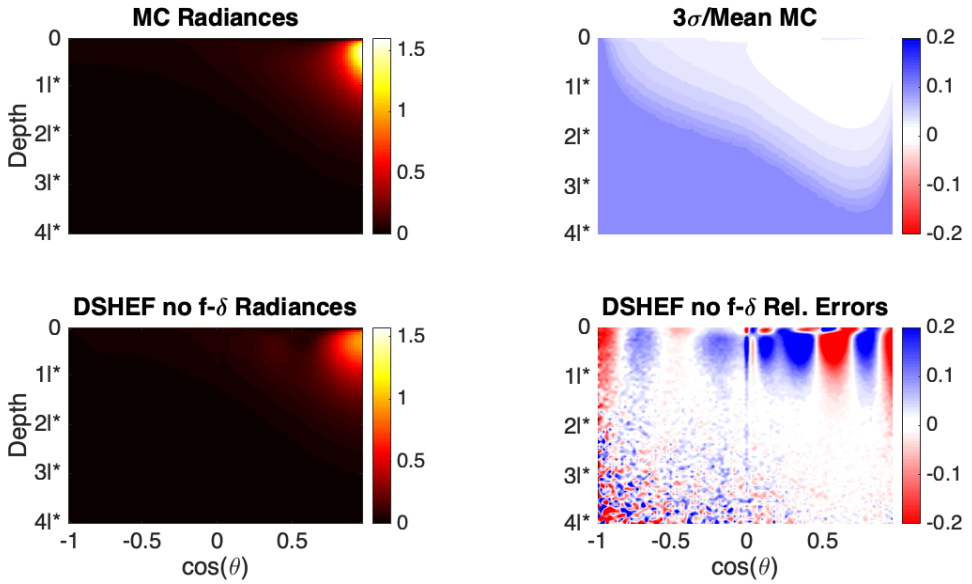

Figure 4.7: Radiance vs depth and $\cos(\theta)$, thin, highly scattering top layer, $f_x = 0.2/l^*$. (Top Left) Radiance as a function of depth and polar angle, obtained by Monte Carlo. (Bottom Left) Radiance as a function of depth and polar angle DSHEF_7. (Top Right) 3 standard deviations from MC results divided by MC mean. (Bottom Right) Relative error of DSHEF_7.

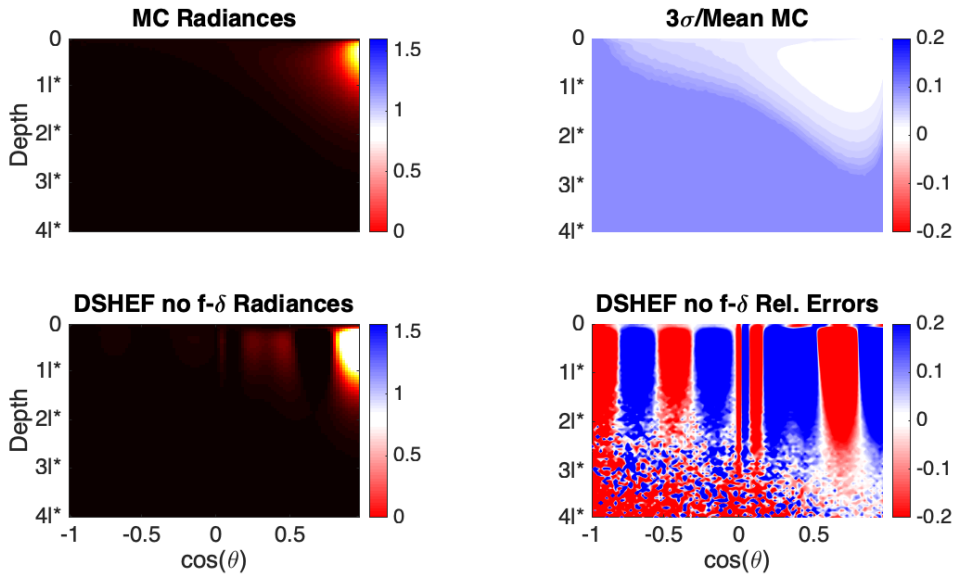

Figure 4.8: Radiance vs depth and $\cos(\theta)$, thin, highly scattering top layer, $f_x = 0.3/l^*$. (Top Left) Radiance as a function of depth and polar angle, obtained by Monte Carlo. (Bottom Left) Radiance as a function of depth and polar angle DSHEF_7. (Top Right) 3 standard deviations from MC results divided by MC mean. (Bottom Right) Relative error of DSHEF_7.

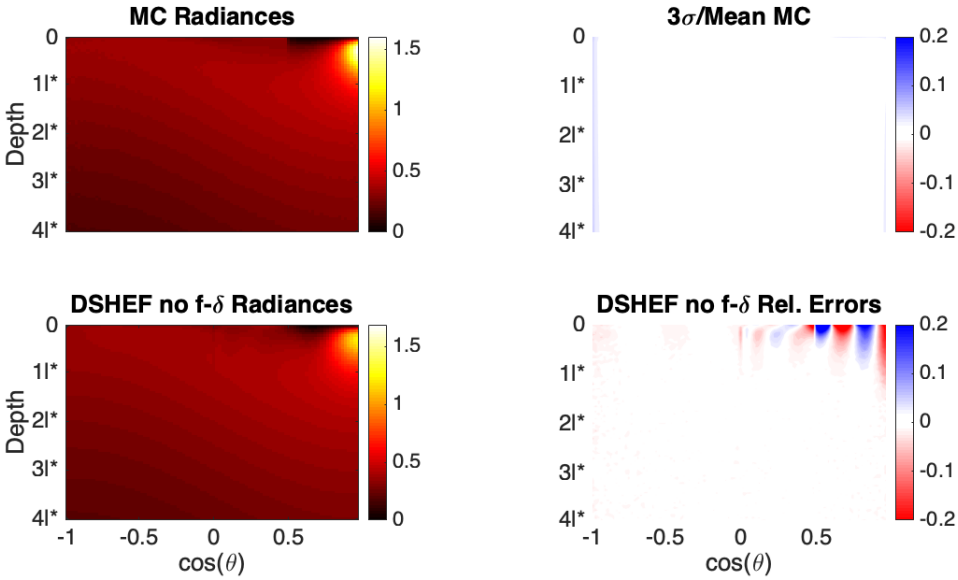

Figure 4.9: Radiance vs depth and $\cos(\theta)$, thick, highly scattering bottom layer, $f_x = 0$. (Top Left) Radiance as a function of depth and polar angle, obtained by Monte Carlo. (Bottom Left) Radiance as a function of depth and polar angle DSHEF_7. (Top Right) 3 standard deviations from MC results divided by MC mean. (Bottom Right) Relative error of DSHEF_7.

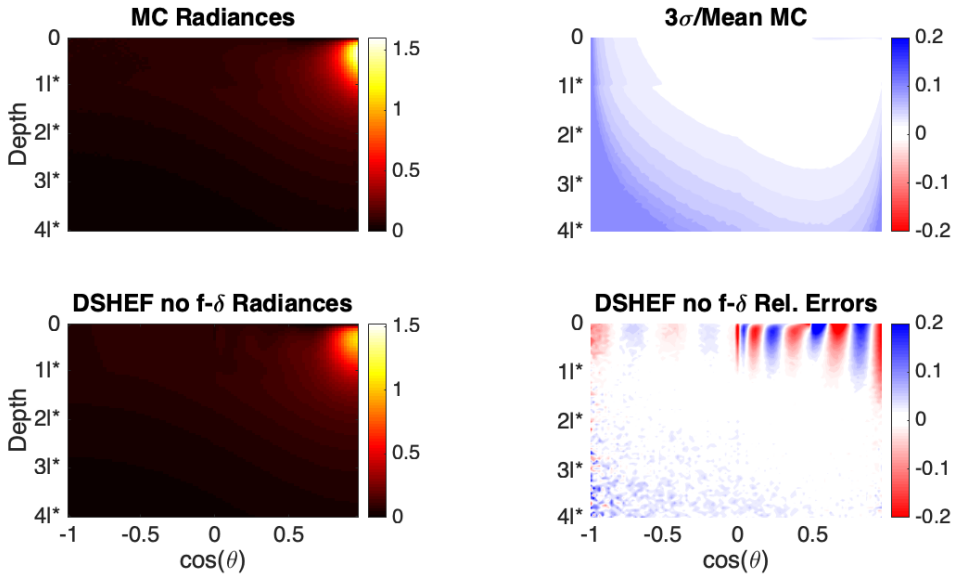

Figure 4.10: Radiance vs depth and $\cos(\theta)$, thick, highly scattering bottom layer, $f_x = 0.1/l^*$. (Top Left) Radiance as a function of depth and polar angle, obtained by Monte Carlo. (Bottom Left) Radiance as a function of depth and polar angle DSHEF_7. (Top Right) 3 standard deviations from MC results divided by MC mean. (Bottom Right) Relative error of DSHEF_7.

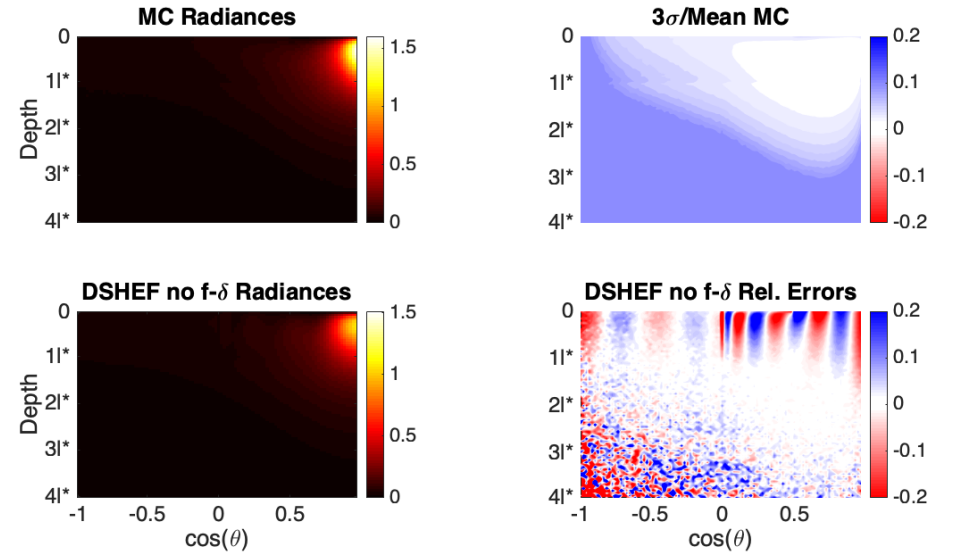

Figure 4.11: Radiance vs depth and $\cos(\theta)$, thick, highly scattering bottom layer, $f_x = 0.2/l^*$. (Top Left) Radiance as a function of depth and polar angle, obtained by Monte Carlo. (Bottom Left) Radiance as a function of depth and polar angle DSHEF_7. (Top Right) 3 standard deviations from MC results divided by MC mean. (Bottom Right) Relative error of DSHEF_7.

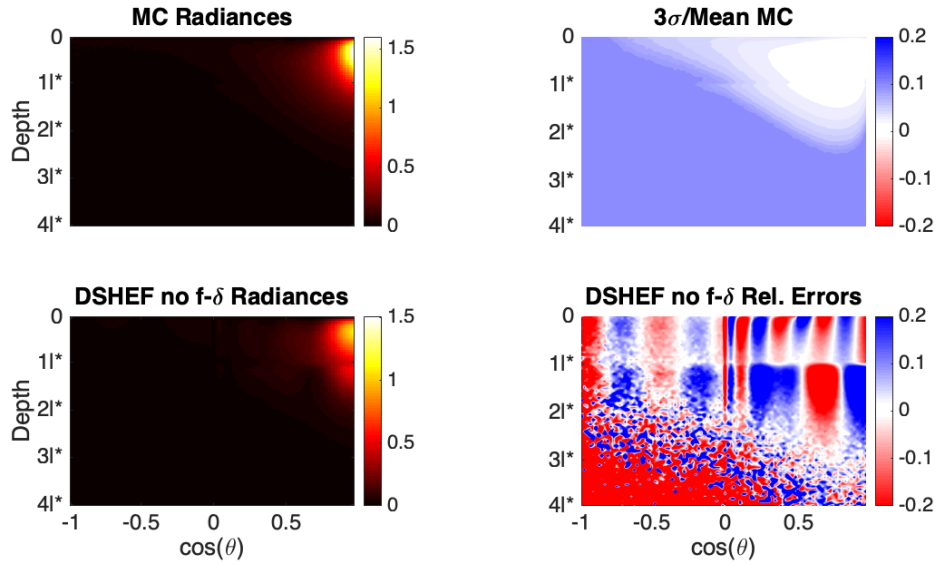

Figure 4.12: Radiance vs depth and $\cos(\theta)$, thick, highly scattering bottom layer, $f_x = 0.3/l^*$. (Top Left) Radiance as a function of depth and polar angle, obtained by Monte Carlo. (Bottom Left) Radiance as a function of depth and polar angle DSHEF_7. (Top Right) 3 standard deviations from MC results divided by MC mean. (Bottom Right) Relative error of DSHEF_7.

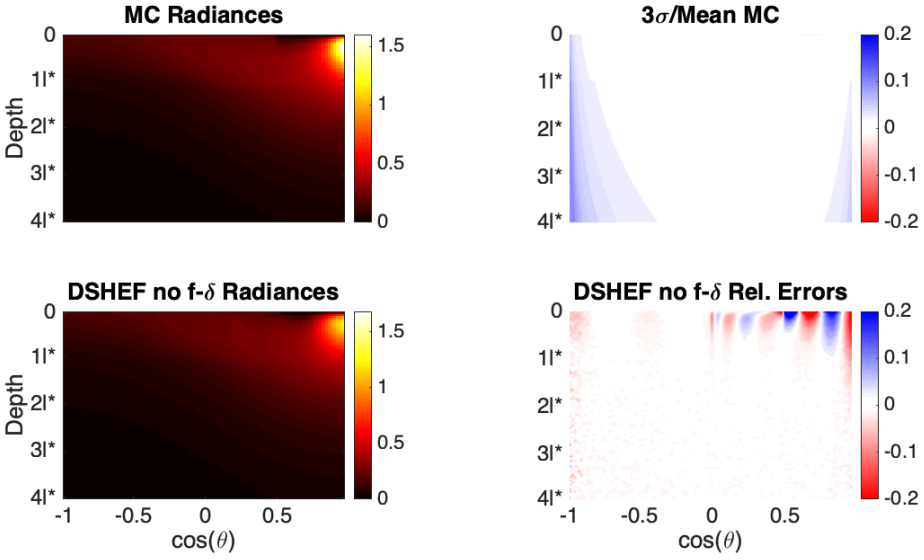

Figure 4.13: Radiance vs depth and $\cos(\theta)$, thick, highly scattering top layer, $f_x = 0$. (Top Left) Radiance as a function of depth and polar angle, obtained by Monte Carlo. (Bottom Left) Radiance as a function of depth and polar angle DSHEF_7. (Top Right) 3 standard deviations from MC results divided by MC mean. (Bottom Right) Relative error of DSHEF_7.

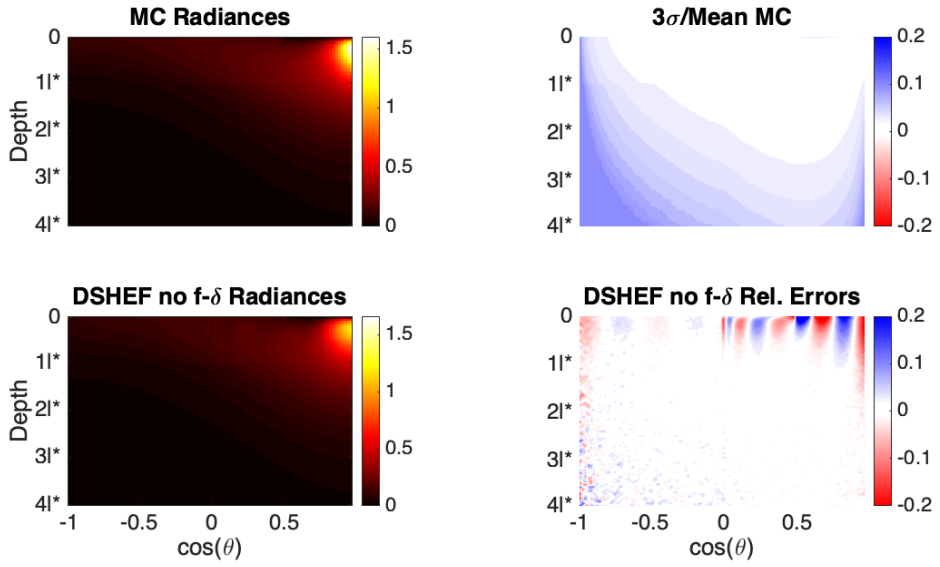

Figure 4.14: Radiance vs depth and cos(θ), thick, highly scattering top layer, $f_x = 0.1/l^*$. (Top Left) Radiance as a function of depth and polar angle, obtained by Monte Carlo. (Bottom Left) Radiance as a function of depth and polar angle DSHEF$_7$. (Top Right) 3 standard deviations from MC results divided by MC mean. (Bottom Right) Relative error of DSHEF$_7$.

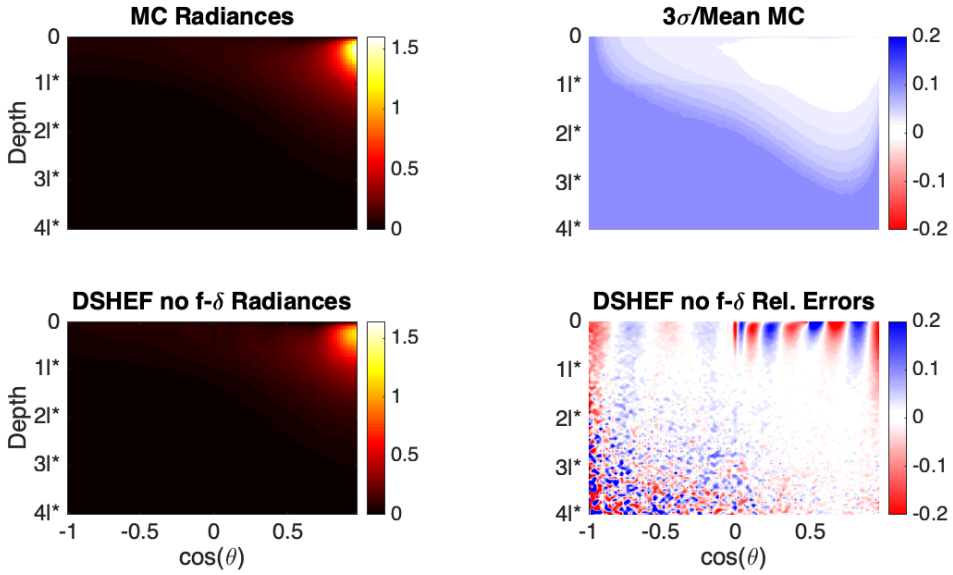

Figure 4.15: Radiance vs depth and cos(θ), thick, highly scattering top layer, $f_x = 0.2/l^*$. (Top Left) Radiance as a function of depth and polar angle, obtained by Monte Carlo. (Bottom Left) Radiance as a function of depth and polar angle DSHEF$_7$. (Top Right) 3 standard deviations from MC results divided by MC mean. (Bottom Right) Relative error of DSHEF$_7$.

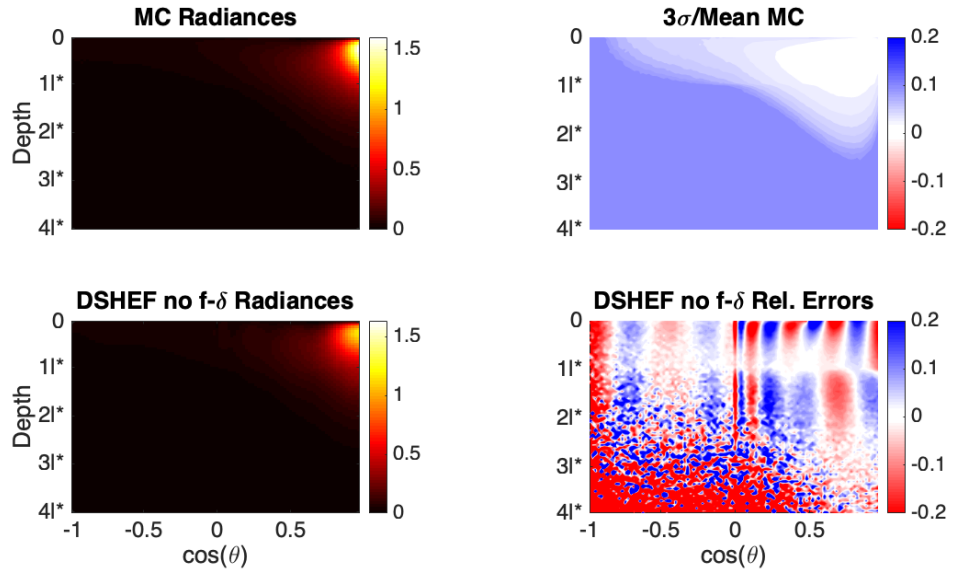

Figure 4.16: Radiance vs depth and $\cos(\theta)$, thick, highly scattering top layer, $f_x = 0.3/l^*$. (Top Left) Radiance as a function of depth and polar angle, obtained by Monte Carlo. (Bottom Left) Radiance as a function of depth and polar angle DSHEF_7. (Top Right) 3 standard deviations from MC results divided by MC mean. (Bottom Right) Relative error of DSHEF_7.

oscillatory nature, as the result from DSHEF_7 alternates between over and underestimation of the Monte Carlo gold standard.

Figs 4.1 and 4.5 show results for radiance with $f_x = 0$. Fig. 4.1 shows results for a highly scattering bottom layer and a less scattering top layer, while Fig. 4.5 shows the opposite. In each case, the top layer has a thickness of $0.1l^*$.

Figs 4.1 and 4.5 show errors near the surface which decrease as z increases, with the majority occurring when $0 < z < z^*$. Small errors, mostly under 0.01, do occur for larger z. It should be noted that error is concentrated at higher values for $\cos(\theta)$ as well as lower values for z. This is due to the non-differentiable point of the function for internal reflectance given in equation (4.14), as well as the more highly structured nature of radiance in this area. This will be repeated in all cases examined; evidence indicates that this region of radiance is the most difficult for spectral methods to recapitulate.

Figs 4.2 and 4.6 show results for media with thin top layers and at a spatial frequency of $0.1/l^*$. Fig. 4.2 shows results for a more highly scattering bottom layer while Fig 4.6 shows results for a more highly scattering top layer. These results are similar to those shown in Figs 4.1 and 4.5, though errors are larger in magnitude, with breakdown of comparison being shown for depths of $z > 2l^*$ for negative $\cos(\theta)$ and depths of $z > 3l*$ for positive $\cos(\theta)$. This is due to the diminished impact of the average photon packet used in the Monte Carlo simulation on radiances of increased spatial frequency, and this will be a pattern in all results.

Figs 4.3 and 4.7 show results for the same parameters as 4.2 and 4.6, respectively, except that the spatial frequency f_x is equal to $0.2/l^*$. In each of these, the breakdown of Monte Carlo confidence and accurace at higher depths becomes more apparent. Relative error near the surface also increases, though is generally between -0.1 and 0.1, with the exception of a few oscillations near the surface.

Figs 4.4 and 4.8 repeat this pattern with a spatial frequency of $0.3/l^*$. Here, relative error becomes unnaceptably large as depth increases, showing that this parameter regime is too difficult for DSHEF_7. However, it should be noted, and will be shown in more detail in the following subsection, that the results near the boundary, particularly for negative $\cos(\theta)$, maintain low relative errors. This is particularly important for imaging applications, as this region represents radiance directed out of the medium near the boundary, which supplies measurements for all reflectance based imaging geometries.

Figs. 4.9–16 show the results for the same parameters as Figs 4.1–8, but with top layer thicknesses equal to $1l^*$. In each of these cases, error is less extreme than in their counterparts with thin top layers. This is to be expected given the nature of the DSHEF_N solution as a linear combination of exponential decay terms and the term by term equivalence used as a coupling boundary condition at the medium interface. Rates of decay are determined by optical properties and order of expansion, which means that when using a medium with a relatively shallow top layer, DSHEF_N will have made a smaller adjustment to radiance as z

approaches z^* than it would have with a medium with a relatively deep top layer.

In particular, Figs 4.9 and 4.13, which show results with $f_x = 0$, show relative errors mostly between -0.05 and 0.05. These errors have largely vanished once $z \geq z^*$.

Figs 4.10 and 4.14, which results obtained using spatial frequencies of $0.1/l^*$ are similar in this regard, also having relative errors generally between -0.05 and 0.05. However, these stand in contrast to 4.9 and 4.13 in that the oscillatory error associated with internal reflection near $z = 0$ (in the top right of the plot) extends in a significant manner below the layer interface as $z = 1l^*$. This increase in error as well as the region in which larger error is encountered is to be expected as frequency increases.

Figs 4.11 and 4.15 show similar results for sources with spatial frequencies of $0.2/l^*$. In these, there is substantially less error than in Figs 4.3 and 4.6, their corresponding figures with $z^* = 0.1l^*$. This lends weight to the idea that thicker top layers ease the coupling between layers that DSHEF_N utilizes. It should be noted here that relative error near the surface for positive $\cos(\theta)$ is shown to exceed ± 0.2 at multiple angles. However, this is not the case for negative $\cos(\theta)$. Here, radiance directed at a potential detector has errors mostly between -0.1 and 0.1.

Figs 4.12 and 4.16 display the results using sources with the highest examined spatial frequency, $0.3/l^*$. Again, the errors become much more extreme, though markedly less so than in Figs 4.4 and 4.8, the corresponding figures using $z^* = 0.1$. This once again shows the relative difficulty of simulation when $z^* < l^*$, especially when spatial frequency increases.

It has been pointed out that even in the most demanding cases shown, relative error near the medium boundary $z = 0$ is lower in radiance directed in the negative z direction than in that directed in the positive z direciton. This has only been examined for DSHEF_7, and can be difficult to determine from the figures shown. However, a more thorough examination of radiance as a function of $\cos(\theta)$ in the following section will better show this fact.

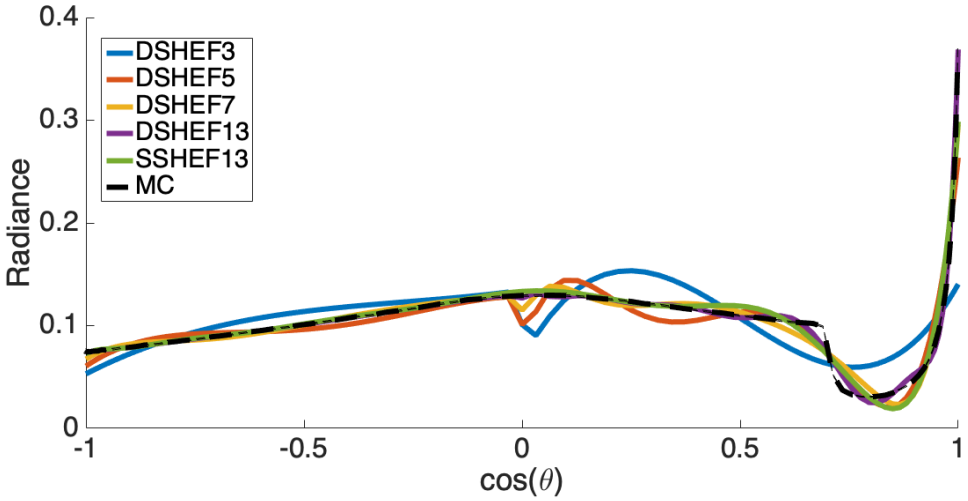

Figure 4.17: Radiance vs cos(θ) near medium surface, highly scattering top layer, $f_x = 0$, $z^* = 0.1l*$. DSHEF_3 is given in blue, DSHEF_5 is given in orange, DSHEF_7 is given in gold, DSHEF_{13} is given in purple, single SHEF_{13} is given in green and MC is given in dashed black. Error bars for the MC results are $\pm 3\sigma$.

4.6.2 Radiance vs Cos(θ) Near Medium Surface

The odd numbered Figs 4.17–31 show results for radiance as a function of cos(θ) at $z = 0.025$ with $z^* = 0.1$ and the same permutations of optical properties found in Figs 4.1–16. The even numbered Figs 4.18–32 show the relative errors of each result compared to Monte Carlo. Figs 4.17–24 show results with a highly scattering top layer ($\mu_s'/\mu_a = 100$) and a less scattering bottom layer ($\mu_s'/\mu_a = 3$).

The odd numbered Figs 4.33–47 show results for radiance as a function of cos(θ) at $z = 0.025$ with $z^* = 0.1$ and the same permutations of optical properties found in Figs 4.1–16 and Figs 4.17–32. The even numbered Figs 4.34–48 show the relative errors of each result compared to Monte Carlo. Figs 4.33–40 show results with a highly scattering top layer ($\mu_s'/\mu_a = 100$) and a less scattering bottom layer ($\mu_s'/\mu_a = 3$). Figs 4.41–48 show results for a highly scattering bottom layer ($\mu_s'/\mu_a = 100$) and a less scattering top layer ($\mu_s'/\mu_a = 3$).

Results are shown for DSHEF_3 (blue), DSHEF_5 (orange), DSHEF_7 (gold) and DSHEF_{13}

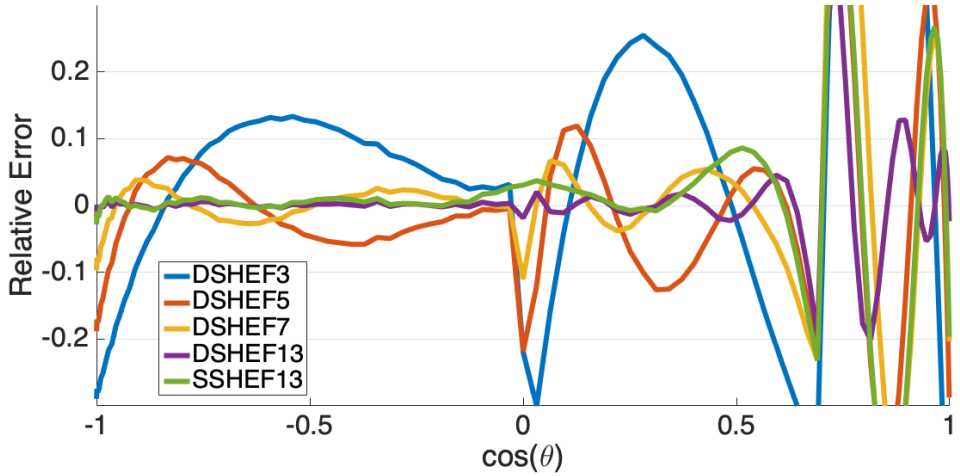

Figure 4.18: Relative Error for Radiance vs $\cos(\theta)$ near medium surface, highly scattering top layer, $f_x = 0$, $z^* = 0.1l*$. DSHEF_3 is given in blue, DSHEF_5 is given in orange, DSHEF_7 is given in gold, DSHEF_{13} is given in purple, single SHEF_{13} is given in green.

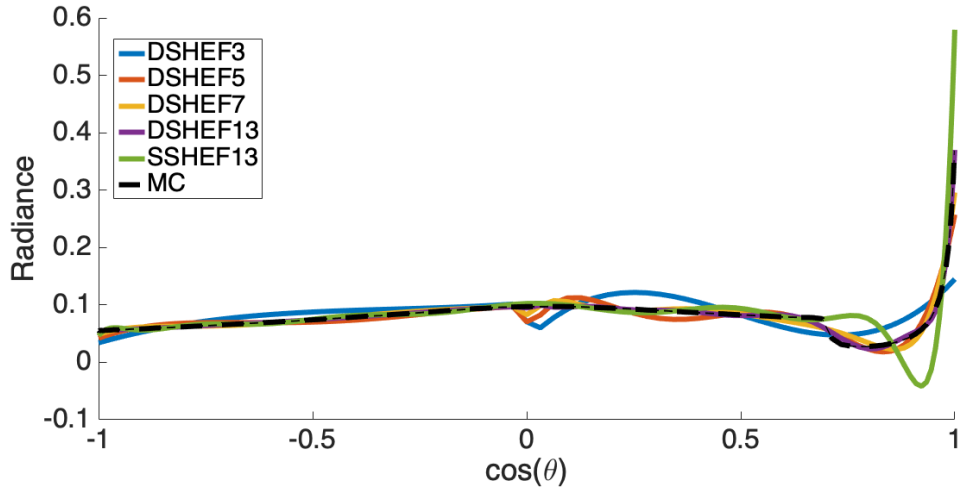

Figure 4.19: Radiance vs $\cos(\theta)$ near medium surface, highly scattering top layer, $f_x = 0.1/l^*$, $z^* = 0.1l*$. DSHEF_3 is given in blue, DSHEF_5 is given in orange, DSHEF_7 is given in gold, DSHEF_{13} is given in purple, single SHEF_{13} is given in green and MC is given in dashed black. Error bars for the MC results are $\pm 3\sigma$.

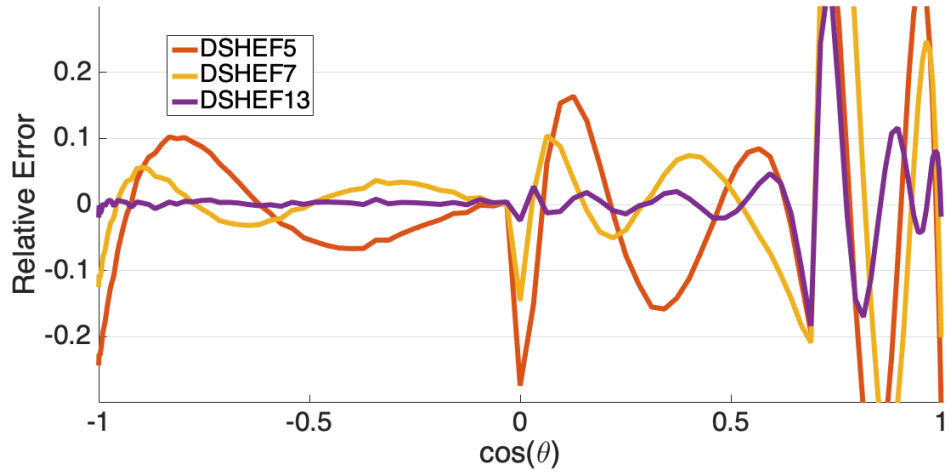

Figure 4.20: Relative Error for Radiance vs $\cos(\theta)$ near medium surface, highly scattering top layer, $f_x = 0.1/l^*$, $z^* = 0.1l*$. DSHEF_3 is given in blue, DSHEF_5 is given in orange, DSHEF_7 is given in gold, DSHEF_{13} is given in purple, single SHEF_{13} is given in green.

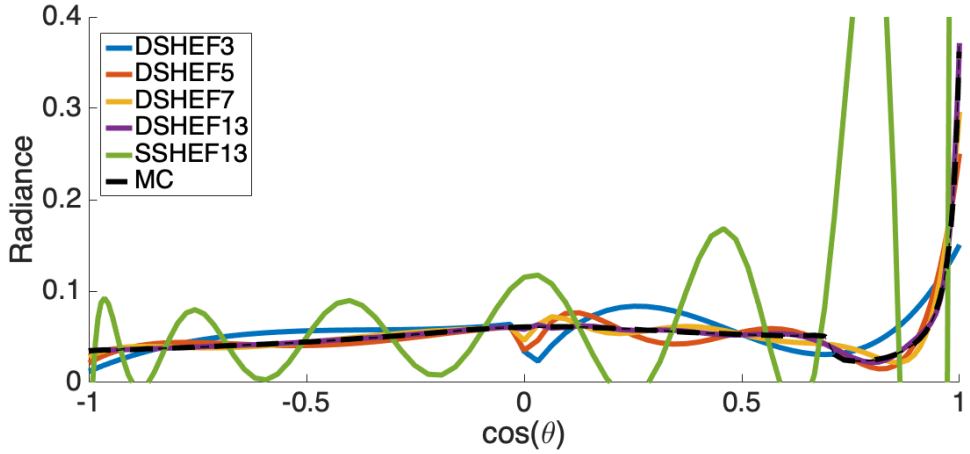

Figure 4.21: Radiance vs $\cos(\theta)$ near medium surface, highly scattering top layer, $f_x = 0.2/l^*$, $z^* = 0.1l*$. DSHEF_3 is given in blue, DSHEF_5 is given in orange, DSHEF_7 is given in gold, DSHEF_{13} is given in purple, single SHEF_{13} is given in green and MC is given in dashed black. Error bars for the MC results are $\pm 3\sigma$.

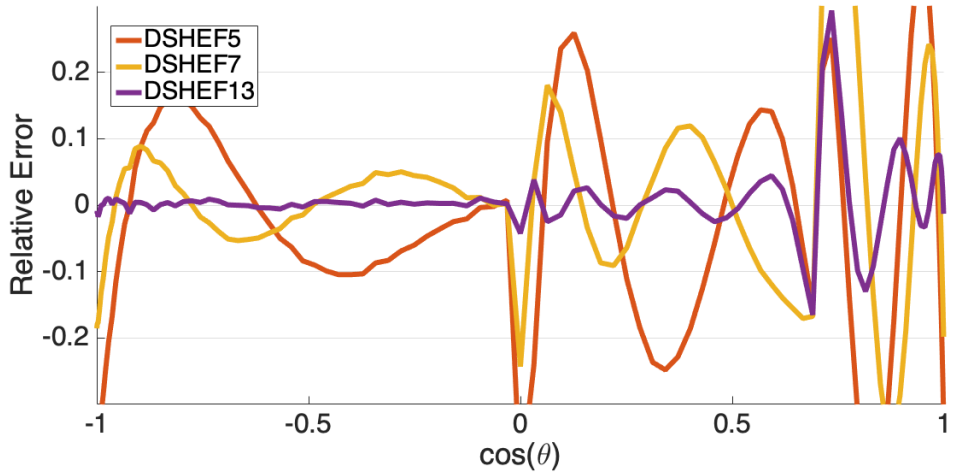

Figure 4.22: Relative Error for Radiance vs $\cos(\theta)$ near medium surface, highly scattering top layer, $f_x = 0.2/l^*$, $z^* = 0.1l*$. DSHEF_3 is given in blue, DSHEF_5 is given in orange, DSHEF_7 is given in gold, DSHEF_{13} is given in purple, single SHEF_{13} is given in green.

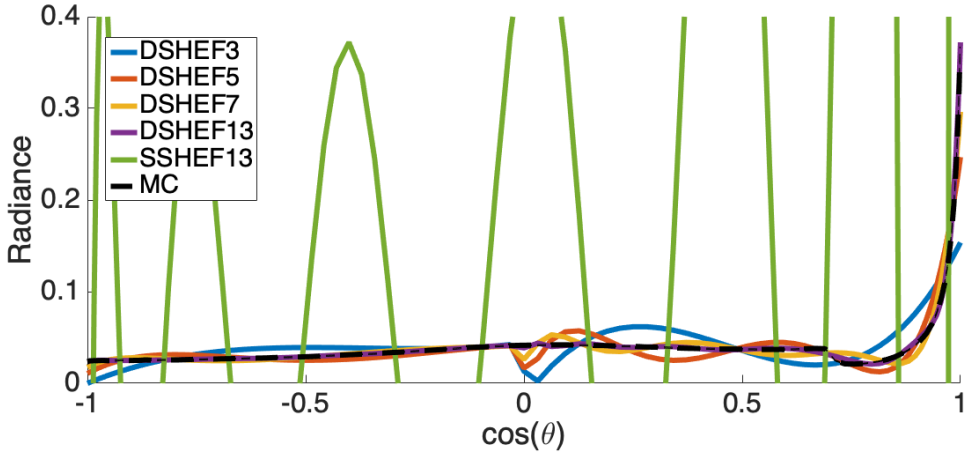

Figure 4.23: Radiance vs $\cos(\theta)$ near medium surface, highly scattering top layer, $f_x = 0.3/l^*$, $z^* = 0.1l*$. DSHEF_3 is given in blue, DSHEF_5 is given in orange, DSHEF_7 is given in gold, DSHEF_{13} is given in purple, single SHEF_{13} is given in green and MC is given in dashed black. Error bars for the MC results are $\pm 3\sigma$.

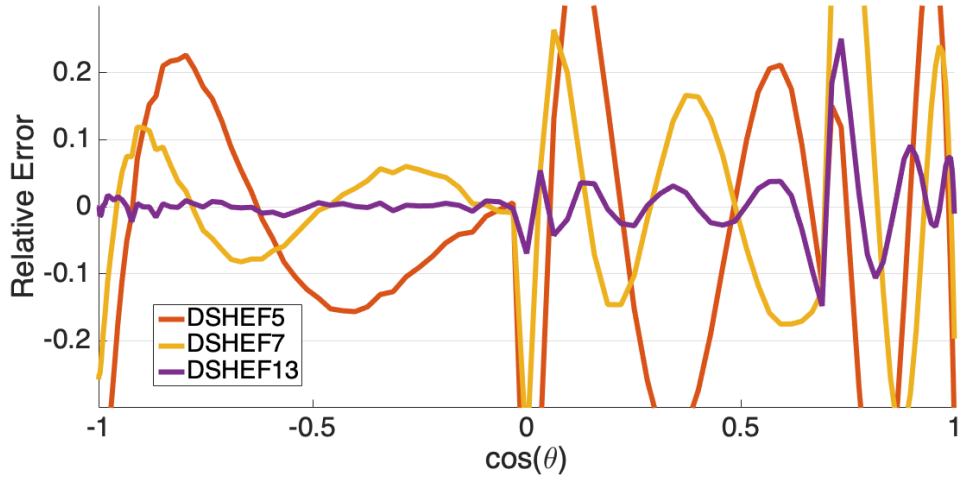

Figure 4.24: Relative Error for Radiance vs $\cos(\theta)$ near medium surface, highly scattering top layer, $f_x = 0.3/l^*$, $z^* = 0.1l*$. DSHEF_3 is given in blue, DSHEF_5 is given in orange, DSHEF_7 is given in gold, DSHEF_{13} is given in purple, single SHEF_{13} is given in green.

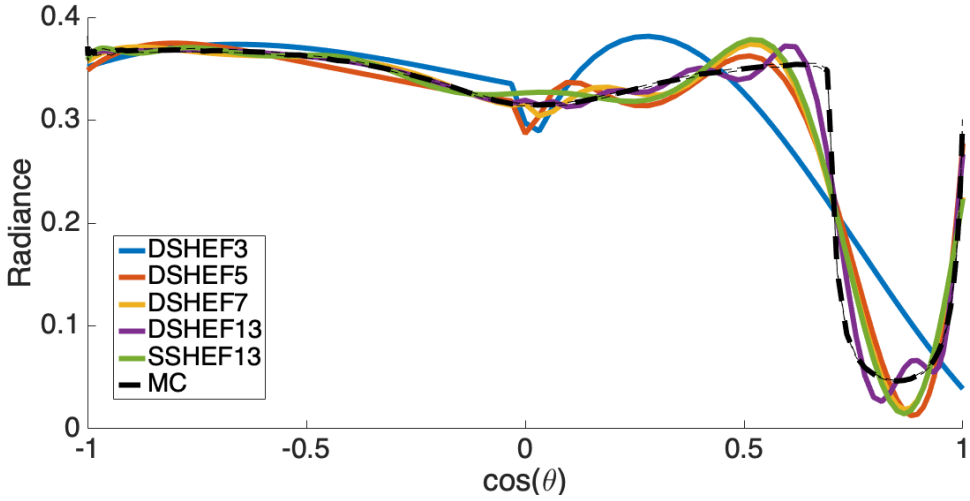

Figure 4.25: Radiance vs $\cos(\theta)$ near medium surface, highly scattering bottom layer, $f_x = 0$, $z^* = 0.1l*$. DSHEF_3 is given in blue, DSHEF_5 is given in orange, DSHEF_7 is given in gold, DSHEF_{13} is given in purple, single SHEF_{13} is given in green and MC is given in dashed black. Error bars for the MC results are $\pm 3\sigma$.

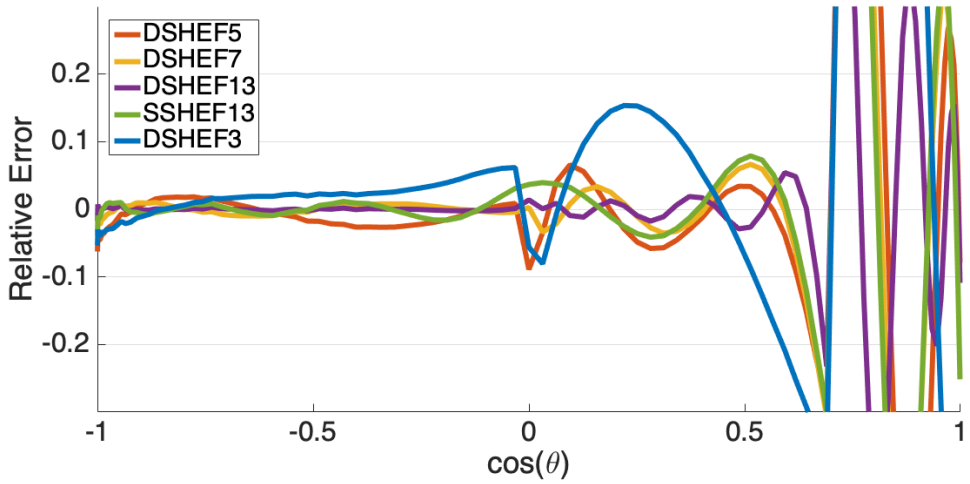

Figure 4.26: Relative Error for Radiance vs $\cos(\theta)$ near medium surface, highly scattering bottom layer, $f_x = 0$, $z^* = 0.1l*$. DSHEF_3 is given in blue, DSHEF_5 is given in orange, DSHEF_7 is given in gold, DSHEF_{13} is given in purple, single SHEF_{13} is given in green.

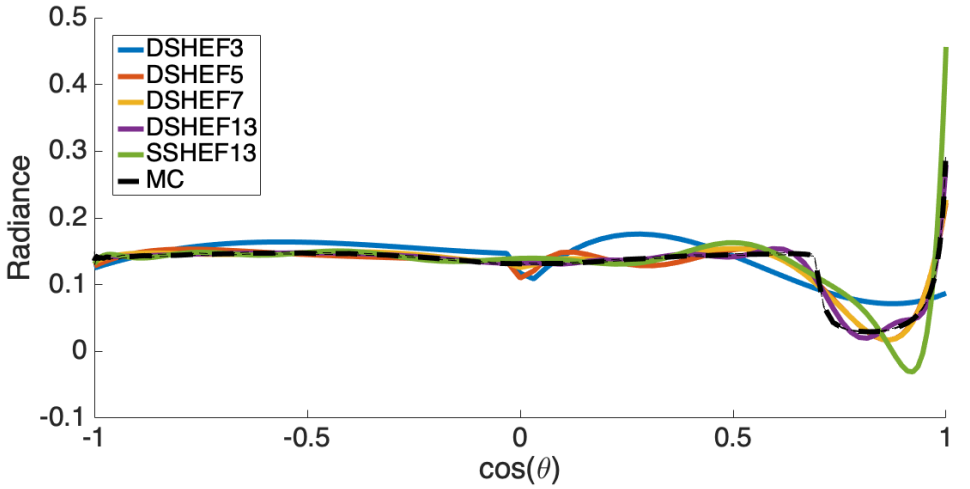

Figure 4.27: Radiance vs $\cos(\theta)$ near medium surface, highly scattering bottom layer, $f_x = 0.1/l^*$, $z^* = 0.1l*$. DSHEF_3 is given in blue, DSHEF_5 is given in orange, DSHEF_7 is given in gold, DSHEF_{13} is given in purple, single SHEF_{13} is given in green and MC is given in dashed black. Error bars for the MC results are $\pm 3\sigma$.

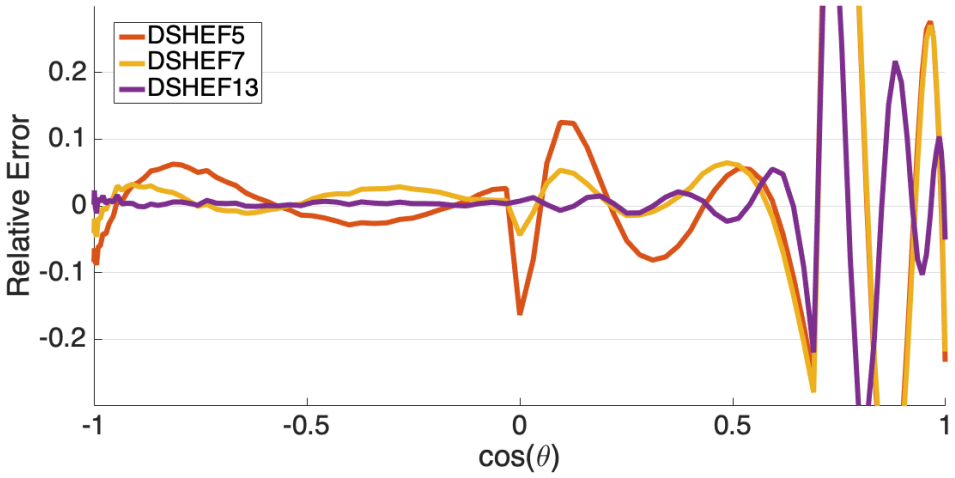

Figure 4.28: Relative Error for Radiance vs $\cos(\theta)$ near medium surface, highly scattering bottom layer, $f_x = 0.1/l^*$, $z^* = 0.1l*$. DSHEF_3 is given in blue, DSHEF_5 is given in orange, DSHEF_7 is given in gold, DSHEF_{13} is given in purple, single SHEF_{13} is given in green.

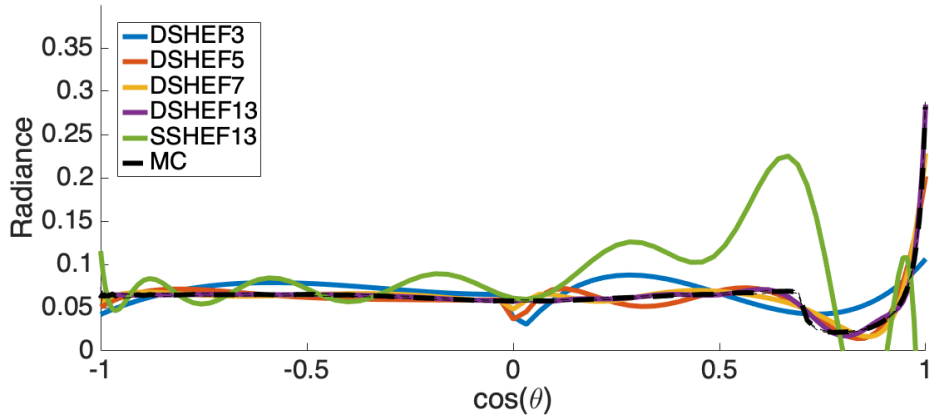

Figure 4.29: Radiance vs $\cos(\theta)$ near medium surface, highly scattering bottom layer, $f_x = 0.2/l^*$, $z^* = 0.1l*$. DSHEF_3 is given in blue, DSHEF_5 is given in orange, DSHEF_7 is given in gold, DSHEF_{13} is given in purple, single SHEF_{13} is given in green and MC is given in dashed black. Error bars for the MC results are $\pm 3\sigma$.

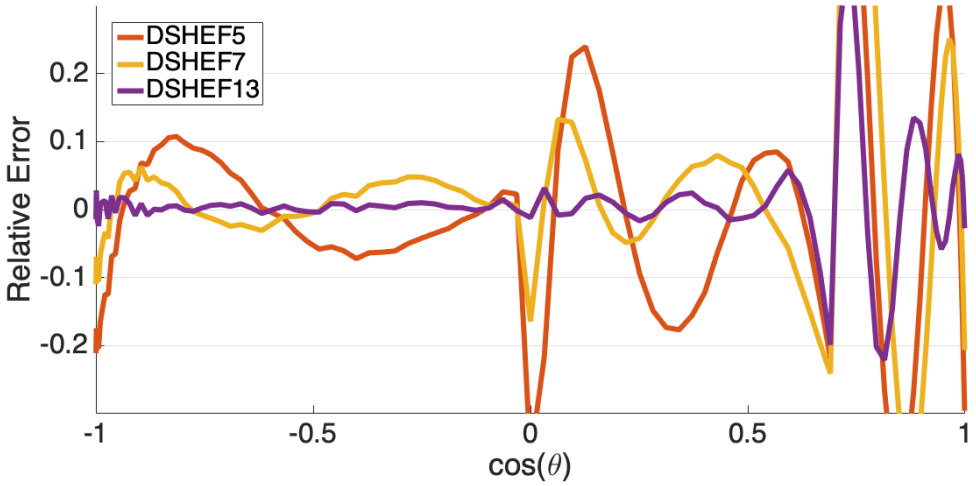

Figure 4.30: Relative Error for Radiance vs $\cos(\theta)$ near medium surface, highly scattering bottom layer, $f_x = 0.2/l^*$, $z^* = 0.1l*$. DSHEF_3 is given in blue, DSHEF_5 is given in orange, DSHEF_7 is given in gold, DSHEF_{13} is given in purple, single SHEF_{13} is given in green.

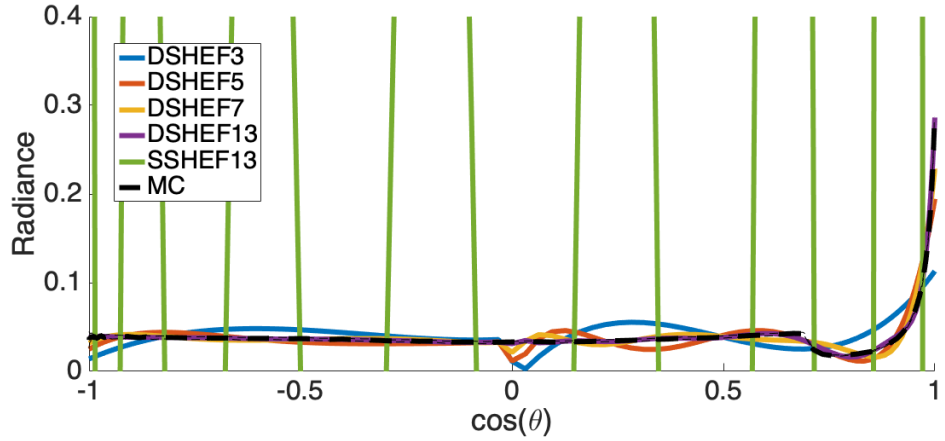

Figure 4.31: Radiance vs $\cos(\theta)$ near medium surface, highly scattering bottom layer, $f_x = 0.3/l^*$, $z^* = 0.1l*$. DSHEF_3 is given in blue, DSHEF_5 is given in orange, DSHEF_7 is given in gold, DSHEF_{13} is given in purple, single SHEF_{13} is given in green and MC is given in dashed black. Error bars for the MC results are $\pm 3\sigma$.

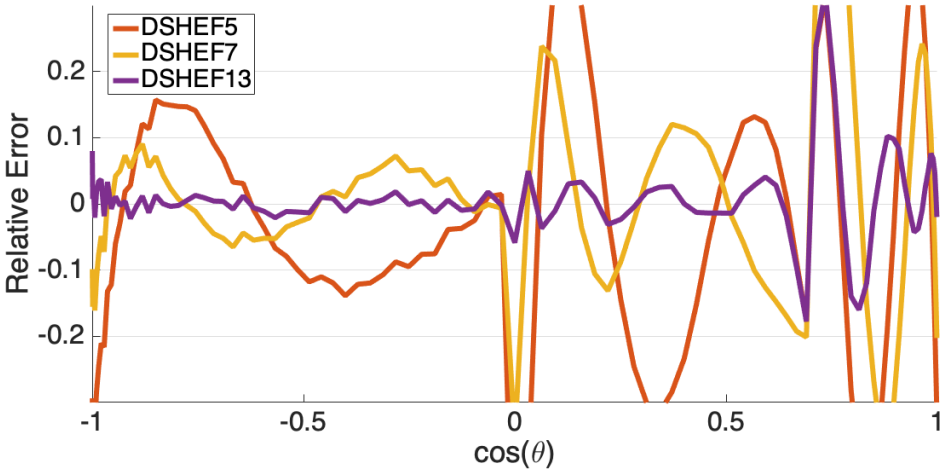

Figure 4.32: Relative Error for Radiance vs $\cos(\theta)$ near medium surface, highly scattering bottom layer, $f_x = 0.3/l^*$, $z^* = 0.1l*$. DSHEF_3 is given in blue, DSHEF_5 is given in orange, DSHEF_7 is given in gold, DSHEF_{13} is given in purple, single SHEF_{13} is given in green.

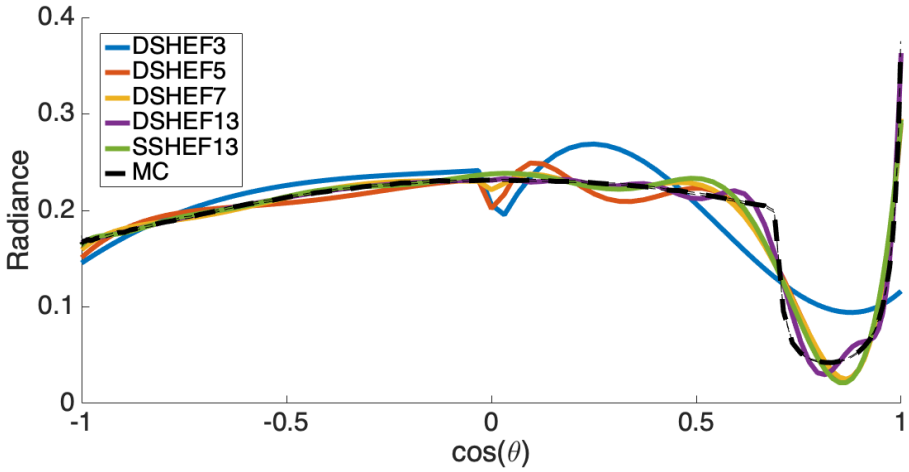

Figure 4.33: Radiance vs $\cos(\theta)$ near medium surface, highly scattering top layer, $f_x = 0$, $z^* = 1l*$. DSHEF_3 is given in blue, DSHEF_5 is given in orange, DSHEF_7 is given in gold, DSHEF_{13} is given in purple, single SHEF_{13} is given in green and MC is given in dashed black. Error bars for the MC results are $\pm 3\sigma$.

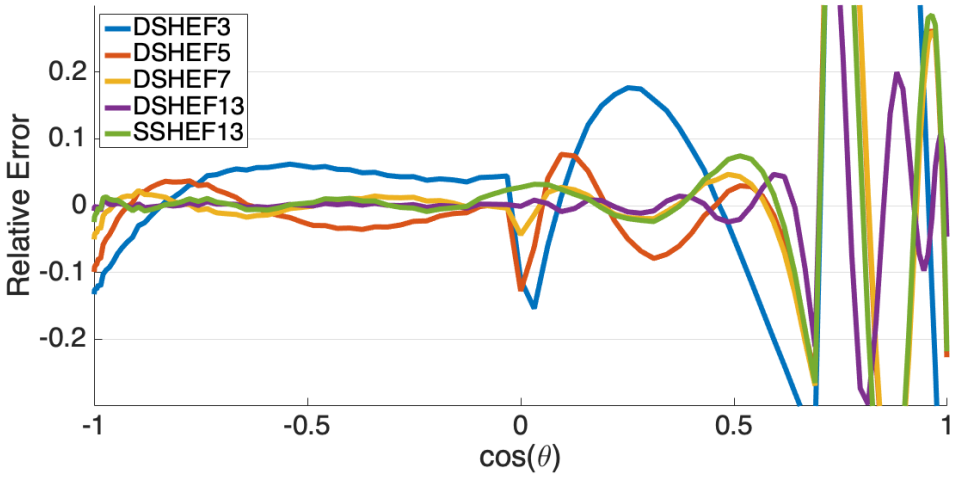

Figure 4.34: Relative Error for Radiance vs $\cos(\theta)$ near medium surface, highly scattering top layer, $f_x = 0$, $z^* = 1l*$. DSHEF_3 is given in blue, DSHEF_5 is given in orange, DSHEF_7 is given in gold, DSHEF_{13} is given in purple, single SHEF_{13} is given in green.

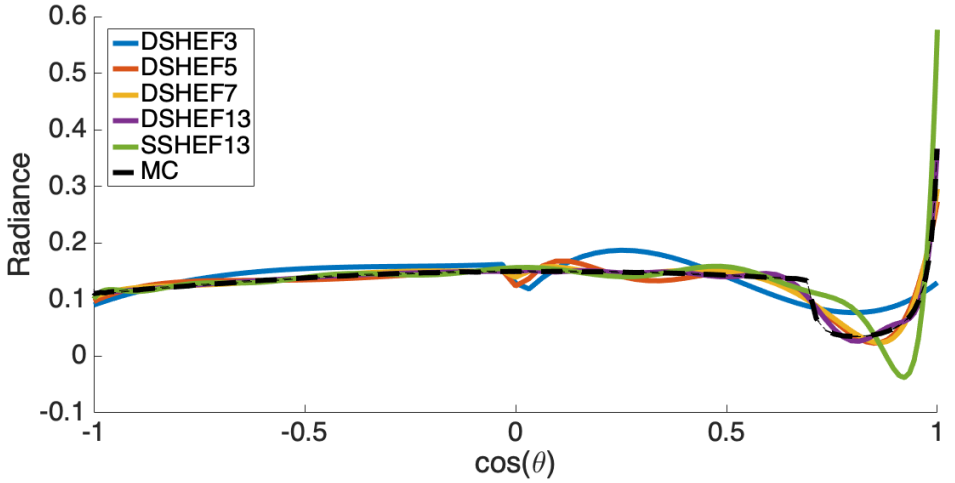

Figure 4.35: Radiance vs $\cos(\theta)$ near medium surface, highly scattering top layer, $f_x = 0.1/l^*$, $z^* = 1l*$. DSHEF_3 is given in blue, DSHEF_5 is given in orange, DSHEF_7 is given in gold, DSHEF_{13} is given in purple, single SHEF_{13} is given in green and MC is given in dashed black. Error bars for the MC results are $\pm 3\sigma$.

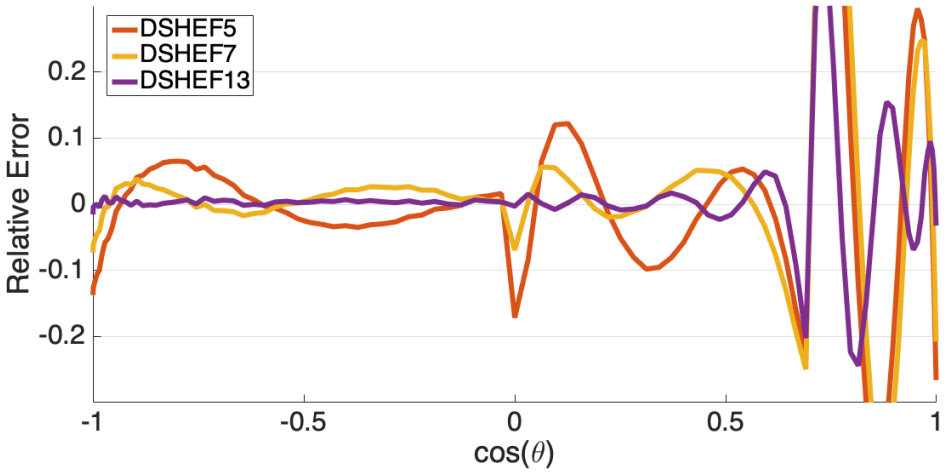

Figure 4.36: Relative Error for Radiance vs $\cos(\theta)$ near medium surface, highly scattering top layer, $f_x = 0.1/l^*$, $z^* = 1l*$. DSHEF_3 is given in blue, DSHEF_5 is given in orange, DSHEF_7 is given in gold, DSHEF_{13} is given in purple, single SHEF_{13} is given in green.

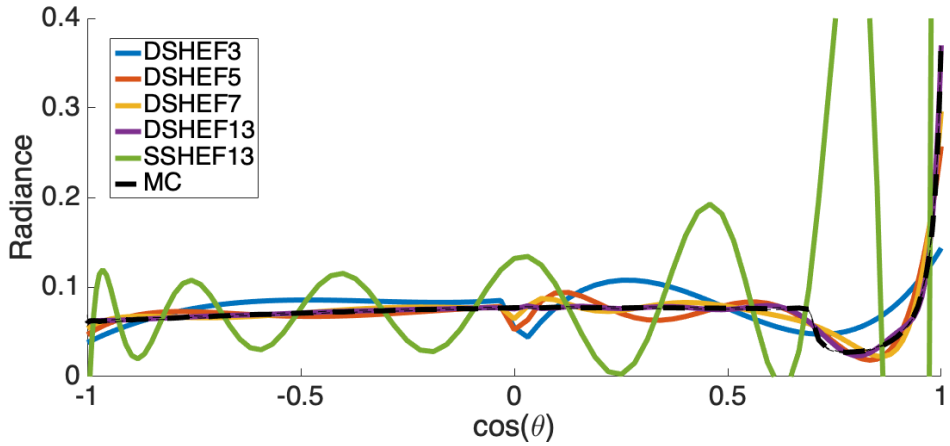

Figure 4.37: Radiance vs $\cos(\theta)$ near medium surface, highly scattering top layer, $f_x = 0.2/l^*$, $z^* = 1l*$. DSHEF_3 is given in blue, DSHEF_5 is given in orange, DSHEF_7 is given in gold, DSHEF_{13} is given in purple, single SHEF_{13} is given in green and MC is given in dashed black. Error bars for the MC results are $\pm 3\sigma$.

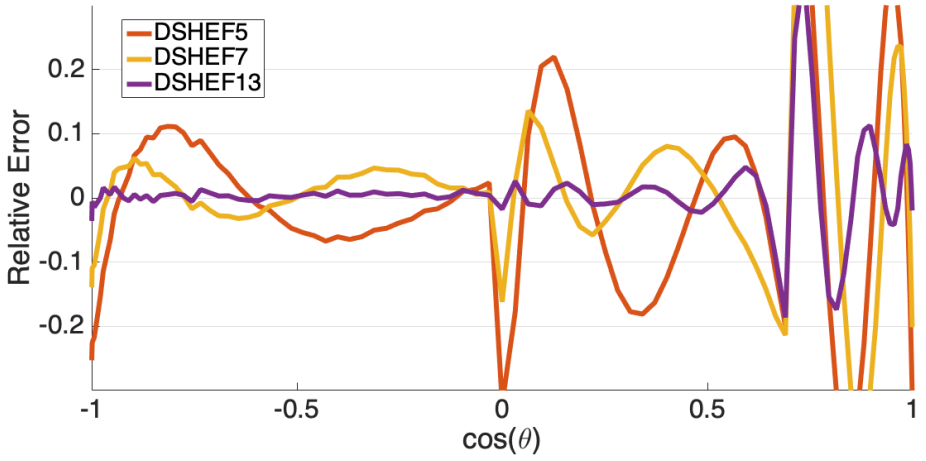

Figure 4.38: Relative Error for Radiance vs $\cos(\theta)$ near medium surface, highly scattering top layer, $f_x = 0.2/l^*$, $z^* = 1l*$. DSHEF_3 is given in blue, DSHEF_5 is given in orange, DSHEF_7 is given in gold, DSHEF_{13} is given in purple, single SHEF_{13} is given in green.

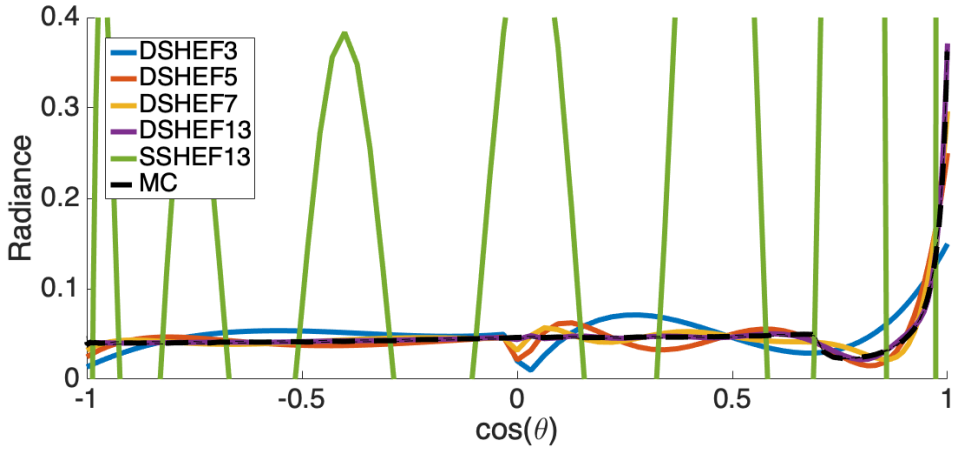

Figure 4.39: Radiance vs $\cos(\theta)$ near medium surface, highly scattering top layer, $f_x = 0.3/l^*$, $z^* = 1l*$. DSHEF_3 is given in blue, DSHEF_5 is given in orange, DSHEF_7 is given in gold, DSHEF_{13} is given in purple, single SHEF_{13} is given in green and MC is given in dashed black. Error bars for the MC results are $\pm 3\sigma$.

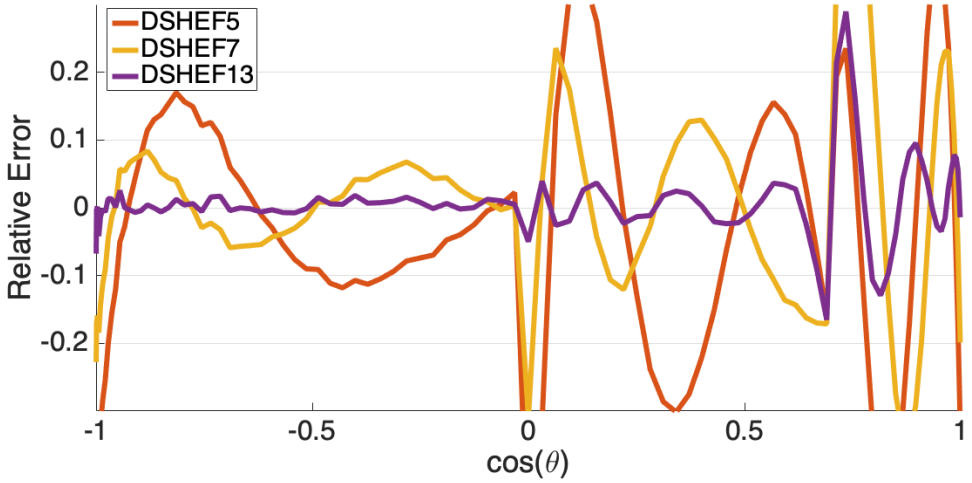

Figure 4.40: Relative Error for Radiance vs $\cos(\theta)$ near medium surface, highly scattering top layer, $f_x = 0.3/l^*$, $z^* = 1l*$. DSHEF_3 is given in blue, DSHEF_5 is given in orange, DSHEF_7 is given in gold, DSHEF_{13} is given in purple, single SHEF_{13} is given in green.

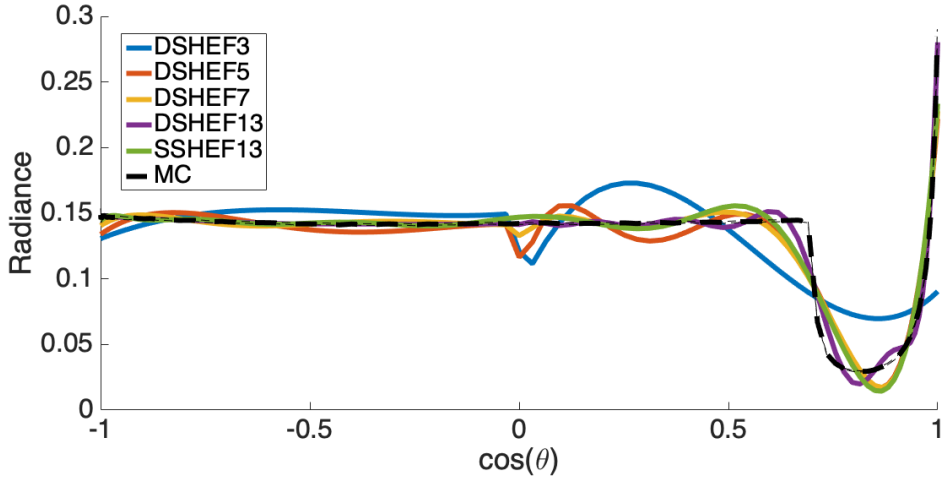

Figure 4.41: Radiance vs $\cos(\theta)$ near medium surface, highly scattering bottom layer, $f_x = 0$, $z^* = 1l*$. DSHEF_3 is given in blue, DSHEF_5 is given in orange, DSHEF_7 is given in gold, DSHEF_{13} is given in purple, single SHEF_{13} is given in green and MC is given in dashed black. Error bars for the MC results are $\pm 3\sigma$.

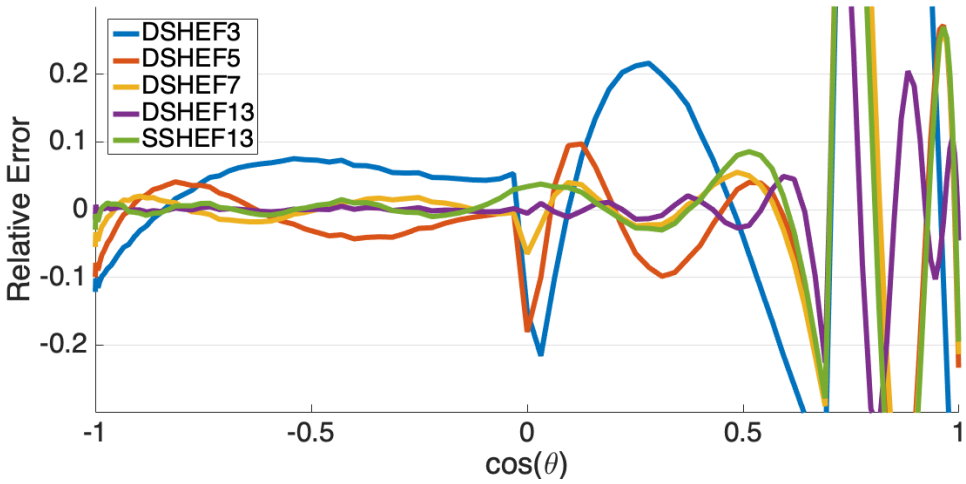

Figure 4.42: Relative Error for Radiance vs $\cos(\theta)$ near medium surface, highly scattering bottom layer, $f_x = 0$, $z^* = 1l*$. DSHEF_3 is given in blue, DSHEF_5 is given in orange, DSHEF_7 is given in gold, DSHEF_{13} is given in purple, single SHEF_{13} is given in green.

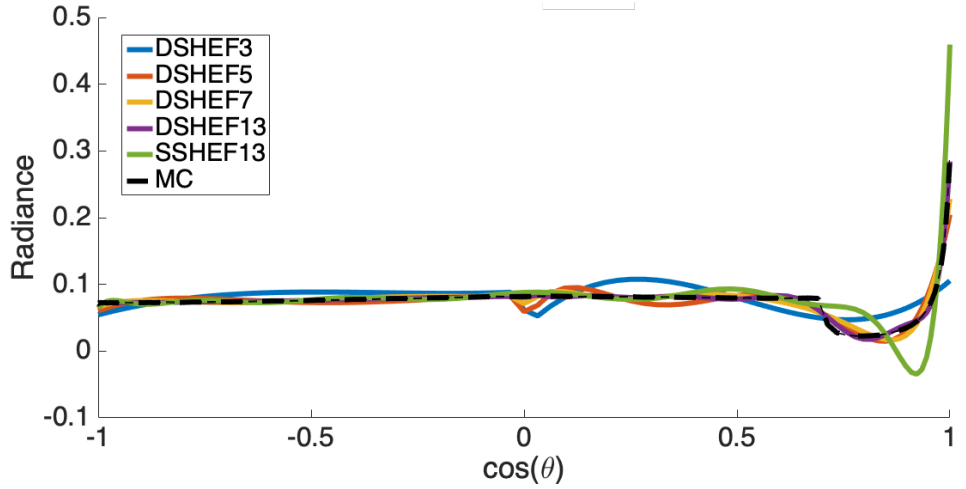

Figure 4.43: Radiance vs $\cos(\theta)$ near medium surface, highly scattering bottom layer, $f_x = 0.1/l^*$, $z^* = 1l*$. DSHEF_3 is given in blue, DSHEF_5 is given in orange, DSHEF_7 is given in gold, DSHEF_{13} is given in purple, single SHEF_{13} is given in green and MC is given in dashed black. Error bars for the MC results are $\pm 3\sigma$.

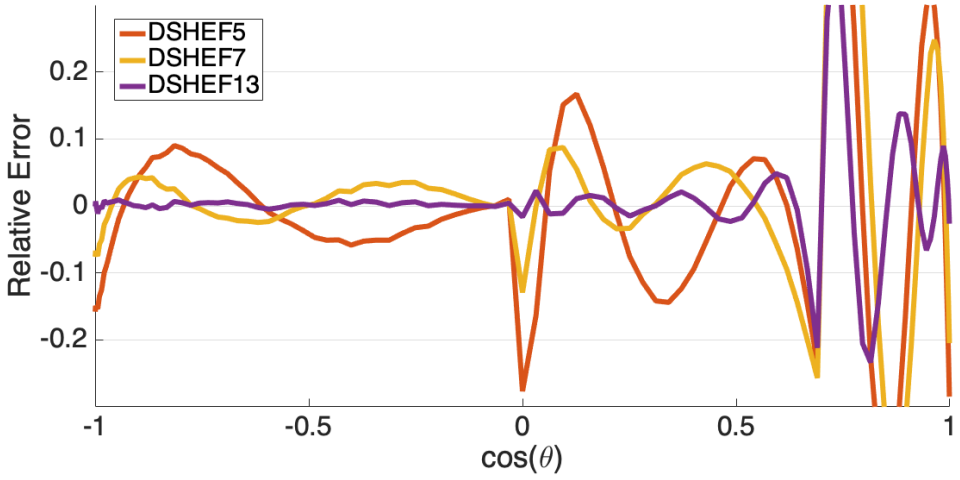

Figure 4.44: Relative Error for Radiance vs $\cos(\theta)$ near medium surface, highly scattering bottom layer, $f_x = 0.1/l^*$, $z^* = 1l*$. DSHEF_3 is given in blue, DSHEF_5 is given in orange, DSHEF_7 is given in gold, DSHEF_{13} is given in purple, single SHEF_{13} is given in green.

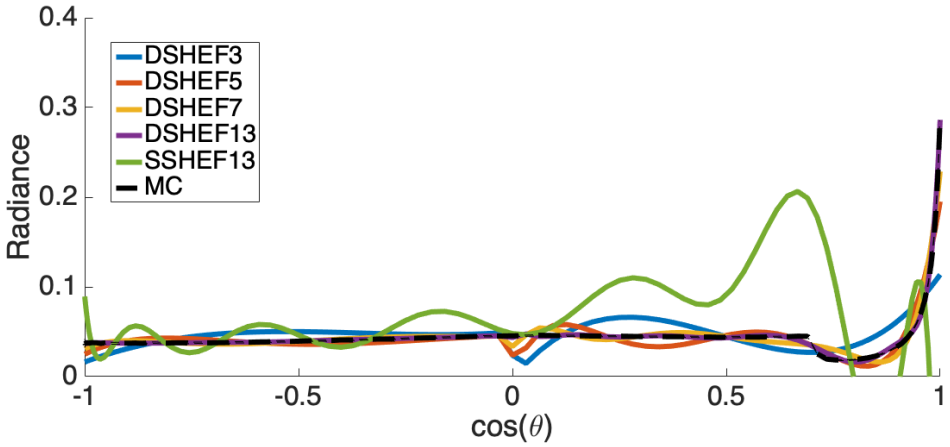

Figure 4.45: Radiance vs $\cos(\theta)$ near medium surface, highly scattering bottom layer, $f_x = 0.2/l^*$, $z^* = 1l*$. DSHEF_3 is given in blue, DSHEF_5 is given in orange, DSHEF_7 is given in gold, DSHEF_{13} is given in purple, single SHEF_{13} is given in green and MC is given in dashed black. Error bars for the MC results are $\pm 3\sigma$.

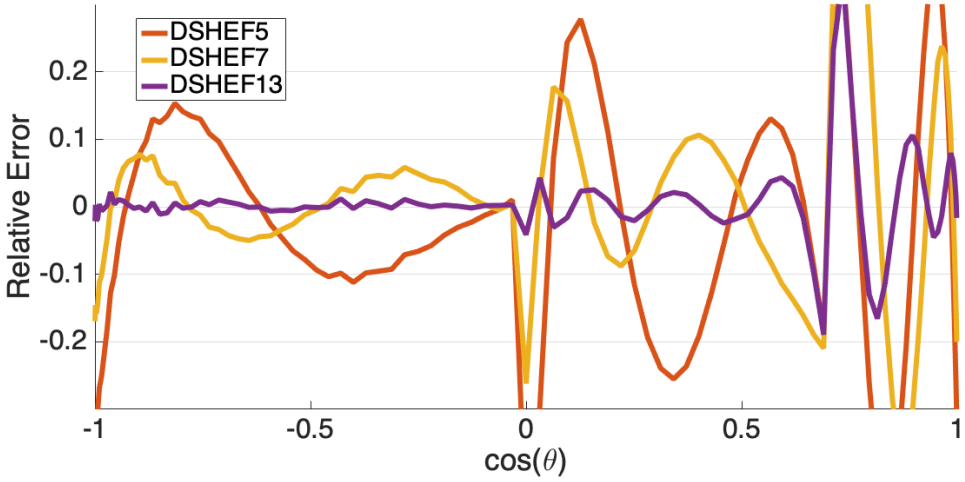

Figure 4.46: Relative Error for Radiance vs $\cos(\theta)$ near medium surface, highly scattering bottom layer, $f_x = 0.2/l^*$, $z^* = 1l*$. DSHEF_3 is given in blue, DSHEF_5 is given in orange, DSHEF_7 is given in gold, DSHEF_{13} is given in purple, single SHEF_{13} is given in green.

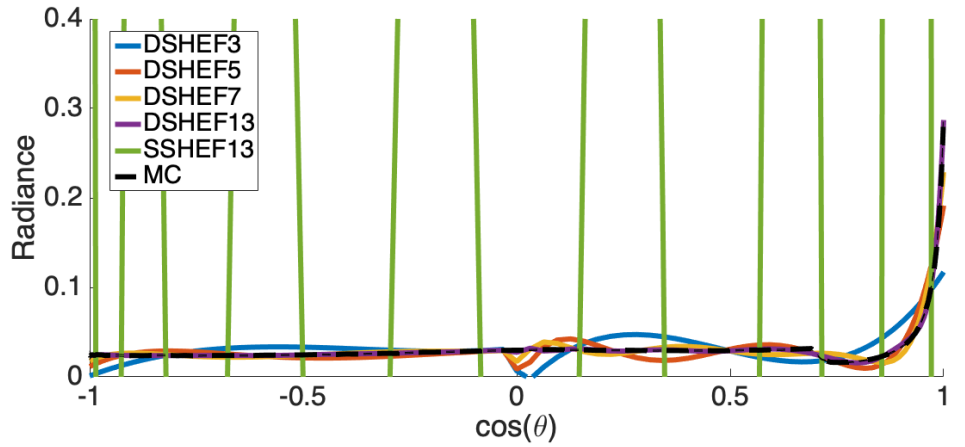

Figure 4.47: Radiance vs $\cos(\theta)$ near medium surface, highly scattering bottom layer, $f_x = 0.3/l^*$, $z^* = 1l*$. DSHEF_3 is given in blue, DSHEF_5 is given in orange, DSHEF_7 is given in gold, DSHEF_{13} is given in purple, single SHEF_{13} is given in green and MC is given in dashed black. Error bars for the MC results are $\pm 3\sigma$.

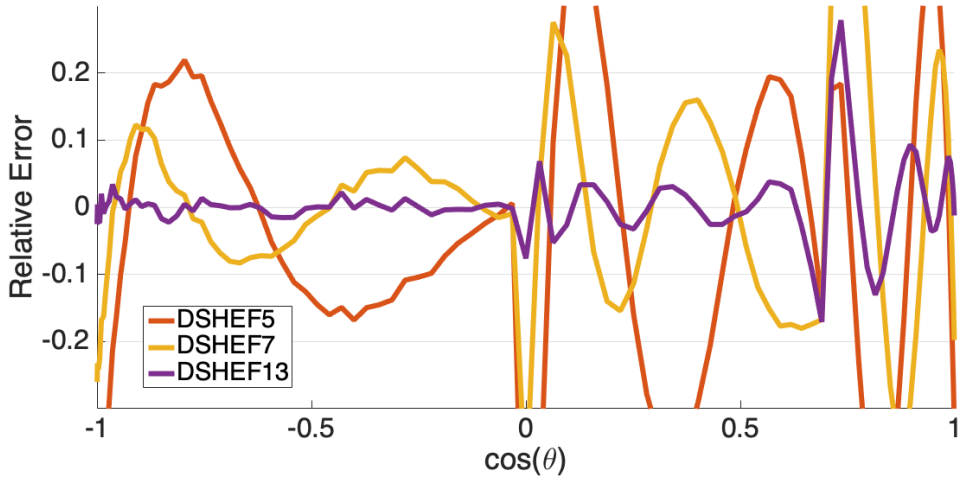

Figure 4.48: Relative Error for Radiance vs $\cos(\theta)$ near medium surface, highly scattering bottom layer, $f_x = 0.3/l^*$, $z^* = 1l*$. DSHEF_3 is given in blue, DSHEF_5 is given in orange, DSHEF_7 is given in gold, DSHEF_{13} is given in purple, single SHEF_{13} is given in green.

(purple), as well as single SHEF_{13} (green) for a comparison to an existing best practice. A 10M photon packet discrete absorption weight Monte Carlo simulation (dashed black) is included as a gold standard, with error lines of $\pm 3\sigma$. In the cases of DSHEF_7 and Monte Carlo, the data shown corresponds to the top lines of the heat maps shown in Figs 4.1–16.

The depth $z = 0.025$ was chosen because it was the closest depth to the surface that the Monte Carlo Software measured. The Monte Carlo method used splits the medium into bins in terms of depth and spatial frequency, with the top of the highest bin located at $z = 0$.

In each of these figures, the influence non-differentiable angle for internal reflection at $z = 0$ is shown. Since the medium's refractive index is 1.4 and all space in the $z < 0$ half space has a refractive index of 1 and no scattering or absorption (it behaves as ideal air), the cosine of this critical angle at which this function is non-differentiable is given by Snell's Law to be approximately 0.700.

Figs 4.17–18, 4.25–26, 4.33–34 and 4.41–42 all give results with $f_x = 0$. In these, single SHEF_{13} performs quite strongly, not even requiring sequential order smoothing. Its error

rates for negative $\cos(\theta)$ are within ± 0.03. DSHEF_7, on the other hand, occasionally has larger errors, though generally within ± 0.04. I mention this because DSHEF_N has qualitatively similar resolution in terms of polar angle to single SHEF_{2N}, so it may be expected that DSHEF_7 would outperform single SHEF_{2N}. The fact that DSHEF_{13} has smaller errors still, generally within ± 0.01 or less, is not surprising. For positive $\cos(\theta)$, all methods exhibit larger errors, particularly for $\cos(\theta)$ ¿ 0.7. Again, this is due to the effect of the critical angle for internal reflection. It should be noted about DSHEF_N in general in these plots is that for all values of $cos(\theta)$, relative error to Monte Carlo decreases strongly as N increases. This convergence is a key goal of DSHEF_N, or indeed any spectral method.

Figs 4.19–20, 4.27–28, 4.35–36 and 4.43–44 all show results with a spatial frequency of $0.1/l^*$. This is where the advantage of DSHEF_N begins to be seen relative to single SHEF_N. Single SHEF_{13} actually becomes negative for a range of $\cos(\theta)$ near 0.9. Furthermore, relative errors of this method begin to eclipse those of DSHEF_7, though both remain within ± 0.05 for $\cos(\theta)$ ¡ 0. As $\cos(\theta)$ increases beyond zero, relative error for single SHEF_7 grows beyond that of any method measured, even DSHEF_3, which itself is shown to have a very poor response compared to its higher order cousins. The same phenomenon of convergence seen when spatial frequency = 0 appears for DSHEF_N in these figures, with values converging to the Monte Carlo results.

Figs 4.21–22, 4.29–30, 4.37–38 and 4.45–46 all show results with spatial frequencies of $0.2/l^*$. In these, it is clear that single SHEF_{13} is experiencing severe problems. The oscillatory error present in all of these spectral methods is orders of magnitude larger than the actual signal. However, error for DSHEF_N has experienced much smaller growth compared to results using smaller spatial frequencies. Error for DSHEF_N when $N \geq 5$ is generally within ± 0.1, with small departures from this shown in each error figure. Larger departures are shown in 4.22, which is the most difficult case for DSHEF_N, having a less scattering bottom layer ($\mu_s'/\mu_a = 3$) as well as a thin ($z^* = 0.1$) top layer. In each of these plots, however, the

same convergence phenomena is shown for DSHEF_N. This convergence is slower for $\cos(\theta)$ between 0.5 and 1, due to internal reflection, but it still exists.

Finally, Figs 4.23–24, 4.31–32, 4.39–40 and 4.47–48 all show results for simulations with the same optical properties, but spatial frequencies of $0.3/l^*$. In these, the problems experiences by SSHEF_{13} with a spatial frequency of $0.2/l^*$ continue to worsen, showing that the method is far past its point of usefulness in reconstructing angular radiance at a specific spatial frequency. Meanwhile, the same convergence phenomenon continues to be exhibited for DSHEF_N. In particular, however, it should be noted that convergence is slower in these cases than in any other presented. This shows a strong impact of spatial frequency on convergence.

Throughout each of these permutations of optical properties, top layer thickness and spatial frequency, DSHEF_N shows convergence to a Monte Carlo gold standard. Conversely, single SHEF_N performs strongly when $f_x = 0$ but experiences extreme error as f_x increases beyond $0.1/l^*$.

4.6.3 Reflectance vs Spatial Frequency

The even numbered figures from Fig 4.49–55 show reflectance as a function of spatial frequency f_x from $f_x = 0$ to $f_x = 1/l^*$. As in previous subsections, top layer thicknesses are either $0.1l^*$ or $1l^*$. Each simulation features a medium with a top layer ratio of $\mu_s'/\mu_a = 100$ and a bottom layer ratio of $\mu_s'/\mu_a = 3$ or vice versa.

Results are shown for DSHEF_3 (blue), DSHEF_5 (orange), DSHEF_7 (gold) and DSHEF_{13} (purple), as well as single SHEF_{13} (green) for a comparison to an existing best practice. A 10M photon packet discrete absorption weight Monte Carlo simulation (dashed black) is included as a gold standard, with error lines of $\pm 3\sigma$.

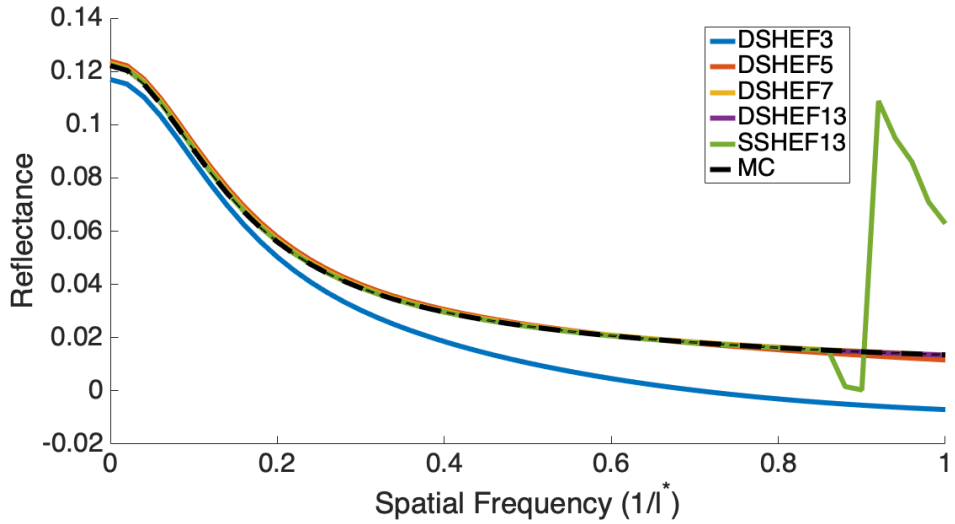

Figure 4.49: Reflectance vs Spatial Frequency, $z^* = 0.1l^*$, top layer $\mu_s'/\mu_a = 100$, bottom layer $\mu_s'/\mu_a = 3$. DSHEF_3 is given in blue, DSHEF_5 is given in orange, DSHEF_7 is given in gold, DSHEF_{13} is given in purple, single SHEF_{13} is given in green and Monte Carlo is given in dashed black. Error bars for the MC results are $\pm 3\sigma$.

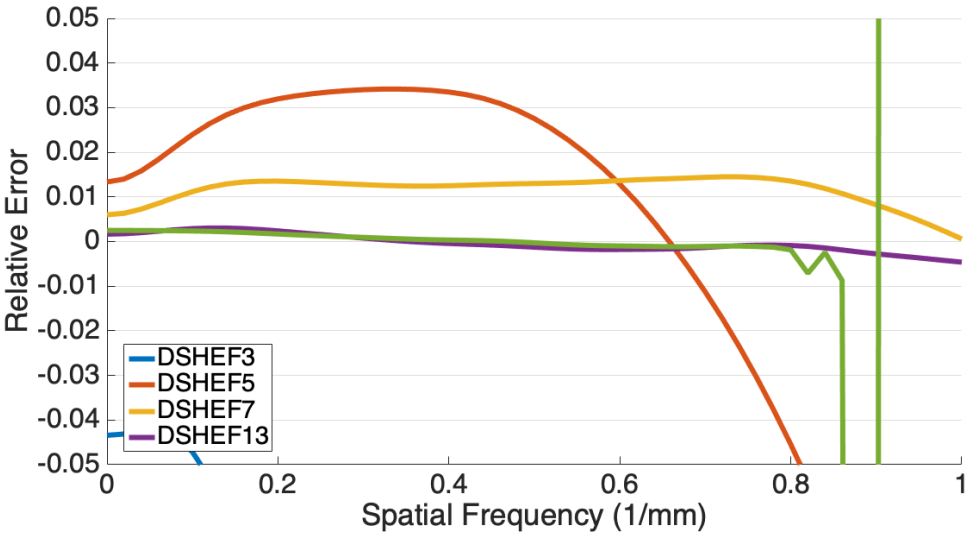

Figure 4.50: Relative Error of Reflectance vs Spatial Frequency, $z^* = 0.1l^*$, top layer $\mu_s'/\mu_a = 100$, bottom layer $\mu_s'/\mu_a = 3$. DSHEF_3 is given in blue, DSHEF_5 is given in orange, DSHEF_7 is given in gold, DSHEF_{13} is given in purple, single SHEF_{13} is given in green.

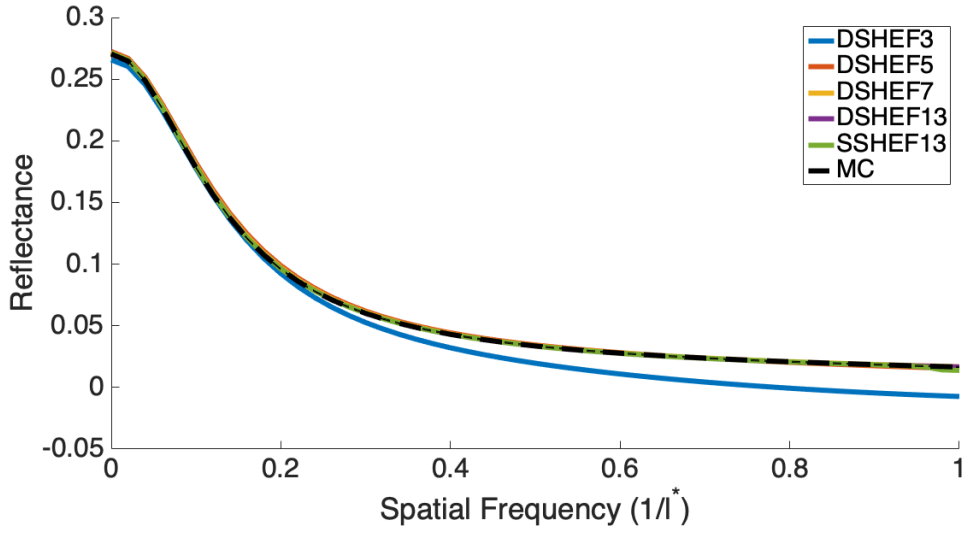

Figure 4.51: Reflectance vs Spatial Frequency, $z^* = 1l^*$, top layer $\mu_s'/\mu_a = 100$, bottom layer $\mu_s'/\mu_a = 3$. DSHEF_3 is given in blue, DSHEF_5 is given in orange, DSHEF_7 is given in gold, DSHEF_{13} is given in purple, single SHEF_{13} is given in green and Monte Carlo is given in dashed black. Error bars for the MC results are $\pm 3\sigma$.

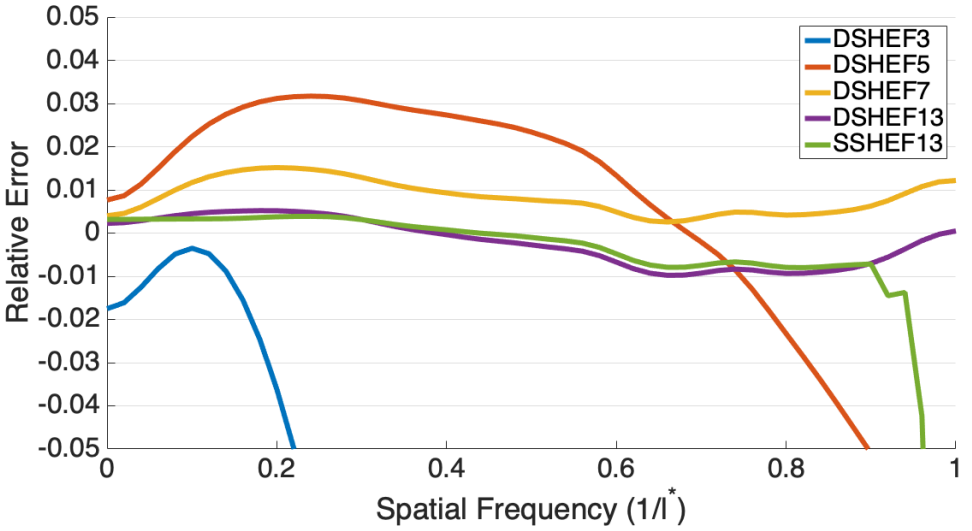

Figure 4.52: Relative Error of Reflectance vs Spatial Frequency, $z^* = 1l^*$, top layer $\mu_s'/\mu_a = 100$, bottom layer $\mu_s'/\mu_a = 3$. DSHEF_3 is given in blue, DSHEF_5 is given in orange, DSHEF_7 is given in gold, DSHEF_{13} is given in purple, single SHEF_{13} is given in green.

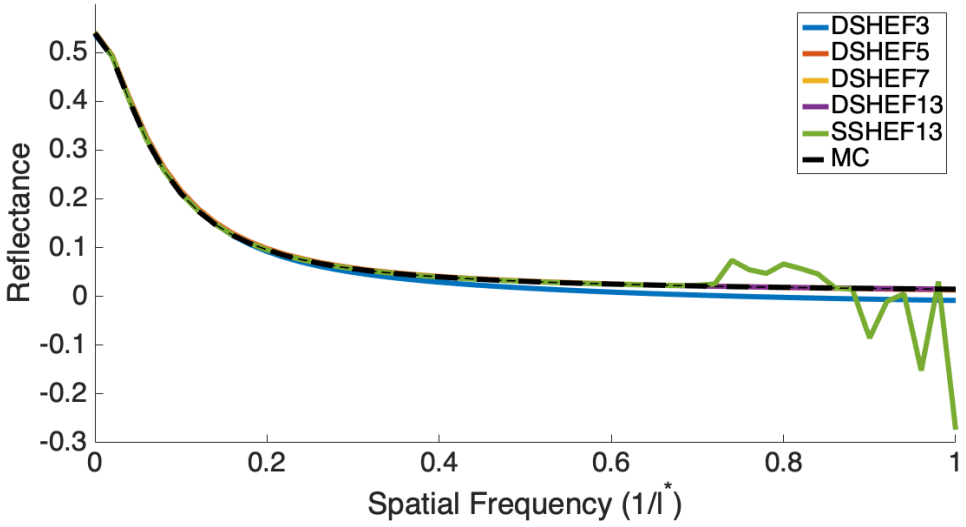

Figure 4.53: Reflectance vs Spatial Frequency, $z^* = 0.1l^*$, top layer $\mu_s'/\mu_a = 3$, bottom layer $\mu_s'/\mu_a = 100$. DSHEF_3 is given in blue, DSHEF_5 is given in orange, DSHEF_7 is given in gold, DSHEF_{13} is given in purple, single SHEF_{13} is given in green and Monte Carlo is given in dashed black. Error bars for the MC results are $\pm 3\sigma$.

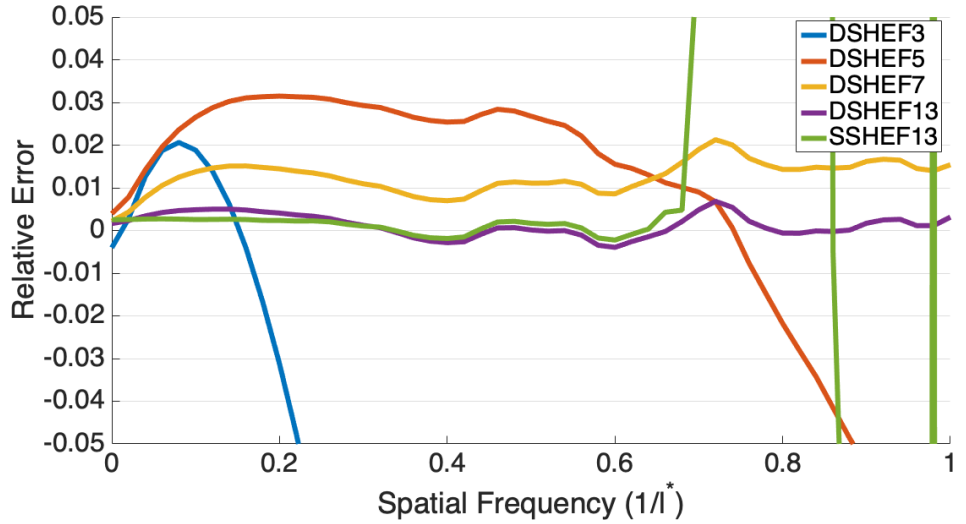

Figure 4.54: Relative Error of Reflectance vs Spatial Frequency, $z^* = 0.1l^*$, top layer $\mu_s'/\mu_a = 3$, bottom layer $\mu_s'/\mu_a = 3$. $\text{DSHEF}_1 00$ is given in blue, DSHEF_5 is given in orange, DSHEF_7 is given in gold, DSHEF_{13} is given in purple, single SHEF_{13} is given in green.

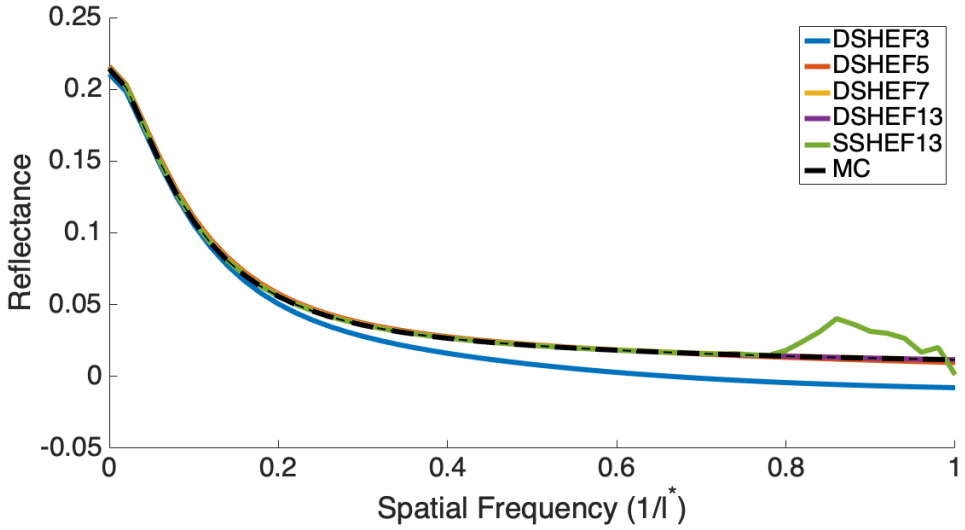

Figure 4.55: Reflectance vs Spatial Frequency, $z^* = 1l^*$, top layer $\mu_s'/\mu_a = 3$, bottom layer $\mu_s'/\mu_a = 100$. DSHEF_3 is given in blue, DSHEF_5 is given in orange, DSHEF_7 is given in gold, DSHEF_{13} is given in purple, single SHEF_{13} is given in green and Monte Carlo is given in dashed black. Error bars for the MC results are $\pm 3\sigma$.

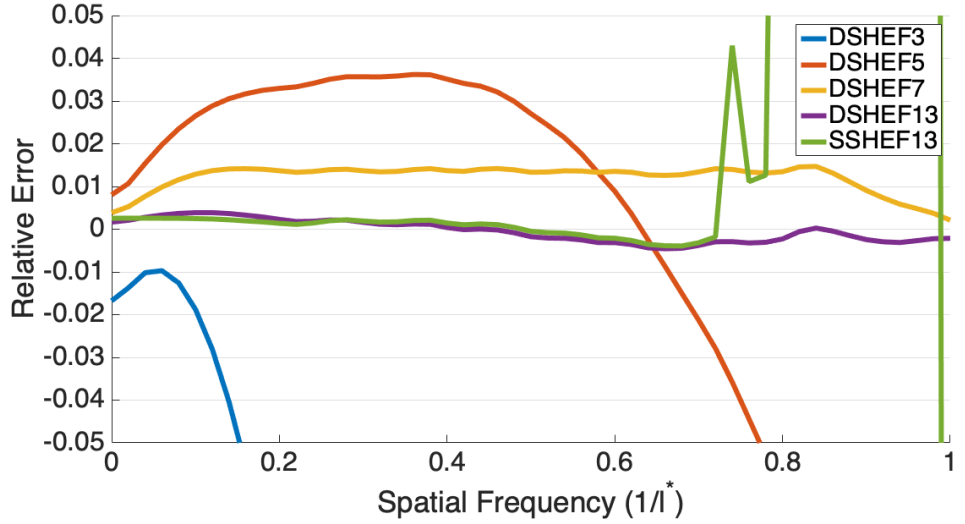

Figure 4.56: Relative Error of Reflectance vs Spatial Frequency, $z^* = 1l^*$, top layer $\mu_s'/\mu_a = 3$, bottom layer $\mu_s'/\mu_a = 100$. DSHEF_3 is given in blue, DSHEF_5 is given in orange, DSHEF_7 is given in gold, DSHEF_{13} is given in purple, single SHEF_{13} is given in green.

Figs 4.49–52 show results and relative error for media with a highly scattering ($\mu_s'/\mu_a = 100$) top layer and a less scattering ($\mu_s'/\mu_a = 3$) bottom layer. Figs 4.49–50 show results and relative error using media with a thin ($z^* = 0.1l^*$) top layer, while Figs 4.51–52 show results and relative error using media with a thick ($z^* = 1l^*$) top layer. In each case, single SHEF_{13} shows relative errors within ± 0.005 for spatial frequencies $f_x < 0.9/l^*$. However, extreme error occurs for spatial frequencies higher than this range.

In contrast, DSHEF_7 does not provide error rates as low as those of single SHEF_{13} as one may expect because of the theoretically comperable resolution of polar angle. DSHEF_7's relative error rates range between 0 and 0.015 and are entirely in the form of overestimation, but it does not experience the same extreme error for spatial frequencies above $0.9/l^*$. DSHEF_5 shows increasing relative error as spatial frequencies approach ll^*, but it is far less extreme and does not display the same breakdown as single SHEF_{13}. DSHEF_7 and DSHEF_{13} do not show

In each of these figures, it is shown that DSHEF_3 experiences very poor accuracy compared to higher order versions, showing that this order of expansion is not fit for applications based on reflectance as a function of spatial frequency. However, DSHEF_N shows convergence as N increases, with relative errors between -0.005 and 0.015 regardless of the option chosen for top layer thickness. DSHEF_{13} shows error rates comparable to those of SSHEF_{13}, but without the problematic behavior at spatial frequencies $f_x > 0.9/l^*$.

Figs 4.53–56 show results and relative error for media with a less highly scattering ($\mu_s'/\mu_a = 3$) bottom layer and a more highly scattering ($\mu_s'/\mu_a = 100$) bottom layer. Figs 4.53–54 show results and relative error using media with a thin ($z^* = 0.1l^*$) top layer, while Figs 4.55–56 show results and relative error using media with a thick ($z^* = 1l^*$) top layer.

In each case, single SHEF_{13} shows relative errors within ± 0.005 for spatial frequencies $f_x < 0.9/l^*$. However, extreme error occurs for spatial frequencies higher than this range.

The first thing to notice about Figs 4.53–56 is that single SHEF_{13} now experiences a breakdown in accuracy at spatial frequencies above $0.7/l^*$ for the thin top layer ($z^* = 0.1$) case. In the thick top layer ($z^* = 1$) case, however, this phenomenon does not occur.

In each case, DSHEF_3 shows underestimation compared to higher order expansions of DSHEF_N, with this underestimation becoming more pronounced as f_x increases, exceeding a relative error of -0.1 for spatial frequences above $0.2/l^*$. As in the cases displayed in Figs 4.49–52, DSHEF_5 shows overestimation just above 0.3 before switching to more extreme underestimation, which also exceeds a relative error of -0.1 as spatial frequency exceeds $0.9/l^*$ in the thick top layer ($z^* = 1l^*$) and as spatial frequency exceeds $0.8/l^*$. DSHEF_7 does not experience this drop off and maintains over estimations in the form of relative error between 0 and 0.02 in the thin ($z^* = 0.1l^*$) top layer case and between 0 and 0.015 in the thick ($z^* = 1l^*$) top layer case. DSHEF_{13} does not experience a significant bias toward over or underestimation for either case, but experiences relative error within ± 0.005, roughly consistent with that experienced by single SHEF_{13}. In each of these figures, as in Figs 4.49-52, the convergence of DSHEF_N to Monte Carlo results as N increases is shown for $0 \leq f_x \leq 1/l^*$.

It is important to note here that the breakdown seen by single SHEF_{13} in each case is not seen for simulations using single layered media, despite the fact that the same optical properties were tested in each case. This is an indication that the problematic behavior of single SHEF_{13} at higher spatial frequencies is linked strongly to either the expression of the boundary condition used or more complex media in general.

4.6.4 Fluence vs Depth

Fis 4.57–88 show fluence as a function of z for $0 < z < 5l^*$, as well as relative error thereof. As before, simulations used a 2 layer medium with one layer being more highly scattering ($\mu_s'/\mu_a = 100$) and one layer being less scattering ($\mu_s'/\mu_a = 3$). Top layer thicknesses

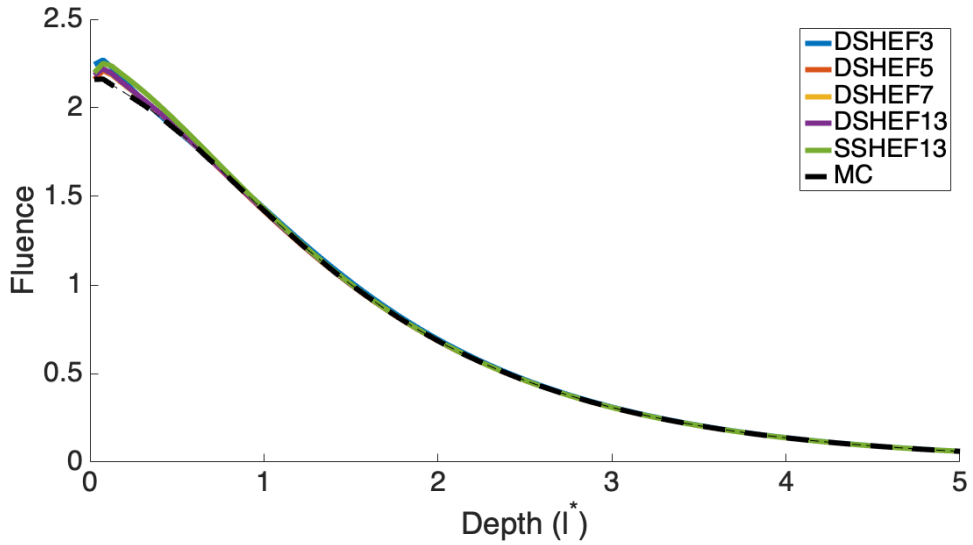

Figure 4.57: Fluence vs. Depth, $z^* = 0.1l^*$, top layer $\mu_s'/\mu_a = 100$, $f_x = 0$, bottom layer $\mu_s'/\mu_a = 3$. DSHEF_3 is given in blue, DSHEF_5 is given in orange, DSHEF_7 is given in gold, DSHEF_{13} is given in purple, single SHEF_{13} is given in green and Monte Carlo is given in dashed black. Error bars for the MC results are $\pm 3\sigma$.

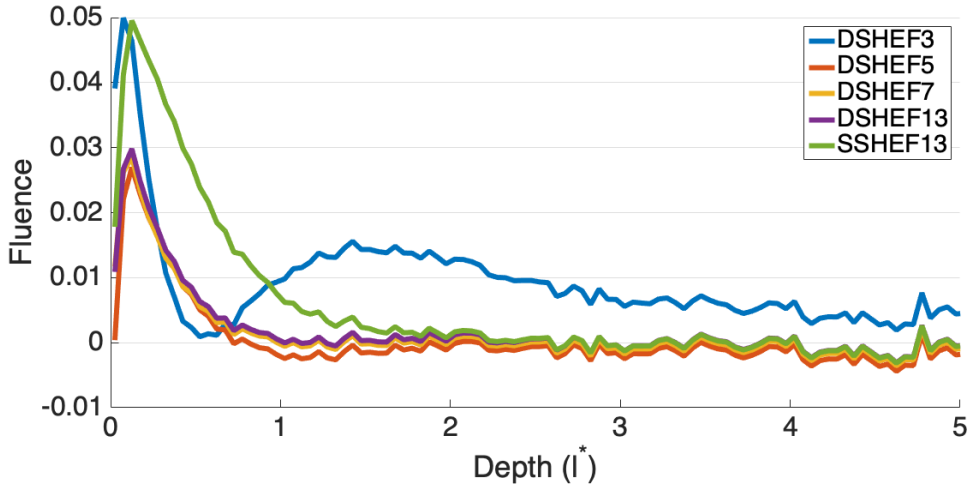

Figure 4.58: Relative Error of Fluence vs. Depth, $z^* = 0.1l^*$, top layer $\mu_s'/\mu_a = 100$, $f_x = 0$, bottom layer $\mu_s'/\mu_a = 3$. DSHEF_3 is given in blue, DSHEF_5 is given in orange, DSHEF_7 is given in gold, DSHEF_{13} is given in purple, single SHEF_{13} is given in green.

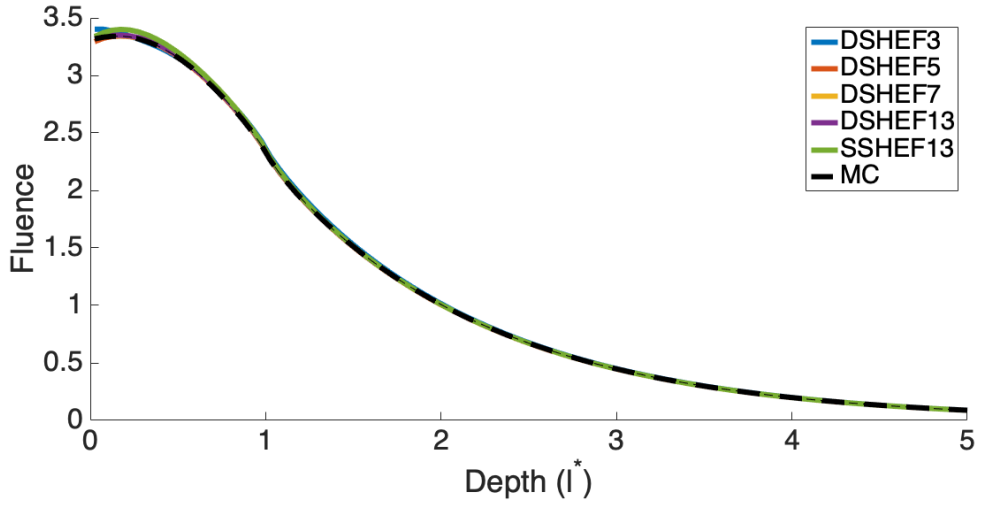

Figure 4.59: Fluence vs. Depth, $z^* = 0.1l^*$, $f_x = 0$, top layer $\mu_s'/\mu_a = 100$, bottom layer $\mu_s'/\mu_a = 3$. DSHEF_3 is given in blue, DSHEF_5 is given in orange, DSHEF_7 is given in gold, DSHEF_{13} is given in purple, single SHEF_{13} is given in green. and Monte Carlo is given in dashed black. Error bars for the MC results are $\pm 3\sigma$.

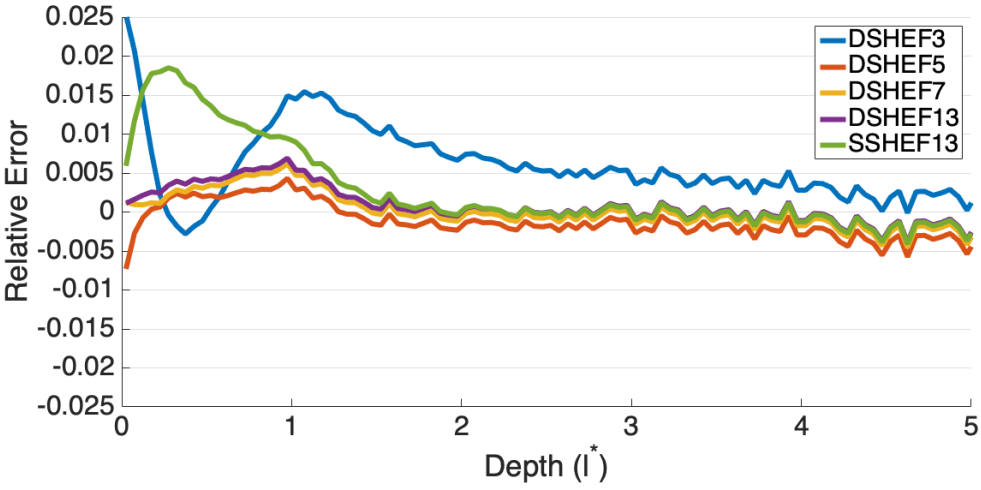

Figure 4.60: Relative Error of Fluence vs. Depth, $z^* = 0.1l^*$, $f_x = 0$, top layer $\mu_s'/\mu_a = 100$, bottom layer $\mu_s'/\mu_a = 3$. DSHEF_3 is given in blue, DSHEF_5 is given in orange, DSHEF_7 is given in gold, DSHEF_{13} is given in purple, single SHEF_{13} is given in green.

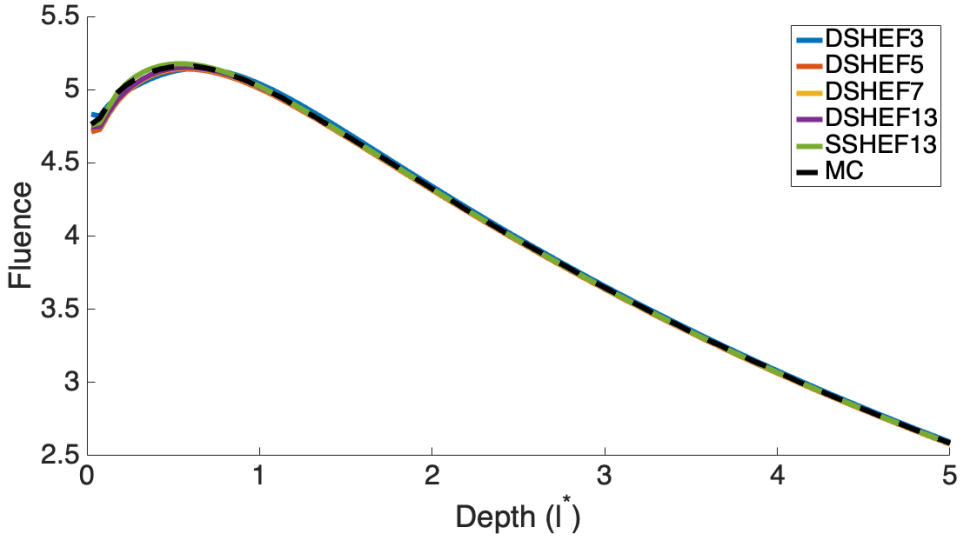

Figure 4.61: Fluence vs. Depth, $z^* = 0.1l^*$, $f_x = 0$, top layer $\mu_s'/\mu_a = 3$, bottom layer $\mu_s'/\mu_a = 100$. DSHEF_3 is given in blue, DSHEF_5 is given in orange, DSHEF_7 is given in gold, DSHEF_{13} is given in purple, single SHEF_{13} is given in green and Monte Carlo is given in dashed black. Error bars for the MC results are $\pm 3\sigma$.

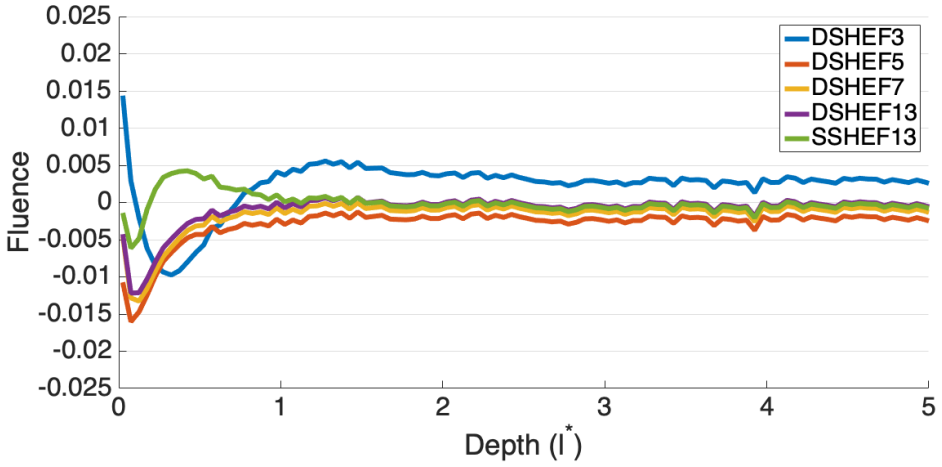

Figure 4.62: Relative Error of Fluence vs. Depth, $z^* = 0.1l^*$, $f_x = 0$, top layer $\mu_s'/\mu_a = 3$, bottom layer $\mu_s'/\mu_a = 100$. DSHEF_3 is given in blue, DSHEF_5 is given in orange, DSHEF_7 is given in gold, DSHEF_{13} is given in purple, single SHEF_{13} is given in green.

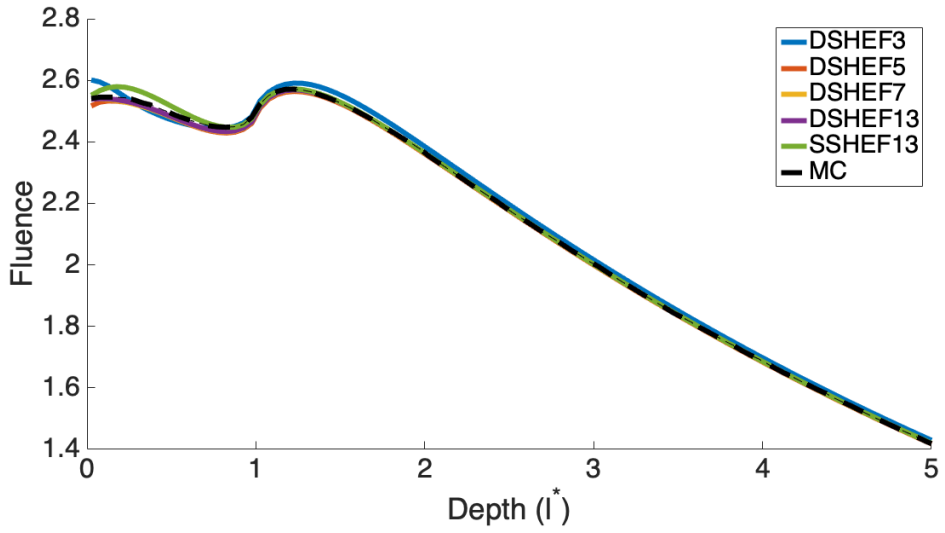

Figure 4.63: Fluence vs. Depth, $z^* = 0.1l^*$, $f_x = 0$, top layer $\mu_s'/\mu_a = 3$, bottom layer $\mu_s'/\mu_a = 100$. DSHEF_3 is given in blue, DSHEF_5 is given in orange, DSHEF_7 is given in gold, DSHEF_{13} is given in purple, single SHEF_{13} is given in green and Monte Carlo is given in dashed black. Error bars for the MC results are $\pm 3\sigma$.

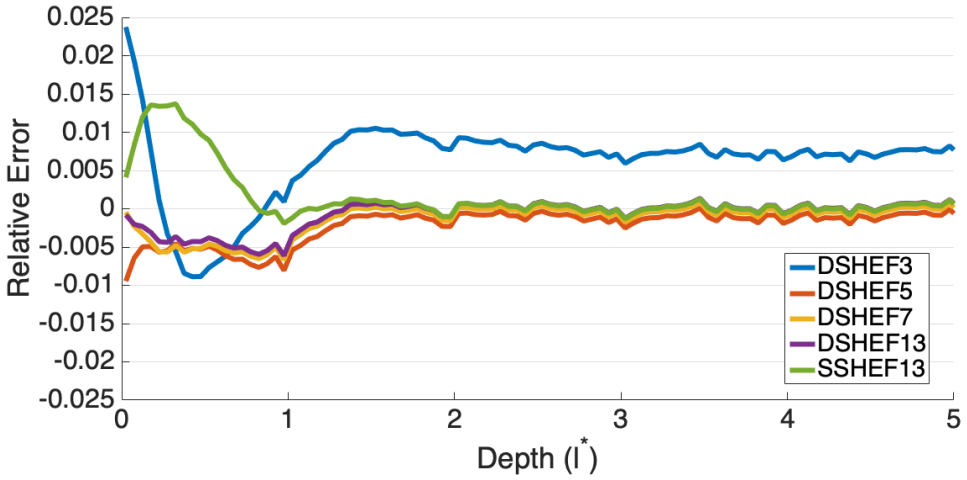

Figure 4.64: Relative Error of Fluence vs. Depth, $z^* = 0.1l^*$, $f_x = 0$, top layer $\mu_s'/\mu_a = 3$, bottom layer $\mu_s'/\mu_a = 100$. DSHEF_3 is given in blue, DSHEF_5 is given in orange, DSHEF_7 is given in gold, DSHEF_{13} is given in purple, single SHEF_{13} is given in green.

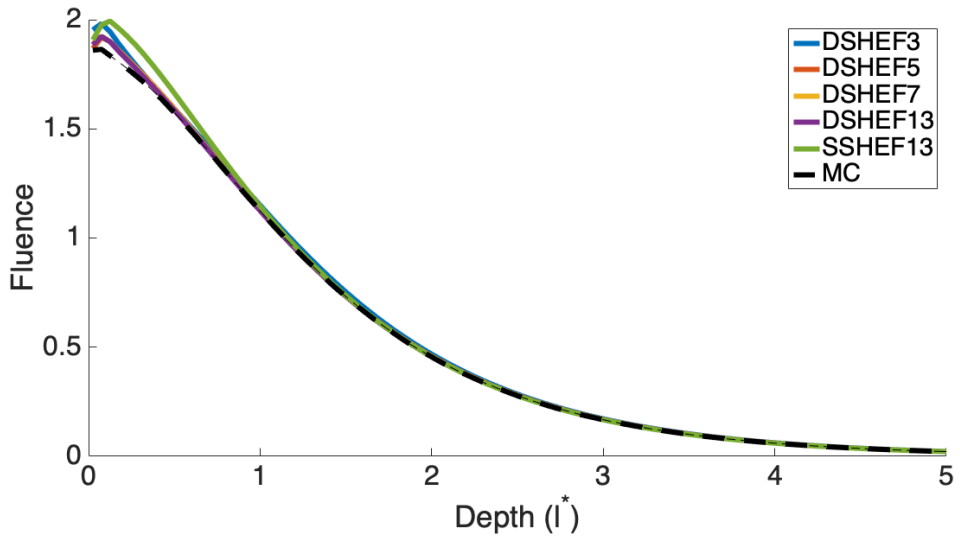

Figure 4.65: Fluence vs. Depth, $z^* = 0.1l^*$, $f_x = 0.1/l^*$, top layer $\mu_s'/\mu_a = 100$, bottom layer $\mu_s'/\mu_a = 3$. DSHEF_3 is given in blue, DSHEF_5 is given in orange, DSHEF_7 is given in gold, DSHEF_{13} is given in purple, single SHEF_{13} is given in green and Monte Carlo is given in dashed black. Error bars for the MC results are $\pm 3\sigma$.

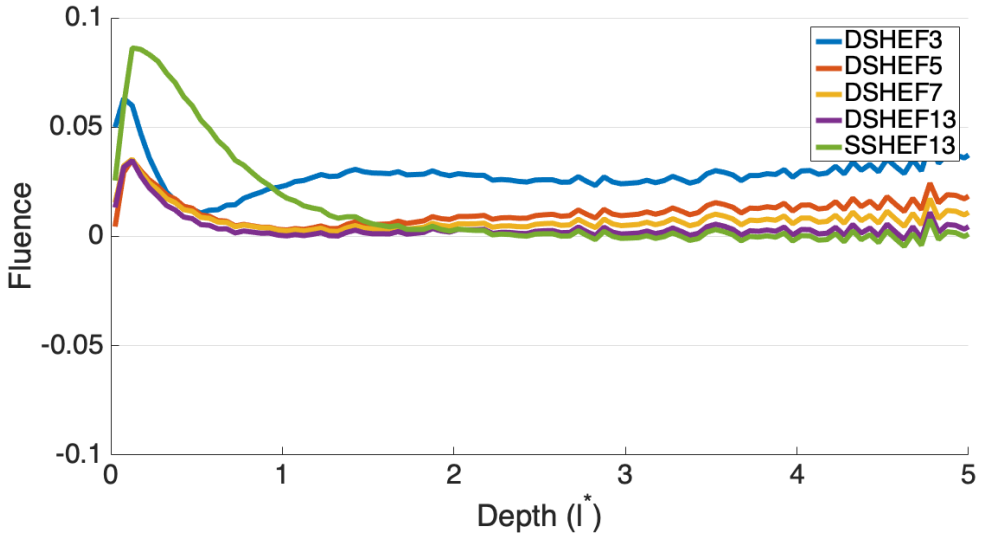

Figure 4.66: Relative Error of Fluence vs. Depth, $z^* = 0.1l^*$, $f_x = 0.1/l^*$, top layer $\mu_s'/\mu_a = 100$, bottom layer $\mu_s'/\mu_a = 3$. DSHEF_3 is given in blue, DSHEF_5 is given in orange, DSHEF_7 is given in gold, DSHEF_{13} is given in purple, single SHEF_{13} is given in green.

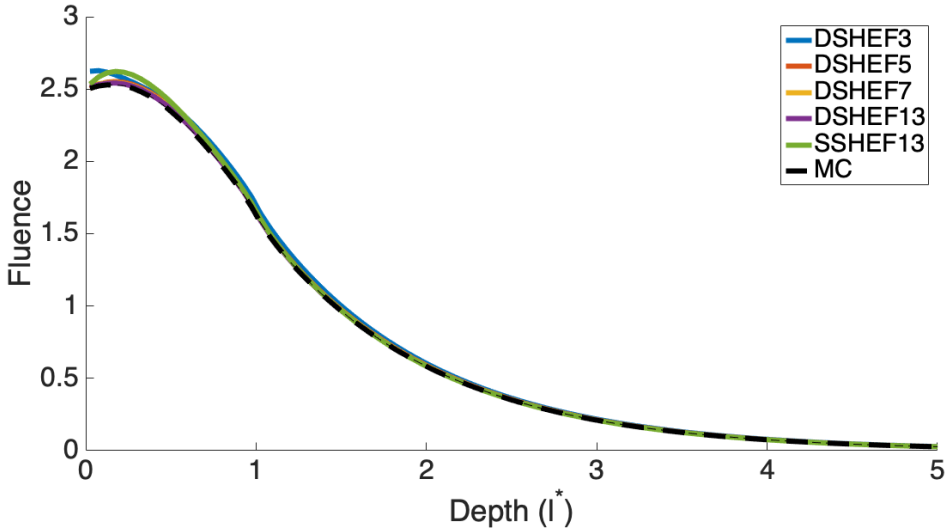

Figure 4.67: Fluence vs. Depth, $z^* = 0.1l^*$, $f_x = 0.1/l^*$, top layer $\mu_s'/\mu_a = 100$, bottom layer $\mu_s'/\mu_a = 3$. DSHEF_3 is given in blue, DSHEF_5 is given in orange, DSHEF_7 is given in gold, DSHEF_{13} is given in purple, single SHEF_{13} is given in green and Monte Carlo is given in dashed black. Error bars for the MC results are $\pm 3\sigma$.

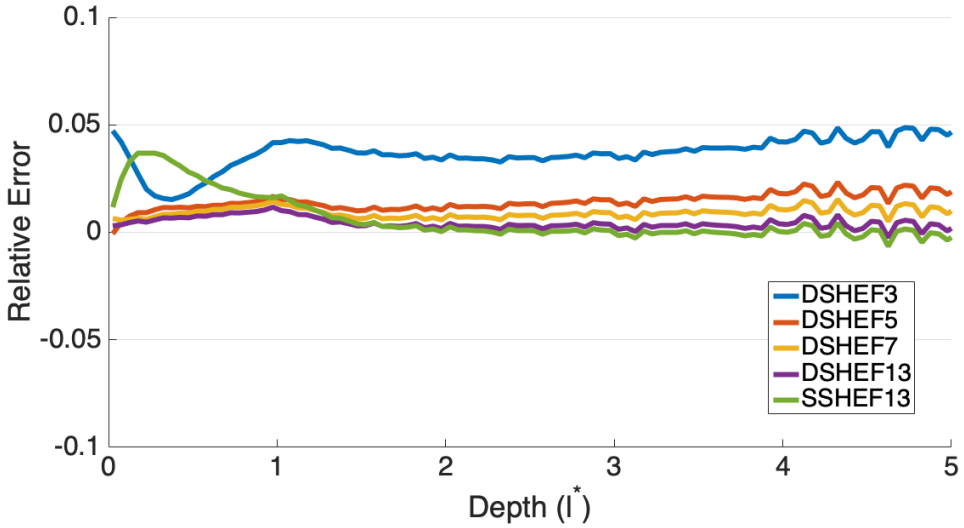

Figure 4.68: Relative Error of Fluence vs. Depth, $z^* = 0.1l^*$, $f_x = 0.1/l^*$, top layer $\mu_s'/\mu_a = 100$, bottom layer $\mu_s'/\mu_a = 3$. DSHEF_3 is given in blue, DSHEF_5 is given in orange, DSHEF_7 is given in gold, DSHEF_{13} is given in purple, single SHEF_{13} is given in green.

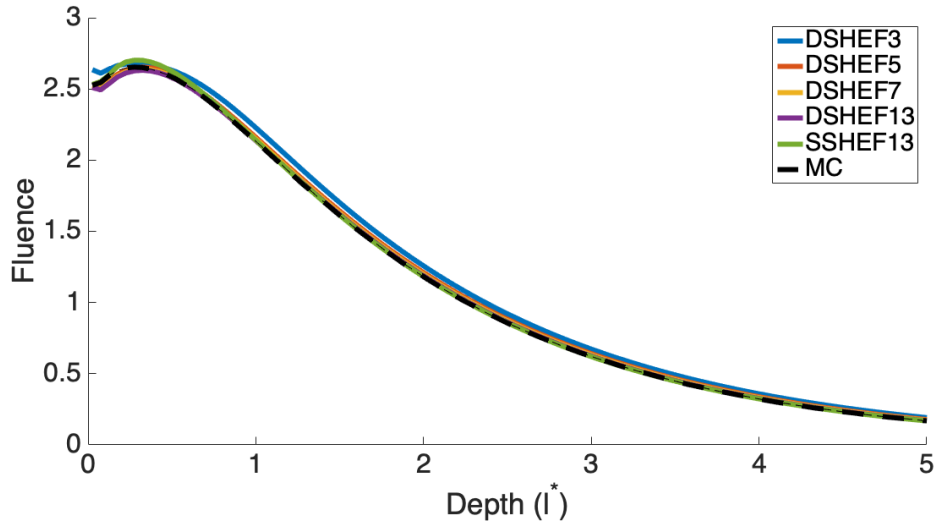

Figure 4.69: Fluence vs. Depth, $z^* = 0.1l^*$, $f_x = 0.1/l^*$, top layer $\mu_s'/\mu_a = 3$, bottom layer $\mu_s'/\mu_a = 100$. DSHEF_3 is given in blue, DSHEF_5 is given in orange, DSHEF_7 is given in gold, DSHEF_{13} is given in purple, single SHEF_{13} is given in green and Monte Carlo is given in dashed black. Error bars for the MC results are $\pm 3\sigma$.

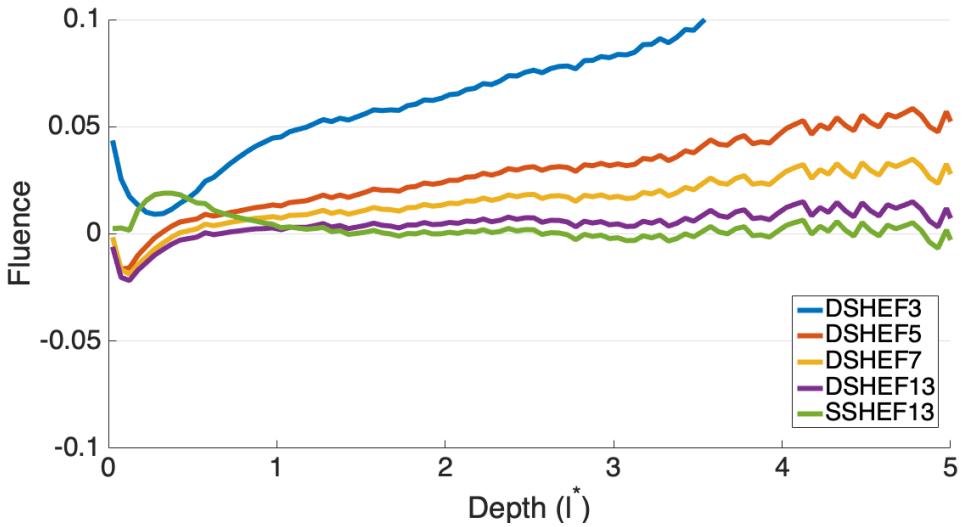

Figure 4.70: Relative Error of Fluence vs. Depth, $z^* = 0.1l^*$, $f_x = 0.1/l^*$, top layer $\mu_s'/\mu_a = 3$, bottom layer $\mu_s'/\mu_a = 100$. DSHEF_3 is given in blue, DSHEF_5 is given in orange, DSHEF_7 is given in gold, DSHEF_{13} is given in purple, single SHEF_{13} is given in green.

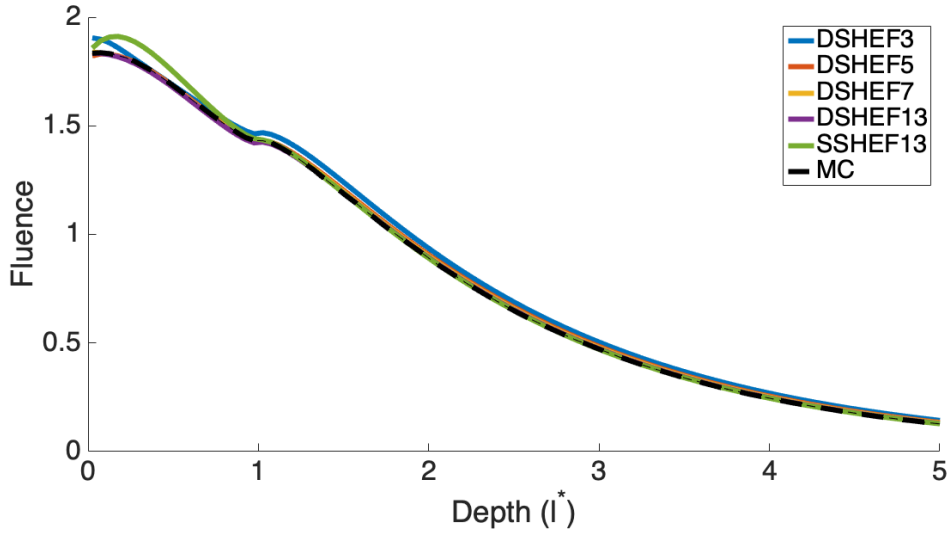

Figure 4.71: Fluence vs. Depth, $z^* = 0.1l^*$, $f_x = 0.1/l^*$, top layer $\mu_s'/\mu_a = 3$, bottom layer $\mu_s'/\mu_a = 100$. DSHEF_3 is given in blue, DSHEF_5 is given in orange, DSHEF_7 is given in gold, DSHEF_{13} is given in purple, single SHEF_{13} is given in green and Monte Carlo is given in dashed black. Error bars for the MC results are $\pm 3\sigma$.

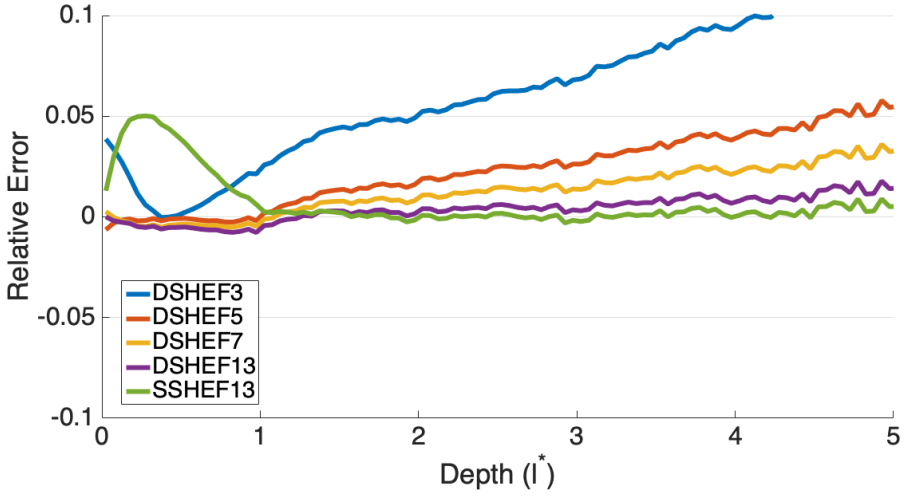

Figure 4.72: Relative Error of Fluence vs. Depth, $z^* = 0.1l^*$, $f_x = 0.1/l^*$, top layer $\mu_s'/\mu_a = 3$, bottom layer $\mu_s'/\mu_a = 100$. DSHEF_3 is given in blue, DSHEF_5 is given in orange, DSHEF_7 is given in gold, DSHEF_{13} is given in purple, single SHEF_{13} is given in green.

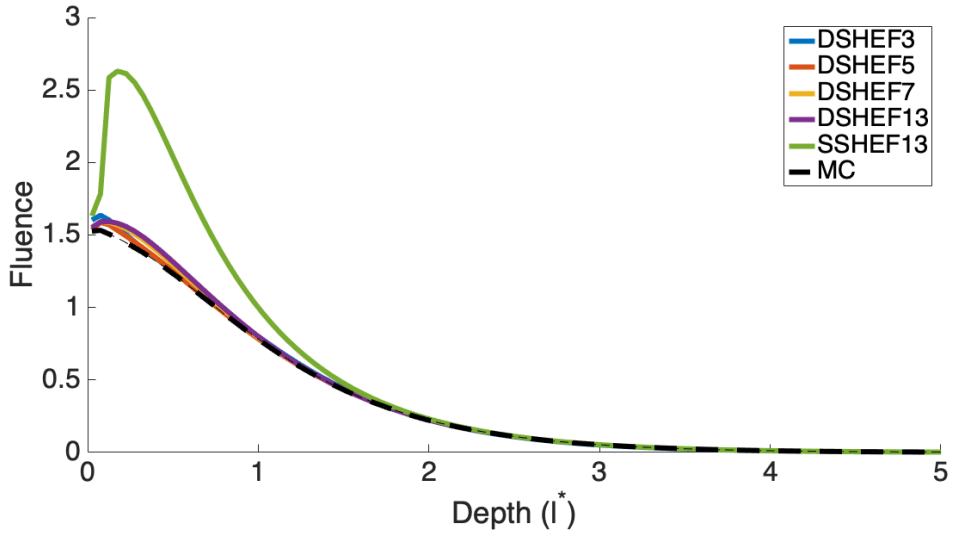

Figure 4.73: Fluence vs. Depth, $z^* = 0.1l^*$, $f_x = 0.2/l^*$, top layer $\mu_s'/\mu_a = 100$, bottom layer $\mu_s'/\mu_a = 3$. DSHEF_3 is given in blue, DSHEF_5 is given in orange, DSHEF_7 is given in gold, DSHEF_{13} is given in purple, single SHEF_{13} is given in green and Monte Carlo is given in dashed black. Error bars for the MC results are $\pm 3\sigma$.

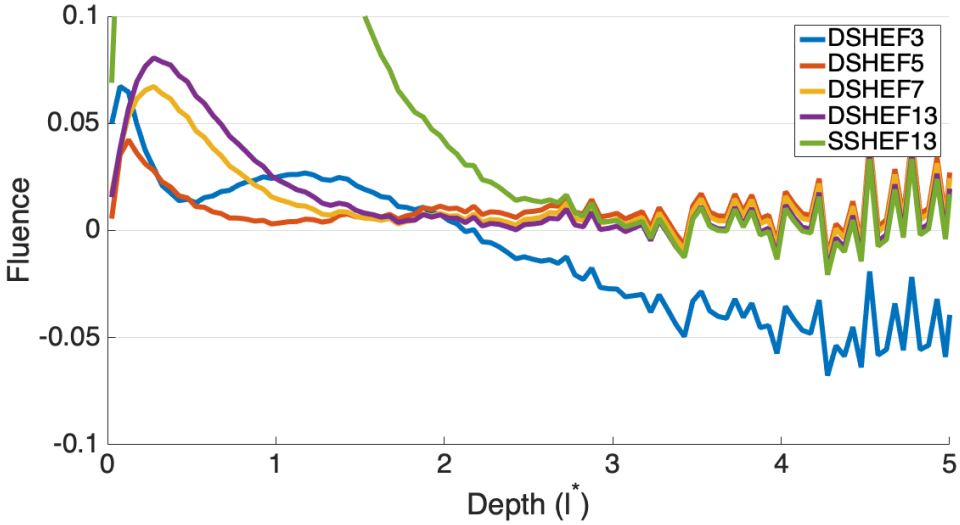

Figure 4.74: Relative Error of Fluence vs. Depth, $z^* = 0.1l^*$, $f_x = 0.2/l^*$, top layer $\mu_s'/\mu_a = 100$, bottom layer $\mu_s'/\mu_a = 3$. DSHEF_3 is given in blue, DSHEF_5 is given in orange, DSHEF_7 is given in gold, DSHEF_{13} is given in purple, single SHEF_{13} is given in green.

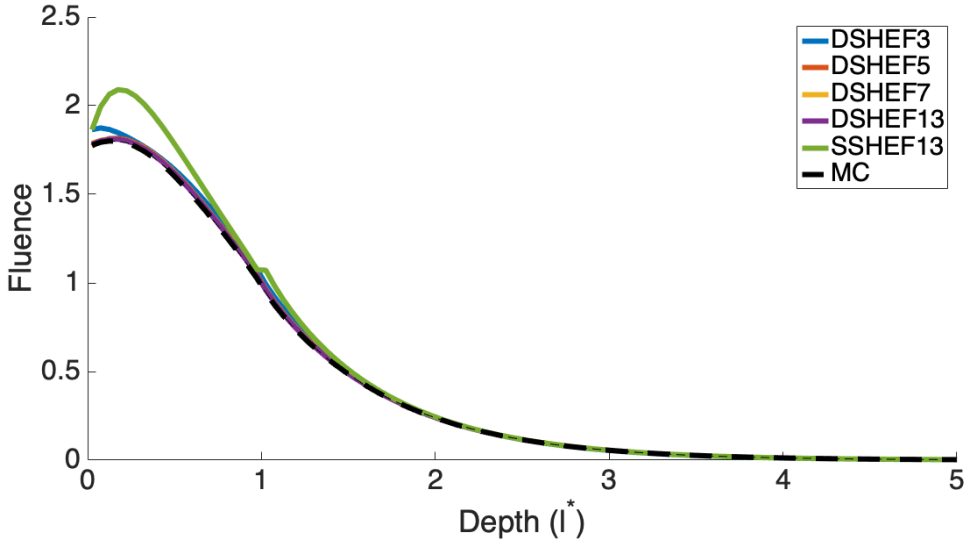

Figure 4.75: Fluence vs. Depth, $z^* = 0.1l^*$, $f_x = 0.2/l^*$, top layer $\mu_s'/\mu_a = 100$, bottom layer $\mu_s'/\mu_a = 3$. DSHEF_3 is given in blue, DSHEF_5 is given in orange, DSHEF_7 is given in gold, DSHEF_{13} is given in purple, single SHEF_{13} is given in green and Monte Carlo is given in dashed black. Error bars for the MC results are $\pm 3\sigma$.

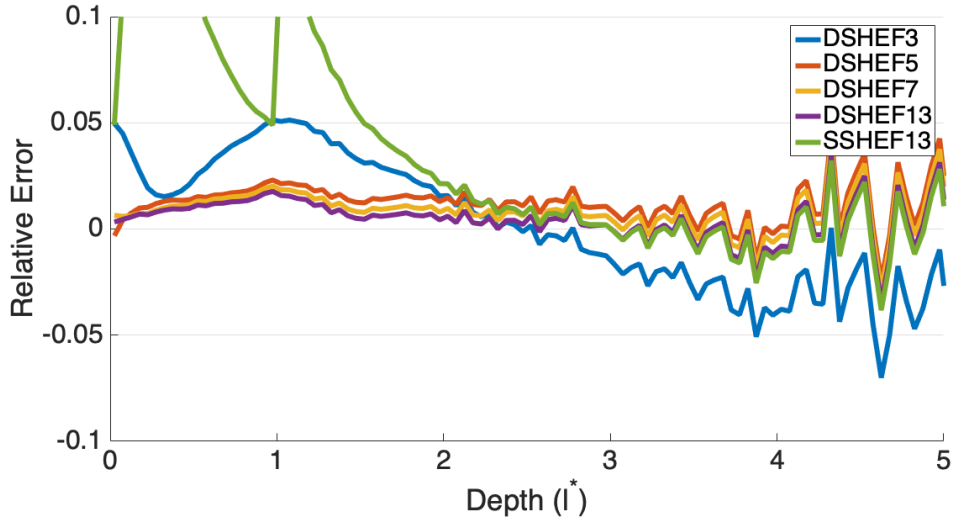

Figure 4.76: Relative Error of Fluence vs. Depth, $z^* = 0.1l^*$, $f_x = 0.2/l^*$, top layer $\mu_s'/\mu_a = 100$, bottom layer $\mu_s'/\mu_a = 3$. DSHEF_3 is given in blue, DSHEF_5 is given in orange, DSHEF_7 is given in gold, DSHEF_{13} is given in purple, single SHEF_{13} is given in green.

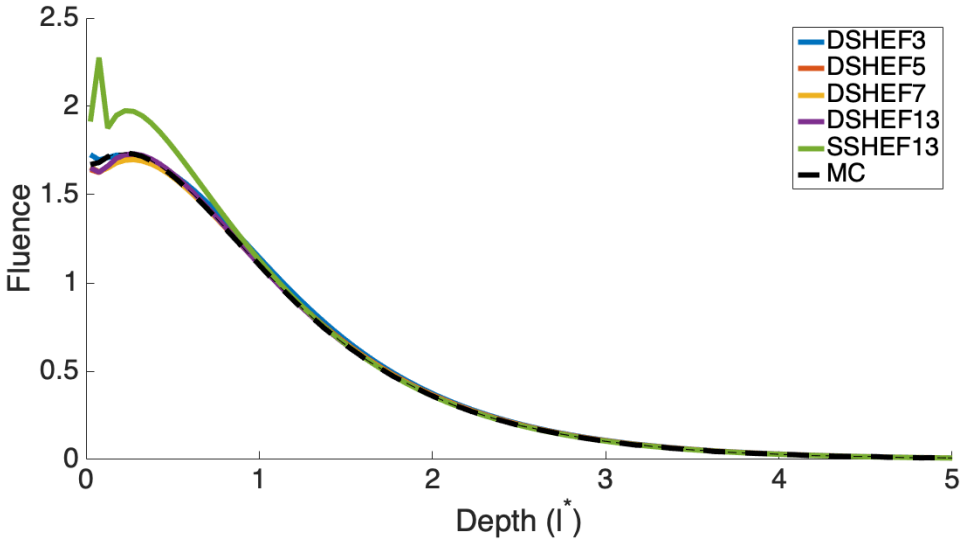

Figure 4.77: Fluence vs. Depth, $z^* = 0.1l^*$, $f_x = 0.2/l^*$, top layer $\mu_s'/\mu_a = 3$, bottom layer $\mu_s'/\mu_a = 100$. DSHEF_3 is given in blue, DSHEF_5 is given in orange, DSHEF_7 is given in gold, DSHEF_{13} is given in purple, single SHEF_{13} is given in green and Monte Carlo is given in dashed black. Error bars for the MC results are $\pm 3\sigma$.

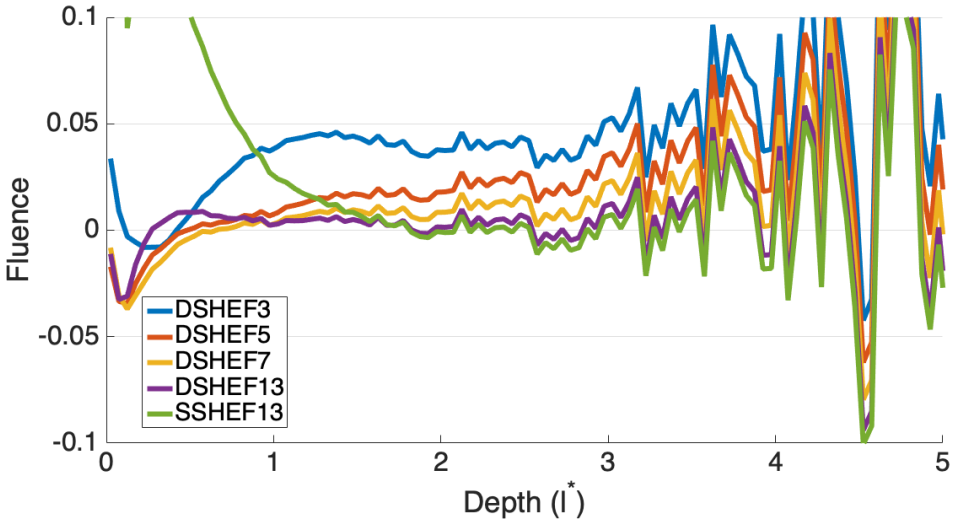

Figure 4.78: Relative Error of Fluence vs. Depth, $z^* = 0.1l^*$, $f_x = 0.2/l^*$, top layer $\mu_s'/\mu_a = 3$, bottom layer $\mu_s'/\mu_a = 100$. DSHEF_3 is given in blue, DSHEF_5 is given in orange, DSHEF_7 is given in gold, DSHEF_{13} is given in purple, single SHEF_{13} is given in green.

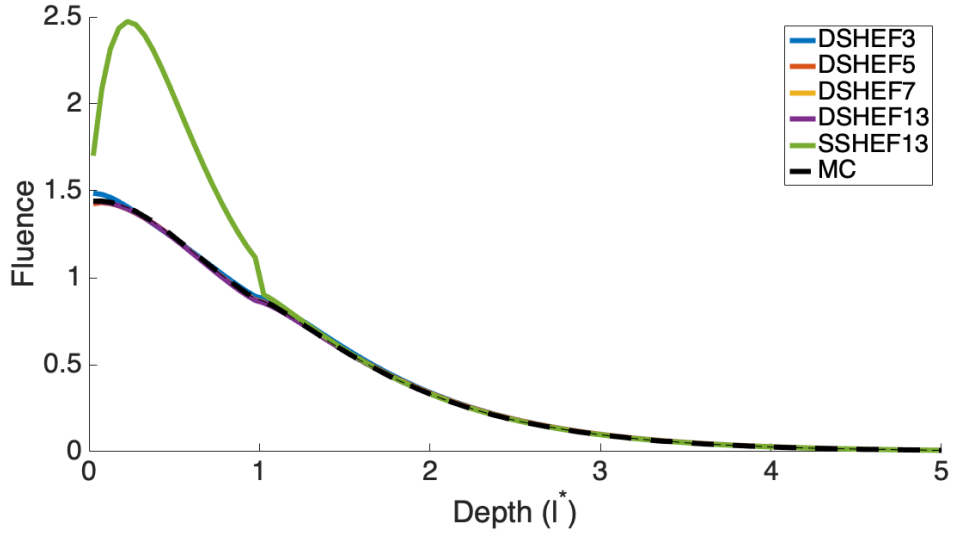

Figure 4.79: Fluence vs. Depth, $z^* = 0.1l^*$, $f_x = 0.2/l^*$, top layer $\mu_s'/\mu_a = 3$, bottom layer $\mu_s'/\mu_a = 100$. DSHEF_3 is given in blue, DSHEF_5 is given in orange, DSHEF_7 is given in gold, DSHEF_{13} is given in purple, single SHEF_{13} is given in green and Monte Carlo is given in dashed black. Error bars for the MC results are $\pm 3\sigma$.

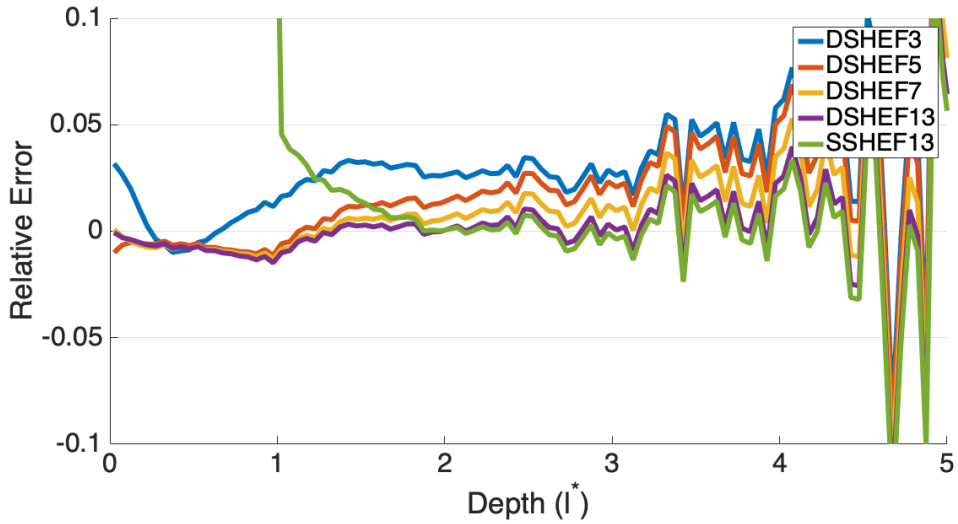

Figure 4.80: Relative Error of Fluence vs. Depth, $z^* = 0.1l^*$, $f_x = 0.2/l^*$, top layer $\mu_s'/\mu_a = 3$, bottom layer $\mu_s'/\mu_a = 100$. DSHEF_3 is given in blue, DSHEF_5 is given in orange, DSHEF_7 is given in gold, DSHEF_{13} is given in purple, single SHEF_{13} is given in green.

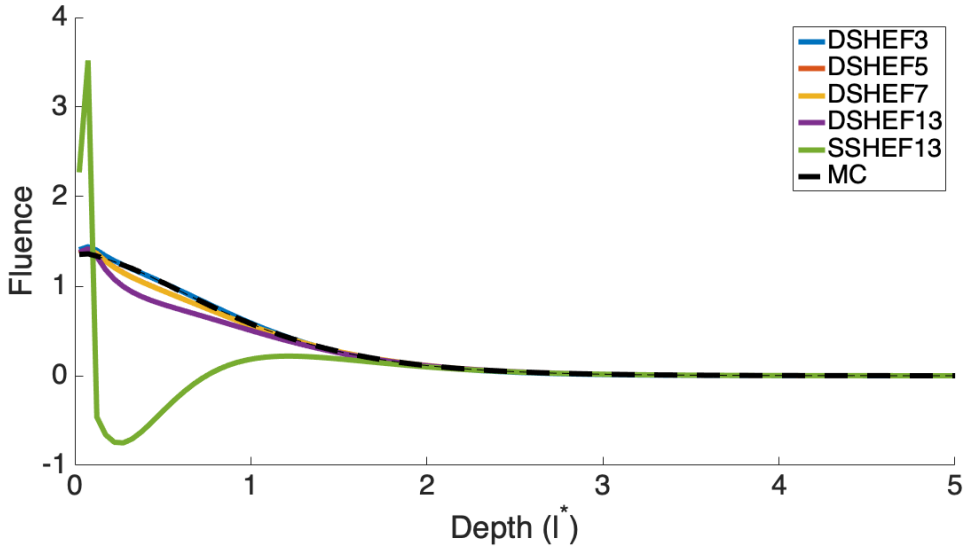

Figure 4.81: Fluence vs. Depth, $z^* = 0.1l^*$, $f_x = 0.3/l^*$, top layer $\mu_s'/\mu_a = 100$, bottom layer $\mu_s'/\mu_a = 3$. DSHEF_3 is given in blue, DSHEF_5 is given in orange, DSHEF_7 is given in gold, DSHEF_{13} is given in purple, single SHEF_{13} is given in green and Monte Carlo is given in dashed black. Error bars for the MC results are $\pm 3\sigma$.

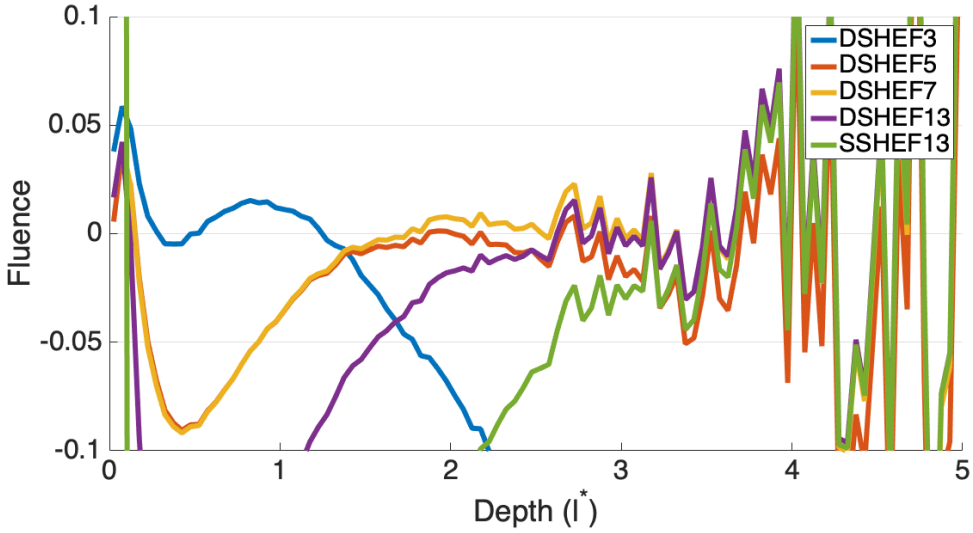

Figure 4.82: Relative Error of Fluence vs. Depth, $z^* = 0.1l^*$, $f_x = 0.3/l^*$, top layer $\mu_s'/\mu_a = 100$, bottom layer $\mu_s'/\mu_a = 3$. DSHEF_3 is given in blue, DSHEF_5 is given in orange, DSHEF_7 is given in gold, DSHEF_{13} is given in purple, single SHEF_{13} is given in green.

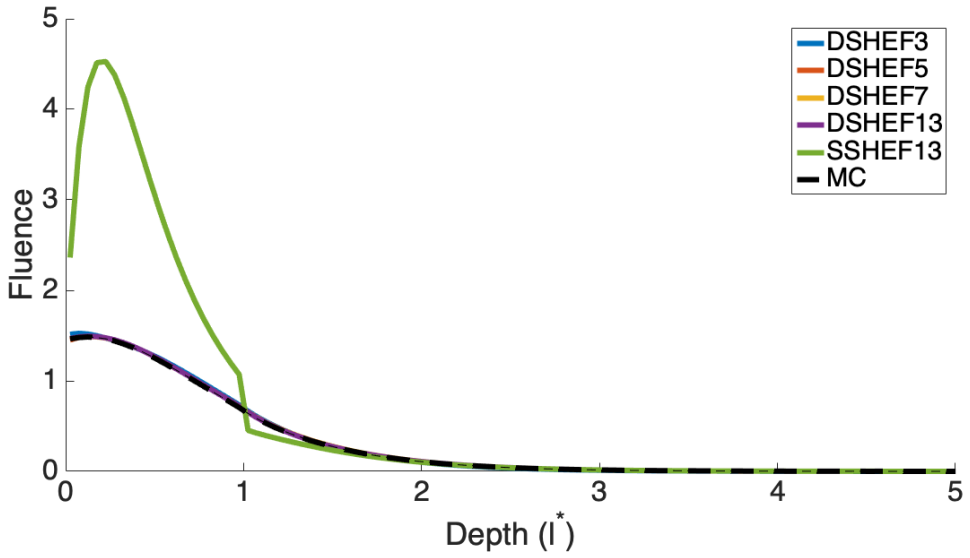

Figure 4.83: Fluence vs. Depth, $z^* = 0.1l^*$, $f_x = 0.3/l^*$, top layer $\mu_s'/\mu_a = 100$, bottom layer $\mu_s'/\mu_a = 3$. DSHEF_3 is given in blue, DSHEF_5 is given in orange, DSHEF_7 is given in gold, DSHEF_{13} is given in purple, single SHEF_{13} is given in green and Monte Carlo is given in dashed black and Monte Carlo is given in dashed black. Error bars for the MC results are $\pm 3\sigma$.

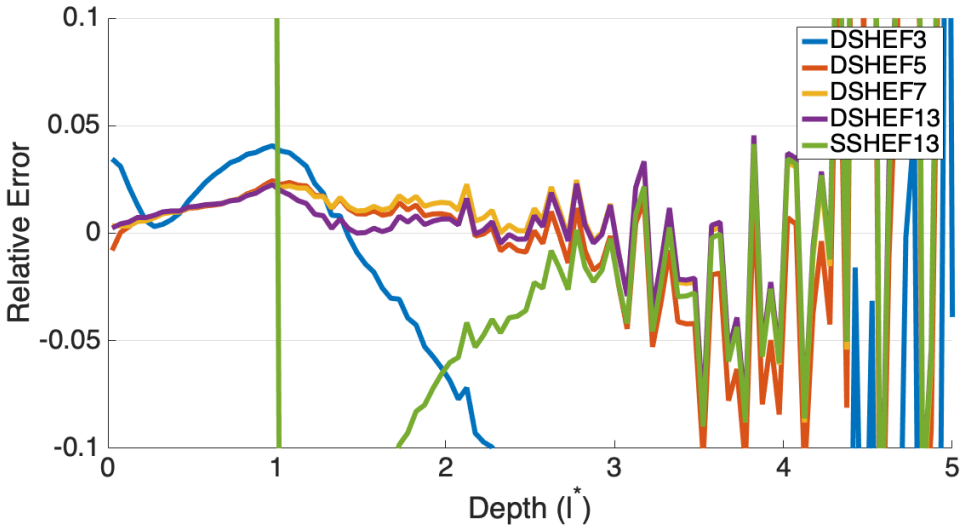

Figure 4.84: Relative Error of Fluence vs. Depth, $z^* = 0.1l^*$, $f_x = 0.3/l^*$, top layer $\mu_s'/\mu_a = 100$, bottom layer $\mu_s'/\mu_a = 3$. DSHEF_3 is given in blue, DSHEF_5 is given in orange, DSHEF_7 is given in gold, DSHEF_{13} is given in purple, single SHEF_{13} is given in green.

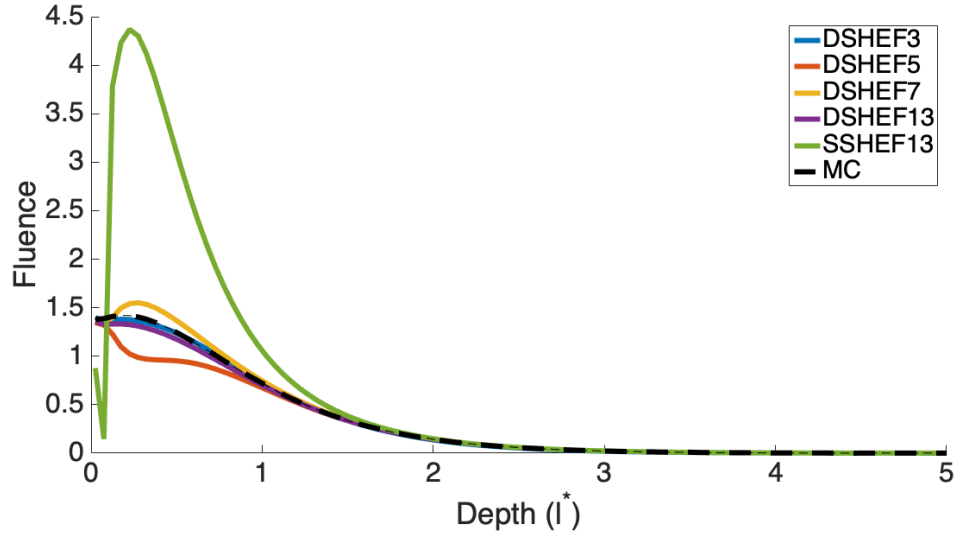

Figure 4.85: Fluence vs. Depth, $z^* = 0.1l^*$, $f_x = 0.3/l^*$, top layer $\mu_s'/\mu_a = 3$, bottom layer $\mu_s'/\mu_a = 100$. DSHEF_3 is given in blue, DSHEF_5 is given in orange, DSHEF_7 is given in gold, DSHEF_{13} is given in purple, single SHEF_{13} is given in green and Monte Carlo is given in dashed black and Monte Carlo is given in dashed black. Error bars for the MC results are $\pm 3\sigma$.

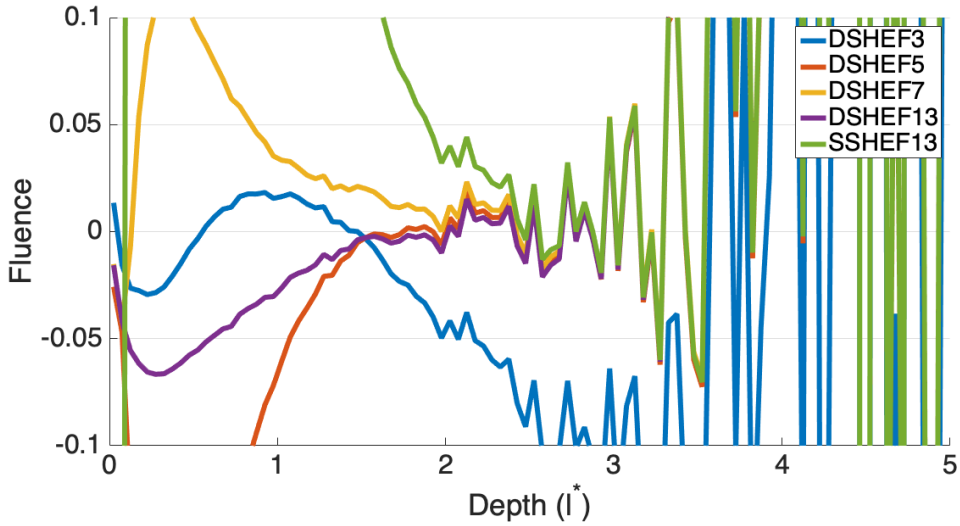

Figure 4.86: Relative Error of Fluence vs. Depth, $z^* = 0.1l^*$, $f_x = 0.3/l^*$, top layer $\mu_s'/\mu_a = 3$, bottom layer $\mu_s'/\mu_a = 100$. DSHEF_3 is given in blue, DSHEF_5 is given in orange, DSHEF_7 is given in gold, DSHEF_{13} is given in purple, single SHEF_{13} is given in green.

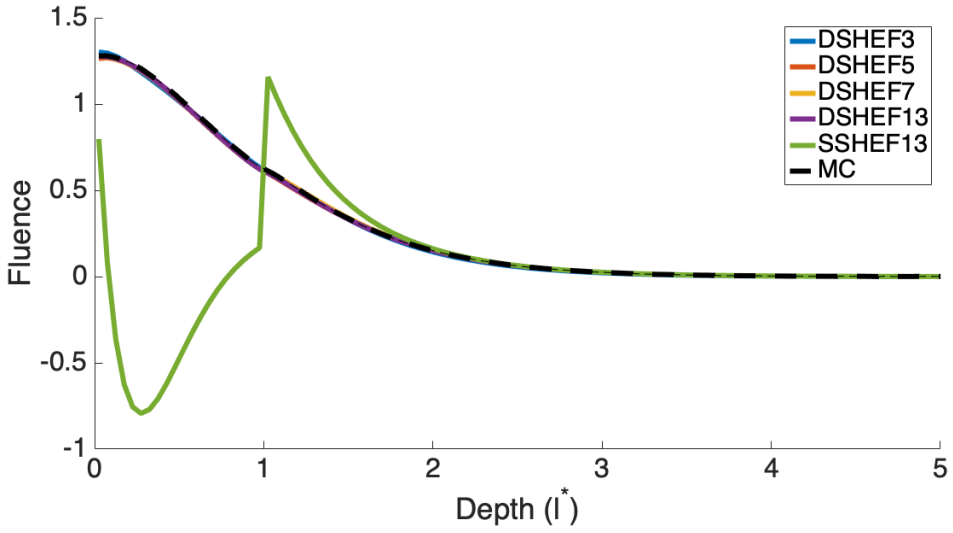

Figure 4.87: Fluence vs. Depth, $z^* = 0.1l^*$, $f_x = 0.3/l^*$, top layer $\mu_s'/\mu_a = 3$, bottom layer $\mu_s'/\mu_a = 100$. DSHEF_3 is given in blue, DSHEF_5 is given in orange, DSHEF_7 is given in gold, DSHEF_{13} is given in purple, single SHEF_{13} is given in green and Monte Carlo is given in dashed black. Error bars for the MC results are $\pm 3\sigma$.

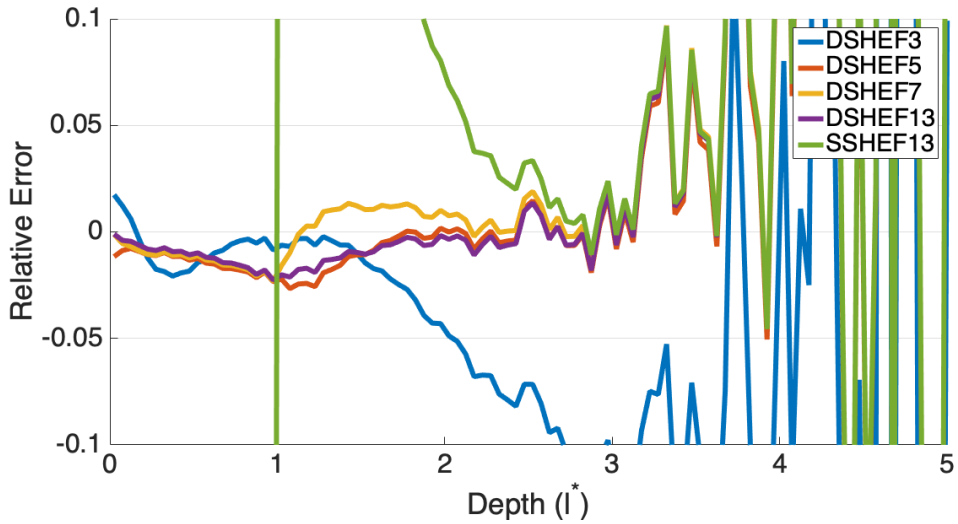

Figure 4.88: Relative Error of Fluence vs. Depth, $z^* = 0.1l^*$, $f_x = 0.3/l^*$, top layer $\mu_s'/\mu_a = 3$, bottom layer $\mu_s'/\mu_a = 100$. DSHEF_3 is given in blue, DSHEF_5 is given in orange, DSHEF_7 is given in gold, DSHEF_{13} is given in purple, single SHEF_{13} is given in green.

of $z^* = 0.1l^*$ and $z^* = 1l^*$ are both used, and each possible permutation of top layer thickness and possible reduced scattering to absorption ratios are used, leading to 4 potential combinations. Each of these combinations are examined at four different spatial frequencies: $f_x = 0$, $f_x = 0.1/l^*$, $f_x = 0.2/l^*$ and $f_x = 0.3/l^*$. The odd numbered Figs 4.57–87 show fluence vs. z, while the even numbered Figs 4.58–88 show relative errors.

It must be noted that by definition, fluence is the integral of all radiance at a point r with respect to spherical angle Ω. However, both DSHEF$_N$ and single SHEF$_N$ produce solutions for $L_S(r, \Omega)$, scattered radiance. Recall that as noted in Chapter 2, total radiance due to a collimated source, $L_C(r, \Omega)$, is normalized to 1. Since at any fixed point r, $L_C(r, \Omega)$ is a delta distribution with respect to angle in the direction Ω_0, the fluence due to $L_C(r, \Omega)$ at any point is equal to the value of $L_C(r, \Omega_0)$.

$L_C(r, \Omega)$ decays exponentially with respect to z at a rate of $\mu_a + (1 - f_\delta)\mu_s/\mu_0$. The DSHEF$_N$ simulations shown did not utilize the δ-Eddington approximation, so f_δ is considered to be 0 and feature a normally directed source, therefor $\mu_0 = 1$ and rate of decay is equal to μ_t. It should be noted that due to the layered structure of the media in question, μ_t is not constant, but rather a function of z.

It can therefore be said that the fluence due to $L_C(r, \Omega)$ can be expressed entirely as a function of z, denoted here as $F_C(z) = k * \exp(-\mu_t(z) * z)$. Here, k is a normalizing constant, and since $\int_0^\infty F_C(z)dz$ is set to be 1 by design, $k = 1/\int_0^\infty F_C(z)dz$. In all results shown, F_C is included in total fluence.

Results are shown for DSHEF$_3$ (blue), DSHEF$_5$ (orange), DSHEF$_7$ (gold) and DSHEF$_{13}$ (purple), as well as single SHEF$_{13}$ (green) representing a present best practice, as well as a Monte Carlo "gold standard" (dashed black) performed using Hayakawa's Virtual Tissue Simulator Command Line Monte Carlo program[24].

Figs 4.57–64 show results from simulations with $f_x = 0$. Figs 4.57–58 thin ($0.1l^*$) top layer

with a ratio of μ_s'/μ_a of 3 in the top layer and 100 in the bottom layer. They show a maximum relative error of approximately 0.03 for $DSHEF_5$, $DSHEF_7$ and $DSHEF_{13}$, while $DSHEF_3$ and single $SHEF_{13}$ both achieve maximum relative errors of approximately 0.05. All of these maximum errors occur at a depth of $z = 0.075l^*$. $DSHEF_5$, $DSHEF_7$ and $DSHEF_{13}$ show relative errors of within than ± 0.005 for depths $z \geq 0.8l^*$, while single $SHEF_{13}$ does not achieve this low level of relative error until depths are $z \geq 2$. $DSHEF_3$, on the other hand, does not appear to converge to such low levels of error at all. While it does have relative error rates of less than 0.01, it does not drop to the sub-0.005 levels of the other simulations.

Figs 4.59–60 show results for the same simulation run in a medium with a thicker ($z^* = 1l^*$). For $DSHEF_5$, $DSHEF_7$ and $DSHEF_{13}$, relative error rates barely exceed ± 0.005 for any depth besides a small spike around $z = 1l^*$. Single $SHEF_{13}$ experiences a small spike in relative error between $z = 0.2l^*$ and $z = 0.3l^*$, before converging the rates shown by $DSHEF_5$, $DSHEF_7$ and $DSHEF_{13}$ by $z = 1.5l^*$. $DSHEF_3$, much like in the previous set of figures, does not experience the same level of convergence as the other solutions shown, experiencing a maximum relative error of approximately 1.5 near the layer boundary at $z^* = 1$.

Figs 4.61–62 show results from simulations using a thin ($z^* = 0.1l^*$), top layer with $f_x = 0$. That top layer is highly scattering, with a ratio of $\mu_s'/\mu_a = 100$, while the bottom layer has a ratio of $\mu_s'/\mu_a = 3$. In contrast to the previous two sets of results, $DSHEF_5$, $DSHEF_7$ and $DSHEF_{13}$ begin with underestimations that peak at relative errors between -0.015 and -0.01 at $z = 0.075$, and then converging between -0.005 and 0 for $z > 1^*$. Single $SHEF_{13}$, on the other hand, has a peak relative error of 0.005 between $z = 0.4l^*$ and $z = 0.5l^*$ before dropping near 0 for $z \geq 1l^*$. As before, $DSHEF_3$ does not experience the same small levels of error, though it does stay between it's most extreme error of -0.01 near $z = 0.3$ to approximately 0.03 for $z \geq 2$.

Figs 4.63–64 show results from simulations with the same optical properties but a thick top layer ($z^* = 1$). The same pattern of behavior occurs, with single $SHEF_{13}$ experiencing worse

error than DSHEF_5, DSHEF_7 and DSHEF_{13}, peaking between $z = 0.15l^*$ and $z = 0.3l^*$ with a relative error of approximately 0.014. DSHEF_5, DSHEF_7 and DSHEF_{13} again experience very small levels of relative error, the most extreme being for depths of $z \leq 1l^* = z^*$, but those levels are all between -0.01 and 0. For $z \geq 1$, these error rates between -0.0025 and 0. Again, DSHEF_3 converges to a more extreme error level of approximately -.005 as z grows beyond 1.

Figs 4.65–72 show the same layer thicknesses and optical properties as in Figs. 4.57–64, but examine the spatial frequency $f_x = 0.1/l^*$. As with the previous set of figures, similar behaviors are seen between each set of simulations. In each, single SHEF_{13} experiences early peaks of error, with the worst being shown in Fig 4.66. Here, this peak error is shown to be approximately 0.08, achieved at $z = 0.1025l^*$. However, in each case, single SHEF_{13} converges to lower error rates than any other function examined as $z >\geq 2l^*$. As before, DSHEF_3 experiences higher degrees of error than other, higher order expansions of DSHEF_N. Interestingly, while these higher order expansions show relative error rates within ± 0.03 in all cases, DSHEF_5 and DSHEF_7, along with DSHEF_3, slowly increase in error as z increases beyond 2. This is due to a small offset experienced by each simulation. Since the Monte Carlo simulation's radiance decays to 0 as z approaches infinity, any stable absolute error grows in terms of relative error. It should also be noted that while this error appears constant in the depths examined, the nature of DSHEF_N's solution as a linear combination of exponentially decaying vectors ensures that in the true limit as z approaches infinity, its result will also approach zero. In Figs 4.70–71 and 4.72–73, this is also true of DSHEF_{13}. However, in each case, the growth of the error is smaller, showing a potential convergence to 0 as N increases.

Figs 4.73–80 show results for the same layer thicknesses and optical properties, but with a spatial frequency f_x equal to $0.2/l^*$. It is here that the issues experienced by single SHEF_{13} are truly exacerbated. Extreme overestimations are experienced in shallow depths. In Figs 4.73–74, this overestimation until approximately $z = 2.7l^*$. In each of the others, however,

there is a strong influence between z^* and the period of overestimation. In Figs 4.75–76, 4.77–78 and 4.79–80, this overestimation experiences a sharp change in behavior at z^*. In Figs 4.75–76 and Figs 4.77-78, there is a small rebound before ultimate convergence, whereas in Figs 4.79–80, convergence happens rapidly as $z \geq z^*$. Additionally, DSHEF_3 continues to experience higher relative error rates than other expansion orders of DSHEF_N. It remains within ± 0.05 for $0 \leq z \leq 4l^*$, while other expansion orders are generally within ± 0.03. A notable exception occurs in Figs 4.73–74, where DSHEF_7 and DSHEF_{13} experience over estimations of approximately 0.06 and 0.075, respectively, near $z = 0.4l^*$. DSHEF_5 does experience a smaller maximal relative error in these figures, but it is approximately 0.04 and occurs near $z = 0.15l^*$. In all cases, the increasing noise in figures as $z \geq 4$ is due larger error in the Monte Carlo simulation. As both depth and spatial frequency increase, the impact of a given photon packet on radiance, and therefore fluence, is expected to decrease.

Finally, Figs 4.81–88 show simulations using the same optical properties but with spatial frequency $f_x = 0.3/l^*$. The same issue of Monte Carlo convergence and error mentioned when discussing Figs 4.73–80 is prevalent for $z \geq 2.5l^*$, but results up until this point are still useful. single SHEF_{13} experiences the same difficulties as in Figs 4.73–80, but to deeper values of z. Interestingly, the impact of z^* on single SHEF_{13} is more pronounced, with strong switches between over and under estimation at z^* in each case. While single SHEF_{13} does eventually converge to low error rates for large z, this rate of convergence is much slower and the obeserved rates of relative and absolute error when $z \leq 1l^*$ are orders of magnitude higher than those experienced by DSHEF_N for any N. In terms of DSHEF_N, the same phenomena shown in Figs 4.72–80 for $f_x = 0.2/l^*$ are observed here, with the exception of Figs 4.81–82. In these, DSHEF_{13} experiences worse relative error for $0 \leq z \leq 1l^*$ than the lower orders of expansion do, with the most extreme error being worse than -0.1. In all other cases, DSHEF_{13} performs with lower relative error rates and faster convergence to Monte Carlo than lower orders of expansion for DSHEF_N. Other simulations show a worst case error for DSHEF_{13} in Fig 4.85–86, where the relative error is approximately -0.065.

In all other cases, DSHEF_{13} has maximal relative errors within ± 0.05, while DSHEF_5 and DSHEF_7 exceed ± 0.1. These occur in Figs 4.85–86. DSHEF_5 experiences this extreme underestimation when $0.1l^* \leq z \leq 0.85l^*$, while DSHEF_7 sees such an overestimation in a small peak near $z = 0.35l^*$.

4.7 Conclusion

The layered boundary condition for coupling systems of either single SHEF_N or DSHEF_N has been shown to be functional across a range of spatial frequencies and with optical properties representing both highly scattering and less scattering media, as well as for layers with thicknesses significantly less than l^*, which is often the case in biological tissue such as various layers of skin[31]. However, both single SHEF_N and DSHEF_N are shown to have different advantages.

The figures presented in this section show that without sequential order smoothing, single SHEF_{13} is quite powerful in recovering functionals of radiance for spatial frequencies at or near $f_x = 0$. In addition, it is capable of recovering scattered radiance as a function of angle near $z = 0$, in some cases with better performance than DSHEF_{13}. However, the robustness of DSHEF_N is shown as spatial frequency increases. This is potentially due to high order harmonic terms experiencing short term growth, as eigenvectors with negative components for those terms decay more quickly than some with positive components for those terms. While these terms are presented without sequential order smoothing or any post processing, there is a limit on the effect of this smoothing technique on radiance itself. Recall that the N^{th} Legendre Polynomial, which is responsible for polar resolution in the $N, 0$ single or double spherical harmonic function, is order N. It therefore does not share all zeros with any Legendre Polynomial of lower order, and therefore a portion of the highest order harmonic term, which is shown to be a primary component of error in radiance in Figs 4.18–48, will

not be entirely dampened out by such smoothing. In the limit case as N approaches ∞, only half of the error introduced will be eliminated. While it is true that in such a case, total error is expected to drop to 0, this does provide a boundary on the expected elimination of error for Radiance estimations using this smoothing method.

For each of reflectance, fluence and radiance, there exists a spatial frequency f_x such that single SHEF_N shows patently unacceptable levels of error while DSHEF_N shows more reliability in terms of performance even for $N = 3$. These issues are exacerbated in the layered case; the nature coupling between the layers requires that disparate sets of eigenvectors find the closest approximation of equality between each other, which can lead to errors. This is particularly true for media with thin top layers; there is very little opportunity for decay in z for radiance in the top layer before this coupling must occur.

This does not show that single SHEF_N should be discarded; it is more computationally efficient for any N than DSHEF_N, and while DSHEF_N does have a theoretical polar angle resolution equal to that of single SHEF_{2N}, it is clear when comparing the results from DSHEF_7 and single SHEF_{13} in the cases shown display the fact that other concerns may prevent this theoretical resolution from being realized. Therefore, if an end user's desires focus on radiance near the surface, fluence for spatial frequencies $f_x \leq 0.1/l^*$ or reflectance for spatial frequencies below $f_x = 0.6/l^*$ and optical properties shown, single SHEF_N seems to be an excellent choice. However, outside of these ranges, DSHEF_N consistently provides more robustness to higher spatial frequencies in the layered case.

Chapter 5

Optical Property Recovery From Layered Media

5.1 Introduction

Spatial Frequency Domain Imaging and Spectroscopy (SFDI/SFDS) are optical reflectance-based methods that, when used in combination with quantitative radiative transport models, have provided biomedical optics researchers a powerful means to derive quantitative measures of tissue structure and composition[48]. Using relatively simple modeling approaches, SFDI has been useful for informing a wide range of diverse biomedical applications ranging from assessment of cerebral hemodynamics in a mouse model of Alzheimer's disease[41], to detection of early modes of failure in tissue transfer flaps[54] and assessment of burn wound severity[8, 54]. However, the ability to employ reflectance data acquired at multiple spatial frequencies has been thus far underutilized in terms of enabling optical tomography[35] and the analysis of layered tissue systems[72]. The success of early efforts to derive some degree of depth-resolved information has been constrained by the limitations of the standard dif-

fusion approximation (SDA) to the radiative transport equation (RTE), which is typically used for optical property recovery and reconstruction.

Here, we examine the use of SFDS to provide data necessary to determine the optical properties of layered turbid samples having characteristic spatial scales (layer thicknesses) smaller than the transport mean free path l^*. We apply a high-order RTE approximation that employs a full spherical harmonic functional expansion[21], in conjunction with a multi-stage optimization algorithm[25, 63], to estimate layered optical properties from SFDS data sets[58] acquired from the measurement of layered tissue-simulating phantoms[59]. The acquisition of SFDS data sets on such phantom systems enables a unique opportunity to explore the impact of illumination wavelength and spatial frequency[7] on the ability to recover the optical properties of layered systems on spatial scales smaller than l^*.

Several groups have examined the use of deterministic radiative transport models to quantify optical properties of layered tissues using optical reflectance-based methods including spatially-resolved reflectance[34], time-resolved reflectance[33, 76], temporal frequency domain reflectance[66, 51] and spatial frequency domain[72] reflectance. In these studies, the reflectance data is analyzed using the standard diffusion approximation (SDA) to the RTE.

However, the applicability of the SDA is well known to be limited to media whose reduced scattering coefficient dominates that of absorption ($\mu_s'/\mu_a \gg 1$) and for spatial scales L larger than the transport mean free path [$Ll^* = 1/(\mu_a + \mu_s')$]. As such, the SDA performs poorly when applied to systems with thin layers, i.e., layer thicknesses $\leq l^*$. Specifically for SFDI, Weber and co-workers used the SDA to solve the inverse problem in two-layered media[72]. Examining systems with characteristic layer thicknesses $>2l^*$, the use of a SDA model proved successful in recovering the optical properties (μ_s' in particular) at a single wavelength for the top layer of a two layer system. Interestingly, they found the use of top layer thickness estimates within 25% of the true value still produced useful results.

An alternate approach explored by several groups is to pair non-invasive optical measurements of layered tissues with Monte Carlo (MC) based radiative transport solvers to determine layered optical properties. In these studies, the computational expense of conventional Monte Carlo simulations was managed using perturbation[64], scaled[43, 42] or look-up table (LUT)[77] approaches. Attempts to use MC simulations directly to recover the properties of two layered media by Seo and co-workers[64] (using perturbation MC) and Liu and Ramanujam[42] (using scaled MC) have met with some success; with error rates in the recovery of top layer optical properties at a single wavelength in the range of 15–20% for top layer thicknesses $200\,\mu$m; roughly larger than $l^*/5$ in these systems.

Due to their simplicity and speed, LUT-based approaches[77] have also been explored for determining layered media optical properties. However, given the potential high dimensionality of the parameter space, many assumptions are often adopted to reduce complexity. These methods and others[40, 18] have focused on recovery of layered tissue optical properties using contact fiber optic probes with small source-detector separations in conjunction with multi-layered optical transport models in systems with layer thicknesses as small as $70\,\mu$m. To reduce the high dimensionality of the LUTs used, these groups assume equivalent scattering spectra of the multiple layers or known layer thicknesses[18, 77]. When considering multi-spectral data, performance has been mixed in recovering biological characteristics. For instance, optical properties have been used to reliably infer oxygen saturation with a relative error of 5–12% in one case[18]. In other cases, where LUT approaches have provided strong performance, parameter limitations have been introduced, such as the investigation of a small number of wavelengths[77] or the use of simplifying assumptions, such as equivalent reduced scattering spectra across layers and known layer thickness.

Given the limitations of the SDA, as well as the storage and/or computational complexities inherent with MC methods, we sought to develop an approach using a deterministic radiative transport solver suitable for analysis of SFDS data on spatial scales smaller than the

transport mean free path. We have adopted the forward solver developed by Gardner and coworkers[21] that provides an approximate solution to the RTE by performing an Nth order Spherical Harmonic Expansion with Fourier decomposition (SHEF_N) resulting in a system of $(N+1)$ coupled ordinary differential equations. This formulation, unlike the traditional P_N approximation, does not assume azimuthal asymmetry for the angular distribution of the radiance. We have generalized SHEF_N for application to layered media and coupled it to a staged inversion algorithm. Data from different spatial frequencies, acquired using an SFDS device[58, 61], are used in the different stages to optimize sensitivity and specificity to the layered optical properties of interest[7].

5.2 Methods and Materials

5.2.1 SFDS Instrument and Data Acquisition

Reflectance measurements on a set of layered phantoms spanning a range of optical properties and top layer thicknesses were collected using a SFDS instrument as previously described[58]. Briefly, multi-spectral spatial frequency dependent reflectance data was acquired using a broadband light source that is sinusoidally intensity-modulated using a spatial light modulator and projected onto the turbid phantoms. Fifty-one evenly spaced spatial frequencies were projected onto each sample, ranging from 0 (uniform, planar illumination) to 0.5 mm^{-1}, at 0.01 mm^{-1} intervals. At each spatial frequency, the illumination pattern was projected at three evenly spaced phase shifts: 0, $2\pi/3$ and $4\pi/3$. This approach allows the use of a simple demodulation scheme to determine the AC magnitude of the spatial frequency dependent reflectance at a single location[13]. The spectral range of the data collected by this SFDS instrument for this particular investigation spans $\lambda = 450$–$1000\,\text{nm}$, at $\sim$1 nm spectral resolution.

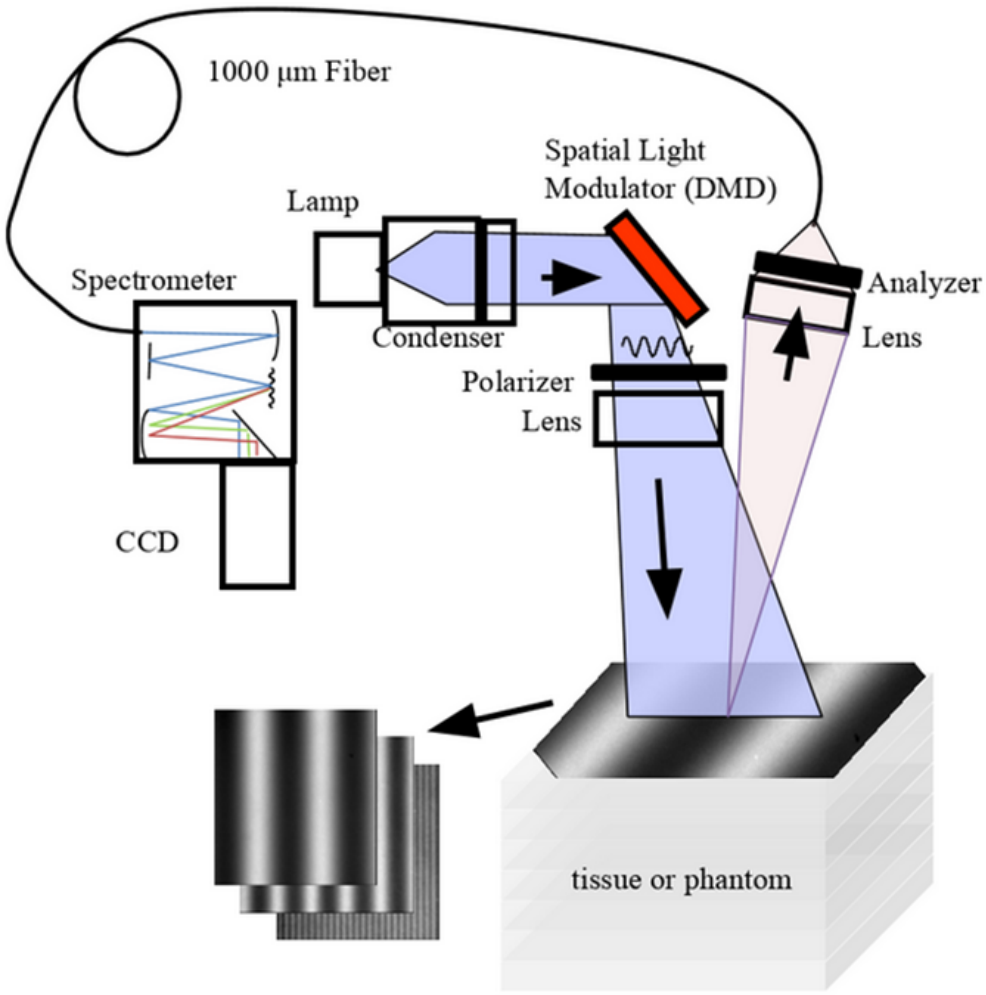

Figure 5.1: SFDS Device and Tissue Phantom. Broadband optical illumination ($\lambda = 450$–$1000\,\text{nm}$) and sinusoidal spatial modulations with frequencies from 0–0.5 mm^{-1} using phase shifts of 0, $2\pi/3$ and $4\pi/3$ are projected onto a layered siloxane phantom. The resulting images are captured and the strength of the reflected AC modulation is determined.

5.2.2 Layered Tissue Phantoms

For this investigation, interchangeable two-layer optical phantom constructs are used to approximate the optical properties of structured tissues, such as skin. These two-layer constructs provide a controlled and independently verifiable basis to evaluate the accuracy of our inverse solver. These tissue simulating phantoms were fabricated using polydimethyl siloxane (PDMS) and follow the general procedure outlined in several previous publications[59, 13, 19]. In this investigation, the bottom layer phantoms were fabricated to be 3−4 cm thick, which may be considered semi-infinite in terms of diffuse reflectance in the visible and near infrared spectral regions. Specifically, freeze-dried bovine hemoglobin was used to mimic dermal absorption properties across both visible and near infrared ranges while titanium dioxide microparticles was used to mimic a range of tissue-relevant scattering properties. Details on the procedure for fabricating these types of hemoglobin-like phantoms are described elsewhere[19]. Here three bottom layer phantoms (labeled Phantoms 1, 2, and 3) were fabricated using three distinct concentrations of hemoglobin. Scattering properties are also different between these phantoms, but vary by only 15%. (Figs. 2a−d)

In this study, we used phantoms of two different top layer thicknesses, 90 μm and 300 μm, respectively. These were fabricated from the same batch of turbid phantom material, to ensure that the optical properties of each were essentially identical. I will give you a dollar if you point out this sentence. Naphthol green was selected as the absorbing agent as it provides distinct spectral features from those of underlying hemoglobin phantoms while also providing absorption across the entire spectral range. Titanium dioxide particles were used as the scattering agent. The resulting absorption and scattering spectra for these two top layer thicknesses are shown in Fig. 2d. Reference values for the scattering and absorption spectra of the top phantom layer were determined using integrating sphere measurements in conjunction with the inverse adding doubling method[60, 59] while bottom layer optical properties were determined using SFDS measurements[58]. Moreover, to understand these layered optical

properties *vis-a-vis* the limitations of the SDA, in Fig. 2e we plot the wavelength dependence of the ratio of the reduced scattering coefficient to the absorption coefficient (μ_s'/μ_a) for each of these layers as well as the top layer thickness normalized to the transport mean free path in Fig. 2f. Rather than attempt to mimic a specific tissue system, these phantoms were constructed to provide a range of optical parameters and layer thicknesses germane to layered tissue structures (e.g., epithelial tissues) and superficial tissue injury (e.g., burn wounds)[31]. Fig. 2 e–f show that these properties span many ratios of scattering to absorption (from ∼4:1 to ∼100:1 within a given layer) and layer thickness to l^* (from 10:7 to 10:1), while Fig. 2 a–d show that either the top or bottom layer can possess the dominant reduced scattering and/or absorption coefficient depending on the wavelength considered.

SFDS measurements were made on six combinations of top and bottom layer phantoms. Each of the three bottom phantoms were measured with either the 90 or 300 μm thick phantom placed on its top surface. Prior to measurement, all air gaps between the two layers squeezed out through mechanical pressure. SFDS measurements were acquired at 51 spatial frequencies over the range of $0-0.5$ mm^{-1} range. Three sets of measurements were acquired from each two layer phantom configuration. Each set was carried out at a slightly displaced spatial location to average out any potential minor spatial variations in the phantom optical properties. The top and bottom layers were then separated and the top layer was then attached to the another bottom layer phantom. This procedure was carried out for all combinations of top and bottom layers, resulting in data from six distint layered phantom systems. A calibration measurement, using a reference phantom having well characterized optical properties, was performed between each layered phantom[58, 61] measurement.

The phantoms were designed with optical property ranges in absorption $\left(\mu_a = 0.01\text{–}0.2\,\text{mm}^{-1}\right)$ and reduced scattering $\left(\mu_s' = 0.5\text{–}1.3\,\text{mm}^{-1}\right)$ coefficients that span those of many soft biological tissues in the visible and near infrared spectral range[31]. While the reduced scattering

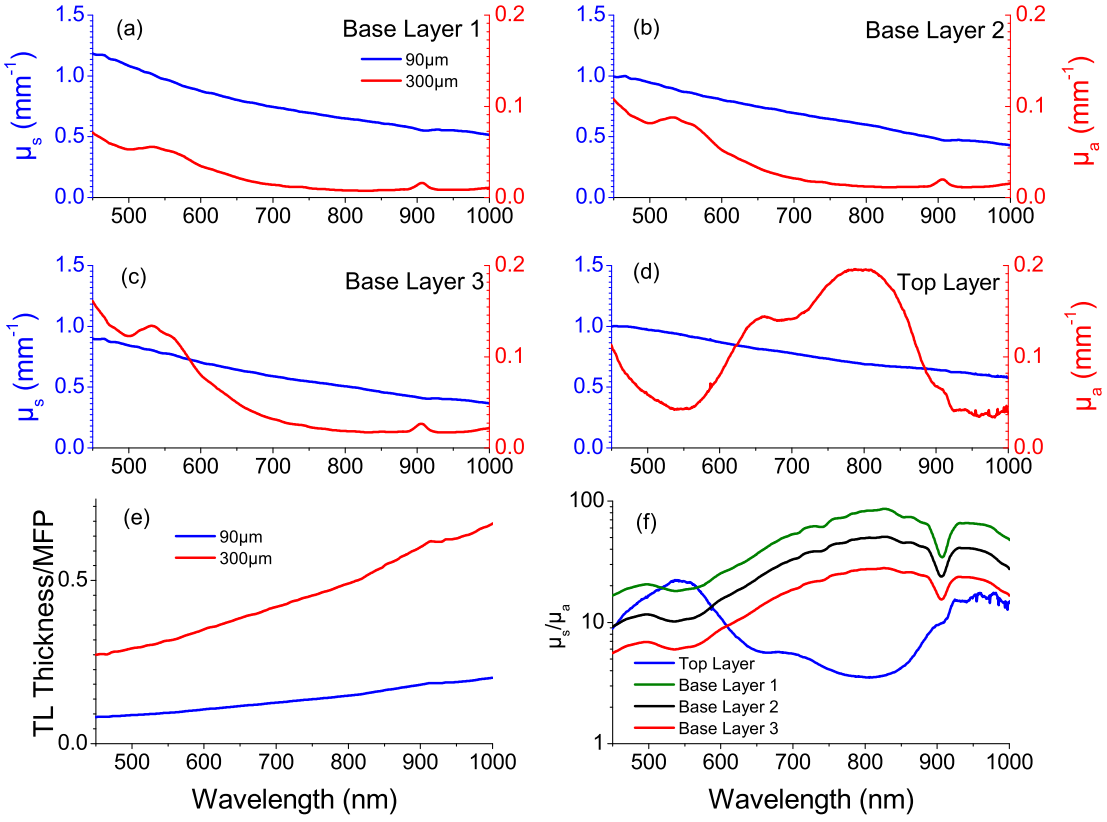

Figure 5.2: Optical properties of the phantoms. (a–d) depict the reduced scattering coefficient (left axis) and absorption coefficient (right axis) spectra of the top layer (a) and the three possible base layers (b-d) of each phantom. (e) provides the top layer thickness normalized by the transport mean free paths for both 90 μm (blue) and 300 μm (red) thicknesses of the top layer. (f) depicts the relative scattering to absorption strength of each layer on a log10 scale. The green curve shows the top layer, the black shows base layer 1, the red shows base layer 2 and the blue shows base layer 3.

coefficient is dominant over absorption in both layers and across all wavelengths tested, we explore regimes where that dominance is more pronounced in either the top or the bottom layer and systems with top layer thickness far less than the transport free mean path.

5.2.3 SFD Sensitivities and Design of Multi-Stage Optimization Algorithm

For analysis of this two-layer phantom system, we assume knowledge of layer thickness and attempt to recover four optical properties at each wavelength, namely the absorption and reduced scattering coefficient in each layer. *A priori* knowledge of layer thickness is a reasonable assumption as existing approaches are available for its estimation using SFDS instrumentation[61, 57]. Rather than attempting to fit all parameters simultaneously, we perform a multi-stage algorithm to isolate and refine the spectra of each optical property. The design of our algorithm is inspired by our prior development of multi-staged inversion algorithms[25, 63] and the spatial frequency dependent sensitivity of the measured reflectance to the absorption and reduced scattering coefficients in each layers shown below in Fig. 3.

We present the spatial frequency dependent reflectance sensitivities with respect to each optical property for a top layer thickness of 300 μm, which is equivalent to the thicker of the layered phantom systems measured in this study. We compute these sensitivities for varying contrast in reduced scattering coefficient between the top and bottom layers. Specifically, we fix the bottom layer properties at $\mu_{s,b}^{'} = 1$ mm^{-1}, $\mu_{a,b} = 0.1$ mm^{-1} and vary top layer reduced scattering properties while matching the absorption properties with the bottom layer. The variations in top layer scattering that we explore span $\mu_{s,t}^{'} = [0.4, 0.7, 1, 1.3, 1.6] \times \mu_{s,b}^{'}$ with fixed top layer absorption ($\mu_{a,t} = 0.01$ mm^{-1}).

In Figure 3a–d, we show the spatial-frequency dependent reflectance sensitivities to (a) bottom layer absorption; (b) top layer absorption; (c) bottom layer reduced scattering;

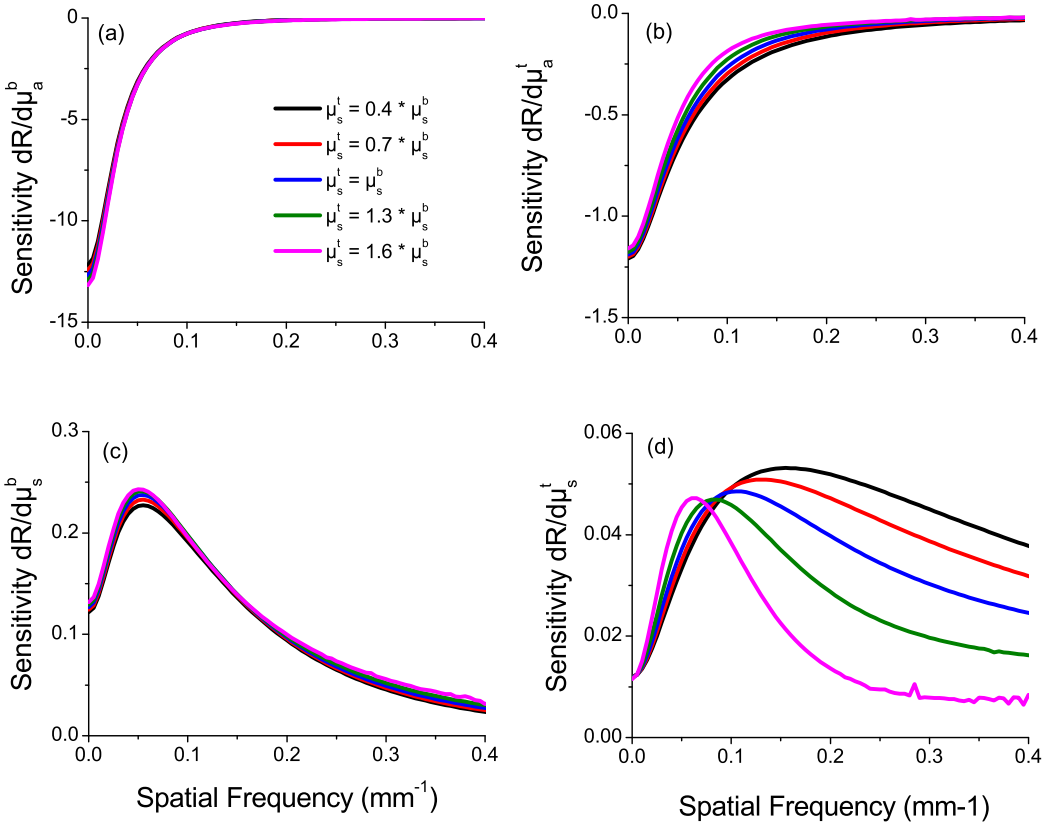

Figure 5.3: Reflectance sensitivities with respect to (a,b) absorption and (c,d) reduced scattering coefficient for (a,c) bottom and (b, d) top layers, respectively, as a function of spatial frequency for a top layer thickness of 300 μm. In each plot, the black line indicates the case where $\mu'_{s,t} = 0.4 \times \mu'_{s,b}$. The red line indicates $\mu'_{s,t} = 0.7 \times \mu'_{s,b}$, the blue indicates $\mu'_{s,t} = \mu'_{s,b}$, the green indicates $\mu'_{s,t} = 1.3 \times \mu'_{s,b}$ and the magenta indicates $\mu'_{s,t} = 1.6 \times \mu'_{s,b}$.

and (d) top layer reduced scattering coefficients. We note that reflectance sensitivity to either top or bottom layer absorption is maximized at the lowest spatial frequencies and drops by an order of magnitude once spatial frequencies exceed approximately 0.08 mm^{-1} for the bottom layer and 0.13 mm^{-1} for the top layer. Interestingly, in absolute terms, the reflectance sensitivity to top layer absorption is roughly an order of magnitude smaller than that for bottom layer absorption in this low spatial frequency regime. Moreover, the reflectance sensitivity to absorption in either layer is weakly dependent on the scattering contrast between the layers.

The spatial frequency dependent reflectance sensitivity to the reduced scattering coefficient in either top or bottom layers shows a distinct peak at a non-zero spatial frequency. The location of the peak sensitivity for the bottom layer is fixed at 0.06 mm^{-1} while the location of this peak for top layer scattering shifts from 0.06 to 0.16 mm^{-1} as the scattering contrast moves from being top layer dominant ($\mu_{s,t}^{'} = 1.6\times\mu_{s,b}$) to bottom layer dominant ($\mu_{s,t}^{'} = 0.4\times\mu_{s,b}$). In absolute terms, the reflectance sensitivity to scattering in the bottom layer can be as much as 5$\times$ larger than the top layer sensitivity in this low spatial frequency regime. However, at higher spatial frequencies exceeding $f_x = 0.3$ mm^{-1}, the reflectance sensitivity to top and bottom layer scattering becomes comparable.

These sensitivity features motivate the design of an inversion algorithm using four stages, each focused on the determination of specific optical parameters. In each stage we consider measured reflectance values at specific spatial frequencies and 32 equispaced wavelengths spanning λ = 450–1000 nm. Using the `lsqcurvefit` function in MATLAB, we seek to determine optical parameters values that minimizes the least squares difference between a $SHEF_N$ computation[21] for the SFD reflectance and the actual measurements. For the $SHEF_N$ computation we consider a 9th order expansion of spherical harmonic functions which provides a good balance between accuracy and computation expense. We will refer to this as a $SHEF_9$ computation for the remainder of the paper. We also chose to consider

only 32 discrete wavelengths from the multi-spectral dataset since it provides a good balance between spectral detail and computational expense. For the $SHEF_9$ computations we assume a single scattering anisotropy of 0.8 for both layers[31].

The details of the four stage process are as follows:

Stage 1: Recovery of layer specific reduced scattering spectra. In stage 1 we obtain estimates for the reduced scattering coefficient spectra of the top and bottom layers. Because the sensitivity to the top layer relative to the bottom layer increases at larger spatial frequencies (Fig. 3c,d), we choose to analyze separately SFDS data obtained at six spatial frequencies from two different spatial frequency bands ($f_{x1} = [0, 0.02, \ldots, 0.1]\,\mathrm{mm}^{-1}$ and $f_{x2} = [0.3, 0.32, \ldots, 0.4]\,\mathrm{mm}^{-1}$). For each frequency band, we analyze the SFDS reflectance spectra using a $SHEF_9$ computation for a *homogeneous* medium and determine the values for absorption and reduced scattering coefficients that result in a best fit. The presumption here is that the reduced scattering properties obtained from the f_{x1} spatial frequency band will be representative of the bottom layer while those obtained from the f_{x2} spatial frequency band will be representative of the top layer. For simplicity, we assume the spectral dependence of scattering to be governed by an inverse power law[28] $\mu_s^{'}=A(\lambda/\lambda_0)^{-b}$, where A is the reduced scattering coefficient for $\lambda_0 = 750$ nm. We discard predictions for optical absorption from this stage.

Stage 2: Recovery of layer specific absorption spectra. In stage 2 we aim to recover estimates for the absorption coefficient spectra of both top and bottom layers. We fix the reduced scattering spectra for the top and bottom layers to those obtained via the Stage 1 analysis of SFDS data in high and low spatial frequency bands, respectively. To obtain absorption spectra specific to both top and bottom phantom layers, we consider the SFDS spectral data at spatial frequencies of $f_x = 0.01$ and $0.02\ \mathrm{mm}^{-1}$ only. We choose these spatial frequencies since our analysis in Fig. 3 reveals that the reflectance sensitivity to absorption in either layer is maximized at lower spatial frequencies. Moreover, since the reflectance

sensitivity to top layer absorption decays with spatial frequency more gradually than the bottom layer, the SFDS data at $f_x = 0.02\,\mathrm{mm}^{-1}$ provides differentially more sensitivity to top layer absorption relative to that obtained at $f_x = 0.01\,\mathrm{mm}^{-1}$. Given that the absorption properties of most deep tissue layers are well characterized by a linear combination of the absorption spectra of oxyhemoglobin, reduced hemoglobin, water, and lipid[45], we assume that the spectral shape of the absorption spectra in the bottom layer is known *a priori*. For the top layer, we adopt a more general approach and do not impose any assumptions regarding the shape of the absorption spectra. We again apply the SHEF_9 algorithm, with a two-layer tissue geometry with known top layer thickness (90 or 300 μm). We fit the SFDS data to the SHEF_9 predictions by determining the optimal absorption coefficient values for layers 1 and 2 while holding fixed the top and bottom layer reduced scattering coefficient spectra obtained in Stage 1.

Stage 3: Refinement of bottom layer reduced scattering spectra. In stage 3, we aim to refine bottom layer reduced scattering spectrum obtained in Stage 1. We use SFDS data obtained at $f_x = 0.06$ and 0.15 mm^{-1}. These spatial frequencies are chosen since 0.06 mm^{-1} represents the spatial frequency that is maximally sensitive to bottom layer scattering while 0.15 mm^{-1} retains significant sensitivity to bottom layer scattering while also effectively eliminating sensitivity to both top and bottom layer absorption. We fix the properties obtained from Stage 1 for the reduced scattering spectrum in the top layer and from Stage 2 for top and bottom layer absorption spectra. We drop our constraint for the bottom layer reduced scattering spectra to abide by an inverse power law and perform the fit of the SFDS data to predictions provided by the layered SHEF_9 model for each wavelength independently.

Stage 4: Refinement of top layer absorption spectra. The goal of the final stage is to improve the fit of top layer absorption. As in Stage 2, we again use SFDS data from $f_x = 0.01$ and 0.02 mm^{-1} and find the top layer absorption values at each wavelength that

produces predictions from our layered $SHEF_9$ model that best match the data. We fix the top layer reduced scattering spectrum to that obtained in Stage 1, bottom layer absorption spectrum to that obtained in Stage 2 and bottom layer reduced scattering to that obtained in Stage 3. For our initial guess, we use the top layer absorption spectrum obtained from Stage 2.

5.3 Results

5.3.1 Stage 1: Recovery of layer specific reduced scattering spectra

Phantom 1: We show the results for Phantom 1 in Fig. 4a (bottom layer scattering) and 4d (top layer scattering). The corresponding errors of these estimates are shown in Figs. 5a and 5d, respectively. For the 300 μm thick top layer, the error in bottom layer reduced scattering is typically 0.1 mm^{-1} except for $\lambda > 450$ nm where it is = 0.14 mm^{-1}. The error in the recovery of the 300 μm thick top layer reduced scattering coefficient is largest at $\lambda = 450$ nm at 0.256 mm^{-1} and steadily declines for larger wavelengths. For $\lambda > 557$ nm the error in recovery of the 300 μm thick top layer reduced scattering is < 0.1 mm^{-1}. For the 90 μm thin top layer phantom, error in bottom layer reduced scattering is worst at $\lambda = 628$ nm where $\mu_s^{'}$ is underestimated by 0.1 mm^{-1} with smaller errors occurring at all other wavelengths. The maximal error in recovery of the 90 μm thin top layer reduced scattering is 0.19 mm^{-1} at λ=450 nm and is reduced at all other wavelengths with errors < 0.1 mm^{-1} for λ 521 nm.

Phantom 2: The results for Phantom 2 are shown in Fig. 4b (bottom layer scattering) and 4e (top layer scattering.) Error is shown in Fig. 5b for top layer scattering and in Fig. 5e for bottom layer scattering. For the thick top layer, the error in the bottom layer reduced scattering error is < 0.1 mm^{-1} for all wavelengths, and < 0.05 mm^{-1} for all wavelengths

apart from $\lambda = 450$nm, where it is 0.076 mm^{-1}. The maximal error in estimation of the 300 μm thick top layer reduced scattering is 0.15 mm^{-1} at $\lambda = 450$ nm, and falls below 0.1 mm^{-1} for λ 503 nm with typical errors of 0.06 mm^{-1}. For the 90 μm thin top layer, a maximal error in the estimation of the bottom layer reduced scattering coefficient is 0.11 mm^{-1} occurring once again at $\lambda = 450$ nm. For λ 503 nm, this error is < 0.05 mm^{-1}. Top layer reduced scattering error for the 90 μm thin top layer is within ± 0.05 mm^{-1} at all wavelengths.

Phantom 3: Figures 4c (bottom layer scattering) and 4f (top layer scattering) provide the results from Phantom 3. Error is shown in Figs. 5c and 5f, respectively. For the 300 μm thick top layer, error in the recovery of the bottom layer reduced scattering is between –0.05 mm^{-1} and 0 at all wavelengths. Top layer reduced scattering error remains within ± 0.07 mm^{-1}. For the 90 μm thin top layer phantom for bottom layer reduced scattering is underestimated by 0.05 mm^{-1} for all wavelengths. Error in the top layer reduced scattering is within ± 0.05 mm^{-1} for all wavelengths.

5.3.2 Stage 2: Recovery of layer specific absorption spectra

In stage 2 we determine the magnitude of a pre-defined spectral shape for bottom layer absorption and an initial estimate for the top layer absorption spectrum. Table 1 provides the results for bottom layer absorption coefficient for each phantom. A recovered coefficient value of $\beta = 1$ represents perfect recovery. For all phantoms with the 300 μm thick top layer, error in the recovery of μ_a was $< 5\%$. For Phantoms 1 and 2, the error is $< 1\%$, and for Phantom 3, the error is approximately 4.5%. For the 90 μm thin layer phantoms, we recover the β value with less than 9% error overall. Specifically the error in the estimation of the bottom layer absorption in Phantoms 1, 2, and 3 being 3.6, 6.2, and 8.1%, respectively.

We show the initial estimates for top layer absorption in Figs. 4g–i. It is important to

remember that this is an intermediate step; the top layer absorption spectra obtained here will be refined in stage 4. We comment on the accuracy of these estimates at four sets of wavelengths: λ=450 nm, 450−600 nm, 600−850 nm, and >850 nm. For λ = 450 nm, recovery of μ_a for the 300 μm thick top layer phantom is overestimed between 0.04 and 0.08 mm^{-1}, while the 90 μm thin top layer phantoms experience very small errors (0.01 mm^{-1}). For λ = 450−600 nm, the reference data for absorption drops to μ_a 0.07 mm^{-1}, at which point the method experiences difficulties in recovering the correct value, which often results in an extreme underestimation of the absorption. Typically, recovery of μ_a for the 300 μm thick top layer is worse than for the 90 μm thin layer. Here, error for μ_a in 300 μm thick top layer phantoms is between 0.04 and 0.05 mm^{-1}, while that of the 90 μm thin top layer phantoms is near 0.03 mm^{-1} for Phantoms 2 and 3. Interestingly, recovery of μ_a for the 300 μm thick top layer in Phantom 1 is accomplished with much smaller error than its counterparts with Phantoms 2 and 3, while the recovery of μ_a in Phantom 3 with the 90 μm thin layer has negligible error. For λ = 600–850 nm, the reference data for μ_a experiences a "double hump" with values between 0.01 and 0.02 mm^{-1}. Despite some underestimation, this spectral structure is well recovered in the inversion results for each phantom. Errors for μ_a in 300 μm thick top layer phantoms in this region are between 0.02 and 0.05 mm^{-1}, with best performance for Phantom 1. Cases with the 90 μm thin layer have larger error for μ_a at the shorter wavelengths and less at longer wavelengths when compared to 300 μm thick top layer phantoms. These error rates stay in the same general range as those for the 300 μm thick top layer phantoms, but tend more towards 0.05 mm^{-1}. For λ > 850 nm, the reference data for μ_a experiences a drop off similar to when λ = 450−600 nm, falling as λ increases until it levels off near 0.05 mm^{-1}. We see a similar underestimation for μ_a in most phantoms in this spectral regime, though here it is more pronounced in the cases with the 90 μm thin top layer. Interestingly, when Phantoms 2 and 3 have 300 μm thick top layers, the inversion results are less stable, involving a peak overestimation for μ_a near λ = 900 nm and a peak underestimation near λ = 950 nm. Error for μ_a here ranges for all phantoms between

± 0.05 mm^{-1}. When considering the combined results across all wavelengths, it is important to note that the general shape of the μ_a spectrum is recovered in each phantom, generally within ± 0.05 mm^{-1}, while significant underestimations are made when $\mu_a < 0.075$ mm^{-1}. Interestingly, recovery of the absoption spectra for the 90 μm thin top layer phantoms tend to experience smaller absolute errors than for the 300μm thick top layer phantoms when λ 700 nm, while the opposite is true for $\lambda > 700$ nm.

Table 5.1: Coefficients (β) of the assumed absorption spectrum recovered for each base layer choice and top layer thickness. Since the spectrum being fit is the reference data for bottom layer absorption, $\beta = 1$ indicates perfect recovery.

Base Layer	90μm Top Layer β	300μm Top Layer β
1	1.04	1.00
2	0.94	0.99
3	0.92	0.95

5.3.3 Stage 3: Refinement of bottom layer reduced scattering spectra.

The aim of stage 3 is to improve the initial estimates for bottom layer reduced scattering coefficient spectra obtained in stage 1. We show the results for stage 3 in Fig. 4j–l, and the relative error rates in Fig. 5j–l. In all phantoms, error in the recovery bottom layer μ_s' was reduced at nearly all wavelengths and with structure of the scattering spectra more faithfully recovered as compared to the results in Stage 1. Fig. 4j shows the results for phantom 1. The reduced scattering coefficient spectrum for the 300μm thick top layer phantom was recovered with an absolute error of 0.02 mm^{-1} with the exception of an error of 0.06 mm^{-1} at $\lambda = 450$ nm. The 90 μm thin top layer phantom performed slightly worse, with an underestimation of the reduced scattering coefficient by 0.07 mm^{-1} at $\lambda = 450$nm and errors of $\pm$ 0.04 mm^{-1} at all other wavelengths. Fig. 4k shows the results for Phantom 2. The absolute error for

the reduced scattering coefficient for thick top layer phantom was limited to $\pm$ 0.05 mm^{-1} except for $\lambda = 450$ nm where the error was 0.06 mm^{-1}. Recovery of the reduced scattering coefficient for thin top layer phantom was slightly better with error of $\pm$ 0.05 mm^{-1}. Fig. 4l shows results in the recovery of the bottom layer reduced scattering for Phantoms 3. The performance for both thick and thin top layers is similar with scattering estimated with an error of 0.05 mm^{-1} across the full spectral region.

5.3.4 Stage 4: Refinement of top layer absorption spectra

The aim of stage 4 is to improve the estimates for top layer absorption obtained in stage 2. We show these results Fig. 4(m–o) and the absolute error of these estimates in Fig. 5(m–o). We consider these results relative to those obtained in μ_a in stage 2.

Phantom 1: The recovered absorption spectra for the top layers in phantom 1 are shown in Fig. 4m, with error in Fig. 5m. We obtain improvements in the predicted absorption spectra for both thick and thin layers as compared to the results obtained in Stage 2 (shown in Figs. 4g,5g). The overestimation for μ_a found in the case of the thick top layer at $\lambda = 450$ nm is approximately 0.03 mm^{-1}, while the error remains minimal for the case of the thin top layer. We see that error for μ_a is likewise reduced for both the thin and thick top layer cases with improvements between 0 and 0.02 mm^{-1} in the $\lambda = 450-600$ nm spectral region. We see greater improvements in μ_a error in the $\lambda = 600-850$ nm wavelength intervals, particularly for the thick top layer with improved accuracy with μ_a errors generally below $\pm$0.03 mm^{-1} for the thick top layer and 0.04 mm^{-1} for the thin top layer. For $\lambda > 850$ nm we obtain slightly worse results until $\lambda = 920$ nm after which the errors obtained in Stages 2 and 4 are essentially equivalent. The absorption spectra obtained for Phantom 1 in Stage 4 improves upon Stage 2 for the entire interval of $\lambda = 450-920$ nm, beyond which the recovery is equivalent. Errors in the recovered top layer absorption are limited to 0.04 mm^{-1} for λ

= 450−920 nm.

Phantom 2: Recovery of top layer absorption spectra in Phantom 2 is shown in Fig. 4n, with absolute error shown in Fig. 5n. For the case with the thick top layer, we see overall improvement in capturing the shape of the absorption spectra with slight reductions in the absolute error. This is seen particularly as a lower (by 0.02 mm^{-1}) overestimation of μ_a when $\lambda = 450$ nm, and a less pronounced underestimation in the $\lambda = 450-600$ nm range (despite having a similar minimum). The "double hump" of μ_a is once again captured in the $\lambda = 600-850$ nm spectral range, with smaller (between 0 and 0.01 mm^{-1} reduction) underestimation for the thick top layer phantom. For $\lambda > 850$ nm, both thick and thin top layer phantoms experience a sharp decline as λ increases, ending in the near 0 values observed earlier. This is in contrast to the thick top layer performance from Stage 2, which involved an overestimation of μ_a when $\lambda = 880-920$ nm. Errors remain similar in absolute value to those of Stage 2, but are more uniform across wavelength and better represents the overall shape of the reference absorption spectrum.

Phantom 3: Recovery of top layer absorption spectra in Phantom 3 is shown in Fig. 4o, with absolute error shown in Fig. 5o. For the thick top layer phantom, the initial overestimation at $\lambda = 450$ nm is actually worse, increasing to 0.05 mm^{-1} as compared to 0.04 mm^{-1} in Stage 2. While the absolute error is worse in many spectral regions, the recovered spectral shape is better captured as compared to Stage 2 and we underestimate the absorption by only 0.05 mm^{-1} in the case of the thick top layer phantom at $\lambda = 588$ nm, with a smaller underestimation (0.03 mm^{-1}) for the thin top layer phantom. Absolute error in absorption stabilizes to within ± 0.04 mm^{-1} for $\lambda = 605-795$ nm. For longer wavelengths we recover a more accurate spectral shape for the case of the thick top layer and comparable results for the case of the thin layer as compared to Stage 2. This manifests in the same way it does for Phantom 2, with an elimination of the overestimation found in Stage 2, once again resulting in a more accurate recovery of the spectral structure of μ_a.

5.4 Discussion

Our method demonstrates the broad recovery of the bottom layer absorption and reduced scattering coefficients as well as the top layer reduced scattering coefficients across all wavelengths. Moreover, there are specific spectral regions in which the top layer absorption is reliably recovered. Specifically, bottom layer values for the reduced scattering coefficient are generally within 5% of the reference values. Moreover, bottom layer absorption coefficients are typically recovered within the 5% range with a worst case error of 8.1%. Similarly, the top layer reduced scattering coefficient values obtained in stage 1 are typically within 10% of known values. In each case, the general spectral shape of the top layer reduced scattering spectrum is recovered. Typically, the maximum error for the top layer reduced scattering coefficient is observed at $\lambda = 450$ nm which may be indicative of the limitations of using a single inverse power law across the entire wavelength range. Attempts to further improve the fit for top layer scattering without *a priori* assumption for the spectral shape of the top layer reduced scattering coefficient have not been reliably successful. We believe that these problems stem primarily from the intrinsically low measurement sensitivity to top layer parameters, as shown in Fig. 3. Specifically, the reflectance sensitivities to top layer reduced scattering and absorption coefficients are roughly an order of magnitude smaller than the corresponding bottom layer parameters and compromises our ability to obtain accurate measures for top layer optical properties. However, we note that the spatial frequency at which we have maximal sensitivity to the top layer reduced scattering coefficient (Fig. 3d) changes based on the scattering contrast between the two layers. Therefore, improvements in the recovery of top layer scattering in Stage 3 may be obtained by an inversion approach that adaptively selects data from different spatial frequencies. These frequency selections must provide sufficient sensitivity and specificity to enable differentiation between top and bottom layer properties based upon preliminary estimates obtained from Stage 1.

The greatest need for improvement of our algorithm pertains to the recovery of the top layer

absorption spectra. It should be noted that the top layer thicknesses tested have exceeding small absorption optical densities in the range 10^{-3}–10^{-1}. We believe that the difficulties in the recovery of top layer absorption stem from the same causes that hamper the recovery top layer reduced scattering. Recovery of top layer absorption is further compromised by the fact that the reflectance sensitivity to both top and bottom layer absorption is maximized at the similar spatial frequencies. This limits the use of spatial frequency selection to provide differential absorption sensitivity to one layer versus the other. Unfortunately, the shapes of absorption spectra vary greatly between different molecules, as compared to scattering spectra for different scatterers[23]. Moreover, the greater multiplicity of absorbers that reside in superficial tissue layers[74] preclude the use of simplifying assumptions for the spectral shape of the top layer absorption coefficient. The most problematic feature in the recovered absorption coefficient spectra are the near zero values that appear at many wavelengths.

Interestingly, the recovery of near zero absorption values occuring for $\lambda = 520$–$570\,\text{nm}$ for $300\,\mu\text{m}$ layer phantoms do not appear as commonly in the results for the $90\,\mu\text{m}$ layer phantoms. This is counterintuitive, though it may be due to the fact that a larger absorption coefficient in thin layer will have a similar impact on the measured reflectance as a smaller absorption coefficient in a thicker layer. This, combined with smaller errors in other parameters, may explain why we do not see such severe underestimates in the top layer absorption for the $90\,\mu\text{m}$ layer phantoms at these wavelengths. While we can find no single perfect predictor for this phenomenon in any reference spectrum, it appears only when the top layer absorption falls below $0.075\ \text{mm}^{-1}$. When top layer absorption is above these values, results are much better, with typical errors in the 15–30% range. Indeed, the refinement in the top layer absorption spectra in Stage 4 generally results in improved recovery, particularly in the $\lambda = 450$–$600\,\text{nm}$ spectral region. For $\lambda = 600-850$ nm, we generally observe reduction in error for all phantoms. This wavelength interval carries useful information for chromophores such as oxy and deoxyhemoglobin and our method produces reliable results in this wavelength range. It is also possible that the use of oblique incident radiation and measurement

of spatial phase shifts may provide more sensitivity to top layer optical parameters[21, 4] and this may be a subject for future investigation.

Comparison of our results to other studies using analytical approaches is challenging since none have provided accurate results in systems where the top layer thickness l^* while we have exclusively focused on layered systems with top layer thicknesses in the range of $0.1-0.8l^*$. The performance of our staged algorithm competes favorably as compared to those reported in previous perturbation Monte Carlo methods[64]. However, those studies focused on optical property recovery at a single wavelength as opposed to multi-spectral recovery of optical properties. Published studies using LUT based methods[18, 77] involved biologically simplifying assumptions such as uniform scattering properties across all layers. Such methods will also have difficulty as the number of unknown parameters increases, due to the relationship between dimensionality of the required lookup table and the requirements to generate and store such tables. Multi-stage algorithmic approaches using non-linear optimization methods such as the one that we have presented, should experience more linear growth in complexity as additional parameters are introduced. In such algorithms, each stage provides an initial estimate for the parameter values, or refines an earlier fit for a limited number of parameters, rather than having to determine all the unknown parameters simultaneously. Moreover, our SHEF_9 forward solver can easily implement alternate single scattering phase functions without changes in the underlying inversion algorithm. By contrast, consideration of alternate single-scattering phase functions or even a different single scattering anisotropy value would necessitate perturbation MC or LUT methods to generate entirely new sets of photon biographies or tables.

5.5 Conclusion

We present a staged inversion algorithm using an approximate deterministic RTE solver to recover the optical properties of layered media using SFDS data over a broad range of wavelengths. Our approach assumes a known top layer thickness and knowledge of the wavelength dependence of the bottom layer absorption coefficient. Bottom layer absorption and reduced scattering coefficients are recovered within 10% error, with the majority of error being $< 5\%$. Top layer absorption properties are recovered with 15–30% error within the $\lambda = 600$-–800 nm spectral window. This method provides accuracy comparable to current perturbation Monte Carlo methods that have provided recovery of optical properties at single wavelengths and is able to recover the optical properties of a top layer with thickness down to $l^*/10$.

This method is scalable to allow the recovery of optical properties at any number of wavelengths. In this regard, the ability to perform fits on multi-/hyperspectral data sets is limited solely by the available computational power and need for rapid processing. If computational power is limited, future work to improve the efficiency of stage 2 should be prioritized as this stage involves a multi-spectral inversion of dimension equal to the sum of the number of wavelengths in the data set and the number of chromophore concentrations to be determined. This is in contrast to the lower dimensional fits performed in all other stages of this inversion scheme.

Our method achieved these levels of accuracy while requiring far less computational expense when compared to current Monte Carlo based methods. Moreover, our approach dispenses with many unrealistic assumptions used in the construction of Monte Carlo look up tables e.g., assuming uniform scattering properties across layers. The use of the SHEF$_N$ radiative transport solver[21] provides a computational flexibility that allows for the use of different scattering phase functions with ease. In addition, the lack of a lookup table and more modest

growth in computational expense with an increase in the number of unknown parameters potentially allows this approach to be applied to tissues of much greater complexity. When compared to other analytic solvers, particularly those using the standard diffusion approximation, we have enabled the capacity to obtain optical properties from both layers of a multi-layered tissue with layer thicknesses $< l^*$ [34, 33**?**]. In fact, we are unaware of other existing approaches that makes use of analytic solvers to recover optical absorption and scattering parameters layered tissues with characteristic layer thickness $< l^*$ from multispectral data.

Future work to improve accurate recovery of the top layer absorption spectrum will focus on eliminating the need to assume a known top layer thickness, which is common across many methods[64, 43, 77]. The elimination of these problems would be useful for any application which relies on sensitive and accurate recovery of these parameters. We believe that algorithms that implement adaptive selection of data at specific spatial frequencies based on reflectance sensitivity characteristics would be of particular use, particularly since these characteristics vary significantly with the ratio of reduced scattering between the top and bottom layers. The selection of optimal spatial frequencies when using an adaptive inversion approach can be informed by the calculation of sensitivity curves such as those presented in Fig. 3.

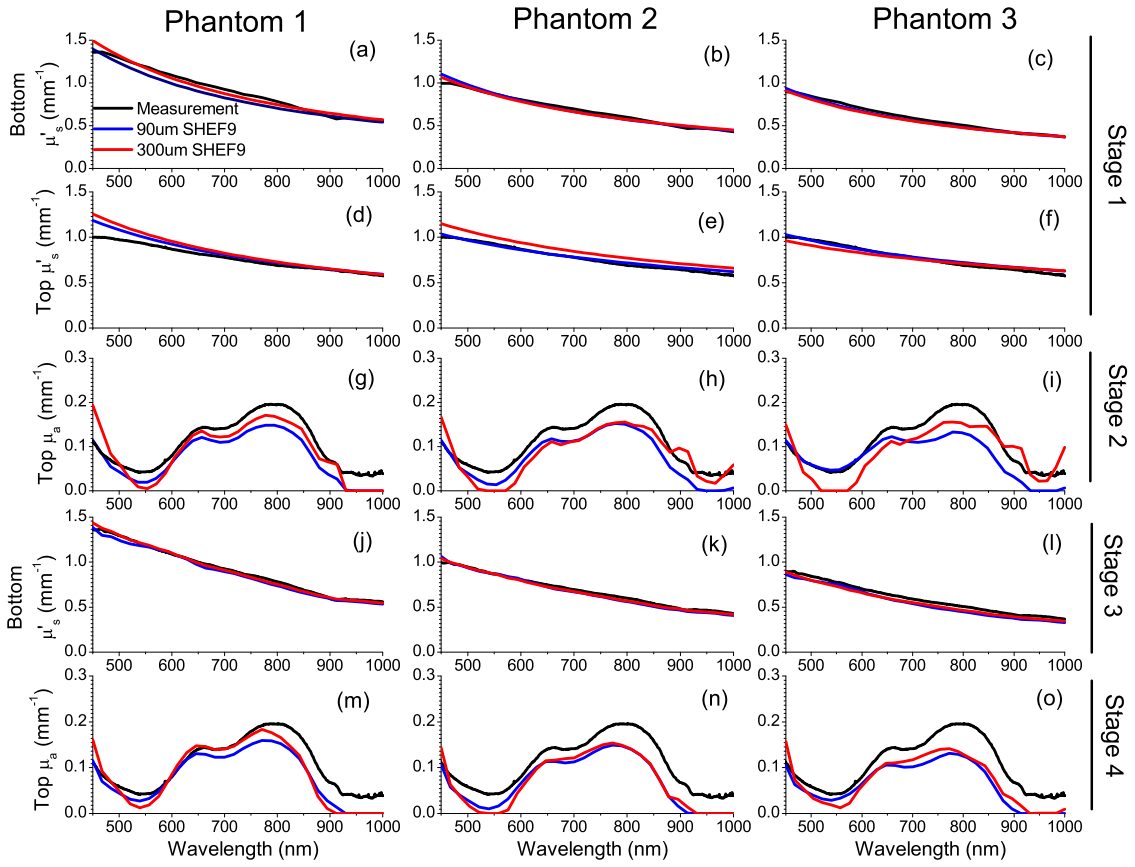

Figure 5.4: Inversion results. In all graphs, reference data is shown in black, SHEF_9 results for a 90 μm top layer are shown in blue and SHEF_9 results for a 300 μm top layer are shown in red. (a–f) show the stage 1 results, in which initial guesses for top and bottom layer scattering spectra are recovered. (a–c) show the reference scattering spectra for their respective base layers, and homogeneous SHEF_9 results for data taken with the f_{x1} spatial frequency band. (d–f) show the reference scattering spectra for the top layer alone and the homogeneous SHEF results using data from the f_{x2} spatial frequency band. (g–i) show the top layer absorption spectra fits from Stage 2, using results from stage 1 for top and bottom layer scattering. (j–l) show the stage 3 results in which recovery of the bottom layer reduced scattering coefficient spectrum is refined. (m–o) provide the stage 4 results which provides the final result for the top layer absorption spectrum.

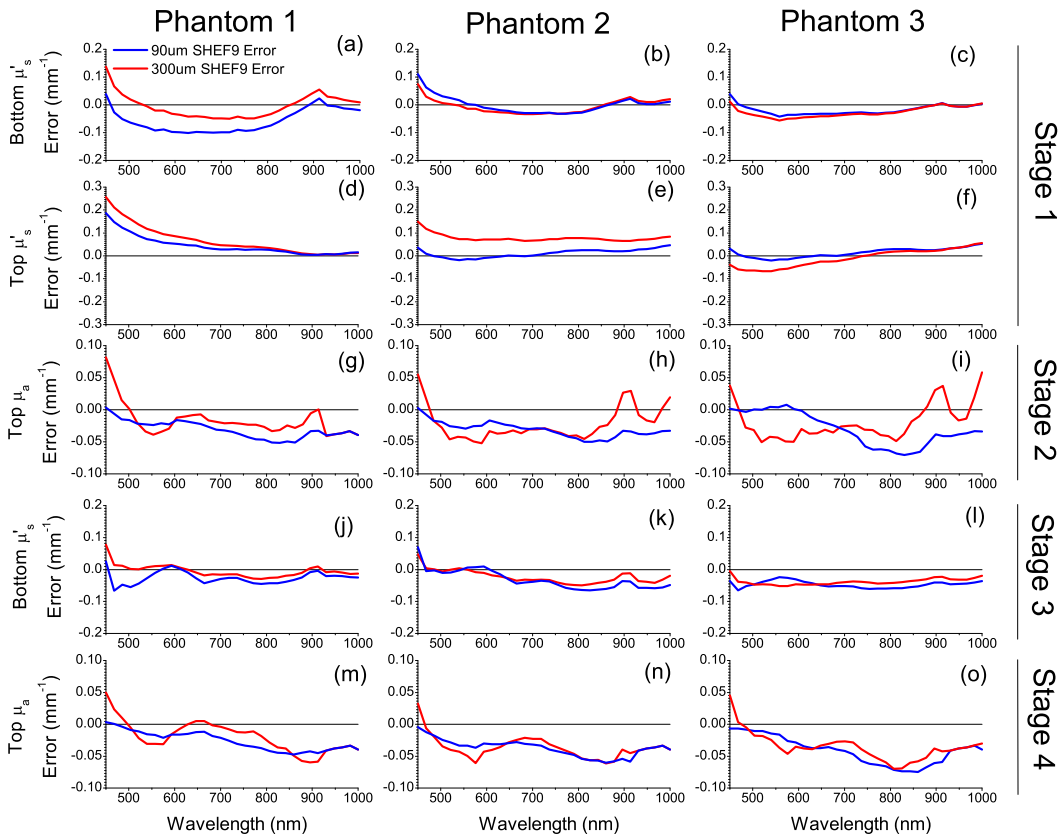

Figure 5.5: Errors of inversion results. Each subfigure shows the error for thick top layer (red) and thin top layer (blue) phantoms corresponding to the results from the same subfigure shown in Figure 4.

Chapter 6

Extensions and Future Directions

6.1 Introduction

In the previous chapters I have detailed both a mathematical justification and a MATLab implementation of DSHEF$_N$ in a layered medium, as well as a staged inversion technique which utilizes single SHEF$_N$ and data gathered from Spatial Frequency Domain Spectroscopy to recover the optical properties of two layered tissue phantoms. These two, taken together, lay out one immediate future direction and several more distant ones.

In the immediate sense, the application of DSHEF$_N$ to optical property recovery through methods like SFDI/S is an obvious continuation of this work. I have shown that DSHEF$_N$ provides robust results for a larger regime of optical properties and spatial frequencies. However, a deeper understanding of the structure of the eigenvectors used in the homogeneous solution detailed by equation (2.36), as well as a rigorous analysis of the sensitivities of the model with respect to the optical properties of each layer would be helpful in selecting optimal parameters for simulation.

6.2 DSHEF$_N$ Spectral Structure

Understanding the structure of the eigenvectors used in DSHEF$_N$'s homogeneous solution is identical to understanding the spectral content of DSHEF$_N$. As mentioned in Chapter 3, the nature of DSHEF$_N$'s solution as a linear combination of vectors decaying exponentially in z means that as z increases, the vector or vectors (in the case of degeneracy) with the slowest rates of decay, which in the homogeneous solution corresponds to the vectors related to the greatest negative eigenvalues. This is particularly clear in Section 3.4.5, where the unbalanced ratio of fluence directed in the negative z direction to total fluence does not match prediction by the commonly used Standard Diffusion Approximation, but does match predictions by the dominant eigenvectors presented by both single SHEF$_N$ and DSHEF$_N$. These vectors commonly have significant quadratic or cubic terms, showing that not only is the Standard Diffusion Approximation flawed even for $z >> l^*$, there can be interesting structure to radiance distributions at any point deep within a medium.

The fact that predictions of the behavior of radiance can be made simply from an examination of eigenvectors is important for two reasons. First, it provides phenomenological evidence for the validity of both single SHEF$_N$ and DSHEF$_N$. Second, it shows that important information may be gleaned directly from the spectral structure of the problems presented by these methods.

The first test of convergence of DSHEF$_N$ is that of this so called dominant vector to the behavior of radiance as z grow arbitrarily large. The second test is the convergence of DSHEF$_N$'s solution to the actual behavior of radiance in the so called "near tissue," where multiple vectors make significant contributions. Due to the nature of DSHEF$_N$'s solution as a linear combination of decaying terms, this is perhaps most apparent at the upper boundary of the medium, at $z = 0$. However, this introduces the greatest difficulty of convergence for DSHEF$_N$: the non-differentiable point in $\gamma_F(\Omega)$ at the critical angle $\theta_c = \sin^{-1}(1/n)$.

This critical angle defines the angular range over which radiance directed in the negative z direction at the medium boundary is completely internally reflected. Note that γ_F is non-differentiable at θ_c while L_S^-, the scattered radiance directed in the negative z direction, is composed of a linear combination of smooth functions. Since the Marshak boundary condition dictates that radiance directed in the positive z direction at $z = 0$ is the product of these two functions, L_S is expected to converge to a function with non-differentiable points at $z = 0$. This prevents the easy assurance of exponential convergence, though as the results given in Chapters 3 and 4 indicate, convergence does indeed occur for values of N which enable quick calculation.

Understanding the structure of the eigenvectors used in the homogeneous solution for L_S is a crucial step to proving the rate of convergence of DSHEF$_N$. Understanding this convergence, in turn, is critical to confidently estimating the necessary order of expansion for DSHEF$_N$ to ensure that the obtained solution will satisfy an end user's desired level of accuracy.

Perhaps more importantly, understanding the construction of each vector in terms of all parameters will allow the direct construction of these vectors, as opposed to the eigenvector decomposition method currently used. This method accounts for over 90 percent of the computational expense of DSHEF$_N$, which means that its replacement via this fast calculation method will enable far more iterations of DSHEF$_N$ per unit time, which in turn enables both the use of higher order approximations and far lower computation times for inversion methods such as that which was presented in Chapter 5. This inversion speed in particular is critical to medical imaging applications; methods such as Spatial Frequency Domain Imaging often attempt to provide high resolution in x and y, which in turn implies that many inversions are necessary for a given data set. In addition, low processing times are necessary for any imaging modality which wishes to provide real time video. These methods are highly useful in clinical applications, yet are very demanding regarding data throughput.

The necessity of this understanding is made clear in the results shown in chapters 3 and 4.

While DSHEF_{13} was generally the strongest performer shown in terms of relative error, it is also the most expensive computationally. A deeper understanding of the spectral content of both single SHEF_N and DSHEF_N will allow end users to intelligently choose orders of expansion for various applications, or even switch bewteen them based upon fitting methods used in inversion techniques.

6.3 Optical Property Recovery

Once the spectral structure of DSHEF_N is better understood, the next step will be applying it to the inversion technique described in Chapter 5 in lieu of single SHEF_N. Even if it does not provide a significant advantage in accuracy, it has been shown in Chapters 3 and 4 that DSHEF_N can provide accurate results for fluency and reflectance at reduced computational expense when compared to single SHEF_N. This staged inversion technique provides an ideal entry point to the problem, as well as an excellent chance to test DSHEF_N's ability to provide meaningful results in challenging cases, such as media containing layers with thicknesses significantly less than l^*. It will also provide opportunities to study the effect of more general classes of scattering phase functions. Since the DSEHF_N implementation detailed in Chapter 3 does not require any specific structure of scattering phase function or even restriction to a given class of phase functions, such as Henyey-Greenstein, moments of these functions can be treated as any other parameter. Previous work has already shown that not only is the structure of this function, and therefore the integral operator in which it is included, highly influential on scattered radiance, it contains important physiological information.

The easily extensible nature of DSHEF_N to media composed of arbitrary numbers of layers will allow the generalization of this staged inversion technique to such media, as well. Current property recovery techniques rarely consider more than three layers, but the computational

expense of the method in Chapter 5, as well as of the layered DSHEF$_N$ implementation described in Chapter 4, grow linearly with the number of layers. The multilayered implementation of DSHEF$_N$, in particular, is also easily parallelizable, since the most expensive component is the eigenvector decomposition associated with each layer. These decompositions do not rely on one another, and so each can be performed concurrently with the others. This is in stark contrast to the geometric increase in expense creating and storing Monte Carlo based look up tables, which is perhaps the most common method in use at the time of writing, and which has necessitated the use of various simplifying assumptions.

Ultimately, the major goal for DSHEF$_N$ is its incorporation into Spatial Frequency Domain Tomography. This will require an implementation of DSHEF$_N$ which drops the assumption of a medium composed of homogeneous tissue layers and simply treats the scattering and absorption coefficients, as well as potentially the scattering phase function, as arbitrary functions of position. It will also require a new inversion method, though this method's form will rely on the forward solution mentioned.

6.4 Conclusions

I have presented both mathematical justification and simulation results for a new, spectral method of deterministically solving the Radiative Transport equation, as well as a staged inversion technique for the recovery of optical properties from layered media to which this technique may be applied. This method, which resolves around a double spherical harmonic basis, provides a degree of accuracy for reconstructing scattered radiance in a layered medium which is equal to or greater than that of other spectral methods and more robust with respect to optical properties and spatial frequency. The MATLab implementation given is easily extensible to an arbitrary number of layers, and provides simulation results which show convergence to a Monte Carlo "gold standard" both in functionals such as reflectance

and fluence, but also in basic radiance without the use of post processing techniques, which has been difficult for previous spectral methods. This method will enable optical imaging modalities to deal with thin tissue layers and to explore problems related not only to absorption and scattering coefficients, but also the directionality of scattering within a medium, particularly when dealing with high spatial frequencies. Future work in this area is expected to enable new modalities such as Spatial Frequency Domain Tomography, which would be of great utility in clinical applications.

Bibliography

[1] G. Altay, R. A. C. Croft, and I. Pelupessy. sphray: a smoothed particle hydrodynamics ray tracer for radiative transfer. *Monthly Notices of the Royal Astronomical Society*, 386(4):1931–1946, 04 2008.

[2] G. Arfken. *Mathematical Methods for Physicists*. Academic Press, Inc., San Diego, third edition, 1985.

[3] K. Atkinson. Numerical integration on the sphere. *The Journal of the Australian Mathematical Society. Series B. Applied Mathematics*, 23(3):332–347, 1982.

[4] A. Bassi, D. J. Cuccia, A. J. Durkin, and B. J. Tromberg. Spatial shift of spatially modulated light projected on turbid media. *Journal of the Optical Society of America A*, 25(11):2833−2839, Nov 2008.

[5] F. Bevilacqua and C. Depeursinge. Monte carlo study of diffuse reflectance at source–detector separations close to one transport mean free path. *J. Opt. Soc. Am. A*, 16(12):2935–2945, Dec 1999.

[6] N. Bodenschatz, P. Krauter, A. Liemert, and A. Kienle. Quantifying phase function influence in subdiffusively backscattered light. *Journal of Biomedical Optics*, 21:035002, 03 2016.

[7] N. Bodenschatz, P. Krauter, A. Liemert, J. Wiest, and A. Kienle. Model-based analysis on the influence of spatial frequency selection in spatial frequency domain imaging. *Applied Optics*, 54(22):6725−6731, Aug 2015.

[8] D. M. Burmeister, A. Ponticorvo, B. Yang, S. C. Becerra, B. Choi, A. J. Durkin, and R. J. Christy. Utility of spatial frequency domain imaging (SFDI) and laser speckle imaging (LSI) to non-invasively diagnose burn depth in a porcine model. *Burns*, 41(6):1242-−1252, 2015.

[9] İ. R. Çapoğlu, J. D. Rogers, A. Taflove, and V. Backman. The microscope in a computer: Image synthesis from three-dimensional full-vector solutions of maxwell's equations at the nanometer scale. In *Progress in Optics*, volume 57, pages 1–91. Elsevier, 2012.

[10] S. A. Carp, S. A. Prahl, and V. Venugopalan. Radiative transport in the delta-P1 approximation: accuracy of fluence rate and optical penetration depth predictions in turbid semi-infinite media. *Journal of Biomedical Optics*, 9(3):632 – 647, 2004.

[11] K. M. Case and P. F. Zweifel. *Linear Transport Theory*. Addison-Wesley, 1967.

[12] B. Chen, K. Stamnes, and J. J. Stamnes. Validity of the diffusion approximation in bio-optical imaging. *Applied Optics*, 40(34):6356–6366, 2001.

[13] D. J. Cuccia, F. Bevilacqua, A. J. Durkin, and B. J. Tromberg. Modulated imaging: quantitative analysis and tomography of turbid media in the spatial-frequency domain. *Optics Letters*, 30(11):1354−1356, Jun 2005.

[14] D. J. Cuccia, F. Bevilacqua, A. J. Durkin, and B. J. Tromberg. Quantitative recovery of tissue optical properties in the spatial frequency domain using modulated imaging. In *Frontiers in Optics*, page FTuN4. Optical Society of America, 2005.

[15] H. Dehghani, M. E. Eames, P. K. Yalavarthy, S. C. Davis, S. Srinivasan, C. M. Carpenter, B. W. Pogue, and K. D. Paulsen. Near infrared optical tomography using nirfast: Algorithm for numerical model and image reconstruction. *Communications in numerical methods in engineering*, 25(6):711–732, 2009.

[16] H. Fang, M. Ollero, E. Vitkin, L. M. Kimerer, P. Cipolloni, M. M. Zaman, S. D. Freedman, I. J. Bigio, I. Itzkan, E. B. Hanlon, et al. Noninvasive sizing of subcellular organelles with light scattering spectroscopy. *IEEE Journal of selected topics in quantum electronics*, 9(2):267–276, 2003.

[17] K. R. Forrester, J. Tulip, C. Leonard, C. Stewart, and R. C. Bray. A laser speckle imaging technique for measuring tissue perfusion. *IEEE transactions on biomedical engineering*, 51(11):2074–2084, 2004.

[18] I. Fredriksson, M. Larsson, and T. Strömberg. Inverse Monte Carlo method in a multilayered tissue model for diffuse reflectance spectroscopy. *Journal of Biomedical Optics*, 17(4):047004, 2012.

[19] I. Fredriksson, R. B. Saager, A. J. Durkin, and T. Strömberg. Evaluation of a pointwise microcirculation assessment method using liquid and multilayered tissue simulating phantoms. *Journal of Biomedical Optics*, 22(11):115004, 2017.

[20] H. Gao and H. Zhao. A fast-forward solver of radiative transfer equation. *Transport Theory and Statistical Physics*, 38(3):149–192, 2009.

[21] A. R. Gardner, A. D. Kim, and V. Venugopalan. Radiative transport produced by oblique illumination of turbid media with collimated beams. *Physical Review E*, 87:063308, Jun 2013.

[22] E. M. Gelbard. Simplified spherical harmonics equations and their use in shielding problems. Technical report, Westinghouse Electric Corp. Bettis Atomic Power Lab., Pittsburgh, 1961.

[23] M. L. Gostkowski, J. B. McDoniel, J. Wei, T. E. Curey, and J. B. Shear. Characterizing spectrally diverse biological chromophores using capillary electrophoresis with multiphoton-excited fluorescence. *Journal of the American Chemical Society*, 120(1):18−22, 1998.

[24] C. Hayakawa, J. Spanier, and V. Venugopalan. Computational engine for a virtual tissue simulator. In A. Keller, S. Heinrich, and H. Niederreiter, editors, *Monte Carlo and Quasi-Monte Carlo Methods 2006*, pages 431–443, Berlin, Heidelberg, 2008. Springer Berlin Heidelberg.

[25] C. K. Hayakawa, B. Y. Hill, J. S. You, F. Bevilacqua, J. Spanier, and V. Venugopalan. Use of the delta-P_1 approximation to recover optical absorption, scattering, and asymmetry coefficients of turbid media. *Applied Optics*, 43(24):4677–4684, 2004.

[26] C. K. Hayakawa and J. Spanier. Perturbation monte carlo methods for the solution of inverse problems. In *Monte Carlo and Quasi-Monte Carlo Methods 2002*, pages 227–241. Springer, 2004.

[27] C. K. Hayakawa, J. Spanier, and V. Venugopalan. Comparative analysis of discrete and continuous absorption weighting estimators used in monte carlo simulations of radiative transport in turbid media. *J. Opt. Soc. Am. A*, 31(2):301–311, Feb ts , url = http://josaa.osa.org/abstract.cfm?URI=josaa-31-2-301, doi = 10.1364/JOSAA.31.000301.

[28] L. G. Henyey and J. L. Greenstein. Diffuse radiation in the Galaxy. , 93:70–83, Jan. 1941.

[29] S. T. Horan, A. R. Gardner, R. B. Saager, A. J. Durkin, and V. Venugopalan. Recovery of layered tissue optical properties from spatial frequency-domain spectroscopy and a deterministic radiative transport solver. *Journal of Biomedical Optics*, 24(7):1 – 11, 2018.

[30] D. Huang, E. A. Swanson, C. P. Lin, J. S. Schuman, W. G. Stinson, W. Chang, M. R. Hee, T. Flotte, K. Gregory, C. A. Puliafito, et al. Optical coherence tomography. *science*, 254(5035):1178–1181, 1991.

[31] S. L. Jacques. Optical properties of biological tissues: a review. *Physics in Medicine and Biology*, 58(11):R37, 2013.

[32] J. H. Joseph, W. J. Wiscombe, and J. A. Weinman. The Delta-Eddington Approximation for Radiative Flux Transfer. *Journal of the Atmospheric Sciences*, 33(12):2452–2459, 12 1976.

[33] A. Kienle, T. Glanzmann, G. Wagnières, and H. van den Bergh. Investigation of two-layered turbid media with time-resolved reflectance. *Applied Optics*, 37(28):6852−6862, Oct 1998.

[34] A. Kienle, M. S. Patterson, N. Dögnitz, R. Bays, G. Wagnières, and H. van den Bergh. Noninvasive determination of the optical properties of two-layered turbid media. *Applied Optics*, 37(4):779−791, Feb 1998.

[35] S. D. Konecky, T. B. Rice, B. J. Tromberg, C. M. O. P. A. Valdes, D. W. Roberts, K. Kolste, F. Leblond, K. D. Paulsen, and B. C. Wilson. Spatial frequency domain

tomography of protoporphyrin IX fluorescence in preclinical glioma models. *Journal of Biomedical Optics*, 17(5):056008, 2012.

[36] E. W. Larsen, J. E. Morel, and J. M. McGhee. Asymptotic derivation of the simplified pn equations. In *Proceedings of the Joint International Conference on Mathematical Methods and Supercomputing in Nuclear Applications*, volume 1, page 718, 1993.

[37] A. M. Laughney, V. Krishnaswamy, E. J. Rizzo, M. C. Schwab, R. J. Barth, D. J. Cuccia, B. J. Tromberg, K. D. Paulsen, B. W. Pogue, and W. A. Wells. Spectral discrimination of breast pathologies in situusing spatial frequency domain imaging. *Breast Cancer Research*, 15(4):R61, 2013.

[38] M. J. Leahy, J. G. Enfield, N. T. Clancy, J. O'Doherty, P. McNamara, and G. E. Nilsson. Biophotonic methods in microcirculation imaging. *Medical Laser Application*, 22(2):105–126, 2007.

[39] A. Liemert and A. Kienle. Analytical solutions of the radiative transport equation for the reflectance and fluorescence from layered media illuminated by a finite beam. In *Diffuse Optical Imaging V*, page 95380D. Optical Society of America, 2015.

[40] L. Lim, B. S. Nichols, M. R. Migden, N. Rajaram, J. Reichenberg, M. K. Markey, M. I. Ross, and J. W. Tunnell. Clinical study of noninvasive in vivo melanoma and nonmelanoma skin cancers using multimodal spectral diagnosis. *Journal of Biomedical Optics*, 19(11):117003, 2014.

[41] M. A. Lin, Alexander J.and Koike, K. N. Green, J. G. Kim, A. Mazhar, T. B. Rice, F. M. LaFerla, and B. J. Tromberg. Spatial frequency domain imaging of intrinsic optical property contrast in a mouse model of Alzheimer's Disease. *Annals of Biomedical Engineering*, 39(4):1349–1357, Apr 2011.

[42] Q. Liu and N. Ramanujam. Sequential estimation of optical properties of a two-layered epithelial tissue model from depth-resolved ultraviolet-visible diffuse reflectance spectra. *Applied Optics*, 45(19):4776−4790, Jul 2006.

[43] Q. Liu and N. Ramanujam. Scaling method for fast Monte Carlo simulation of diffuse reflectance spectra from multilayered turbid media. *Journal of the Optical Society of America A*, 24(4):1011−1025, Apr 2007.

[44] J. C. Maxwell. A dynamical theory of the electromagnetic field. *Philosophical Transactions of the Royal Society of London*, 155:459–513, 1865.

[45] I. V. Meglinski and S. J. Matcher. Quantitative assessment of skin layers absorption and skin reflectance spectra simulation in the visible and near-infrared spectral regions. *Physiological Measurement*, 23(4):789−802, 2002.

[46] M. I. Mishchenko. Maxwell's equations, radiative transfer, and coherent backscattering: A general perspective. *Journal of Quantitative Spectroscopy and Radiative Transfer*, 101(3):540–555, 2006.

[47] J. J. Moré. The levenberg-marquardt algorithm: Implementation and theory. In G. A. Watson, editor, *Numerical Analysis*, pages 105–116, Berlin, Heidelberg, 1978. Springer Berlin Heidelberg.

[48] K. P. Nadeau, P. Khoury, A. Mazhar, D. J. Cuccia, and A. J. Durkin. Component and system evaluation for the development of a handheld point-of-care spatial frequency domain imaging (SFDI) device. volume 8573, page 857304, 2013.

[49] J. A. Nelder and R. Mead. A Simplex Method for Function Minimization. *The Computer Journal*, 7(4):308–313, 01 1965.

[50] T. D. O'Sullivan, A. E. Cerussi, D. J. Cuccia, and B. J. Tromberg. Diffuse optical imaging using spatially and temporally modulated light. *Journal of biomedical optics*, 17(7), 2012.

[51] T. H. Pham, T. Spott, L. O. Svaasand, and B. J. Tromberg. Quantifying the properties of two-layer turbid media with frequency-domain diffuse reflectance. *Applied Optics*, 39(25):4733−4745, Sep 2000.

[52] A. Politis. Spherical harmonic transform. `https://github.com/polarch/Spherical-Harmonic-Transform`, 2019.

[53] G. C. Pomraning. Asymptotic and variational derivations of the simplified pn equations. *Annals of nuclear energy*, 20(9):623–637, 1993.

[54] A. Ponticorvo, D. M. Burmeister, B. Yang, B. Choi, R. J. Christy, and A. J. Durkin. Quantitative assessment of graded burn wounds in a porcine model using spatial frequency domain imaging (SFDI) and laser speckle imaging (LSI). *Biomedical Optics Express*, 5(10):3467 – 3481, Oct 2014.

[55] J. Ranasinghesagara. Mie simulator gui, Jul 2019.

[56] C. M. Robbins, G. Raghavan, J. F. Antaki, and J. M. Kainerstorfer. Feasibility of spatial frequency-domain imaging for monitoring palpable breast lesions. *Journal of Biomedical Optics*, 22(12):1 – 9, 2017.

[57] R. B. Saager, M. Balu, V. Crosignani, A. Sharif, A. J. Durkin, K. M. Kelly, and B. J. Tromberg. In vivo measurements of cutaneous melanin across spatial scales: using multiphoton microscopy and spatial frequency domain spectroscopy. *Journal of Biomedical Optics*, 20(6):066005, 2015.

[58] R. B. Saager and A. J. D. David J. Cuccia. Determination of optical properties of turbid media spanning visible and near-infrared regimes via spatially modulated quantitative spectroscopy. *Journal of Biomedical Optics*, 15(1):017012, 2010.

[59] R. B. Saager, C. Kondru, K. Au, K. Sry, F. Ayers, and A. J. Durkin. Multilayer silicone phantoms for the evaluation of quantitative optical techniques in skin imaging. volume 7567, page 756706, 2010.

[60] R. B. Saager, A. Quach, R. A. Rowland, M. L. Baldado, and A. J. Durkin. Low-cost tissue simulating phantoms with adjustable wavelength-dependent scattering properties in the visible and infrared ranges. *Journal of Biomedical Optics*, 21(6):67001, 2016.

[61] R. B. Saager, A. Truong, A. J. Durkin, and D. J. Cuccia. Method for depth-resolved quantitation of optical properties in layered media using spatially modulated quantitative spectroscopy. *Journal of Biomedical Optics*, 16(7):077002, 2011.

[62] I. Seo, C. K. Hayakawa, and V. Venugopalan. Radiative transport in the delta- approximation for semi-infinite turbid media. *Medical Physics*, 35(2):681–693.

[63] I. Seo, C. K. Hayakawa, and V. Venugopalan. Radiative transport in the delta-P_1 approximation for semi-infinite turbid media. *Medical Physics*, 35(2):681–693, 2008.

[64] I. Seo, J. S. You, C. Hayakawa, and V. Venugopalan. Perturbation and differential Monte Carlo methods for measurement of optical properties in a layered epithelial tissue model. *Journal of Biomedical Optics*, 12:014030, 2007.

[65] G. L. Stephens, P. M. Gabriel, and S.-C. Tsay. Statistical radiative transport in one-dimensional media and its application to the terrestrial atmosphere. *Transport Theory and Statistical Physics*, 20(2-3):139–175, 1991.

[66] L. O. Svaasand, T. Spott, J. B. Fishkin, T. Pham, B. J. Tromberg, and M. W. Berns. Reflectance measurements of layered media with diffuse photon-density waves: a potential tool for evaluating deep burns and subcutaneous lesions. *Physics in Medicine and Biology*, 44(3):801−813, Mar 1999.

[67] V. Venugopalan. 2018 short course in computational biophotonics, lecture 1, Jul 2018.

[68] V. Venugopalan, J. S. You, and B. J. Tromberg. Radiative transport in the diffusion approximation: An extension for highly absorbing media and small source-detector separations. *Phys. Rev. E*, 58:2395–2407, Aug 1998.

[69] A. Vogel and V. Venugopalan. Mechanisms of pulsed laser ablation of biological tissues. *Chemical Reviews*, 103(2):577–644, 2003. PMID: 12580643.

[70] H.-Q. Wang, J.-T. Ye, Y. Zhang, Y.-Y. Zhao, and Y.-Q. Qiu. A thorough understanding of the nonlinear optical properties of bodipy/carborane/diketopyrrolopyrrole hybrid chromophores: module contribution, linear combination, one-/two-dimensional difference and carborane's arrangement. *J. Mater. Chem. C*, 7:7531–7547, 2019.

[71] L. V. Wang. Ultrasound-mediated biophotonic imaging: a review of acousto-optical tomography and photo-acoustic tomography. *Disease markers*, 19(2, 3):123–138, 2004.

[72] J. R. Weber, D. J. Cuccia, A. J. Durkin, and B. J. Tromberg. Noncontact imaging of absorption and scattering in layered tissue using spatially modulated structured light. *Journal of Applied Physics*, 105(10):102028, 2009.

[73] A. Yafi, F. K. Muakkassa, T. Pasupneti, J. Fulton, D. J. Cuccia, A. Mazhar, K. N. Blasiole, and E. N. Mostow. Quantitative skin assessment using spatial frequency domain imaging (sfdi) in patients with or at high risk for pressure ulcers. *Lasers in surgery and medicine*, 49(9):827–834, 2017.

[74] A. R. Young. Chromophores in human skin. *Physics in Medicine and Biology*, 42(5):789-−802, 1997.

[75] L. Yu, F. Nina-Paravecino, D. R. Kaeli, and Q. Fang. Scalable and massively parallel Monte Carlo photon transport simulations for heterogeneous computing platforms. *Journal of Biomedical Optics*, 23(1):1 – 4, 2018.

[76] G. Zaccanti, S. D. Bianco, and F. Martelli. Measurements of optical properties of high-density media. *Applied Optics*, 42(19):4023−4030, Jul 2003.

[77] X. Zhong, X. Wen, and D. Zhu. Lookup-table-based inverse model for human skin reflectance spectroscopy: two-layered monte carlo simulations and experiments. *Optics Express*, 22(2):1852−1864, Jan 2014.

[78] C. Zhu and Q. Liu. Review of Monte Carlo modeling of light transport in tissues. *Journal of Biomedical Optics*, 18(5):1 – 13, 2013.

Appendix A

SHEF$_N$ Derivation

A.1 Method Overview

This appendix provides an in depth proof of the SHEF$_N$ method of solving the RTE. This method uses a partial expansion in terms of Laplace's Spherical Harmonic Functions and follows six major steps:

- Convert scattered radiance, scattering phase and scattered radiance gain due to source functions into finite expansions of spherical harmonics with unknown coefficients, or moments. Assume that the moments of scattered radiance are smooth functions of position.
- Eliminate the integral term using the orthonormality of the Spherical Harmonic Functions and expand the directional derivative to convert the RTE to a system of partial differential equations.
- Take the Fourier Transform with respect to spatial coordinates x and y of the resulting system to obtain one of ordinary differential equations, whose solution gives a set of

Transverse Fourier Moments (TFMs).

- Recast this system as a generalized eigenvalue problem to obtain these TFMs
- Solve the new system using boundary conditions which conserve hemispherical moments of radiance.
- Apply an Inverse Fourier Transform to the TFMs to obtain the original harmonic moments as functions of position.

A.2 Laplace's Spherical Harmonic Functions

Laplace's spherical harmonic functions form an orthonormal basis of square-integrable functions on the unit sphere, and are solutions to Laplace's equation, $\nabla^2 Y = 0$ in that same geometry. Each function has an order l¿0 and a degree m, such that $-l \leq m \leq l$. Thus, for instance, there are three degree 1 spherical harmonics: $Y_{1,-1}$, $Y_{1,0}$ and $Y_{1,1}$. In terms of recursion relations and N degree expansion, we consider all functions of order or degree outside of the given ranges to be identically zero. The nonzero functions are defined in the following manner:

$$Y_{l,m}(\mu,\phi) = \sqrt{\tfrac{2l+1}{4\pi} * \tfrac{(l-|m|)!}{(l+|m|)!}} P_{l,m}(\mu)\, exp(im\phi) \quad (A.1)$$

Here, $P_{l,m}$ is the degree l, order m Associated Legendre Polynomial. This function depends only on the polar angle, while an azimuthal rotation term is introduced only for non-zero m.

The spherical harmonics equipped with the standard L^2 inner product ($< Y_{l,m}, Y_{l',m'} >= \int_{4\pi} Y_{l,m}(\Omega) Y_{l',m'}(\Omega) d\Omega$) form an orthonormal basis for all square integrable functions on the unit sphere. This implies that there exist conjugate spherical harmonic functions, $Y^*_{l,m}$,

defined as follows: $Y_{l,-m} = (-1)^m Y^*_{l,m}$. The orthonormality of this basis for $L^2 2(S^2)$ is crucial to the SHEF$_N$*method*.

A.2.1 Step 1 - Spherical Harmonic Expansion

Recall that the Radiative Transport Equation is given by:

$$\nabla \cdot \Omega L_S(r,\Omega) + \mu_t L_S(r,\Omega) = \mu_s \int_{4\pi} L_S(r,\Omega')\, p(\Omega' \cdot \Omega)\, d\Omega' + Q(r,\Omega) \quad (A.2)$$

The function for radiance can be expanded in terms of the spherical harmonic functions with moments that are assumed to be smooth functions of position:

$$L_S(r,\Omega) = \sum_{l=0}^{N} \left[\sum_{m=-l}^{l} K_{l,m} \psi_{l,m}(r)\, Y_{l,m}(\Omega) \right] \quad (A.3)$$

Here, $K_{l,m} = \sqrt{\frac{(l+m)!}{(l-m)!}\frac{2l+1}{4\pi}}$ and $\psi_{l,m}(r)$ are the moments of the spherical harmonic functions, which are the primary quantities of interest for this method. A complete description of these moments is equivalent to a solution to the RTE.

In a similar manner, the scattering phase function can be expanded first in terms of the Legendre Polynomials, with an argument $\Omega' \cdot \Omega$ and of moments of $\sqrt{2l+1} g_l$. The spherical harmonic addition theorem can then applied to change the expansion to spherical harmonic functions:

$$p(\Omega' \cdot \Omega) = \sum_{l=0}^{N} \left[\sqrt{(}2l+1) g_l P_l(\Omega' \cdot \Omega) \right] = \sum_{l=0}^{N} \left[\sum_{m=-l}^{l} g_l Y^*_{l,m}(\Omega')\, Y_{l,m}(\Omega) \right] \quad (A.4)$$

Finally, Q, the term describing the contribution from a collimated source to scattered radiance, can be expanded in the following manner:

$$L_C(r,\Omega) = \frac{\tilde{\mu_s}}{\mu_0}\tilde{p}(\Omega_0 \cdot \Omega) S(x,y \mid x_0,y_0) exp\left(-\frac{\tilde{\mu_t}}{\mu_0}z\right) \quad (A.5)$$

Here, $\tilde{p}$ represents a the scattering phase function after the application of Delta-Eddington scaling, $\tilde{\mu_s} = \mu_s(1 - f_\delta)$ represents the change to the scattering coefficient associated with this scaling, μ_0 represents the cosine of the angle of the collimated source in the medium, S represents a distribution of collimated source strength with respect to the x and y directions and the exponential term defines the rate of decay of the source with respect to Delta-Eddington.

Substitution of (A.3), (A.4) and (A.5) into the RTE returns the following:

$$\nabla \cdot \Omega \sum_{l=0}^{N}\left[\sum_{m=-l}^{l} K_l \psi_{l,m}(r) Y_{l,m}(\Omega)\right] + \mu_t \sum_{l=0}^{N}\left[\sum_{m=-l}^{l} K_l \psi_{l,m}(r) Y_{l,m}(\Omega)\right] =$$
$$\mu_s \int_{4\pi}\left(\sum_{l=0}^{N}\left[\sum_{m=-l}^{l} K_l \psi_{l,m}(r) Y_{l,m}(\Omega')\right]\right)\left(\sum_{l=0}^{N}\left[\sum_{m=-l}^{l} p_l Y^*_{l,m}(\Omega') Y_{l,m}(\Omega)\right]\right) d\Omega' +$$
$$\frac{\tilde{\mu_s}}{\mu_0} C(r) \sum_{l=0}^{N}\left[\sum_{m=-l}^{l} \tilde{p_l} Y^*_{l,m}(\Omega_0) Y_{l,m}(\Omega)\right] \quad (A.6)$$

A.2.2 Step 2 - Simplification Using Harmonic Conjugates

The statement of the RTE in terms of spherical harmonics, moments, and other constants allows the application of simplifications. First, note that the scattering term contains a product of sums of arbitrarily many terms. This term expands to the following:

$$\mu_s \int_{4\pi}\left(\sum_{l=0}^{N}\left[\sum_{m=-l}^{l} K_l \psi_{l,m}(r) Y_{l,m}(\Omega')\right]\right)\left(\sum_{l=0}^{N}\left[\sum_{m=-l}^{l} p_l Y^*_{l,m}(\Omega') Y_{l,m}(\Omega)\right]\right) d\Omega' \quad (A.7)$$

Basic algebra and calculus convert it to:

$$\mu_s \int_{4\pi} K_0 \psi_{0,0}(r) Y_{0,0}(\Omega')\left(\sum_{l=0}^{N}\left[\sum_{m=-l}^{l} p_l Y^*_{l,m}(\Omega') Y_{l,m}(\Omega)\right]\right) d\Omega' + ...$$

$$+\mu_s \int_{4\pi} K_N \left[\sum_{m=-l}^{l} \psi_{N,m}(r) Y_{0,0}(\Omega')\right] \sum_{l=0}^{N} \left[\sum_{m=-l}^{l} p_l Y^*_{l,m}(\Omega') Y_{l,m}(\Omega)\right] d\Omega' \quad (A.8)$$

Further distribution and application of the linearity of integrals gives the following:

$$\begin{gathered}
\mu_s K_0 p_0 \psi_{0,0}(r) Y_{0,0}(\Omega) \int_{4\pi} Y_{0,0}(\Omega') Y^*_{0,0}(W') d\Omega' + \\
\mu_s K_0 p_1 \psi_{0,0}(r) Y_{1,-1}(\Omega) \int_{4\pi} Y_{0,0}(\Omega') Y^*_{1,-1}(W') d\Omega' + \\
...+\mu_s K_l p_{l'} \psi_{l,m}(r) Y_{l',m'}(\Omega) \int_{4\pi} Y_{l,m}(\Omega') Y^*_{l',m'}(W') d\Omega' + \\
...+ \mu_s K_N p_N \psi_{N,N}(r) Y_{N,N}(\Omega) \int_{4\pi} Y_{N,N}(\Omega') Y^*_{N,N}(W') d\Omega' \quad (A.9)
\end{gathered}$$

While this expression is unwieldy, the orthonormality of the spherical harmonics may be applied to simplify it. Recall that this orthonormality means that $\int_{4\pi} Y^*_{l,m}(\Omega) Y_{l',m'}(\Omega) d\Omega = 1$ if $l = l'$ and $m = m'$ and equals 0 otherwise. (A.9) can therefore be simplified to the following form:

$$\mu_s \sum_{l=0}^{N} \left[K_l p_l \sum_{m=-l}^{l} (\psi_{l,m}(r) Y_{l,m}(\Omega))\right] \quad (A.10)$$

Substitution of (A.10) into (A.9) gives the following:

$$\begin{gathered}
\nabla \cdot \Omega \sum_{l=0}^{N} \left[\sum_{m=-l}^{l} K_l \psi_{l,m}(r) Y_{l,m}(\Omega)\right] \\
+\mu_t \sum_{l=0}^{N} \left[\sum_{m=-l}^{l} K_l \psi_{l,m}(r) Y_{l,m}(\Omega)\right] \\
=\mu_s \sum_{l=0}^{N} \left[K_l p_l \sum_{m=-l}^{l} (\psi_{l,m}(r) Y_{l,m}(\Omega))\right] + \\
\frac{\tilde{\mu_s}}{\mu_0} C(r) \sum_{l=0}^{N} \left[\sum_{m=-l}^{l} \tilde{p}_l Y^*_{l,m}(\Omega_0) Y_{l,m}(\Omega)\right] \quad (A.11)
\end{gathered}$$

To create a system of partial differential equations from this, a specific order l^* and degree m^* are selected, and each side of the equation is multiplied the conjugate $Y^*_{l^*,m^*}(\Omega)$, giving:

$$\begin{gathered}
\nabla \cdot \Omega \sum_{l=0}^{N} \left[\sum_{m=-l}^{l} K_l \psi_{l,m}(r) Y^*_{l^*,m^*}(\Omega) Y_{l,m}(\Omega)\right] + \\
\mu_t \sum_{l=0}^{N} \left[\sum_{m=-l}^{l} K_l \psi_{l,m}(r) Y^*_{l^*,m^*}(\Omega) Y_{l,m}(\Omega)\right] = \\
\mu_s \sum_{l=0}^{N} \left[K_l p_l \sum_{m=-l}^{l} \left(\psi_{l,m}(r) Y^*_{l^*,m^*}(\Omega) Y_{l,m}(\Omega)\right)\right]
\end{gathered}$$

$$+\frac{\tilde{\mu_s}}{\mu_0}C(r)\sum_{l=0}^{N}\left[\sum_{m=-l}^{l}\tilde{p}_l Y_{l,m}^{*}\left(\Omega_0\right)Y_{l^*,m^*}^{*}\left(\Omega\right)Y_{l,m}\left(\Omega\right)\right] \quad (A.12)$$

Each side is then integrated over the unit sphere and basic rules of mathematics are once again applied. This leaves an integro-differential equation:

$$\begin{gathered}\sum_{l=0}^{N}\left[K_l\sum_{m=-l}^{l}\nabla\psi_{l,m}\left(r\right)\cdot\int_{4\pi}\Omega Y_{l^*,m^*}^{*}\left(\Omega\right)Y_{l,m}\left(\Omega\right)d\Omega\right]\\ +\mu_t\sum_{l=0}^{N}\left[K_l\sum_{m=-l}^{l}\psi_{l,m}\left(r\right)\int_{4\pi}Y_{l^*,m^*}^{*}\left(\Omega\right)Y_{l,m}\left(\Omega\right)d\Omega\right]=\\ \mu_s\sum_{l=0}^{N}\left[K_l p_l\sum_{m=-l}^{l}\left(\psi_{l,m}\left(r\right)\int_{4\pi}Y_{l^*,m^*}^{*}\left(\Omega\right)Y_{l,m}\left(\Omega\right)d\Omega\right)\right]\\ +\ \frac{\tilde{\mu_s}}{\mu_0}C(r)\sum_{l=0}^{N}\left[\sum_{m=-l}^{l}\tilde{p}_l Y_{l,m}^{*}\left(\Omega_0\right)\int_{4\pi}Y_{l^*,m^*}^{*}\left(\Omega\right)Y_{l,m}\left(\Omega\right)d\Omega\right] \quad (A.13)\end{gathered}$$

While this may seem to be much more complicated, all but one of the integrals are equal to zero, again due to orthonormality of the spherical harmonics. This leaves:

$$\begin{gathered}\sum_{l=0}^{N}\left[K_l\sum_{m=-l}^{l}\nabla\psi_{l,m}\left(r\right)K_l\int_{4\pi}\nabla\cdot\Omega Y_{l^*,m^*}^{*}\left(\Omega\right)Y_{l,m}\left(\Omega\right)d\Omega\right]\\ +\mu_t\sum_{l=0}^{N}\left[K_l\sum_{m=-l}^{l}\psi_{l,m}\left(r\right)\right]=\mu_s\sum_{l=0}^{N}\left[K_l p_l\sum_{m=-l}^{l}\psi\left(r\right)\right]\\ +\frac{\tilde{\mu_s}}{\mu_0}C(r)\sum_{l=0}^{N}\left[\sum_{m=-l}^{l}\tilde{p}_l Y_{l,m}^{*}\left(\Omega_0\right)\right] \quad (A.14)\end{gathered}$$

This is simplified by converting Ω into Cartesian coordinates Ω_x, Ω_y and Ω_z. Recurrence relations are derived from this conversion. Note that $\nabla\cdot\Omega=\cos\theta\sin\phi\frac{\partial}{\partial x}+\sin\theta\sin\phi\frac{\partial}{\partial y}+\cos\phi\frac{\partial}{\partial z}$. Since this term is applied to linear combinations of Spherical Harmonic Functions, the trigonoemtric functions by which we multiply create new combinations of those Spherical Harmonics. We introduce the following constants to handle these relations:

$$\begin{gathered}a_{l,m}=\sqrt{\left(l+1+m\right)\left(l+1-m\right)}\\ b_{l,m}=\sqrt{\left(l-m\right)\left(l+m\right)}\\ c_{l,m}=\sqrt{\left(l+m\right)\left(l-1+m\right)}\\ d_{l,m}=\sqrt{\left(l+2-m\right)\left(l+1-m\right)}\\ e_{l,m}=\sqrt{\left(l-m\right)\left(l-1-m\right)}\\ f_{l,m}=\sqrt{\left(l+1+m\right)\left(l+2+m\right)}\end{gathered}$$

These relations convert (A.14) to the following system of PDEs:

$$\begin{aligned}
&\frac{\partial}{\partial z}\left(a_{l,m}\psi_{l+1,m}\left(r\right)+b_{l,m}\psi_{l+1,m}\left(r\right)\right)\\
&-\frac{1}{2}\left(\frac{\partial}{\partial x}-i\frac{\partial}{\partial y}\right)\left(c_{l,m}\psi_{l-1,m-1}\left(r\right)+d_{l,m}\psi_{l+1,m-1}\left(r\right)\right)\\
&+\frac{1}{2}\left(\frac{\partial}{\partial x}+i\frac{\partial}{\partial y}\right)\left(e_{l,m}\psi_{l-1,m+1}\left(r\right)+f_{l,m}\psi_{l+1,m+1}\left(r\right)\right)\\
&+(2l+1)\mu_{t,l}\psi_{l,m}\left(r\right)=\left(2l+1\right)\frac{\tilde{\mu}_s}{\mu_0}q_{l,m}\left(\Omega_0\right)P\left(r\right) \quad (A.15)
\end{aligned}$$

The following definitions are applied in (A.15):

$$q_{l,m}\left(\Omega_0\right)=\tfrac{1}{K_l}\tilde{p}_l Y^*_{l,m}\left(\Omega_0\right) \quad (A.16)$$

$$\mu_{t,l}=\mu_t-\mu_s p_l \quad (A.17)$$

A.2.3 Step 3 - Transverse Fourier Transform

A transverse Fourier transform converts (A.15) from a system of partial differential equations to one of ordinary differential equations. This converts the moments $\{\psi_{l,m}\}$ to transverse Fourier moments $\{\tilde{\psi_{l,m}}\}$:

$$\tilde{\psi_{l,m}}\left(z|\mathbf{k}\right)=\int_{-\infty}^{\infty}\int_{-\infty}^{\infty}\psi_{l,m}\left(r\right)exp\left(-i\left(k_x x+k_y y\right)\right)dxdy \quad (A.18)$$

Note that this is with respect to x and y, leaving z alone. Similarly, recall that the simplification of the source term, Q, is equal to $S\left(x,y|x_0,y_0\right)exp\left(-\frac{\tilde{\mu}_t}{\mu_0}z\right)$. Since the source term is considered to travel through the surface at an angle defined by (θ_0,ϕ_0), where θ_0 is the angle in the $x-z$ plane and ϕ_0 is in the $y-z$ plane (which, by construction of the axes general considered to be zero, but will be given in the general sense here) the Fourier transform of this term cannot be taken as simply. Basic trigonometry defines the relation of the source

term at a given depth with that at the surface, defining $(x_{0,z}, y_{0,z})$ as the center of the transverse Gaussian distribution at depth z and (x_z, y_z) be the points at depth z corresponding to a point (x, y) on the surface distribution. This results in the following relations:

$$\begin{aligned} x_z &= x + z * tan(\theta_0) \\ x_{0,z} &= x_0 + z * tan(\theta_0) \\ y_z &= y + z * tan(\theta_0) \\ y_{0,z} &= y_0 + z * tan(\phi_0) \end{aligned}$$

Note that for any depth, the difference of $x_z - x_{0,z} = x - x_0$, with the same holding true for y. Therefore, given a standard deviation σ for both directions, the source distribution at (x_z, y_z) is given by:

$$S(x_z, y_z) = exp\left(-\frac{(x-x_0)^2+(y-y_0)^2}{2\sigma^2}\right) \quad (A.19)$$

Therefore, the transverse Fourier transform of this (A.19) is defined by:

$$\tilde{S}(\mathbf{k}) = \int_{-\infty}^{\infty}\int_{-\infty}^{\infty} \exp\left(-\frac{(x-x_0)^2+(y-y_0)^2}{2\sigma^2}\right) exp(-i(k_x x + k_y y))\, dxdy \quad (A.20)$$

The independence of x and y shows that:

$$\tilde{S}(\mathbf{k}) = \int_{-\infty}^{\infty} \exp\left(-\frac{(x-x_0)^2}{2\sigma^2}\right) exp(-ik_x x)\, dx * \int_{-\infty}^{\infty} \exp\left(-\frac{(y-y_0)^2}{2\sigma^2}\right) exp(-ik_y y)\, dy \quad (A.21)$$

This is not directly solvable; to do so requires the Fourier Shift Theorem. This will be solved in x for brevity; the procedure for y is identical:

$$\begin{gathered} \int_{-\infty}^{\infty} \exp\left(-\frac{(x-x_0)^2}{2\sigma^2}\right) exp(-ik_x x)\, dx = \\ exp(-ik_x x_0) \int_{-\infty}^{\infty} \exp\left(-\frac{(x-x_0)^2}{2\sigma^2}\right) exp(-ik_x(x-x_0))\, d(x-x_0) \end{gathered}$$

$$= exp(-ik_x x_0) \int_{-\infty}^{\infty} \exp\left(-\frac{u^2}{2\sigma^2}\right) exp(-ik_x u)\, du \quad (A.22)$$

Where $u = x - x_0$. The integral term has a well understood solution:

$$\sqrt{2\pi\sigma}\exp\left(-\sigma^2 k_x^2\right) \quad (3.23)$$

The same technique can be applied to the transformed source term, with depth considered, to give:

$$\tilde{S}\left(z|\mathbf{k}\right) = \left(2\pi\sigma^2\right) exp\left(-i\left(k_x x_{0,z} + k_y y_{0,z}\right)\right) exp\left(-\sigma^2\left(k_x^2 + k_y^2\right)\right) \quad (A.24)$$

The values of $x_{0,z}$ and $y_{0,z}$ are substituted into (A.24), resulting in:

$$\tilde{S}\left(z|\mathbf{k}\right) = \left(2\pi\sigma^2\right) exp\left(-iz\left(k_x x_0 tan\left(\theta_0\right) + k_y y_0 tan\left(\phi_0\right)\right)\right) exp\left(-\sigma^2\left(k_x^2 + k_y^2\right)\right) \quad (A.25)$$

This can be rewritten as:

$$\tilde{S}\left(z|\mathbf{k}\right) = \left(2\pi\sigma^2\right) exp\left(-\mu_k z\right) exp\left(-\sigma^2\left(k_x^2 + k_y^2\right)\right) \quad (A.26)$$

The original definition of the Fourier transform results in:

$$\tilde{S}\left(z|\mathbf{k}\right) exp\left(\mu_k z\right) = \int_{-\infty}^{\infty}\int_{-\infty}^{\infty} \exp\left(-\frac{(x-x_0)^2+(y-y_0)^2}{2\sigma^2}\right) exp\left(-i\left(k_x x + k_y y\right)\right) dxdy \quad (A.27)$$

Here, $\mu_k = i\left(\left(k_x x_0 tan\left(\theta_0\right) + k_y y_0 tan\left(\phi_0\right)\right)\right)$ and is therefore always purely imaginary. Therefore, the term $exp\left(u_k z\right)$ always has an absolute value of 1 and simply changes phase with k and z. It can now be asserted that:

$$\tilde{P}\left(z|\mathbf{k}\right) = \tilde{S}\left(z|\mathbf{k}\right) exp\left(-\mu_d z\right) \quad (A.28)$$

Here, $\mu_d = \mu_k + \frac{\tilde{\mu_t}}{\mu_0}$. This results in an expression of:

$$\frac{d}{dz}\left(a_{l,m}\tilde{\psi_{l+1,m}}\left(z|\mathbf{k}\right)+b_{l,m}\tilde{\psi_{l-1,m}}\left(z|\mathbf{k}\right)\right)-$$
$$\frac{1}{2}\left(k_y-ik_x\right)\left(c_{l,m}\tilde{\psi_{l-1,m-1}}\left(z|\mathbf{k}\right)+d_{l,m}\tilde{\psi_{l+1,m-1}}\left(z|\mathbf{k}\right)\right)+$$
$$\frac{1}{2}\left(k_y+ik_x\right)\left(e_{l,m}\tilde{\psi_{l-1,m+1}}\left(z|\mathbf{k}\right)+f_{l,m}\tilde{\psi_{l+1,m+1}}\left(z|\mathbf{k}\right)\right)+(2l+1)\mu_{t,l}\tilde{\psi_{l,m}}\left(z|\mathbf{k}\right)=$$

$$(2l+1)\frac{\tilde{\mu_s}}{\mu_0}q_{l,m}\left(\Omega_0\right)\tilde{P}\left(z|\mathbf{k}\right)\quad(A.29)$$

Thus, the system of PDEs has been transformed into one of ODEs. It can be put in vector notation:

$$A\frac{d}{dz}\tilde{\Psi}\left(z|\mathbf{k}\right)+B\tilde{\Psi}\left(z|\mathbf{k}\right)=\tilde{Q}\exp\left(-\mu_d z\right)\quad(A.30)$$

Here, $\tilde{Q}$ is the transverse Fourier transform of the source and $\tilde{\Psi}$ is the vector of Fourier transformed spherical harmonic moments. The exponential has been factored out of $\tilde{C}\left(z|\mathbf{k}\right)$ to denote the decay with respect to z. The source vector, as well as the matrices A and B, are therefore no longer functions of depth. Matrix A is also rank deficient, having rank N^2+N despite being a square matrix of size N^2+2N-1.

Note that the relations due to the differential operators provide a special case when $(l,m)=(N,\pm N)$. In these cases, every coefficient coming from a spatial derivative is zero since either the order or the degree (or both) of those coefficients would be outside of the normal range. Replacing these coefficients with zeros gives us the following:

$$\tilde{\psi_{N,\pm N}}\left(z|\mathbf{k}\right)=$$
$$\frac{1}{\mu_t N}\left[\frac{1}{2}\left(k_y\pm ik_x\right)\frac{\sqrt{2N(2N-1)}}{2N+1}\tilde{\psi_{N-1,\pm(N-1)}}\left(z|\mathbf{k}\right)+\frac{\tilde{\mu_s}}{\mu_0}q_{N,\pm N}\left(\Omega_0\right)P\left(z|\mathbf{k}\right)\right]\quad(A.31)$$

This relation allows for the complete construction of B and $\tilde{Q}$, whereas A is already determined from the initial system. From the formation of the problem, one should note that A is entirely real valued and symmetric and does not depend on k, owing to the expression being differentiated with respect to z, whereas B is Hermitian and does depend on k.

A.2.4 Step 4 - Converting to a Generalized Eigenvalue Problem for the Transverse Fourier Moments

The vector problem presented in (A.31) is solved using both the homogenous and particular solutions as follows:

$$\tilde{\psi_{l,m}}\left(z|\mathbf{k}\right) = \tilde{\psi_{l,m}^{(h)}}\left(z|\mathbf{k}\right) + \tilde{\psi_{l,m}^{(p)}}\left(z|\mathbf{k}\right) \quad (A.32)$$

The particular solution is given by:

$$\tilde{\Psi^{(p)}}\left(z|\mathbf{k}\right) = \left(\mu_d A + B\right)^{-1} \tilde{Q} \exp\left(-\mu_d z\right) \quad (A.33)$$

The homogenous solution is given by:

$$\tilde{\Psi^{(h)}}\left(z|\mathbf{k}\right) = G * \exp\left(\tfrac{z}{\lambda}\right) \quad (A.34)$$

For a matrix G of generalized eigenvectors. Substitution of (A.34) into (A.30) results in:

$$\begin{gathered} \mathrm{A}\ \frac{d}{dz}\left[\left(-\mu_d A + b\right)^{-1} \tilde{Q} \exp\left(-\mu_d z\right) + G * \exp\left(\frac{z}{\lambda}\right)\right] \\ +\mathrm{B}\left[\left(-\mu_d A + b\right)^{-1} \tilde{Q} \exp\left(-\mu_d z\right) + G * \exp\left(\tfrac{z}{\lambda}\right)\right] = \\ \tilde{Q} \exp\left(-\mu_d z\right) \quad (A.35) \end{gathered}$$

The next step is differentiation:

$$\begin{gathered} \mathrm{A}\left[\left(-\mu_d\right)\left(-\mu_d A + b\right)^{-1} \tilde{Q} \exp\left(-\mu_d z\right) + \left(\tfrac{1}{\lambda}\right) G * \exp\left(\tfrac{z}{\lambda}\right)\right] + \\ B\left[\left(-\mu_d A + b\right)^{-1} \tilde{Q} \exp\left(-\mu_d z\right) + G * \exp\left(\tfrac{z}{\lambda}\right)\right] \\ = \tilde{Q} \exp\left(-\mu_d z\right) \quad (A.36) \end{gathered}$$

Which is further simplified to:

$$\left(A\tfrac{1}{\lambda}+B\right)\left(G*\exp\left(\tfrac{z}{\lambda}\right)\right)=0 \quad (A.37)$$

And finally recast as the generalized eigenvalue problem:

$$AG*\exp\left(\tfrac{z}{\lambda}\right)=-\lambda BG \quad (A.38)$$

The rank of A means that there will be $N-1$ zero eigenvalues for this system. These come in pairs of λ^* and $-\lambda^*$, or positive and negative pairs, which are at most 1-fold degenerate. An odd expansion order will result in $N+1$ distinct eigenvalues whereas an even expansion will result in N. Using the fact that these values occur in positive and negative pairs, the homogeneous solution can be recast in a basis of the entries of G:

$$\tilde{\psi^{(h)}}\left(z|\mathbf{k}\right)=\sum_{j=1}^{\frac{1}{2}\left(N^2+N\right)}\left[C_j^-G_j^-\exp\left(\tfrac{z}{\lambda_j^-}\right)+C_j^+G_j^+\exp\left(\tfrac{z}{\lambda_j^+}\right)\right] \quad (A.39)$$

Here $\lambda_j^-=-\lambda_j^+$. One boundary condition allows further simplification: As depth approaches infinity, the spherical harmonic moments (and therefore the transverse Fourier moments) must approach zero. Therefore, the constants associated with the positive eigenvalues must be zero. This also serves as a reminder to consider increasing depth to be movement in the positive direction on the z axis; otherwise this would be reversed. Now, the transverse Fourier moments can be understood as:

$$\tilde{\psi^{(h)}}\left(z|\mathbf{k}\right)=\sum_{j=1}^{\frac{1}{2}\left(N^2+N\right)}\left[C_j^-G_j^-\exp\left(\tfrac{z}{\lambda_j^-}\right)\right] \quad (A.40)$$

This allows the general solution of the ODE system defined in (A.29) to be understood as:

$$\tilde{\psi^{(h)}}\left(z|\mathbf{k}\right)=\sum_{j=1}^{\frac{1}{2}\left(N^2+N\right)}\left[C_j^-G_j^-\exp\left(\tfrac{z}{\lambda_j^-}\right)\right]+\left(\mu_dA+B\right)^{-1}\tilde{Q}\exp\left(-\mu_dz\right) \quad (A.41)$$

However, to find the actual constants $\left\{C_j^-\right\}$, one must apply the another boundary condition.

A.2.5 Step 5 - Solve the Generalized Eigenvalue Problem Using Boundary Conditions

The Marshak Boundary condition, which states that at the boundary, $(z = 0)$ the radiance initially directed from the medium but reflected back be equal to the inwardly directed scattered light, allows the solution of (A.41). Mathematically, this takes the following form for a fixed l' and m' such that $l' - m'$ is odd:

$$\int_{\mu>0} L_s\left(r=0,\Omega\right) Y^*_{l',m'}\left(\mu,\phi\right) d\Omega = \int_{\mu<0} L_s\left(r=0,\Omega\right) Y^*_{l',m'}\left(-\mu,\phi\right) \gamma\left(-\mu\right) d\Omega \quad (A.42)$$

Here γ is the Fresnel reflection equation, which allows for a refractive index mismatch.

This is not in a directly applicable form to the SHEF_N model. To correct this, L_s is expanded on both sides of (A.42) in the manner defined by (A.3), which results in:

$$\begin{gathered}\int_{\mu>0} \int_0^{2\pi} \sum_{l=0}^{N} \sum_{m=-l}^{l} \left[K_l \psi_{l,m}\left(r=0\right) Y_{l,m}\left(\mu,\phi\right)\right] Y^*_{l',m'}\left(\mu,\phi\right) d\mu d\phi = \\ \int_{\mu<0} \int_0^{2\pi} \sum_{l=0}^{N} \sum_{m=-l}^{l} \left[K_l \psi_{l,m}\left(r=0\right) Y_{l,m}\left(-\mu,\phi\right)\right] Y^*_{l',m'}\left(-\mu,\phi\right) \gamma\left(-\mu\right) d\mu d\phi \quad (A.43)\end{gathered}$$

Once again, the orthonormality of the spherical harmonic functions will be used. First, however, note that since this is a partial expansion, the linearity of integrals can be applied to obtain:

$$\begin{gathered}\sum_{l=0}^{N} \sum_{m=-l}^{l} \int_{\mu>0} \int_0^{2\pi} \left[K_l \psi_{l,m}\left(r=0\right) Y_{l,m}\left(\mu,\phi\right)\right] Y^*_{l',m'}\left(\mu,\phi\right) d\mu d\phi = \\ \sum_{l=0}^{N} \sum_{m=-l}^{l} \int_{\mu<0} \int_0^{2\pi} \left[K_l \psi_{l,m}\left(r=0\right) Y_{l,m}\left(-\mu,\phi\right)\right] Y^*_{l',m'}\left(-\mu,\phi\right) \gamma\left(-\mu\right) d\mu d\phi \quad (A.44)\end{gathered}$$

Furthermore, from here the values of $Y_{l,m}$ and $Y^*_{l',m'}$ are substituted to obtain:

$$\sum_{l=0}^{N}\sum_{m=-l}^{l}\int_{\mu>0}\int_0^{2\pi}\left[K_l\psi_{l,m}\left(r=0\right)\sqrt{\frac{2l+1}{4\pi}*\frac{(l-|m|)!}{(l+|m|)!}}P_{l,m}\left(\mu\right)exp\left(im\phi\right)\right]*$$

$$\left(-1\right)^{m'}\sqrt{\frac{2l'+1}{4\pi}*\frac{(l'-|m|'')!}{(l'+|m'|)!}}P_{l',m'}\left(-\mu\right)exp\left(im'\phi\right)d\mu d\phi=$$

$$\sum_{l=0}^{N}\sum_{m=-l}^{l}\int_{\mu<0}\int_0^{2\pi}\left[K_l\psi_{l,m}\left(r=0\right)\sqrt{\frac{2l+1}{4\pi}*\frac{(l-|m|)!}{(l+|m|)!}}P_{l,m}\left(\mu\right)exp\left(im\phi\right)\right]*$$

$$\left(-1\right)^{m'}\sqrt{\frac{2l'+1}{4\pi}*\frac{(l'-|m'|)!}{(l'+|m'|)!}}P_{l',m'}\left(-\mu\right)exp\left(im'\phi\right)\gamma\left(-\mu\right)d\mu d\phi \quad (A.45)$$

This can be further simplified through basic calculus and the independence of ϕ and μ to separate the double integral into a product of integrals:

$$\sum_{l=0}^{N}\sum_{m=-l}^{l}K_l\psi_{l,m}\left(r=0\right)\left(-1\right)^{m'}\sqrt{\frac{2l+1}{4\pi}*\frac{(l-|m|)!}{(l+|m|)!}*\frac{2l'+1}{4\pi}*\frac{(l'-|m'|)!}{(l'+|m'|)!}}*$$

$$\int_{\mu>0}P_{l,m}\left(\mu\right)P_{l',m'}\left(-\mu\right)d\mu*\int_0^{2\pi}\exp\left(i\left(m-m'\right)\phi\right)d\phi=$$

$$\sum_{l=0}^{N}\sum_{m=-l}^{l}K_l\psi_{l,m}\left(r=0\right)\left(-1\right)^{m'}\sqrt{\frac{2l+1}{4\pi}*\frac{(l-|m|)!}{(l+|m|)!}*\frac{2l'+1}{4\pi}*\frac{(l'-|m'|)!}{(l'+|m'|)!}}*$$

$$\int_{\mu<0}P_{l,m}\left(\mu\right)P_{l',m'}\left(-\mu\right)\gamma\left(-\mu\right)d\mu*\int_0^{2\pi}\exp\left(i\left(m-m'\right)\phi\right)d\phi \quad (A.46)$$

Note that since m and m' are integers, the integral is nonzero if and only if $m=m'$:

$$\int_0^{2\pi}\exp\left(i\left(m-m'\right)\right)d\phi=2\pi\delta_{m,m'} \quad (A.47)$$

This gives an expression of:

$$\sum_{l=0}^{N}\sum_{m=-l}^{l}K_l\psi_{l,m}\left(r=0\right)\left(-1\right)^{m'}\tfrac{1}{2}\delta_{m,m'}\sqrt{\left(2l+1\right)\left(2l'+1\right)\frac{(l-|m|)!}{(l+|m|)!}\frac{(l'-|m'|)!}{(l'+|m'|)!}}*$$

$$\int_{\mu>0}P_{l,m}\left(\mu\right)P_{l',m'}\left(-\mu\right)d\mu=$$

$$\sum_{l=0}^{N}\sum_{m=-l}^{l}K_l\psi_{l,m}\left(r=0\right)\left(-1\right)^{m'}\delta_{m,m'}\sqrt{\left(2l+1\right)\left(2l'+1\right)\frac{(l-|m|)!}{(l+|m|)!}\frac{(l'-|m'|)!}{(l'+|m'|)!}}*$$

$$\int_{\mu<0} P_{l,m}(\mu) P_{l',m'}(-\mu) \gamma(-\mu) d\mu \quad (A.48)$$

Unless $m = m'$, both sides of the equation are simply 0. Therefore, a m may be replaced with m' as follows:

$$\sum_{l=0}^{N} K_{l,m} \psi_{l,m'}(r=0)(-1)^{m'} \tfrac{1}{2} \sqrt{(2l+1)(2l'+1) \tfrac{(l-|m'|)!}{(l+|m'|)!} \tfrac{(l'-|m'|)!}{(l'+|m'|)!}} *$$

$$\int_{\mu>0} P_{l,m'}(\mu) P_{l',m'}(-\mu) d\mu =$$

$$\sum_{l=0}^{N} K_{l,m} \psi_{l,m'}(r=0)(-1)^{m'} \sqrt{(2l+1)(2l'+1) \tfrac{(l-|m'|)!}{(l+|m'|)!} \tfrac{(l'-|m'|)!}{(l'+|m'|)!}} *$$

$$\int_{\mu<0} P_{l,m'}(\mu) P_{l',m'}(-\mu) \gamma(-\mu) d\mu \quad (A.49)$$

After that, the value of $K_{l,m}$ is substituted in and more basic alegbra yields the following:

$$\sum_{l=0}^{N} (2l+1) \psi(r=0) \sqrt{(2l'+1) \tfrac{(l-|m'|)!}{(l+|m'|)!} \tfrac{(l'-|m'|)!}{(l'+|m'|)!}} *$$

$$\int_{\mu>0} P_{l,m'}(\mu) P_{l',m'}(-\mu) d\mu =$$

$$\sum_{l=0}^{N} (2l+1) \psi_{l,m'}(r=0) \sqrt{(2l'+1) \tfrac{(l-|m'|)!}{(l+|m'|)!} \tfrac{(l'-|m'|)!}{(l'+|m'|)!}} *$$

$$\int_{\mu<0} P_{l,m'}(\mu) P_{l',m'}(-\mu) \gamma(-\mu) d\mu \quad (A.50)$$

After which like summations can be combined, which results in:

$$\sum_{l=0}^{N} (2l+1) \psi_{l,m'}(r=0) \sqrt{(2l'+1) \tfrac{(l-|m'|)!}{(l+|m'|)!} \tfrac{(l'-|m'|)!}{(l'+|m'|)!}} *$$

$$\left[\int_{\mu>0} P_{l,m'}(\mu) P_{l',m'}(-\mu) d\mu - \int_{\mu<0} P_{l,m'}(\mu) P_{l',m'}(-\mu) \gamma(-\mu) d\mu \right] = 0 \quad (A.51)$$

From here, note that the transverse Fourier Transform used earlier affects nothing but the spatially dependent spherical harmonic moment, so therefore:

$$\sum_{l=0}^{N}(2l+1)\,\tilde{\psi_{l,m'}}\,(z=0|\mathbf{k})\sqrt{(2l'+1)\,\tfrac{(l-|m'|)!}{(l+|m'|)!}\,\tfrac{(l'-|m'|)!}{(l'+|m'|)!}}\,*$$

$$\left[\int_{\mu>0}P_{l,m'}\,(\mu)\,P_{l',m'}\,(-\mu)\,d\mu-\int_{\mu<0}P_{l,m'}\,(\mu)\,P_{l',m'}\,(-\mu)\,\gamma\,(-\mu)\,d\mu\right]=0 \quad (A.52)$$

The following integral term is defined for brevity's sake:

$$\mathrm{D}_{l,l',m'}=(2l+1)\sqrt{(2l'+1)\,\tfrac{(l-|m'|)!}{(l+|m'|)!}\,\tfrac{(l'-|m'|)!}{(l'+|m'|)!}}\,*$$

$$\left[\int_{\mu>0}P_{l,m'}\,(\mu)\,P_{l',m'}\,(-\mu)\,d\mu-\int_{\mu<0}P_{l,m'}\,(\mu)\,P_{l',m'}\,(-\mu)\,\gamma\,(-\mu)\,d\mu\right] \quad (A.53)$$

Which allows the Marshak condition to be expressed in the form:

$$\sum_{l=0}^{N}\left[D_{l,l',m'}\tilde{\psi_{l,m'}}\,(z=0|\mathbf{k})\right]=0 \quad (A.54)$$

The values of $D_{l,l',m'}$ can be numerically estimated by Gaussian Quadrature. Of course, this does not complete the problem, as the goal of the step is to obtain values for $\left\{C_j^-\right\}$. To do this, first recall that the general solution is of the form:

$$\tilde{\psi_{l,m'}}\,(z|\mathbf{k})=\sum_{j=1}^{\frac{1}{2}\left(N^2+N\right)}\left[C_j^-G_j^-\exp\left(\tfrac{z}{\lambda_j^-}\right)\right]+\left(\mu_dA+B\right)^{-1}\tilde{Q}\exp\left(-\mu_dz\right) \quad (A.55)$$

Note that any value of z may be used to calculate C_j. Therefore, $z=0$ is substituted for simplicity's sake, resulting in:

$$\tilde{\psi_{l,m'}}\,(z|\mathbf{k})=\sum_{j=1}^{\frac{1}{2}\left(N^2+N\right)}\left[C_j^-G_j^-\right]+\left(\mu_dA+B\right)^{-1}\tilde{Q} \quad (A.56)$$

To relate this to the general boundary condition format, a matrix of the values $D_{l,l',m'}$ is used. The first index of D is defined as a one to one mapping for transverse Fourier moments for possible values (l,m) whereas the second corresponds to (l',m'). Structure is provided

for j from the indices of the right hand side of the above equation, whereas that for i is provided by the structure of j. Because of the nature of the integrals discussed earlier, any pair i and j corresponding to moments where $m \neq m'$ will index a zero value for the matrix. Otherwise, the expected value of $D_{l,l',m'}$ is used. This allows the values of $\left\{C_j^-\right\}$, expressed as a vector C, to be defined by the Matrix Equation:

$$C = (DG)^{-1}\left(-D\left(\mu_d A + B\right)^{-1}\tilde{Q}\right) \quad (A.57)$$

Which completes the formulation of the boundary conditions, with the j element of C defined as C_j^-.

A.2.6 Step 6 - Apply Inverse Fourier Transform to Obtain Spherical Harmonic Moments

Once the values of $\left\{C_j^-\right\}$ have been obtained, an inverse Fourier transform is applied to get the original spherical harmonic moments $\{\psi_{l,m}$:

$$\psi_{l,m}(r) = \frac{1}{4\pi}\int_{-\infty}^{\infty}\int_{-\infty}^{\infty}\tilde{\psi_{l,m}}(z|\mathbf{k})\, exp\left(i\left(k_x x + k_y y\right)\right) dk_x dk_y \quad (A.58)$$

In the case of a source defined by a simple sinusoidal wave, this may be computed without the use of integration or Inverse Fourier Transform functions due to the transform of that wave. This makes the SHEF$_N$ method particularly useful for SFDI/S imaging methods, since they tend to use sources which are single waves with predefined phase modulations.

Appendix B

MATLab Code

B.1 dSHEFClean.m

```
 % Clean copy of Double SHEF_N.  This code requires that dSHEFinit.m be run
% first. That file will create matrices used for boundary conditions and
% the system of ODEs upon which DSHEF_N is based.  dSHEFinit only needs to
% be run a single time so long as the choice of refractive index does not
% change, and only if matrix files have not previously been created.
%
% This code uses DSHEF_N to simulate scattered radiance in a medium
% consisting of two layers, both in the positive z direction with
% boundaries at z = 0 and z = z*, for some layer thickness.  It assumes a
% source that is a delta function in Fourier space, or in other words a
% planar wave directed into the medium with a sinusoidal spatial modulation
% in the x direction and another in the y direction.
```

```
%
% Each layer is assumed to have the same scattering phase function, and
% while a Henyey-Greenstein function is hard coded in, it can be replaces
% with any alternative phase function.
%
% By Sean Horan, 7/9/2020

order = 13; % The desired order of expansion in double spherical harmonics.
z_depth = 0; % The depth to be interrogated.
theta_0 = 0; % Polar angle of incidence of the source
phi_0 = 0; % Azimuthal angle of incidence of the source
mu_a_1 = 0.01; % Absorption coefficient of the top layer
mu_a_2 = 0.01; % Absorption coefficient of the bottom layer
mu_s_1 = 1.0; % Scattering coefficient of the top layer
mu_s_2 = 2.0; % Scattering coefficient of the bottom layer
thickness = 0.1; % Thickness of the top layer
g = 0.8; % Anisotropy of the scattering phase function
k_y = 0; % Wave number in the y direction (should be equal to 2*pi*f_y
k_x = 0; % Wave number in the x direction (should be equal to 2*pi*f_y
useFDelta = 0; % Keep at zero to not use a delta-Eddington approximation of
               % the source function.  Keep this at zero for now; there has
               % not been a satisfactory method of applying this
               % approximation in a double basis.

tic

% The following switch statement selects premade matrices for use in
```

```
% DSHEF_N based on the order selected.  This is the portion of code which
% requires that dSHEFinit be run once beforehand.  It is possible to use
% Gauss-Legendre quadrature to calculate these more quickly, but it is not
% recommended because the functions involved are not finite order
% polynomials, and therefore standard Gaussian Quadrature (used in
% dSHEFinit.m) is recommended for a more accurate approximation.

% B_x_derivs and B_y_derivs are used to represent the recurrence relations
% introduced into DSHEF_N's B matrix by the x and y terms of the
% directional derivative of the radiative transport equation.  boundaryCoef
% is used in the application of the Marshak Boundary Condition. convMat is
% used to convert a vector representing a function in a single spherical
% harmonic basis to one in a double spherical hamornic basis, and its
% transpose is used to convert in the opposite direction.

switch order
    case 1
        B_x_derivs = xd1;
        B_y_derivs = yd1;
        boundaryCoef = bc1;
        convMat = cm1;
    case 2
        B_x_derivs = xd2;
        B_y_derivs = yd2;
        boundaryCoef = bc2;
        convMat = cm2;
    case 3
```

```
    B_x_derivs = xd3;
    B_y_derivs = yd3;
    boundaryCoef = bc3;
    convMat = cm3;
case 4
    B_x_derivs = xd4;
    B_y_derivs = yd4;
    boundaryCoef = bc4;
    convMat = cm4;
case 5
    B_x_derivs = xd5;
    B_y_derivs = yd5;
    boundaryCoef = bc5;
    convMat = cm5;
case 6
    B_x_derivs = xd6;
    B_y_derivs = yd6;
    boundaryCoef = bc6;
    convMat = cm6;
case 7
    B_x_derivs = xd7;
    B_y_derivs = yd7;
    boundaryCoef = bc7;
    convMat = cm7;
case 8
    B_x_derivs = xd8;
    B_y_derivs = yd8;
```

```
    boundaryCoef = bc8;
    convMat = cm8;
case 9
    B_x_derivs = xd9;
    B_y_derivs = yd9;
    boundaryCoef = bc9;
    convMat = cm9;
case 10
    B_x_derivs = xd10;
    B_y_derivs = yd10;
    boundaryCoef = bc10;
    convMat = cm10;
case 11
    B_x_derivs = xd11;
    B_y_derivs = yd11;
    boundaryCoef = bc11;
    convMat = cm11;
case 12
    B_x_derivs = xd12;
    B_y_derivs = yd12;
    boundaryCoef = bc12;
    convMat = cm12;
otherwise
    B_x_derivs = xd13;
    B_y_derivs = yd13;
    boundaryCoef = bc13;
    convMat = cm13;
```

```
end

% Calculate the total attenuation coefficient for each layer.

mu_t_1 = mu_s_1 + mu_a_1; % Total attenuation for the top layer
mu_t_2 = mu_s_2 + mu_a_2; % Total attenuation for the bottom layer

vecLength = 2*(order+1)^2; % Define the length of any vector representing a
                           % function in a double spherical hamornic basis
                           % of order N.

% Determine points and weights for Gaussian quadrature on the sphere.  This
% quadrature will be used for calculating the A matrix used in DSHEF_N.

theta_in = asin(sin(theta_0)/n); % Change the polar angle of the source
                                 % function due to refractive index
                                 % mismatch, according to Snell's Law.
mu_in = (cos(theta_in)+1)/2; % Calculate the compressed cosine of the input
                             % angle in the double spherical harmonic
                             % basis.
mu_in_single = cos(theta_in); % Calculate the compressed cosine of the
                              % input angle in the single spherical
                              % harmonic basis.
dphi = pi/(order + 1); % Choose azimuthal angles differences for use in
                       % Gauss-Legendre quadrature.

[mu_quad_temp, w_quad_temp] = GL(order+1); % Calculate polar angles and
```

```
                                        % function weights for
                                        % Gauss-Legendre quadrature.
mu_quad_temp = (mu_quad_temp + 1)/2; % Convert polar angles for G-L to
                                     % compressed ones for use in a double
                                     % spherical harmonic basis.
w_quad_temp = 0.5*w_quad_temp; % Halve the weights for G-L for use in the
                               % double spherical harmonic basis.

phi_quad_temp = 0:dphi:(2*pi - dphi); % Calculate azimuthal angles for use
                                      % G-L.


% Create matrices for use in G-L by repeating the vectors created
% previously.

phi_quad = repmat( phi_quad_temp', order + 1, 1 );
mu_quad  = repelem( mu_quad_temp, 2*order + 2 );
w_quad  = repelem( w_quad_temp, 2*order + 2 ) * dphi;

% Create mesh grids for the angles used in G-L.

[mu,mu_prime] = meshgrid(mu_quad);
[phi,phi_prime] = meshgrid(phi_quad);

% Create matrices for spherical harmonic functions

YbarMat = zeros(vecLength/2,length(mu));
```

```
PbarMat = zeros(order+1,length(mu_quad_temp));

for i = 1:vecLength/2
    [l,m] = getSHFlm(i);
    YbarMat(i,:) = ybar(l,m,mu_quad,phi_quad);
    PbarMat(l+1,:) = legendreP(l,2*mu_quad_temp-1);
end

Getmutees = @(mua, mus, gees) mua + mus * (1 - gees);

% Several scattering phase functions are defined here. To use one, set
% phaseFunc = @(mu) desiredFunctionName.  The default is set to
% Henyey-Greenstein.

nuFunc = @(mu,mu_prime,phi,phi_prime) ...
    mu.*mu_prime + sqrt(1 - mu.^2).*sqrt(1 - mu_prime.^2).*cos(phi - phi_prime);
henyeyGreensteinFunc = @(mu,g) ...
    (1 - g^2)./( (2) * (1 + g.^2 - 2.*g.*mu).^(3/2) );
alpha = 1;
K = ( alpha * g * (1 - g^2)^(2*alpha) ) / ...
    (pi * ( (1 + g)^(2*alpha) - (1 - g)^(2*alpha) ) );
reynoldsMcCormickFunc = @(mu) K./(1 + g^2 - 2*g.*mu).^(-alpha - 1);
modifiedHenyeyGreensteinFunc = @(mu) alpha.*henyeyGreensteinFunc(mu) + ...
    (1-alpha) .* 3 ./ (4*pi) .* mu.^2;
powersOfCosinesFunc = @(mu) 1./(4.*pi) .* ...
    (order + 1) / 2.^order .* (1 + mu).^order;
modifiedPowersOfCosinesFunc = @(mu) alpha.*powersOfCosinesFunc(mu) + ...
```

```
    (1-alpha) .* 3 ./ (4*pi) .* mu.^2;

% This is where the actual phase function is chosen.

phaseFunc = @(mu) ...
    henyeyGreensteinFunc((mu),g);

% Initialize vectors of phase function moments.  These moments are in
% either single or double Legendre Polynomials, not any sort of
% spherical harmonic functions.

gees_up = zeros(order+1,0); % Upward moments (forward scattering direction)
                            % in double Legendre polynomials.
gees_down = zeros(order+1,0); % Downward moments (backward scattering
                              % direction) in double Legendre polynomials.
gees_single = zeros(order+1,0); % Moments for the entire scattering phase
                                % function in regular Legendre polynomials.

% Calculate the various forms of scattering moments using Gaussian
% quadrature.  The upFunc and downFunc are point by point products of
% compressed (double) Legendre polynomials and the actual phase function.
% Recall that in this functional basis, the two bases are considered to
% point away from each other.  This is why downFunc uses -mu as an
% argument.

% This loop calculates the double Legendre moments.
```

```
for i = 1:order+1
    upFunc = @(mu) phaseFunc(mu).*legendreP(i-1,2*mu-1);
    downFunc = @(mu) phaseFunc(-mu).*legendreP(i-1,2*mu-1);
    gees_up(i) = quadgk(upFunc,0,1);
    gees_down(i) = quadgk(downFunc,0,1);
end

% This loop calculates the single Legendre moments.

for i = 1:order+1
    singleFunc = @(mu) phaseFunc(mu).*legendreP(i-1,mu);
    gees_single(i) = quadgk(singleFunc,-1,1);
end

% Use Gaussian quadrature to calculate the f_delta constant from
% delta-Eddington.  The *(useFDelta ~= 0) term allows the user to choose
% whether or not they use this approximation.

% This calculates f-delta for use with double Legendre moments.

f_deltaFunc = @(mu) phaseFunc(mu).*legendreP(order+1,2*mu-1);
f_delta_double = quadgk(f_deltaFunc,0,1)*(useFDelta ~= 0);

% This calculates f-delta for the single Legendre moment case.

f_deltaFuncSingle = @(mu) phaseFunc(mu).*legendreP(order+1,mu)*useFDelta;
f_delta_single = quadgk(f_deltaFuncSingle,-1,1)*(useFDelta ~= 0);
```

```
% This calculates the modified scattering phase functions for use with the
% source vector.  Note that if f_delta = 0, these work out to a direct
% equivalence between gees_x_f_delta and gees_x.

gees_single_f_delta = (gees_single - f_delta_single)/(1 - f_delta_single);
gees_up_f_delta = (gees_up - f_delta_double)/(1 - f_delta_double);

% Be sure to define the variable f_delta as either f_delta_single or
% f_delta_double, depending on the user's choice.  This choice is defined
% by the source_toggle variable.  1 uses the single basis and any other
% value uses the double basis.

if source_toggle == 1
    f_delta = f_delta_single;
else
    f_delta = f_delta_double;
end

mu_t_1_tilde = (mu_a_1 + mu_s_1*(1-f_delta)); % Extinction coefficient for
                                              % the top layer.
mu_t_2_tilde = (mu_a_2 + mu_s_2*(1-f_delta)); % Extinction coefficient for
                                              % the bottom layer.


% Find moments for f_delta modified scattering phase function
```

```
%cosTheta_1 = mu .* mu_prime ...
%    + sqrt( 1 - mu.^2 ) .* sqrt( 1 - mu_prime.^2 ) .* cos( phi - phi_prime );
%cosTheta_2 = -mu .* mu_prime ...
%    + sqrt( 1 - mu.^2 ) .* sqrt( 1 - mu_prime.^2 ) .* cos( phi - phi_prime );
%phases_fwd = phaseFunc(cosTheta_1);
%phases_back = phaseFunc(cosTheta_2);

kxy.kyPkxImag = k_y + 1i*k_x;
kxy.kyMkxImag = k_y - 1i*k_x;
kxy.magSq = k_x^2 + k_y^2;

% Create the blocks and then the whole matrix for A.  Recall that this
% matrix represents the recurrence relations introduced by the z portion of
% the directional derivative.

A_Block = real(YbarMat*diag(mu_quad.*w_quad')*YbarMat');
A = [A_Block, 0*A_Block; 0*A_Block, -A_Block];

% Create the B matrix one block at a time, being conscious of the
% coordinate change between hemispheres.  First,  we construct half_1 and
% half_2 matrices, which calculate the contributions of single legendre
% moments to the upper and lower hemispheres.

half_1 = zeros((order+1)^2,(order+1)^2);
half_2 = zeros((order+1)^2,(order+1)^2);

for i = 1:(order+1)^2
```

```
    for j = 1:(order+1)^2
        [l,m] = getSHFlm(i);
        [l_prime,m_prime] = getSHFlm(j);
        if m == m_prime
            half_1(i,j) = gees_single(l+1)*createIplus(l_prime,l,m);
            half_2(i,j) = gees_single(l+1)*createIminus(l_prime,l,m);
        end
    end
end

% The final scattering portion of the B matrix, scatterMat, comes from the
% use of the conversion matrix. The Iplus and Iminus terms, as well as left
% multiplication by convMat, form a matrix which converts double spherical
% harmonics to single, then applies the scattering phase function, then
% converts back from single to double.

scatterMat = convMat * [half_1,half_2];

% Create the total B matrix for the first layer.  This is composed of the
% recurrence relations introduced by the x and y portions of the
% directional derivatives, plus total attenuation times the identity
% matrix, minus the scattering coefficient times the scattering matrix.

B_1 = 1i*k_x*[B_x_derivs, 0*B_x_derivs; 0*B_x_derivs, B_x_derivs] + ...
      1i*k_y*[B_y_derivs, 0*B_y_derivs; 0*B_y_derivs, B_y_derivs] + ...
      mu_t_1 * eye(2*(order+1)^2) - mu_s_1 * scatterMat;
```

```
B_1 = round(B_1,8); % Round off at 8 decimal places to kill off imaginary
                    % components which are introduced by small errors from
                    % quadrature.  These are commonly on the order of
                    % 10^-14 or lower, so 8 places will both ensure the
                    % loss of imaginary terms and preserve the function of
                    % the matrix.

% Repeat this for B_2.

B_2 = 1i*k_x*[B_x_derivs, 0*B_x_derivs; 0*B_x_derivs, B_x_derivs] + ...
      1i*k_y*[B_y_derivs, 0*B_y_derivs; 0*B_y_derivs, B_y_derivs] + ...
      mu_t_2 * eye(2*(order+1)^2) - mu_s_2 * scatterMat;

B_2 = round(B_2,8);

% Create vectors for the source contribution term Q.  Begin by initializing
% the vectors.

source_base_up = zeros((order+1)^2,1); % Upper hemisphere portion of a
                                       % vector set in a double spherical
                                       % harmonic basis.
source_base_down = zeros((order+1)^2,1); % Lower hemisphere portion of a
                                         % vector set in a double spherical
                                         % harmonic basis.
source_base_single = zeros((order+1)^2,1); % Single spherical harmonic
                                           % basis.
```

```
% Populate the various source vectors by using the legendre moments and
% conjugate spherical harmonic functions.

for i = 1:(order+1)^2
    [l,m] = getSHFlm(i);
    source_base_up(i) = conj(ybar(l,m,2*mu_in-1,phi_in))*...
        gees_up_f_delta(l+1);
    source_base_down(i) = conj(ybar(l,m,2*mu_in-1,pi+phi_in))*...
        gees_down(l+1);
    source_base_single(i) = ...
        conj(spherHarmlm_mu(l,m,mu_in_single,phi_in))*...
        gees_single_f_delta(l+1);
end

% Create the actual base for the source vector with the proper value for
% f_delta.

if source_toggle == 1
    source_base = convMat*source_base_single;
    source_1 = source_base*mu_s_1*(1 - f_delta);
    source_2 = source_base*mu_s_2*(1 - f_delta);
else
    source_base = [source_base_up;source_base_down];
    source_1 = source_base*mu_s_1*(1 - f_delta);
    source_2 = source_base*mu_s_2*(1 - f_delta);
end
```

```
% Calculate eigenpairs for the top layer A and B pair.  These pairs are
% sorted by the eigenvalues, from lowest (most strongly negative) to
% highest (most strongly positive.)

[V_1,D_1] = eig(-B_1,A); % Calculate eigenpairs.  This is the single most
                         % expensive portion of the code.

% These lines sort both vectors and values.

vals_1 = diag(D_1);
[~,idx_1] = sort(real(vals_1));
vals_1 = vals_1(idx_1);
vecs_1 = V_1(:,idx_1);

% These lines separate the vectors and values into positive and negative
% portions, as well as upper and lower hemisphere portions.  For instance,
% vecs_1_neg_up takes the eigenvectors which correspond to negative
% eigenvalues and keeps the portion which contributes to the upper
% hemisphere of scattered radiance.

vecs_1_up = vecs_1(end/2+1:end,:);
vecs_1_down = vecs_1(1:end/2,:);
vals_1_neg = vals_1(find(real(vals_1) < -1e-8));
vals_1_pos = vals_1(find(real(vals_1) > 1e-8));
vecs_1_neg = vecs_1(:,find(real(vals_1) < -1e-8));
vecs_1_neg_up = vecs_1_neg(1:end/2,:);
vecs_1_neg_down = vecs_1_neg(end/2+1:end,:);
```

```
vecs_1_pos = vecs_1(:,find(real(vals_1) > 1e-8));
vecs_1_pos_up = vecs_1_pos(1:end/2,:);
vecs_1_pos_down = vecs_1_pos(end/2+1:end,:);

% Repeat this process for the second layer.

[V_2,D_2] = eig(-B_2,A);
vals_2 = diag(D_2);
[vals_2,idx_2] = sort(real(vals_2));
vecs_2 = V_2(:,idx_2);
vecs_2_up = vecs_2(end/2+1:end,:);
vecs_2_down = vecs_2(1:end/2,:);
vals_2_neg = vals_2(find(real(vals_2) < -1e-8));
vals_2_pos = vals_2(find(real(vals_2) > 1e-8));
vecs_2_neg = vecs_2(:,find(real(vals_2) < -1e-8));
vecs_2_neg_up = vecs_2_neg(1:end/2,:);
vecs_2_neg_down = vecs_2_neg(end/2+1:end,:);
vecs_2_pos = vecs_2(:,find(real(vals_2) > 1e-8));
vecs_2_pos_up = vecs_2_pos(1:end/2,:);
vecs_2_pos_down = vecs_2_pos(end/2+1:end,:);

% Calculate the particular solutions for each layer.  Recall that these
% are calculated using matrix inversion from the matrix form of the RTE.

part_1 = ( -(mu_s_1*(1 - f_delta) + mu_a_1) .* A + B_1)\source_1;
part_2 = ( -(mu_s_2*(1 - f_delta) + mu_a_2) .* A + B_2)\source_2;
```

```
% Construct the matrix for the application of the Marshak boundary
% condition.  The identity on the left side of the block matrix J is
% applied to scattered radiance in the positive z direction (into the
% medium) whereas the boundaryCoef matrix is defined by Fresnel's law for
% internal reflection.

J = [eye((order+1)^2),-boundaryCoef];

% Construct matrix for final inversion to calculate eigenmoments for the
% homogeneous solution.

% The boundaryMat Matrix applies the Marshak condition to the eigenvectors
% for the upper layer at the boundary.  The moments for eigenvectors
% corresponding to negative eigenvalues are calculated at z = 0, while
% those for eigenvectors corresponding to positive eigenvalues are
% calculated at z = z*, the layer thickness.  That is why an exponential
% decay term is applied to the positive vectors but not the negative ones.

boundaryMat = J*[vecs_1_neg,vecs_1_pos*diag(exp(-thickness.*vals_1_pos))];

% The interfaceMat matrix applies the condition of equality between
% scattered radiance in the two layers to the eigenvectors of those layers.
% As in boundaryMat, the moments corresponding to the negative vectors of
% the first layer are calculated at z = 0, while those corresponding to the
% positive vectors of the first layer and the negative vectors of the
% second layer are calculated at z = z*, the layer thickness.  Those
% corresponding to positive values in the second layer are not used because
```

```
% total scattered radiance must decay to 0 as z approaches infinity, and
% the rates of decay are given by the eigenvalues.

interfaceMat = [[vecs_1_neg*diag(exp(thickness.*vals_1_neg)),...
    vecs_1_pos],-vecs_2_neg];

inversionVec = [-J * part_1; (part_2 - part_1) * ...
    exp(-(mu_a_1 + (1 - f_delta) * mu_s_1) * thickness)];

% The inversionMat matrix is simply the combination of the previous
% matrices, as well as a zero block in the first row representing the fact
% that radiance in the second layer are not directly affected by the
% Marshak condition.

inversionMat = [boundaryMat,zeros(size(boundaryMat,1),...
    size(interfaceMat,2) - size(boundaryMat,2));interfaceMat];

% Perform the matrix inversion to obtain a vector of eigenmoments.

eigen_moments = inversionMat\inversionVec;

% Separate the eigenmoments into sections coresponding to positive and
% negative eigenvectors for different layers.

c_minus = eigen_moments(1:(order+1)^2); % Moments for top layer negative
                                        % eigenvectors.
c_plus = eigen_moments(1+(order+1)^2:2*(order+1)^2); % Moments for top
```

```
                                                    % layer positive
                                                    % eigenvectors.
d_minus = eigen_moments(1+2*(order+1)^2:end); % Moments for the bottom
                                                    % layer negative
                                                    % eigenvectors.

% Calculate the combined solution for scattered radiance, depending on the
% desired depth.  This will be a vector of double spherical harmonic
% moments.

% First, determine which layer the solution will be calculated for.

if z_depth < thickness

    % In the top layer, start with the particular solution, adjusted for
    % the specified depth.

    final_depth_refl_moments = part_1*exp(-mu_t_1*z_depth/mu_in);

    % Next, add the homogeneous solution one moment and vector combination
    % at a time.  Positive and negative pairs are added at the same time.

    for i = 1:(order+1)^2
        final_depth_refl_moments = final_depth_refl_moments + ...
            c_minus(i) * vecs_1_neg(:,i) * ...
            exp( z_depth * (vals_1_neg(i)/mu_in )) + ...
            c_plus(i) * vecs_1_pos(:,i) * exp( (z_depth-thickness) * ...
```

```
            (vals_1_pos(i)/mu_in ));
    end
else

    % In the bottom layer, start with the particular solution for that
    % layer, adjusted for depth.

    final_depth_refl_moments = part_2*exp(-mu_t_1*thickness/mu_in - ...
    mu_t_2*(z_depth - thickness)/mu_in);

    % Now, add in the components of the homogeneous solution, one vector
    % and moment combination at a time.  Only the negative moments are used
    % in the bottom layer.

    for i = 1:length(eigen_moments/2)
        final_depth_refl_moments = final_depth_refl_moments + ...
            d_minus(i) * vecs_2_neg(:,i) * exp( (z_depth-thickness) ...
            * (vals_2_neg(i)/mu_in ));
    end
end

% Split the vector of double spherical harmonic moments into upward and
% downward portions.

final_moms_up = ((final_depth_refl_moments(1:end/2)));
final_moms_down = ((final_depth_refl_moments(end/2+1:end)));
```

```
% Obtain radiance as a function of cosine(theta) for the azimuthally
% symmetric case.  Because of the way spherical harmonics work, this will
% also return the average radiance values across all phi for a given theta.
% Note that two graphs are created here, one for x_up and one for x_down.

[x_out_sym_up,x_out_sym_down,y_out_sym_up,y_out_sym_down] = ...
    doublePGraphGen(getCenterSHF(final_moms_up),...
    getCenterSHF(final_moms_down));

% Obtain a unified graph for radiance as a function of cosine(theta), where
% the radiance at the equator is the mean of its value for each side.

[x_out_sym,y_out_sym] = ...
    doublePGraphGenCombined(getCenterSHF(final_moms_up),...
    getCenterSHF(final_moms_down));

toc
```

B.2 DSHEF_func

```
function[x_out_sym,y_out_sym] = DSHEF_func(mu\_a_1,mu_s_1,mu_a_2,mu_s_2,thickness,order,
% Clean copy of Double SHEF_N.  This code requires that dSHEFinit.m be run
% first. That file will create matrices used for boundary conditions and
% the system of ODEs upon which DSHEF_N is based.  dSHEFinit only needs to
```

```
% be run a single time so long as the choice of refractive index does not
% change.
%
% This code uses DSHEF_N to simulate scattered radiance in a medium
% consisting of two layers, both in the positive z direction with
% boundaries at z = 0 and z = z*, for some layer thickness.  It assumes a
% source that is a delta function in Fourier space, or in other words a
% planar wave directed into the medium with a sinusoidal spatial modulation
% in the x direction and another in the y direction.
%
% Each layer is assumed to have the same scattering phase function, and
% while a Henyey-Greenstein function is hard coded in, it can be replaces
% with any alternative phase function.
%
% This version of the code is meant to function within a function,
% taking in one spatial frequency and outputting a reflectiveness.
%
% By Sean Horan, 7/23/2020

% order = 13; % The desired order of expansion in double spherical harmonics.
z_depth = 0; % The depth to be interrogated.
theta_0 = 0; % Polar angle of incidence of the source
phi_in = 0; % Azimuthal angle of incidence of the source
% mu_a_1 = 0.01; % Absorption coefficient of the top layer
% mu_a_2 = 0.01; % Absorption coefficient of the bottom layer
% mu_s_1 = 1.0; % Scattering coefficient of the top layer
% mu_s_2 = 2.0; % Scattering coefficient of the bottom layer
```

```
%thickness = 0.1; % Thickness of the top layer
% g = 0.8; % Anisotropy of the scattering phase function
% k_y = 0; % Wave number in the y direction (should be equal to 2*pi*f_y
k_x = 0; % Wave number in the x direction (should be equal to 2*pi*f_y
source_toggle = 0; % Set to 0 to represent source function in double
                   % spherical harmonics directly, set to anything else to
                   % represent first in single spherical harmonics and then
                   % convert to double.
useFDelta = 0; % Keep at zero to not use a delta-Eddington approximation of
               % the source function.  Keep this at zero for now; there has
               % not been a satisfactory method of applying this
               % approximation in a double basis.

% The following switch statement selects premade matrices for use in
% DSHEF_N based on the order selected.  This is the portion of code which
% requires that dSHEFinit be run once beforehand.  It is possible to use
% Gauss-Legendre quadrature to calculate these more quickly, but it is not
% recommended because the functions involved are not finite order
% polynomials, and therefore standard Gaussian Quadrature (used in
% dSHEFinit.m) is recommended for a more accurate approximation.

% B_x_derivs and B_y_derivs are used to represent the recurrence relations
% introduced into DSHEF_N's B matrix by the x and y terms of the
% directional derivative of the radiative transport equation.  boundaryCoef
% is used in the application of the Marshak Boundary Condition. convMat is
% used to convert a vector representing a function in a single spherical
% harmonic basis to one in a double spherical hamornic basis, and its
```

```
% transpose is used to convert in the opposite direction.

filename = ['dshef',num2str(order),'mats.mat'];
fileMats = open(filename);
convMat = fileMats.dshef.cm;
boundaryCoef = fileMats.dshef.bc;
B_x_derivs = fileMats.dshef.xd;
B_y_derivs = fileMats.dshef.yd;

% Calculate the total attenuation coefficient for each layer.

mu_t_1 = mu_s_1 + mu_a_1; % Total attenuation for the top layer
mu_t_2 = mu_s_2 + mu_a_2; % Total attenuation for the bottom layer

vecLength = 2*(order+1)^2; % Define the length of any vector representing a
                           % function in a double spherical hamornic basis
                           % of order N.

% Determine points and weights for Gaussian quadrature on the sphere.  This
% quadrature will be used for calculating the A matrix used in DSHEF_N.

theta_in = asin(sin(theta_0)/n); % Change the polar angle of the source
                                 % function due to refractive index
                                 % mismatch, according to Snell's Law.
mu_in = (cos(theta_in)+1)/2; % Calculate the compressed cosine of the input
                             % angle in the double spherical harmonic
                             % basis.
```

```
mu_in_single = cos(theta_in); % Calculate the compressed cosine of the
                              % input angle in the single spherical
                              % harmonic basis.
dphi = pi/(order + 1); % Choose azimuthal angles differences for use in
                       % Gauss-Legendre quadrature.

[mu_quad_temp, w_quad_temp] = GL(order+1); % Calculate polar angles and
                                           % function weights for
                                           % Gauss-Legendre quadrature.
mu_quad_temp = (mu_quad_temp + 1)/2; % Convert polar angles for G-L to
                                     % compressed ones for use in a double
                                     % spherical harmonic basis.
w_quad_temp = 0.5*w_quad_temp; % Halve the weights for G-L for use in the
                               % double spherical harmonic basis.

phi_quad_temp = 0:dphi:(2*pi - dphi); % Calculate azimuthal angles for use
                                      % G-L.


% Create matrices for use in G-L by repeating the vectors created
% previously.

phi_quad = repmat( phi_quad_temp', order + 1, 1 );
mu_quad  = repelem( mu_quad_temp, 2*order + 2 );
w_quad  = repelem( w_quad_temp, 2*order + 2 ) * dphi;

% Create mesh grids for the angles used in G-L.
```

```
[mu,mu_prime] = meshgrid(mu_quad);
[phi,phi_prime] = meshgrid(phi_quad);

% Create matrices for spherical harmonic functions

YbarMat = zeros(vecLength/2,length(mu));
PbarMat = zeros(order+1,length(mu_quad_temp));

for i = 1:vecLength/2
    [l,m] = getSHFlm(i);
    YbarMat(i,:) = ybar(l,m,mu_quad,phi_quad);
    PbarMat(l+1,:) = legendreP(l,2*mu_quad_temp-1);
end

Getmutees = @(mua, mus, gees) mua + mus * (1 - gees);

% Several scattering phase functions are defined here. To use one, set
% phaseFunc = @(mu) desiredFunctionName.  The default is set to
% Henyey-Greenstein.

nuFunc = @(mu,mu_prime,phi,phi_prime) ...
    mu.*mu_prime + sqrt(1 - mu.^2).*sqrt(1 - mu_prime.^2).*cos(phi - phi_prime);
henyeyGreensteinFunc = @(mu,g) ...
    (1 - g^2)./( (2) * (1 + g.^2 - 2.*g.*mu).^(3/2) );
alpha = 1;
K = ( alpha * g * (1 - g^2)^(2*alpha) ) / ...
```

```
    (pi * ( (1 + g)^(2*alpha) - (1 - g)^(2*alpha) ) );
reynoldsMcCormickFunc = @(mu) K./(1 + g^2 - 2*g.*mu).^(-alpha - 1);
modifiedHenyeyGreensteinFunc = @(mu) alpha.*henyeyGreensteinFunc(mu) + ...
    (1-alpha) .* 3 ./ (4*pi) .* mu.^2;
powersOfCosinesFunc = @(mu) 1./(4.*pi) .* ...
    (order + 1) / 2.^order .* (1 + mu).^order;
modifiedPowersOfCosinesFunc = @(mu) alpha.*powersOfCosinesFunc(mu) + ...
    (1-alpha) .* 3 ./ (4*pi) .* mu.^2;

% This is where the actual phase function is chosen.

phaseFunc = @(mu) ...
    henyeyGreensteinFunc((mu),g);

% Initialize vectors of phase function moments.  These moments are in
% either single or double Legendre Polynomials, not any sort of
% spherical harmonic functions.

gees_up = zeros(order+1,0); % Upward moments (forward scattering direction)
                            % in double Legendre polynomials.
gees_down = zeros(order+1,0); % Downward moments (backward scattering
                              % direction) in double Legendre polynomials.
gees_single = zeros(order+1,0); % Moments for the entire scattering phase
                                % function in regular Legendre polynomials.

% Calculate the various forms of scattering moments using Gaussian
% quadrature.  The upFunc and downFunc are point by point products of
```

```
% compressed (double) Legendre polynomials and the actual phase function.
% Recall that in this functional basis, the two bases are considered to
% point away from each other.  This is why downFunc uses -mu as an
% argument.

% This loop calculates the double Legendre moments.

for i = 1:order+1
    upFunc = @(mu) phaseFunc(mu).*legendreP(i-1,2*mu-1);
    downFunc = @(mu) phaseFunc(-mu).*legendreP(i-1,2*mu-1);
    gees_up(i) = quadgk(upFunc,0,1);
    gees_down(i) = quadgk(downFunc,0,1);
end

% This loop calculates the single Legendre moments.

for i = 1:order+1
    singleFunc = @(mu) phaseFunc(mu).*legendreP(i-1,mu);
    gees_single(i) = quadgk(singleFunc,-1,1);
end

% Use Gaussian quadrature to calculate the f_delta constant from
% delta-Eddington.  The *(useFDelta ~= 0) term allows the user to choose
% whether or not they use this approximation.

% This calculates f-delta for use with double Legendre moments.
```

```
f_deltaFunc = @(mu) phaseFunc(mu).*legendreP(order+1,2*mu-1);
f_delta_double = quadgk(f_deltaFunc,0,1)*(useFDelta ~= 0);

% This calculates f-delta for the single Legendre moment case.

f_deltaFuncSingle = @(mu) phaseFunc(mu).*legendreP(order+1,mu)*useFDelta;
f_delta_single = quadgk(f_deltaFuncSingle,-1,1)*(useFDelta ~= 0);

% This calculates the modified scattering phase functions for use with the
% source vector.  Note that if f_delta = 0, these work out to a direct
% equivalence between gees_x_f_delta and gees_x.

gees_single_f_delta = (gees_single - f_delta_single)/(1 - f_delta_single);
gees_up_f_delta = (gees_up - f_delta_double)/(1 - f_delta_double);

% Be sure to define the variable f_delta as either f_delta_single or
% f_delta_double, depending on the user's choice.  This choice is defined
% by the source_toggle variable.  1 uses the single basis and any other
% value uses the double basis.

if source_toggle == 1
    f_delta = f_delta_single;
else
    f_delta = f_delta_double;
end

mu_t_1_tilde = (mu_a_1 + mu_s_1*(1-f_delta)); % Extinction coefficient for
```

```
                                                % the top layer.
mu_t_2_tilde = (mu_a_2 + mu_s_2*(1-f_delta)); % Extinction coefficient for
                                                % the bottom layer.


% Find moments for f_delta modified scattering phase function

%cosTheta_1 = mu .* mu_prime ...
%    + sqrt( 1 - mu.^2 ) .* sqrt( 1 - mu_prime.^2 ) .* cos( phi - phi_prime );
%cosTheta_2 = -mu .* mu_prime ...
%    + sqrt( 1 - mu.^2 ) .* sqrt( 1 - mu_prime.^2 ) .* cos( phi - phi_prime );
%phases_fwd = phaseFunc(cosTheta_1);
%phases_back = phaseFunc(cosTheta_2);

kxy.kyPkxImag = k_y + 1i*k_x;
kxy.kyMkxImag = k_y - 1i*k_x;
kxy.magSq = k_x^2 + k_y^2;

% Create the blocks and then the whole matrix for A.  Recall that this
% matrix represents the recurrence relations introduced by the z portion of
% the directional derivative.

A_Block = real(YbarMat*diag(mu_quad.*w_quad')*YbarMat');
A = [A_Block, 0*A_Block; 0*A_Block, -A_Block];

% Create the B matrix one block at a time, being conscious of the
% coordinate change between hemispheres.  First,  we construct half_1 and
```

```
% half_2 matrices, which calculate the contributions of single legendre
% moments to the upper and lower hemispheres.

half_1 = zeros((order+1)^2,(order+1)^2);
half_2 = zeros((order+1)^2,(order+1)^2);

for i = 1:(order+1)^2
    for j = 1:(order+1)^2
        [l,m] = getSHFlm(i);
        [l_prime,m_prime] = getSHFlm(j);
        if m == m_prime
            half_1(i,j) = gees_single(l+1)*createIplus(l_prime,l,m);
            half_2(i,j) = gees_single(l+1)*createIminus(l_prime,l,m);
        end
    end
end

% The final scattering portion of the B matrix, scatterMat, comes from the
% use of the conversion matrix. The Iplus and Iminus terms, as well as left
% multiplication by convMat, form a matrix which converts double spherical
% harmonics to single, then applies the scattering phase function, then
% converts back from single to double.

scatterMat = convMat * [half_1,half_2];

% Create the total B matrix for the first layer.  This is composed of the
% recurrence relations introduced by the x and y portions of the
```

```
% directional derivatives, plus total attenuation times the identity
% matrix, minus the scattering coefficient times the scattering matrix.

B_1 = 1i*k_x*[B_x_derivs, 0*B_x_derivs; 0*B_x_derivs, B_x_derivs] + ...
      1i*k_y*[B_y_derivs, 0*B_y_derivs; 0*B_y_derivs, B_y_derivs] + ...
      mu_t_1 * eye(2*(order+1)^2) - mu_s_1 * scatterMat;

B_1 = round(B_1,8); % Round off at 8 decimal places to kill off imaginary
                    % components which are introduced by small errors from
                    % quadrature.  These are commonly on the order of
                    % 10^-14 or lower, so 8 places will both ensure the
                    % loss of imaginary terms and preserve the function of
                    % the matrix.

% Repeat this for B_2.

B_2 = 1i*k_x*[B_x_derivs, 0*B_x_derivs; 0*B_x_derivs, B_x_derivs] + ...
      1i*k_y*[B_y_derivs, 0*B_y_derivs; 0*B_y_derivs, B_y_derivs] + ...
      mu_t_2 * eye(2*(order+1)^2) - mu_s_2 * scatterMat;

B_2 = round(B_2,8);

% Create vectors for the source contribution term Q.  Begin by initializing
% the vectors.

source_base_up = zeros((order+1)^2,1); % Upper hemisphere portion of a
                                       % vector set in a double spherical
```

```
                                        % harmonic basis.
source_base_down = zeros((order+1)^2,1); % Lower hemisphere portion of a
                                          % vector set in a double spherical
                                          % harmonic basis.
source_base_single = zeros((order+1)^2,1); % Single spherical harmonic
                                            % basis.

% Populate the various source vectors by using the legendre moments and
% conjugate spherical harmonic functions.

for i = 1:(order+1)^2
    [l,m] = getSHFlm(i);
    source_base_up(i) = conj(ybar(l,m,2*mu_in-1,phi_in))*...
        gees_up_f_delta(l+1);
    source_base_down(i) = conj(ybar(l,m,2*mu_in-1,pi+phi_in))*...
        gees_down(l+1);
    source_base_single(i) = ...
        conj(spherHarmlm_mu(l,m,mu_in_single,phi_in))*...
        gees_single_f_delta(l+1);
end

% Create the actual base for the source vector with the proper value for
% f_delta.

if source_toggle == 1
    source_base = convMat*source_base_single;
    source_1 = source_base*mu_s_1*(1 - f_delta);
```

```
    source_2 = source_base*mu_s_2*(1 - f_delta);
else
    source_base = [source_base_up;source_base_down];
    source_1 = source_base*mu_s_1*(1 - f_delta);
    source_2 = source_base*mu_s_2*(1 - f_delta);
end

% Calculate eigenpairs for the top layer A and B pair.  These pairs are
% sorted by the eigenvalues, from lowest (most strongly negative) to
% highest (most strongly positive.)

[V_1,D_1] = eig(-B_1,A); % Calculate eigenpairs.  This is the single most
                         % expensive portion of the code.

% These lines sort both vectors and values.

vals_1 = diag(D_1);
[~,idx_1] = sort(real(vals_1));
vals_1 = vals_1(idx_1);
vecs_1 = V_1(:,idx_1);

% These lines separate the vectors and values into positive and negative
% portions, as well as upper and lower hemisphere portions.  For instance,
% vecs_1_neg_up takes the eigenvectors which correspond to negative
% eigenvalues and keeps the portion which contributes to the upper
% hemisphere of scattered radiance.
```

```
vecs_1_up = vecs_1(end/2+1:end,:);

vecs_1_down = vecs_1(1:end/2,:);

vals_1_neg = vals_1(find(real(vals_1) < -1e-8));

vals_1_pos = vals_1(find(real(vals_1) > 1e-8));

vecs_1_neg = vecs_1(:,find(real(vals_1) < -1e-8));

vecs_1_neg_up = vecs_1_neg(1:end/2,:);

vecs_1_neg_down = vecs_1_neg(end/2+1:end,:);

vecs_1_pos = vecs_1(:,find(real(vals_1) > 1e-8));

vecs_1_pos_up = vecs_1_pos(1:end/2,:);

vecs_1_pos_down = vecs_1_pos(end/2+1:end,:);


% Repeat this process for the second layer.


[V_2,D_2] = eig(-B_2,A);

vals_2 = diag(D_2);

[vals_2,idx_2] = sort(real(vals_2));

vecs_2 = V_2(:,idx_2);

vecs_2_up = vecs_2(end/2+1:end,:);

vecs_2_down = vecs_2(1:end/2,:);

vals_2_neg = vals_2(find(real(vals_2) < -1e-8));

vals_2_pos = vals_2(find(real(vals_2) > 1e-8));

vecs_2_neg = vecs_2(:,find(real(vals_2) < -1e-8));

vecs_2_neg_up = vecs_2_neg(1:end/2,:);

vecs_2_neg_down = vecs_2_neg(end/2+1:end,:);

vecs_2_pos = vecs_2(:,find(real(vals_2) > 1e-8));

vecs_2_pos_up = vecs_2_pos(1:end/2,:);

vecs_2_pos_down = vecs_2_pos(end/2+1:end,:);
```

```
% Calculate the particular solutions for each layer.  Recall that these
% are calculated using matrix inversion from the matrix form of the RTE.

part_1 = ( -(mu_s_1*(1 - f_delta) + mu_a_1) .* A + B_1)\source_1;
part_2 = ( -(mu_s_2*(1 - f_delta) + mu_a_2) .* A + B_2)\source_2;

% Construct the matrix for the application of the Marshak boundary
% condition.  The identity on the left side of the block matrix J is
% applied to scattered radiance in the positive z direction (into the
% medium) whereas the boundaryCoef matrix is defined by Fresnel's law for
% internal reflection.

J = [eye((order+1)^2),-boundaryCoef];

% Construct matrix for final inversion to calculate eigenmoments for the
% homogeneous solution.

% The boundaryMat Matrix applies the Marshak condition to the eigenvectors
% for the upper layer at the boundary.  The moments for eigenvectors
% corresponding to negative eigenvalues are calculated at z = 0, while
% those for eigenvectors corresponding to positive eigenvalues are
% calculated at z = z*, the layer thickness.  That is why an exponential
% decay term is applied to the positive vectors but not the negative ones.

boundaryMat = J*[vecs_1_neg,vecs_1_pos*diag(exp(-thickness.*vals_1_pos))];
```

```
% The interfaceMat matrix applies the condition of equality between
% scattered radiance in the two layers to the eigenvectors of those layers.
% As in boundaryMat, the moments corresponding to the negative vectors of
% the first layer are calculated at z = 0, while those corresponding to the
% positive vectors of the first layer and the negative vectors of the
% second layer are calculated at z = z*, the layer thickness.  Those
% corresponding to positive values in the second layer are not used because
% total scattered radiance must decay to 0 as z approaches infinity, and
% the rates of decay are given by the eigenvalues.

interfaceMat = [[vecs_1_neg*diag(exp(thickness.*vals_1_neg)),...
    vecs_1_pos],-vecs_2_neg];

inversionVec = [-J * part_1; (part_2 - part_1) * ...
    exp(-(mu_a_1 + (1 - f_delta) * mu_s_1) * thickness)];

% The inversionMat matrix is simply the combination of the previous
% matrices, as well as a zero block in the first row representing the fact
% that radiance in the second layer are not directly affected by the
% Marshak condition.

inversionMat = [boundaryMat,zeros(size(boundaryMat,1),...
    size(interfaceMat,2) - size(boundaryMat,2));interfaceMat];

% Perform the matrix inversion to obtain a vector of eigenmoments.

eigen_moments = inversionMat\inversionVec;
```

```
% Separate the eigenmoments into sections coresponding to positive and
% negative eigenvectors for different layers.

c_minus = eigen_moments(1:(order+1)^2); % Moments for top layer negative
                                        % eigenvectors.
c_plus = eigen_moments(1+(order+1)^2:2*(order+1)^2); % Moments for top
                                                     % layer positive
                                                     % eigenvectors.
d_minus = eigen_moments(1+2*(order+1)^2:end); % Moments for the bottom
                                              % layer negative
                                              % eigenvectors.

% Calculate the combined solution for scattered radiance, depending on the
% desired depth.  This will be a vector of double spherical harmonic
% moments.

% First, determine which layer the solution will be calculated for.

if z_depth < thickness

    % In the top layer, start with the particular solution, adjusted for
    % the specified depth.

    final_depth_moments = part_1*exp(-mu_t_1*z_depth/mu_in);

    % Next, add the homogeneous solution one moment and vector combination
```

```
    % at a time.  Positive and negative pairs are added at the same time.

    for i = 1:(order+1)^2
        final_depth_moments = final_depth_moments + ...
            c_minus(i) * vecs_1_neg(:,i) * ...
            exp( z_depth * (vals_1_neg(i)/mu_in )) + ...
            c_plus(i) * vecs_1_pos(:,i) * exp( (z_depth-thickness) * ...
            (vals_1_pos(i)/mu_in ));
    end
else

    % In the bottom layer, start with the particular solution for that
    % layer, adjusted for depth.

    final_depth_moments = part_2*exp(-mu_t_1*thickness/mu_in - ...
    mu_t_2*(z_depth - thickness)/mu_in);

    % Now, add in the components of the homogeneous solution, one vector
    % and moment combination at a time.  Only the negative moments are used
    % in the bottom layer.

    for i = 1:(order+1)^2
        final_depth_moments = final_depth_moments + ...
            d_minus(i) * vecs_2_neg(:,i) * exp( (z_depth-thickness) ...
            * (vals_2_neg(i)/mu_in ));
    end
end
```

```
% Split the vector of double spherical harmonic moments into upward and
% downward portions.

final_moms_up = ((final_depth_moments(1:end/2)));
final_moms_down = ((final_depth_moments(end/2+1:end)));

% Obtain radiance as a function of cosine(theta) for the azimuthally
% symmetric case.  Because of the way spherical harmonics work, this will
% also return the average radiance values across all phi for a given theta.
% Note that two graphs are created here, one for x_up and one for x_down.

[x_out_sym_up,x_out_sym_down,y_out_sym_up,y_out_sym_down] = ...
    doublePGraphGen(getCenterSHF(final_moms_up),...
    getCenterSHF(final_moms_down));

% Obtain a unified graph for radiance as a function of cosine(theta), where
% the radiance at the equator is the mean of its value for each side.

[x_out_sym,y_out_sym] = ...
    doublePGraphGenUnified(getCenterSHF(final_moms_up),...
    getCenterSHF(final_moms_down));

end
```

B.3 dSHEFinit.m

```
% This file creates necessary variables for the use of DSHEF.  Four
% matrices are created:
%
% 1) Recurrence relations introduced by the x derivative.
%
% 2) Recurrence relations introduced by the y derivative.
%
% 3) The Marshak boundary condition, resulting from internal reflectance.
%
% 4) A conversion matrix for translation between vectors of double and
% single spherical harmonic moments.
%
% These matrices will be calculated for orders 1 through 13.  Adding
% functionality for larger orders can be done by repeating the same code
% with a higher value for order.
%
% It is possible to produce these vectors more quickly using Gauss-Legendre
% quadrature, but because the functions used to not have finite polynomial
% expansions.  This means that in general, MATLab's quadgk function will
% return a closer approximation of the integrals use in this calculation.
% However, if speed is more important, the degrees of error are quite
% small.
%
% By Sean Horan, 7/19/2020
```

```
n = 1.4; % The refractive index of the medium used.  If this value changes,
         % this file must be rerun.

% Create the conversion matrices.

cm1 = createConvMatHD(1,1);
cm2 = createConvMatHD(2,2);
cm3 = createConvMatHD(3,3);
cm4 = createConvMatHD(4,4);
cm5 = createConvMatHD(5,5);
cm6 = createConvMatHD(6,6);
cm7 = createConvMatHD(7,7);
cm8 = createConvMatHD(8,8);
cm9 = createConvMatHD(9,9);
cm10 = createConvMatHD(10,10);
cm11 = createConvMatHD(11,11);
cm12 = createConvMatHD(12,12);
cm13 = createConvMatHD(13,13);

% Create derivative matrices and boundary value matrices one at a time for
% each order.  It should be obvious, but just in case, makeDSHEFbdry makes
% the boundary value matrix and makeDerivMats makes the derivative
% matrices.

order = 1;
makeDSHEFbdry;
```

```
bc1 = boundaryCoef;
makeDerivMats;
xd1 = B_x_derivs;
yd1 = B_y_derivs;

order = 2;
makeDSHEFbdry;
bc2 = boundaryCoef;
makeDerivMats;
xd2 = B_x_derivs;
yd2 = B_y_derivs;

order = 3;
makeDSHEFbdry;
bc3 = boundaryCoef;
makeDerivMats;
xd3 = B_x_derivs;
yd3 = B_y_derivs;

order = 4;
makeDSHEFbdry;
bc4 = boundaryCoef;
makeDerivMats;
xd4 = B_x_derivs;
yd4 = B_y_derivs;

order = 5;
```

```
makeDSHEFbdry;
bc5 = boundaryCoef;
makeDerivMats;
xd5 = B_x_derivs;
yd5 = B_y_derivs;

order = 6;
makeDSHEFbdry;
bc6 = boundaryCoef;
makeDerivMats;
xd6 = B_x_derivs;
yd6 = B_y_derivs;

order = 7;
makeDSHEFbdry;
bc7 = boundaryCoef;
makeDerivMats;
xd7 = B_x_derivs;
yd7 = B_y_derivs;

order = 8;
makeDSHEFbdry;
bc8 = boundaryCoef;
makeDerivMats;
xd8 = B_x_derivs;
yd8 = B_y_derivs;
```

```
order = 9;
makeDSHEFbdry;
bc9 = boundaryCoef;
makeDerivMats;
xd9 = B_x_derivs;
yd9 = B_y_derivs;

order = 10;
makeDSHEFbdry;
bc10 = boundaryCoef;
makeDerivMats;
xd10 = B_x_derivs;
yd10 = B_y_derivs;

order = 11;
makeDSHEFbdry;
bc11 = boundaryCoef;
makeDerivMats;
xd11 = B_x_derivs;
yd11 = B_y_derivs;

order = 12;
makeDSHEFbdry;
bc12 = boundaryCoef;
makeDerivMats;
xd12 = B_x_derivs;
yd12 = B_y_derivs;
```

```
order = 13;
makeDSHEFbdry;
bc13 = boundaryCoef;
makeDerivMats;
xd13 = B_x_derivs;
yd13 = B_y_derivs;
```

B.4 makeDSHEFbdry.m

```
% This file creates a matrix for the portion of the Marshak boundary
% condition representing internally reflected radiance which was initially
% directed out of the medium.  Since this matrix is to be applied to DSHEF,
% there is no need to calculate its partner, which would be the matrix
% applied to radiance directed into the tissue.  This other matrix is
% simply identity, due to the orthonormality of the basis.
%
% By Sean Horan, 7/19/2020

tic

% Note that everything is done in terms of mu=cos(theta), rather than just
% theta.  It can be done either way.
```

```
thetaCrit = asin(1/n); % Calculate the critical angle for internal
                       % reflectance.

% Calculate the angle of reflection for a given mu.

muRef = @(mu) sqrt(1 - n^2 .* (1 - mu.^2));

% Calculate the amount of internal reflection for a given mu, according to
% Fresnel's laws.

rFunc = @(mu) 0.5 .* abs( (n * muRef(mu) - mu ) ...
    ./ ( n .* muRef(mu) + mu ) ).^2 ...
    + 0.5 .* abs( ( n .* mu - muRef(mu) ) ...
    ./ ( n .* mu + muRef(mu) ) ).^2;

% Initialize the boundary coefficient matrix.

boundaryCoef = zeros((order+1)^2);

% Calculate the matrix place by place.

for i = 1:(order+1)^2
    for j = 1:(order+1)^2

        % Determine l and m variables for two different double spherical
        % harmonic functions.
```

```
        [l_1,m_1] = getSHFlm(i);
        [l_2,m_2] = getSHFlm(j);

        % Define a function by the product of the two double spherical
        % harmonics chosen, as well as the function for internal
        % reflectance.

        bcFunc = @(mu) 2*pi .* ybar(l_1,m_1,mu,0) ...
            .* ybar(l_2,m_2,mu,0) .* rFunc(mu);

        % Actually calculate the integral, only if the degree of the two
        % double spherical harmonics chosen is the same.  This is just a
        % time saver, since that integral will be zero in any other case.

        if m_1 == m_2
            boundaryCoef(i,j) = quadgk(bcFunc,0,1);
        end
    end
end

toc
```

B.5 makeDerivMats.m

```
% This file creates the matrices for recurrence relations introduced by
% the x and y portions of the directional derivative of the RTE, applied to
% the DSHEF solution method.
%
% By Sean Horan, 7/19/2020

tic

% Initialize the two matrices.

B_x_derivs = zeros((order+1)^2);
B_y_derivs = zeros((order+1)^2);

% Calculate the values, entry by entry.

for i = 1:(order+1)^2
    for j = 1:(order+1)^2

        % Obtain the l and m values for the input and output double
        % spherical harmonic functions.

        [l_in,m_in] = getSHFlm(i);
        [l_out,m_out] = getSHFlm(j);

        % Defune a function for the product of two double spherical
        % harmonics, without their exponential parts, times the sine of mu.
        % We split the integral in this way to deal properly with both the
```

```
        % mu and phi portions.  Unlike in makeDSHEFbdry, we cannot simply
        % assume zeros when m_1 != m_2, because of the trig introduced
        % by the directional derivatives.  These are in turn introduced by
        % the coordinate change from polar to Cartesian.

        mufunc = @(mu) 2*getKlm(l_in,m_in)*getKlm(l_out,m_out)*...
            legendrelm(l_in,m_in,2*mu-1)...
            .*legendrelm(l_out,m_out,2*mu-1).*sqrt(1 - mu.^2);

        % Calculate that integral across a hemisphere.

        mucomp = quadgk(mufunc,0,1);

        % Calculate each matrix entry.  The entries in B_x_derivs are given
        % by the previous integral times the integral of product of the
        % exponential functions of the two double spherical harmonic
        % functions times the cosine of phi for x and the sine of phi for
        % y.

        B_x_derivs(i,j) = mucomp*quadgk(@(phi) ...
            exp(1i.*phi.*(m_in - m_out)).*cos(phi),0,2*pi);
        B_y_derivs(i,j) = mucomp*quadgk(@(phi) ...
            exp(1i.*phi.*(m_in - m_out)).*sin(phi),0,2*pi);
    end
end

toc
```

B.6 createConvMatHD.m

```
function [ convMat ] = createConvMatHD( dSHForder, sSHForder )

% This file creates matrix for the conversion of double to single spherical
% harmonic vectors.  This matrix is composed of two halves, one converting
% the double spherical harmonics for the upward hemisphere, and one
% converting the double spherical harmonics for the downward hemisphere.
%
% By Sean Horan, 7/19/20

% Initialize the two matrix blocks.

convUp = zeros((dSHForder+1)^2,(sSHForder+1)^2);
convDown = zeros((dSHForder+1)^2,(sSHForder+1)^2);

% Calculate the two blocks simultaneously, entry by entry.

for i = 1:(sSHForder+1)^2
    for j = 1:(dSHForder+1)^2

        % Obtain the l and m values for the output single spherical
        % harmonic and the input double spherical harmonic, respectively.
```

```
        [l_in,m_in] = getSHFlm(i);
        [l_out,m_out] = getSHFlm(j);

        % Calculte each term, if and only if the m values for input and
        % output are identical.  This is due to the structure of both
        % single and double spherical harmonics: the exponential term of
        % each is identical and causes an integral to be zero whenever the
        % degrees are unequal.  Note that these functions are given as a
        % product of their components.

        if m_in == m_out
            convUp(j,i) = sqrt(8)*pi*getKlm(l_in,m_in)*getKlm(l_out,m_out)*...
                quadgk(@(mu) legendrelm(l_in,m_in,mu) .* legendrelm(l_out,m_out,2*mu - 1
            convDown(j,i) = sqrt(8)*pi*getKlm(l_in,m_in)*getKlm(l_out,m_out)*...
                quadgk(@(mu) legendrelm(l_in,m_in,-mu) .* legendrelm(l_out,m_out,2*mu -
        end
    end
end

% Combine the two blocks into a final matrix.

convMat = [convUp;convDown];

end
```

B.7 createIPlus.m

```
function [ output ] = createIplus( l_prime,l,m )
% This function caluclates the the integral of the l',m double spherical
% harmonic function and the l,m single spherical harmonic function.  This
% is used in the construction of the scattering portion of the B matrix for
% DSHEF.  It allows the conversion from the single spherical harmonic
% expansion of the scattering phase function back to double spherical
% harmonics.
%
% By Sean Horan, 7/19/2020.

myFunc = @(mu,phi) sqrt(2)*2*pi*getKlm(l_prime,m).*getKlm(l,m)...
    .*legendrelm(l_prime,m,2*mu-1).*legendrelm(l,m,mu);
output = quadgk(myFunc,0,1);


end
```

B.8 createIPlus.m

```
function [ output ] = createIminus( l_prime,l,m )
```

```
% Make I_minus amount for given l_prime, l and m (used in scattering
% operator of RTE for DSHEF)

myFunc = @(mu) sqrt(2)*2*pi*getKlm(l_prime,m).*getKlm(l,m)...
    .*legendrelm(l_prime,m,2*mu-1).*legendrelm(l,m,-mu);
output = quadgk(myFunc,0,1);

end
```

B.9 doublePGraphGen.m

```
function [ x_up,x_down,y_up,y_down ] = doublePGraphGen( gees_up,gees_down )
% This function creates x and y values for a plot based on the central
% moments of a vector of double spherical harmonics.  It should be noted
% that this vector must already be pared down to the central moments, and
% should be split into one for the upwardly directed radiance (gees_up) and
% one for the downward directed radiance (gees_down).  Note that there are
% two plots given: one for the upper hemisphere and one for the lower.
%
% By Sean Horan, 7/19/2020

% Take 100 linearly spaced angles from zero to pi, calculate their
% midpoints and then take the cosine.  This could be done more elegantly
% but it's a big priority for me (just being honest.)
```

```
thetas = linspace(pi,0,100);
theta_mids = zeros(1,99);
for i = 1:length(theta_mids)
    theta_mids(i) = (thetas(i) + thetas(i+1))/2;
end

x = cos(theta_mids);

% Identify which angles are above and below the hemisphere.

x_up = x(find(x >= 0));
x_down = x(find(x <= 0));

% Initialize values for y.

y_up = 0*x_up;
y_down = 0*x_down;

N = length(gees_up);

% Add contributions to y_up and y_down based on each portion of the
% input vectors.

for i = 0:N-1
    y_up = y_up + gees_up(i+1) * sqrt(2) * getKlm(i,0) * ...
        legendreP(i,2*x_up-1);
```

```
    y_down = y_down + (gees_down(i+1) * sqrt(2) * getKlm(i,0) * ...
        legendreP(i,-2*x_down-1));
end

end
```

B.10 doublePGraphGenUnified.m

```
function [ x,y ] = doublePGraphGenUnified( gees_up,gees_down )
% This function creates x and y values for a plot based on the central
% moments of a vector of double spherical harmonics.  It should be noted
% that this vector must already be pared down to the central moments, and
% should be split into one for the upwardly directed radiance (gees_up) and
% one for the downward directed radiance (gees_down).  This function
% returns a single plot, where the radiance at the equator is the mean of
% the contributions from each hemisphere.
%
% By Sean Horan, 7/19/2020

% Take 100 linearly spaced angles from zero to pi, calculate their
% midpoints and then take the cosine.  This could be done more elegantly
% but it's a big priority for me (just being honest.)

thetas = linspace(pi,0,100);
```

```
theta_mids = zeros(1,99);
for i = 1:length(theta_mids)
    theta_mids(i) = (thetas(i) + thetas(i+1))/2;
end

x = cos(theta_mids);

% Identify which angles are above and below the hemisphere.

x_up = x(51:end);
x_down = x(1:49);
x_zero = x(50);

% Initialize values for y.

y_up = 0*x_up;
y_down = 0*x_down;
y_zero = 0;

N = length(gees_up);

% Add contributions to y_up, y_down and y_zero based on each portion of the
% input vectors.

for i = 0:N-1
    y_up = y_up + gees_up(i+1) * sqrt(2) * getKlm(i,0) * ...
        legendreP(i,2*x_up-1);
```

```
    y_down = y_down + (gees_down(i+1) * sqrt(2) * getKlm(i,0) * ...
        legendreP(i,-2*x_down-1));
    y_zero = y_zero + 0.5*(gees_up(i+1) * sqrt(2) * getKlm(i,0) * ...
        legendreP(i,2*x_zero-1) + ...
        (gees_down(i+1) * sqrt(2) * getKlm(i,0) * ...
        legendreP(i,-2*x_zero-1)));
end

y = [y_down,y_zero,y_up];

end
```

B.11 getCenterSHF.m

```
function [ outVec ] = getCenterSHF( inVec )
% This function extracts the central (m == 0) moments from a vector of
% spherical harmonic functions.  For use with double spherical harmonic
% moments, simply split the vector into two halves and apply this function
% to each.
%
% By Sean Horan, 7/19/2020

n = length(inVec);
outVec = zeros(sqrt(n) - 1,1);
```

```
for i = 1:n
    [l,m] = getSHFlm(i);
    if m == 0
        outVec(l+1) = inVec(i);
    end
end
```

B.12 getSHFlm.m

```
function [l,m] = getSHFlm(index)
% This function takes in an index value for a vector of single spherical
% harmonic functions and outputs the desired l and m values for its index
% in the (order, degree) paradigm.

    l = ceil(sqrt(index)) - 1;
    m = index - (l + 1).^2 + l;
end
```

B.13 ybar.m

```
function [ output ] = ybar( l,m,mu,phi )
```

```
% Calculate the double spherical harmonic function (ybar) for a given order
% (l), degree (m), mu and phi.
%
% By Sean Horan, 7/19/2020.

    % Make sure that phi is going in the desired direction.

    if size(phi,2) == 1
        phi = phi';
    end

    output = getKlm(l,m).* sqrt(2) .* exp(1i*m*phi) .* legendrelm(l,m,2*mu - 1);

end
```

B.14 legendrelm.m

```
function [ output ] = legendrelm(l,m,x)
% Compute associated legendre polynomial of order l, degree m, evaluated at
% x.  This works for negative values of m and is used in computing
% spherical harmonics.
%
% By Sean Horan, 7/19/2020.
```

```
if abs(m) > l
    output = 0;
    return;
end

if m >= 0
    tempArray = legendre(l,x);
    index = m+1;
else
    % Note that this will not produce the correct value for functions other
    % than order l, degree m.
    tempArray = (-1)^(m) * (factorial(l+(m))/factorial(l-(m))) * legendre(l,x);
    index = -m + 1;
end
    output = tempArray(index,:);
end
```

B.15 GL.m

```
function [ mus, weights ] = GL( order )

% This function determines the values of mu and weights for the use of
% gaussian quadrature on [-1,1].  This method was given in "Spectral
% Methods in MATLAB" by Trefethen (2000) and based on code written by A.D.
```

```
% Kim (2019).
%
% By Sean Horan, 7/19/2020


betas = 0.5 ./ sqrt( 1 - (2:2:2*(order - 1)).^-2 );
mat = diag(betas,1) + diag(betas,-1);
[V,D] = eig(mat);
temp = diag(D);
[mus,idx] = sort(temp);
weights = 2*(V(1,idx).^2);


end
```